Search for Light Bosons in Exotic Decays of the 125 GeV Higgs Boson

Dissertation

zur Erlangung des Doktorgrades
an der Fakultät für Mathematik,
Informatik und Naturwissenschaften
Fachbereich Physik
der Universität Hamburg

vorgelegt von

Danyer Pérez Adán

aus

Havanna, Kuba

Hamburg
2020

Hiermit erkläre ich an Eides statt, dass ich die vorliegende Dissertationsschrift selbst verfasst und keine anderen als die angegebenen Quellen und Hilfsmittel benutzt habe.

I hereby declare, on oath, that I have written the present dissertation by my own and have not used other than the acknowledged resources and aids.

Hamburg, den 11. Februar 2020 Danyer Pérez Adán

Gutachter der Dissertation:	Dr. Alexei Raspereza Prof. Dr. Elisabetta Gallo
Zusammensetzung der Prüfungskommission:	Prof. Dr. Robin Santra Prof. Dr. Elisabetta Gallo Dr. Sarah Heim Prof. Dr. Bernd A. Kniehl Dr. Alexei Raspereza
Vorsitzender der Prüfungskommission:	Prof. Dr. Robin Santra
Datum der Disputation:	5. Mai 2020
Vorsitzender des Fach-Promotionsausschusses Physik:	Prof. Dr. Günter H. W. Sigl
Leiter des Fachbereichs Physik:	Prof. Dr. Wolfgang Hansen
Dekan der Fakultät MIN:	Prof. Dr. Heinrich Graener

ABSTRACT

A search for pairs of light bosons produced from decays of the 125 GeV Higgs boson is presented. The search covers the light boson mass region where the particle could have an enhanced decay rate to a pair of τ leptons, according to different models and scenarios. The leptonic decay channels corresponding to the 4τ and $2\mu 2\tau$ final states are used. The search is based on proton-proton collisions collected by the CMS experiment in 2016 at a center-of-mass energy of $\sqrt{s} = 13$ TeV. This dataset corresponds to an integrated luminosity of 35.9 fb^{-1}.

The analysis is motivated by many theories beyond the Standard Model that suggest modifications in the Higgs sector. The prevailing tendency among these new models is to extend the group structure of the scalar sector, thus resulting in an increased number of physical states in their spectrum. The additional bosons could couple to both the 125 GeV Higgs boson and the rest of the particles in the theory, which allows their detection through different production and decay mechanisms.

Two different approaches used for the analysis of the data are presented. The first strategy targets boosted event topologies, occurring for light bosons with masses between 4 and 15 GeV. The second method employs a modified event selection technique combined with a more powerful final discriminant to be able to extend the mass range up to 21 GeV. In both approaches, no significant deviation beyond the expectation from the Standard Model is observed. Observed and expected upper limits at 95% confidence level on the product of the Higgs boson production cross-section relative to that in the Standard Model and the branching fraction into the 4τ final state are set. Interpretations of the experimental results in the context of a specific theoretical model are also provided.

ZUSAMMENFASSUNG

Diese Arbeit präsentiert eine Suche nach neuen leichten Bosonen, die paarweise im Zerfall des 125-GeV-Higgs-Bosons entstehen. Die Suche deckt einen Bereich der Masse der leichten Bosonen ab, für den man erwartet dass diese Teilchen mit grösserer Wahrscheinlichkeit in ein Paar von τ Leptonen zerfallen, wie von verschiedenen Modellen vorhergesagt. Ereignisse werden untersucht bei denen im Endzustand vier Leptonen auftreten, entweder vier τ Leptonen oder zwei τ und zwei μ Leptonen. Für die Suche werden die vom CMS Experiment im Jahr 2016 bei einer Schwerpunktsenergie von $\sqrt{s} = 13$ TeV aufgezeichneten Proton-Proton-Kollisionen verwendet. Die analysierte Datenmenge enspricht einer integrierten Luminosität von 35.9 fb^{-1}.

Die Analyse ist dadurch motiviert dass in vielen Theorien neuer Physik ausserhalb des Standardmodells Modifizierungen des Higgs Sektors vorhergesagt werden. Eine vorherrschende Tendenz ist die Erweiterung der Gruppenstruktur des skalaren Sektors, die zu einer erhöhten Anzahl von physikalischen Zuständen im Teilchenspektrum führt. Die zusätzlichen Bosonen könnten sowohl an das 125-GeV-Higgs-Boson als auch an andere bekannte Teilchen koppeln, was ihre Detektierung durch verschiedene Produktions- und Zerfallfsmechanismen ermöglicht.

Zwei verschiedene Ansätze werden in der Analyse der Daten verfolgt. Die erste Strategie ist es nach den neuen Teilchen in *boosted* (kollimierten) Ereignistopologien zu schauen, die man für leichte Bosonen mit Massen zwischen 4 und 15 GeV erwartet. In der zweiten Methode wird eine modifizierte Ereignisselektion mit einer speziellen schlagkräftigen multivariaten Signal-zu Untergrunddiskriminierung kombiniert, die es ermöglicht den untersuchten Massenbereich bis auf 21 GeV zu erweitern. Als Ergebnis stellt sich heraus dass für beide Ansätze die Daten mit den Raten der Untergrundprozesse, die vom Standardmodell vorhergesagt werden, übereinstimmen, d.h. es wird kein signifikanter Überschuss beobachtet der die Präsenz neuer Teilchen anzeigen würde. Aus den Daten werden obere Ausschlussgrenzen auf 95% *Confidence Level* auf das Produkt des Wirkungsquerschnittes für Higgs Boson Produktion relativ zum Standardmodell und des Zerfalls-Verzweigungsverhältnisses in den 4τ Endzustand bestimmt und mit den erwarteten Grenzen verglichen. Die erzielten experimentellen Resultate werden auch im Kontext spezifischer Modelle neuer Physik erörtert und interpretiert.

CONTENTS

CHAPTER

1

INTRODUCTION

For many years the human being has been trying to conceive a theory of the universe that is beautiful enough to be able to describe all phenomena existing in nature, and sufficiently consistent to be repeatedly tested and verified by experimental results. After having deeply studied the results of many experiments over the last centuries, scientists decided to take the old route that invites to examine physical systems based on their elementary constituents. This led to the emergence of the field of *particle physics* in the 20th century, a mathematical formulation of the behavior of systems at fundamental level mostly based on theories also born in this century such as Special Relativity (SR) [1] and Quantum Mechanics (QM) [2]. Within this branch of physics, for quite a long time, there has been a theory that, so far, meets one of the two pillars mentioned at the beginning of this chapter. The name given to that mathematical construction is the Standard Model (SM). Certainly, the SM has been a remarkably successful theory that has had the bliss that no confirmed experimental evidence has been found against it [3–6]. Just a few years ago, the already theoretically-predicted missing piece of the SM was found at the Large Hadron Collider (LHC), when the two largest collaborations announced the discovery of a particle with characteristics similar to those of the Higgs boson [7,8]. That breakthrough further strengthened the credibility of the SM, and once more demonstrated the high degree of predictivity of the theory. However, it is notorious that the SM is an incomplete theory, due to the impossibility of incorporating all the forces known in nature into its theoretical framework. The exclusion of gravity from the theory is not the only drawback, there exists another variety of problems to be accounted for. The list of limitations of the SM comprises the absence of an explanation for the dark matter and the dark energy, the incapability to generate a sufficient amount of baryon asymmetry, the hierarchy problem, and many others. All this, together with the inexplicable group structure and number of parameters presented, leaves the SM far from being the ultimate theory of the universe.

In pursuit of this goal, physicists have continued developing new models capable to reach the magnificent experimental performance of the SM, but also with the possibility to solve

some of its deficiencies. Novel approaches like supersymmetry, grand unified theories, quantum gravity, and string theory offer diverse solutions for one or several problems [9, 10]. One of the SM sectors that mostly undergo modifications in the new models is that involving the Higgs boson, partly due to the recent discovery of this scalar boson and its low production rate at the LHC, which limits the possibilities of precisely measuring all the properties of the particle. Additionally, the versatility presented by the scalar fields makes them very suitable for new models willing to provide answers to the various unknown aspects. In particular, the hierarchy problem is intrinsically related to the scalar nature of the SM Higgs boson, therefore, any attempt to try to unravel it implies modifications in that sector.

The changes entailed by the design of the new theories are generally accompanied by the inclusion of a larger number of scalars in their field content; in other cases, they bring certain modifications in the interactions and properties of the discovered 125 GeV mass eigenstate. For instance, most supersymmetric models require the presence of an additional $SU(2)$ doublet, in relation to the SM, in order to ensure holomorphy and help to cancel anomalies [11], which is then reflected in a larger number of scalar physical states. At the same time, these and other types of models allow the existence of mixing among the different scalar components of the fields, thus altering the couplings of the SM-like Higgs boson with the rest of particles, compared to those predicted in the SM. Those are parts of the reasons why, currently, the search for additional bosons and the high-precision tests are the preferential ways to probe the Higgs sector beyond the SM.

In the current context, there are still conditions that favor those models possessing a light boson in their spectrum [12]. In the presence of coupling between the light bosons and the SM-like Higgs, there may be exotic decays of the 125 GeV state into pairs of these light particles, when kinematically allowed. The light bosons tend to couple to other SM particles as well, so, in principle, they could be detected via these interactions, either in production or decay mode. However, in most theories, the couplings of the light bosons to SM fermions are significantly reduced due to a common small parameter, therefore, its detection through direct production mechanisms becomes highly unfeasible. On the contrary, in decays, the suppression is common to all partial decay widths, therefore, the small parameter does not produce any effect on the branching ratios. All that constitutes a great incentive to look for light bosons produced in decays of the SM-like Higgs boson. This thesis embarks on that search using the decays of light bosons into pairs of leptons, specifically those involving taus and muons.

The thesis is structured as follows. The next chapter is dedicated to reviewing the most fundamental theoretical aspects concerning the field of particle physics. The third chapter is devoted to the physics related to the Higgs sector. Aspects of the scalar sector are discussed both within the SM framework and beyond. In turn, the introduction of the new theories serves to explain in more detail the motivations for this work. The fourth chapter is intended to present the experimental setup where this work is carried out, i.e., the CMS experiment at the LHC. The fifth chapter introduces the physics analysis and describes the first approach adopted in the search. A review of some statistics topics indispensable for data analysis and processing is also included. The sixth chapter addresses an alternative approach designed to increase the effectiveness of the search over a wider range of light boson masses. Also in this chapter, interpretations of the experimental results in the context of a specific theoretical model are provided. The last chapter is dedicated to summarizing the work presented in this thesis, as well as discussing the perspectives for the future.

CHAPTER

2

ELEMENTS OF THEORY

Contents

The almost contemporaneous emergence of the SR and QM, two of the greatest physics innovations of the last century, challenged our real knowledge of the universe. On the one hand, SR allowed us to describe phenomena that manifest themselves at very high speeds such as length contraction, time dilation, universal speed limit, relativity of simultaneity and mass-energy equivalence. On the other hand, QM proposed a completely new understanding of processes at very small scales, providing us with impressive predictions in subatomic structures. New concepts like quantization, wave-particle duality and uncertainty principle appeared to drastically change the way we used to understand the microscopic world.

Physicists did not take long to confront simultaneously both theories, and by doing so, new phenomena that could not be explained by the physics at that time arose. Einstein had taught us that mass and energy are concepts of identical nature, whereas Heisenberg's uncertainty principle [13] implied that the energy of a system can widely fluctuate over a small interval of time. So, a substantial variation of the energy in a system could lead to the appearance of new matter, and any naive attempt to construct a relativistic theory of the one-particle Schrödinger equation [14] would fail. Several associated problems were found [15] when Klein-Gordon and Dirac tried to promote the non-relativistic Schrödinger theory to a relativistic one. The mere fact of giving a relativistic treatment to quantum mechanics unequivocally led to a multi-particle relativistic quantum theory; this formalism was called Quantum Field Theory (QFT).

This chapter is devoted to QFT, offering a glimpse into the most elementary aspects that make this formalism the fundamental basis of modern particle physics. From the SM of particle physics to most of the physics beyond the SM, all of them rely on QFT; so once the fundamentals of QFT are known, one can build any particular theory. Being the small theoretical review presented in this chapter a very well-known physics, it is worth emphasizing that most of the elements here treated are part of the content of several textbooks [15–20]. Those books constitute the main bibliography utilized for this chapter, other more topic-specific references will be included along the different sections.

2.1 Classical Field Theory

As the development of theoretical physics progressed, scientists realized that mathematical models of reality, such as Maxwell's theory of electromagnetism, could be compactified within the same framework through a variational principle. Later, this was also implemented in the special and general theories of relativity [21]. This mathematical construction was not only

useful in deriving the equations of motion, but also an important instrument for identifying symmetries of the theory and, therefore, knowing the conserved physical quantities.

2.1.1 Lagrangian Field Theory

In the classical field theory, each point in space-time is associated with a continuous physical quantity denoted as $\phi(x^\mu)$ (the real scalar field is chosen for simplicity). As it is commonly used, x^μ has been taken to denote the space-time four-vector. Any classical field theory tends to be expressed mathematically by using a Lagrangian density that is subjected to an action principle [16]

$$S = \int d^4x \mathcal{L}(\phi(x^\mu), \partial_\mu \phi(x^\mu)). \tag{2.1}$$

Now the principle of least action can be applied to obtain the equation of motion for the field $\phi(x^\mu)$; the general form of this equation is the so-called Euler-Lagrange equation of the calculus of variations, whose solutions make stationary the action S in an arbitrarily small neighborhood of $\phi(x^\mu)$. Another important quantity, essential for the canonical quantization formalism, is the canonically conjugate field defined as

$$\pi(x^\mu) = \frac{\partial \mathcal{L}}{\partial \dot{\phi}(x^\mu)}. \tag{2.2}$$

Taking the equal time Poisson bracket of the field $\phi(x^\mu)$ and its conjugate field $\pi(x^\mu)$ yields [17]

$$\begin{aligned} \{\phi(\boldsymbol{x}, t), \pi(\boldsymbol{x'}, t)\}_{PB} &= \delta^3(\boldsymbol{x} - \boldsymbol{x'}), \\ \{\phi(\boldsymbol{x}, t), \phi(\boldsymbol{x'}, t)\}_{PB} &= \{\pi(\boldsymbol{x}, t), \pi(\boldsymbol{x'}, t)\}_{PB} = 0, \end{aligned} \tag{2.3}$$

where $\mathbf{x}$ indicates a spacial vector and $\{\cdot, \cdot\}_{\mathrm{PB}}$ refers to the classical Poisson bracket. The Eq. (2.3) is analogous to the relation between x_i and p_i in classical mechanics, the one that was then transformed into a commutation relation of two operators and gave birth to the QM. Thus, it is not unreasonable to think that the same approach could be applied to the field and its conjugate; and indeed, this procedure is known as canonical quantization and will be treated later (see Subsec. 2.3.1).

2.1.2 Conservation Laws

As already mentioned, the Lagrangian density also allows knowing the different transformations that leave invariant the action. A mathematician named Emmy Noether came up with one of the most elegant theorems of field theory; this directly links the symmetries found in a Lagrangian density with the conservation laws that obey the system described by this Lagrangian [22]. Mathematically, the theorem is based on assuming infinitesimal changes in coordinates $\delta x^\mu = x'^\mu - x^\mu$ and an infinitesimal variation in the field $\delta\phi(x^\mu) = \phi'(x'^\mu) - \phi(x^\mu)$. The total variation of the Lagrange density is required to be equal to zero under these trans-

formations, then

$$\frac{\partial f_\mu}{\partial x_\mu} = 0,$$
$$f_\mu = \frac{\partial \mathcal{L}}{\partial(\partial^\mu \phi)}\delta\phi - (\frac{\partial \mathcal{L}}{\partial(\partial^\mu \phi)}\frac{\partial \phi}{\partial x^\nu} - g_{\mu\nu}\mathcal{L})\delta x^\nu, \tag{2.4}$$

where $\partial^\mu \equiv \frac{\partial}{\partial x_\mu}$ and $g_{\mu\nu}$ is the metric tensor. The first equation is easy to associate with the differential form of the continuity equation in electrodynamics. Just as in electrodynamics this relation implies the conservation of the electric charge, in this case, it implies the conservation of a quantity whose current density is given by f_μ. Noether's theorem then reveals itself: *Each continuous symmetry transformation leads to a conservation law.* Some important particular cases are highlighted below.

Translational invariance: Only translations in space-time $x'^\mu = x^\mu + \epsilon^\mu$ are assumed. In this case, being $\phi(x^\mu)$ a scalar, the variation of this is expected to vanish. Then Eq. (2.4) takes the form $\partial^\mu \mathcal{T}_{\mu\nu}\epsilon^\nu = 0$. The magnitude $\mathcal{T}_{\mu\nu}$ is called the canonical energy-momentum tensor and, since each ϵ^ν represents an independent translation, there are four conserved quantities ($\nu = 0, \ldots, 3$). These four quantities are the components of the energy-momentum four-vector and correspond to the energy and momentum conservation law.

Lorentz (Rotational) invariance: Apart from pure translations, rotations also form an important class of transformations in space-time. The most general form of these rotations in Minkowski space involves mixtures between spatial and temporal coordinates. In differential form, the transformation is expressed as: $x'^\mu = x^\mu + \delta\omega^{\mu\nu}x_\nu$, where ω is antisymmetric. Now, when applying Eq. (2.4), the resulting expression reads $\partial^\mu \mathcal{M}_{\mu\nu\lambda}\delta\omega^{\nu\lambda} = 0$, where the tensor $\mathcal{M}_{\mu\nu\lambda}$, antisymmetric on indices $\nu\lambda$, plays the role of tensor of angular momentum. Due to the fact that this tensor is antisymmetric, it contains six independent components, thus implying six conserved quantities. Those are the three components of the orbital angular momentum and three more components of the spin angular momentum.

Internal transformation invariance: Another type of symmetry transformation completely different from the previous two is the so-called internal symmetry transformation. These symmetry transformations account for additional degrees of freedoms that the fields possess; that could be the case of field components that transform into each other under this type of transformations. A possible differential form for a field variation given such a transformation (space-time translations or rotations are now ignored $\delta x_\mu = 0$) could be $\delta\phi_a = i\varepsilon \sum_b \lambda_{ab}\phi_b$. Then, when plugging in this expression in Eq. (2.4), a constant of the motion called Noether charge shows up. Some examples of Noether charges very often used in particle physics are the electric charge, hypercharge, color charge, and isospin.

It is evident the important role that symmetries play in explaining the origin of the conservation laws. The significance of symmetries in modern physics is enormous, and specifically in QFT, symmetries become the backbone of its mathematical construction. That is why the next section is especially dedicated to group theory, a crucial element in the formulation of any theoretical model in particle physics.

2.2 Review of Group Theory in QFT

Although group theory is a discipline of mathematics [23–28], it is a subject that concerns any who is involved in the study of fundamental physics. Group theory is the mathematics underlying the concept of symmetry, and as seen before, symmetry can provide information about the constants of motion of a system. The notion of symmetry already appears in classical physics with concepts like the principle of equivalence of inertial frames or the gauge invariance of Maxwell's equations, but it is in QM when this becomes even more important. In QM, concepts like indistinguishability of identical particles or degeneracy of states are profoundly related to the group structure embedded in a given physical system. Moreover, the idea of fundamental constituents of matter is reflected in the indivisibility character and classification power that irreducible representations provide to the group theory. The purpose of this section is to go over the main ingredients of group theory, focusing particularly on Lie groups, which have extensively been used in particle physics. The content of this section is mainly based on the two references [25, 28], although other references were also consulted for specific topics.

Generally, a group is a non-empty set G equipped with one binary operation (represented by $\circ$) that satisfies the following axioms:

1. Closure: If $a \in G$ and $b \in G$, then $a \circ b \in G$
2. Associativity: $a \circ (b \circ c) = (a \circ b) \circ c$ for all $a, b, c \in G$
3. There is an element $e \in G$ called the identity such that $a \circ e = e \circ a = a$ for any $a \in G$
4. For each $a \in G$, there is an element $d \in G$ called the inverse of a such that $a \circ d = e = d \circ a$

Additionally, a group is said to be abelian if its operation is commutative: $a \circ b = b \circ a$ for all $a, b \in G$, and a group for which this is not true is said to be non-abelian. Groups can be classified according to whether they are finite or infinite, discrete or continuous. An example of a finite discrete group is the permutation symmetric group S_n, while the so-called "additive group of integers" is part of the infinite discrete groups [24]. However, a continuous group is necessarily infinite, since any infinitesimal change in the label (parameter) of the group would give rise to a new group element. Among the continuous groups are the Lie groups, which are the main subject of this section. In not strictly rigorous terms, one could say that a Lie group is a continuous group whose elements are described by one or more real parameters. Lie groups play an important role in subjects like infinite-dimensional representation theory, algebraic topology, and Riemannian geometry [25]; and in physics, they have become a fundamental tool to construct modern quantum field theories.

2.2.1 Group Representations

Since the definition of a group is quite abstract, it is natural to wonder how this concept is handled algebraically. Part of the answer is contained in the concept of *group representation*. A representation of a group provides a realization of the group action by means of the group of transformations of a certain mathematical structure. More formally, one can say that a group representation is a group homomorphism from the group to the group of invertible linear maps on a vector space [28], such that the map $\pi(g)$, where $g \in G$, satisfies the relation

$\pi(g_1)\pi(g_2) = \pi(g_1 \circ g_2)$ for all $g_1, g_2 \in G$. If in addition, the map is isomorphic, that is, one-to-one, then the representation is said to be faithful; otherwise, it is unfaithful.

It is easy to see now that the notion of representing group elements by matrices is intuitive, due to the fact that these encode linear maps. The standard action of matrices on vectors in a given vector space becomes a natural way to represent the group action. For example, when thinking of rotation in the 3-dimensional space (3D rotation group, often denoted $SO(3)$), one typically has in mind a 3×3 matrix. In this case, the 3×3 matrix is orthogonal since a rotation is a distance-preserving transformation. When this case is generalized to any dimension n, then such rotations are covered by the group of $n \times n$ orthogonal matrices of determinant 1, the so-called special orthogonal group, denoted as $SO(n)$.

In principle one can construct many different representations of a group, however, it is important to focus on some specific type of representations that really capture the essence of the group's action. The next example shows how one can construct different representations of the same group. The example makes use of the symmetric group S_2, which can be viewed as a group composed of two operations on two different objects: the first one swaps the objects (non-identity element) and the second one leaves them as they are (identity element). Calling the first group element S and the second E, a 1-dimensional representation of this group can be easily constructed by assigning $\rho(S) = -1$ and $\rho(E) = 1$, where $\rho(\cdot)$ denotes a specific representation of the element $\cdot$, and the group operation is the real number multiplication. A 2-dimensional representation can be constructed as well if the elements $\rho'(S) = \left(\begin{smallmatrix} 0 & 1 \\ 1 & 0 \end{smallmatrix}\right)$ and $\rho'(E) = \left(\begin{smallmatrix} 1 & 0 \\ 0 & 1 \end{smallmatrix}\right)$ are used under the matrix multiplication operation. As seen in this example, many different representations of the same group can be built, and sometimes even an infinite number of them. Coming back to the previous example, one can take two $n \times n$ matrices being $\mathbb{I}_n$ (identity) the first one and $-\mathbb{I}_n$ the second one. Under matrix multiplication, these two matrices will furnish an n-dimensional representation of the S_2 group. So, by varying the dimension n, an infinity of representations could be obtained. However, it will be seen that this mere fact is not the real question that representation theory needs to answer.

2.2.1.1 Equivalent Representations

It is well known from linear algebra that two matrices related by a similarity transformation represent the same linear operator under two possibly different bases. It is easy to show that a representation of a group element $\rho(g)$ could be converted into another representation by means of a similarity transformation. Let the matrix S be invertible, and

$$\rho'(g) = S^{-1}\rho(g)S, \tag{2.5}$$

then it can be proven through the group composition law that, in fact, $\rho'(g)$ is also a representation $\rho'(g_1)\rho'(g_2) = \rho'(g_1 \circ g_2)$. It can be thought of $\rho(g)$ and $\rho(g')$ as being the same representation with different choices of basis. In such a case, the representations $\rho(g)$ and $\rho(g')$ are said to be *equivalent*.

2.2.1.2 Irreducible Representations

Now, coming back again to the example of the S_2 group. It was seen that a n-dimensional representation of this group can be generated by constructing two block-diagonal matrices,

namely $\rho_n(S) = \underbrace{\rho(S) \oplus \ldots \oplus \rho(S)}_{n}$ and $\rho_n(E) = \underbrace{\rho(E) \oplus \ldots \oplus \rho(E)}_{n}$. But this does not reveal anything new about the group structure, the same result could be simply obtained using the building block representation $\rho(\cdot)$. The representation $\rho_n(\cdot)$ is known as *reducible*, and it is usually expressed as a direct sum of the representations it reduces into. Since the 1-dimensional representation $\rho(\cdot)$ can not be decomposed into smaller ones, it is clearly called *irreducible*. The main task of representation theory is to determine whether a given representation is irreducible or not, and to enumerate all possible irreducible representations (irreps) of a group.

One interesting fact that should not be overlooked is the role conferred to irreps in physics. Introducing the term "irreducibility" in physics leads instantly to think of the concept of fundamental constituents. Both concepts were a matter of discussion within the physics community during the twentieth century; their unquestionable connection began to give mathematical structure to the way the microworld behaved. The work of many decades trying to make the math fit eventually gave rise to the emergence of fundamental particle physics.

2.2.1.3 Unitary Representations

Other interesting classes of representations on complex vector spaces are the *unitary* group representations, which preserve the notion of length given by some inner product. These are representations characterized by the group of complex matrices U that satisfy

$$UU^\dagger = U^\dagger U = \mathbb{I}, \tag{2.6}$$

where $\mathbb{I}$ is the identity matrix. This group of representations is particularly important for QM, where they are extensively used.

2.2.1.4 Two Important Theorems

There are two theorems in representation theory that, because of their relevance, are impossible to ignore.

Schur's lemma: The first one is the so-called Schur's lemma [28], which provides a criterion that must be satisfied for a representation to be irreducible. It was developed within the framework of the representation theory of finite groups, but it admits generalizations to Lie groups and Lie algebras. The lemma states the following: *If $\rho(g)$ is an irreducible representation of a finite group G and if there is some matrix A such that $A\rho(g) = \rho(g)A$ for all g, then $A = \lambda\mathbb{I}$ for some constant λ.* Schur's lemma is very important in representation theory to prove other theorems and to characterize irreps, but physics also benefits from it. As mentioned before, physicists in the twentieth century where trying to find "good labels" for what they called fundamental particles, and they found that properties like mass and spin could represent a set of physical states[1]. As it is easy to realize, these "good labels" would be related to identity operators multiplied by some constant (see later in Subsec. 2.2.2.3: Casimir operators), and according to Schur's lemma, the only requirement that should be imposed for this to be so is that the states (particles) transform under some irreps of the

[1]This can be exemplified by the well-known equation for spin states $S^2 |s, m_s\rangle = s(s+1) |s, m_s\rangle$, where s labels all the states $|s, m_s\rangle$, independently of the value of m_s.

group. In this way, fundamental particles can be directly associated with the irreps of the symmetry groups present in the theory describing them.

Great orthogonality theorem: This is one of the theorems that can be proved with the help of Schur's lemma [29]. *Let $\rho^{(\alpha)}(g)_{nm}$ be a matrix element of an irreducible unitary matrix representation $\rho^{(\alpha)}(\cdot)$ of a finite group G with N_g elements, then*

$$\sum_{g\in G}^{N_g} \rho^{(\alpha)}(g)^{\dagger}_{nm}\, \rho^{(\beta)}(g)_{n'm'} = \delta_{\alpha\beta}\delta_{nn'}\delta_{mm'}\frac{N_g}{d_\alpha}, \tag{2.7}$$

where α and β denote two possible different representations with dimensions d_α and d_β, and the sum is over all elements of G. Among other interesting aspects, this theorem allows proving that the number of irreducible representations of a finite group is also finite. The above constitutes a powerful tool for representation theory, whose main task is to find all of those representations.

2.2.2 From Lie Group to Lie Algebra

In this subsection, the topic of Lie groups will be particularly addressed, due to its invaluable contribution to the particle physics field. Understanding the nature of groups such as $SU(2)$ and $SU(3)$ was crucial in the identification of the elementary constituents. In particular, the irreducible representations of $SU(3)$ led to the notion of quarks, whereas the $SU(2)$ group, at that moment, had already played its important role in describing the spin theory. Furthermore, the group of symmetries of the space-time was accommodated in the Poincaré group, also a Lie group, whose contribution is not only for particle physics, but also for special relativity, classical electrodynamics, and several other branches of physics. Moreover, with the development of the gauge theories, the Lie groups showed its great potential to describe interactions among particles, and this resulted in a very important class of mathematical formulations called Yang-Mills theories [30].

2.2.2.1 Exponential Mapping

As mentioned before, a Lie group is a continuous group, i.e. in which all elements $g \in G$ depend on a continuous set of parameters

$$g = g(\alpha), \quad \alpha = \{\alpha_a\}, \;\; a = 1, \ldots, N. \tag{2.8}$$

The identity element e is commonly set such that $e = g(\alpha)|_{\alpha=0}$, with the objective to make any representation of $\rho(\alpha)|_{\alpha=0}$ equal to the corresponding identity matrix $\mathbb{I}$. Any group element can then be expanded in Taylor series around the identity

$$\rho(\delta\alpha) = \mathbb{I} + iX_a\delta\alpha_a + \ldots, \quad X_a \equiv -i\frac{\partial}{\partial\alpha_a}\rho(\alpha)|_{\alpha=0}, \tag{2.9}$$

where Einstein's summation rule of repeated indices is being considered. The differential $\delta\alpha$ denotes an infinitesimal change in the $\{\alpha_a\}$ parameters, and the $\{X_a\}$ are known as group generators. Note that the factor i is included in order for the group representation to fulfill the unitarity condition (2.6), which results in a hermiticity requirement for the generators $X_a^{\dagger} = X_a$. Now comes Lie's profound idea: any finite change in the parameter α_a can be

treated as an infinite number of infinitesimal changes $\delta\alpha_a$. The above, equipped with the group multiplication law, leads to the equality

$$\rho(\alpha) = \lim_{k\to\infty}\left(\mathbb{I} + i\frac{\alpha_a X_a}{k}\right)^k = \exp(i\alpha_a X_a). \tag{2.10}$$

This is called the exponential map, and it is a crucial mechanism for passing information between the Lie group and the Lie algebra.

2.2.2.2 Lie Algebra

Now, one can make use of the group multiplication law and the exponential map to get an important characteristic of Lie groups. The elements of the group can be parametrized by assigning different sets of parameters to each of them; for instance, the parameters $\{\beta_b\}$ with $b = 1, \ldots, N$ serve to represent another group element $\rho(\beta)$ distinct from $\rho(\alpha)$. The composition of two elements $\rho(\alpha)$ and $\rho(\beta)$ must result in another group element, which is parametrized by parameters $\{\gamma_c\}$ with $c = 1, \ldots, N$, namely $\exp(i\alpha_a X_a)\exp(i\beta_b X_b) = \exp(i\gamma_c X_c)$. Now, with the help of the properties of continuity and differentiability of the group elements, the above expression can be expanded up to quadratic order

$$\begin{aligned} i\gamma_c X_c &= \ln[1 + (\exp(i\alpha_a X_a)\exp(i\beta_b X_b) - 1)] \\ &= i\alpha_a X_a + i\beta_b X_b - \frac{1}{2}[\alpha_a X_a, \beta_b X_b] + \ldots, \end{aligned} \tag{2.11}$$

where $[\cdot,\cdot]$ is the commutator. Since the generators are linear operators, the linear terms can be grouped together on one side, leading to the relation $[\alpha_a X_a, \beta_b X_b] = i\varepsilon_c X_c$. Taking into account that the relation must hold for any choice of parameters, it is concluded that

$$[X_a, X_b] = i f_{abc} X_c. \tag{2.12}$$

For unitary group representations (Subsec. 2.2.1.3), the factors f_{abc} have to be real numbers and, by construction, they are antisymmetric with respect to the indices a and b. The group generators also satisfy the Jacobi identity

$$[X_a, [X_b, X_c]] + [X_b, [X_c, X_a]] + [X_c, [X_a, X_b]] = 0. \tag{2.13}$$

The expression (2.12) is known as *Lie algebra*, and the numbers f_{abc} are called *structure constants of the group*. The structure constants determine the Lie algebra, which essentially determines the Lie group. The structure of the infinite group has been reduced to a set of finite number of generators obeying certain relation, therefore, it is only necessary to focus on the algebra of the Lie group and not in its entire composition. This is the most important characteristic of the Lie groups, and what makes them so well manipulable in algebraic terms.

2.2.2.3 Lie Group and Lie Algebra Representations

Due to this direct interrelation between the Lie group and the Lie algebra, a connexion between their representations is also expected. In fact, it turns out that every finite-dimensional representation of a Lie group induces a representation of the corresponding Lie algebra. For

instance, the existence of a unitary representation of the group will intermediately induce a hermitian representation of the algebra.

Aside from the trivial representation, there are a couple of important representations worth mentioning. One of those is the representation resulting from interpreting the elements of the group as operators acting by matrix multiplication on a vector space; this is known as the *fundamental or standard representation*, sometimes used to refer to a smallest-dimensional faithful representation. For instance, when dealing with $SO(3)$, the fundamental representation is known as the vector representation since the elements of the group act on the vectors of the $\Re^3$ vector space.

Another no less important representation is the adjoint representation, which is defined by means of the structure constants. First, the $N \times N$ matrices $[T_a]_{bc} \equiv -if_{abc}$ are defined, being N the number of parameters (α_a) required to specify a group element. It can be proven with the help of the Jacobi identity (Eq. (2.13)) that the structure constants satisfy certain relation, which can be rewritten in terms of the T_a matrices as

$$[T_a, T_b] = if_{abc}T_c. \tag{2.14}$$

So, in general, the structure constants furnish a representation, known as the *adjoint*, whose dimension is given by the number of generators. The generator themselves can be chosen to form a vector space on which can be acted via the adjoint representation. The action of the algebra can be more formally defined as

$$ad_{X_a}(X_b) = [X_a, X_b], \tag{2.15}$$

where X_a and X_b are both elements of the Lie algebra, and the notation $ad(\cdot)$ is often used to denote the Lie algebra representation. This action induces an action of the group elements on the vector space, which is derived by making use of the Baker-Campbell-Hausdorff formula [28], and it reads

$$Ad_g(X_a) = gX_ag^{-1}, \tag{2.16}$$

with $g \in G$ and $Ad(\cdot)$ denoting the adjoint representation of the group. A direct application of the two representation mentioned above will be seen when discussing the topic of gauge theories (Sec. 2.4) in particle physics.

An important characteristic of the so-called semi-simple Lie algebras is the existence of Casimir invariants. Semi-simple Lie algebra refers to a direct sum of simple Lie algebras (non-abelian Lie algebras whose only ideals are 0 and the algebra itself, see rigorous definition in [28]). For those algebras, the second-order Casimir operator is defined as $C = h^{ab}T_aT_b$, with T_a being some matrix representation of this algebra and $h^{ab} = (h_{ab})^{-1} = (-f_{acd}f_{bdc})^{-1}$. This Casimir operator happens to commute with all the generators

$$[C, T_a] = 0. \tag{2.17}$$

Since this is true for all the representations, the use of Schur's lemma allows concluding that the Casimir operator is proportional to the identity $C = C(r)\,\mathbb{I}$. A given algebra might have more than one Casimir operator, and the number of these is related to the rank of the Lie algebra, which is simply the number of simultaneously diagonalizable generators. A theorem states that the number of independent Casimir operators is equal to the rank of the Lie

algebra. The Casimir operators can increase in order, depending on how many generators are being multiplied to construct them. In particular, the universal enveloping algebra [31] provides a nice definition of generalized Casimir invariants, and treats them as homogeneous polynomials $C_k = d^{i_1 \cdots i_k} T_{i_1} \cdots T_{i_k}$, with $d^{i_1 \cdots i_k}$ symmetric invariant tensors of the adjoint representation. Each of these generalized operators must commute with all the generators $[C_k, T_a] = 0$. There are some publications describing how to construct generalized Casimir invariants like [32].

The proportionality constant $C(r)$ is associated with a given representation, so its value is a distinctive feature of such a representation. Due to this fact, the Casimir operators are said to characterize the irreducible representations of the group. This, together with the discussion in Subsec. 2.2.1.4, helps to clarify why the Casimir operators are the fundamental tool for classifying physical states when the system obeys certain symmetries transformations.

2.2.2.4 Tensor Product Representations

Generating high dimension representation using tensor products of smaller ones is very useful in QM since it is very common having to deal with multiparticle physical states that are composed of identical constituents. The addition of angular momentum is a very well known case where this method can be applied. Some of the properties of tensors offer a very practical way of generating new representations of a Lie group out of composing, for instance, fundamental representations, which are generally quite known and studied.

Let $\rho_1(\cdot)$ and $\rho_2(\cdot)$ be two representations of a Lie group g; the tensor product representation of these is defined as

$$(\rho_1 \otimes \rho_2)(g) = \rho_1(g) \otimes \rho_2(g), \tag{2.18}$$

where the new representation acts on the vector space formed by the tensorial product of the two subspaces. Let $T_1(\cdot)$ and $T_2(\cdot)$ be the representations of the Lie algebra X, then it is straightforward to check using the exponential map that

$$(T_1 \otimes T_2)(X) = T_1(X) \otimes \mathbb{I} + \mathbb{I} \otimes T_2(X), \tag{2.19}$$

being $\mathbb{I}$ the identity operator. This shows that, while the tensor product rule for elements of the group is multiplicative, for the elements of the algebra is additive; this has direct implications in QM. One is that most of the physical observables that correspond to generators in the Lie algebra are additive, and that is the case of the four-momentum and the angular momentum, just to mention a few. In contrast, other operators that are elements of the symmetry group, such as parity, are multiplicative quantum numbers.

Before continuing, it is worth recalling what a tensor is. A possible approach in defining a tensor is based on tensor products of vector spaces [33]. A type (r, s) tensor is defined in this context as an element of the tensor product of vector spaces, which reads $\Lambda^r_s(V) = \underbrace{V^* \otimes \cdots \otimes V^*}_{\text{r times}} \otimes \underbrace{V \otimes \cdots \otimes V}_{\text{s times}}$, where V denotes a finite-dimensional vector space, and V^* denotes its dual space. A representation of g on V^* is required to be specified, the so-called *dual* representation, which in terms of matrix representation is just the inverse transpose of the matrices representing g on the original vector space. Putting it all together produces the general tensor product representation, which is just an active version of the

tensor transformation law

$$[\rho_s^r(g)\Lambda]^{m_1\ldots m_s}_{n_1\ldots n_r} = [\rho^{-1}(g)]^{k_1}_{n_1}\cdots[\rho^{-1}(g)]^{k_r}_{n_r}\,[\rho(g)]^{m_1}_{l_1}\cdots[\rho(g)]^{m_s}_{l_s}\;\Lambda^{l_1\ldots l_s}_{k_1\ldots k_r}. \tag{2.20}$$

It is important to be aware that even the tensor product of two irreducible representations of a Lie group is usually not irreducible, so less will be the one given by the composition of multiple irreps. Therefore, one often finds the problem of trying to decompose this tensorial products into irreducible pieces. Fortunately, for semi-simple groups, the tensor product representation $\rho_1(g)\otimes\rho_2(g)$ is decomposable

$$\rho_1(g)\otimes\rho_2(g) = \varrho_1(g)\oplus\cdots\oplus\varrho_k(g), \tag{2.21}$$

where the $\varrho_i(g)$ are irreducible representations of g. There exist a couple of very famous methods for decomposing tensorial products, such as the Young tableaux for $SU(n)$, and the Clebsch-Gordan decomposition, mainly used in $SU(2)$ [34]. The Clebsch-Gordan decomposition for the particular cases of $SU(2)$ and $SU(3)$ groups will be seen in more detail in Subsecs. 2.2.3.1 and 2.2.3.2 respectively.

2.2.3 Lie Groups in Particle Physics

Modern particle physics is based primarily on gauge theories of Lie groups, but some groups stand out for their particular importance; without these, none of the most currently employed physical theories could even be conceived. The group of space-time transformations known as the Poincaré group [35] is one of them, and not only does it play an important role in theories such as the SM, but it also gives rise to the appearance of supersymmetric theories. The $SU(2)$ group [28] began to play an important role since the discovery of the spin, and along with the $U(1)$ group, it is also the basis of the electroweak theory. There is also the group responsible for the "eightfold way", the $SU(3)$ group, which shapes the theory of the strong interactions between quarks and gluons. All these groups will be reviewed in this subsection individually, because of the importance that high energy physics confer on them.

2.2.3.1 The group $SU(2)$

The group $SU(2)$ (special unitary group of degree 2), consisting of the 2×2 complex matrices U, such that $U^\dagger U = UU^\dagger = \mathbb{I}_2$ and $\det U = 1$, is a three-parameter Lie group[2]. Its algebra is

$$[X_a, X_b] = i\varepsilon_{abc}X_c, \tag{2.22}$$

where ε_{abc} represents the totally antisymmetric Levi-Civita symbol. The well-known Pauli matrices (often multiplied by a factor) form the fundamental 2-dimensional representation

$$T_1 = \frac{1}{2}\begin{pmatrix}0 & 1\\ 1 & 0\end{pmatrix},\quad T_2 = \frac{1}{2}\begin{pmatrix}0 & -i\\ i & 0\end{pmatrix},\quad T_3 = \frac{1}{2}\begin{pmatrix}1 & 0\\ 0 & -1\end{pmatrix}. \tag{2.23}$$

[2]The dimension of a $SU(n)$ Lie group is n^2-1.

This representation acts on 2-dimensional vectors known as $SU(2)$ doublets (sometimes also called spinors) $\varphi'^{\alpha} = U^{\alpha}_{\beta}\varphi^{\beta}$, being $U^{\alpha}_{\beta} = \exp(i\gamma_k T_k)^{\alpha}_{\beta}$, and $\alpha, \beta = 1, 2$. In order to introduce a scalar product, it is useful to define the spinor (with subscript) φ_α such that $\varphi'_\alpha \varphi'^{\alpha} = \varphi_\alpha \varphi^\alpha$. Then, φ_α has to transform like $\varphi'_\alpha = (U^{\beta}_{\alpha})^* \varphi_\beta$, but this is just the complex-conjugate transformation law for φ^α, so $\varphi^{*\alpha}$ tends to be identified with φ_α. For $SU(2)$, it is easy to check that these two representations (U^* and U) are related by a similarity transformation, becoming equivalent representations. However, this is not the case of higher degree $SU(n)$ groups.

The adjoint representation is given by

$$(T_i^{(ad)})_{jk} = -if_{ijk} = -i\varepsilon_{ijk}, \tag{2.24}$$

$$T_1^{(ad)} = \begin{pmatrix} 0 & 0 & 0 \\ 0 & 0 & i \\ 0 & -i & 0 \end{pmatrix}, \quad T_2^{(ad)} = \begin{pmatrix} 0 & 0 & i \\ 0 & 0 & 0 \\ -i & 0 & 0 \end{pmatrix}, \quad T_3^{(ad)} = \begin{pmatrix} 0 & -i & 0 \\ i & 0 & 0 \\ 0 & 0 & 0 \end{pmatrix}.$$

As already seen in Subsec. 2.2.2.3, the Casimir operators serve to label a given irrep. Since these are proportional to the identity operator, their eigenvalues may be used to label the irreps of a Lie group. The eigenvalues of the diagonal generators (those simultaneously diagonalized) can be used to label the basis vectors within a given irrep. In particular, for $SU(2)$, which is a rank 1 Lie algebra, only one Casimir operator exists. The eigenvalues of this Casimir operator are denoted as j, and they are going to denominate the irreps. The eigenvalues of the diagonal generator are denoted as m, so that in the Dirac bra-ket notation the states can be labeled in the associated vector space basis as $|j, m\rangle$. Then, it is convenient to define instead (see Cartan-Weyl basis [25]) the raising and lowering operators $J_\pm := X_1 \pm iX_2$, for which it is not difficult to prove that

$$J_\pm |j, m\rangle = \sqrt{j(j+1) - m(m \pm 1)}\, |j, m \pm 1\rangle . \tag{2.25}$$

In particular, $J_\pm |j, \pm j\rangle = 0$, implying that the values of m are bounded $-j \leq m \leq j$, and that they label a $(2j+1)$-dimensional representation. For each spin-j representation, the Casimir operator is then given by $C = \frac{1}{2}\sum_i X_i^2 = \frac{X_3}{2} + \frac{J_+^2}{4} + \frac{J_-^2}{4}$, and since it is proportional to the identity, one can take the trace and get the proportionality constant. Finally, the Casimir operator reads

$$C(j) = \frac{1}{2} j(j+1)\, \mathbb{I}_{2j+1}. \tag{2.26}$$

Summarizing, the irreps of $SU(2)$ are $(2j+1)$-dimensional, with $j = \frac{1}{2}, 1, \frac{3}{2}, 2, \frac{5}{2} \cdots$.

Back to the topic of tensor product representations (Subsec. 2.2.2.4), now focusing on $SU(2)$, there exists a well-studied method called Clebsch-Gordan decomposition [34] that allows performing an explicit direct sum decomposition of the tensor product of two irreps. The general result of such a decomposition is

$$(2j_1 + 1) \otimes (2j_2 + 1) = \bigoplus_{J=|j_1-j_2|}^{J=|j_1+j_2|} (2J + 1). \tag{2.27}$$

For example, when adding two spin-$\frac{1}{2}$ particles the decomposition reads $\mathbf{2} \otimes \mathbf{2} = \mathbf{3} \oplus \mathbf{1}$, where "**2**" is indicating the dimension of the irrep. The previous example is the famous case where two spin-$\frac{1}{2}$ states are added, resulting in one *singlet* and one *triplet*. The example also suggests that the tensor product of two fundamental representations of $SU(2)$ gives the adjoint representation plus the trivial representation. This is a general feature of $SU(n)$; the tensor product of the fundamental representation and its complex conjugate (both the same for $SU(2)$) decomposes into the adjoint representation plus the trivial representation.

2.2.3.2 The group $SU(3)$

The group $SU(3)$, which corresponds to the set of 3×3 complex matrices U, such that $U^\dagger U = UU^\dagger = \mathbb{I}_3$ and $\det U = 1$, is an eight-parameter Lie group. The best known representation of this algebra is the one given by the Gell-Mann matrices (T_a, $a = 1, \ldots, 8$), which furnish the fundamental representation

$$T_1 = \begin{pmatrix} 0 & 1 & 0 \\ 1 & 0 & 0 \\ 0 & 0 & 0 \end{pmatrix}, \quad T_2 = \begin{pmatrix} 0 & i & 0 \\ -i & 0 & 0 \\ 0 & 0 & 0 \end{pmatrix}, \quad T_3 = \begin{pmatrix} 1 & 0 & 0 \\ 0 & -1 & 0 \\ 0 & 0 & 0 \end{pmatrix}, \quad T_4 = \begin{pmatrix} 0 & 0 & 1 \\ 0 & 0 & 0 \\ 1 & 0 & 0 \end{pmatrix}$$

$$T_5 = \begin{pmatrix} 0 & 0 & i \\ 0 & 0 & 0 \\ -i & 0 & 0 \end{pmatrix}, \quad T_6 = \begin{pmatrix} 0 & 0 & 0 \\ 0 & 0 & 1 \\ 0 & 1 & 0 \end{pmatrix}, \quad T_7 = \begin{pmatrix} 0 & 0 & 0 \\ 0 & 0 & -i \\ 0 & i & 0 \end{pmatrix}, \quad T_8 = \frac{1}{\sqrt{3}} \begin{pmatrix} 1 & 0 & 0 \\ 0 & 1 & 0 \\ 0 & 0 & -2 \end{pmatrix}. \tag{2.28}$$

Already for $SU(3)$, one has to distinguish two non-equivalent 3-dimensional representations; the fundamental one, given by the transformation law $\varphi'^{\alpha} = U^{\alpha}_{\beta}\varphi^{\beta}$, and the conjugate representation $\varphi'_{\alpha} = U^{*\beta}_{\alpha}\varphi_{\beta}$, with $\alpha, \beta = 1, 2, 3$. These two transformations are commonly denoted by **3** and $\bar{\mathbf{3}}$ respectively. The adjoint representation is generated, as usually, through the structure constants f_{abc} of the Lie algebra (Eq. (2.12)). The structure constants can be related to the Gell-Mann matrices via the formula [36]

$$f_{abc} = \frac{1}{4i}\mathbf{Tr}([T_a, T_b]T_c). \tag{2.29}$$

As it can be noticed in Eq. (2.28), there are two diagonal elements, so there are also two Casmir operators given by the equations

$$C_2 = \delta_{ab}X_aX_b, \qquad C_3 = g_{abc}X_aX_bX_c, \tag{2.30}$$

where δ_{ab} denotes the Kronecker delta, and the completely symmetric coefficient is given by $g_{abc} = \frac{1}{4}\mathbf{Tr}(\{T_a, T_b\}T_c)$. Consequently, the irreps can be labeled by two constants (m, n). Following the corresponding Cartan-Weyl procedure leads to an expression relating the dimension $\mathbf{D}$ of the irrep and the two parameters (m, n)

$$\mathbf{D} = \frac{1}{2}(m+1)(n+1)(m+n+2). \tag{2.31}$$

So, for instance, $(1,0)$ and $(0,1)$ label two 3-dimensional representations, namely $\mathbf{3}$ and $\bar{\mathbf{3}}$ respectively. The adjoint is represented by $(1,1)$, clearly a self conjugate representation. The irreps are identified by the eigenvalues of the two Casimir operators, whose diagonal forms are

$$C_2(m,n) = \frac{m^2+mn+n^2+3m+3n}{3}\,\mathbb{I}_{\mathbf{D}},$$
$$C_3(m,n) = \frac{(m-n)(3+m+2n)(3+n+2m)}{18}\,\mathbb{I}_{\mathbf{D}}. \tag{2.32}$$

To build higher-dimensional representations, irreducible representations are multiplied together using the tensor approach, as it was already seen. For $SU(3)$, there is also an analytic form of the Clebsch-Gordan decomposition [37] given by the combination of the two formulas bellow

$$(m_1,n_1)\otimes(m_2,n_2) = \sum_{i=0}^{\min(m_1,n_2)}\sum_{j=0}^{\min(m_2,n_1)}(m_1-i,m_2-j;n_1-j,n_2-i),$$
$$(r,r';s,s') = (r+r',s+s')\oplus\sum_{k=1}^{\min(r,r')}(r+r'-2k,s+s'+k)\oplus\sum_{k=1}^{\min(s,s')}(r+r'+k,s+s'-2k). \tag{2.33}$$

From these, the following decomposition can be derived $\mathbf{3}\otimes\bar{\mathbf{3}} = \mathbf{8}\oplus\mathbf{1}$. In the case of $SU(3)$, the appearance of the adjoint ($\mathbf{8}$) in this decomposition has been of great relevance for particle physics, since, for example, in quantum chromodynamics, gluons are commonly thought of as carrying both color and anticolor for some physical interpretations. Besides, at the time of the "particle zoo" era, the $\mathbf{8}$ irrep was immediately associated with the observed octet of pseudoscalar mesons, made of bound states of a quark and an antiquark. The Eq. (2.33) also leads to another highly celebrated result in particle physics $\mathbf{3}\otimes\mathbf{3}\otimes\mathbf{3} = \mathbf{10}\oplus\mathbf{8}\oplus\mathbf{8}\oplus\mathbf{1}$; this was another victory for the quark model, then able to explain the existence of the baryon octet and decuplet.

2.2.3.3 The Poincaré group

The Poincaré group, known as the group of Minkowski space-time isometries, is a ten-dimensional non-abelian Lie group. It is formed by two subgroups, the abelian group of translations and the Lorentz group. The Lorentz group is the group of 4×4 matrix transformations Λ^μ_ν $(\mu,\nu = 0,1,2,3)$ that leaves the Minkowski metric $\eta_{\mu\nu} = \mathrm{diag}(1,-1,-1,-1)$ invariant

$$\Lambda^\mu_\rho\,\eta_{\mu\nu}\,\Lambda^\nu_\sigma = \eta_{\rho\sigma}. \tag{2.34}$$

By applying the rule of multiplication of determinants to Eq. (2.34), the condition $\det\Lambda = \pm1$ is obtained. Expanding now Eq. (2.34) for $\rho = 0$ and $\sigma = 0$, a second condition for the first diagonal element arises $(\Lambda^0_0)^2 \geq 1$. As seen in Subsec. 2.2.2.1, to obtain a continuous Lie group transformation, an expansion around the identity element is required. However, for certain combinations of $\det\Lambda$ and Λ^0_0 ($\det\Lambda \neq 1$ or $\Lambda^0_0 \leq -1$), the Λ^μ_ν is very far from resembling the identity. This implies that the complete Lorentz group will not be connected in topological

terms, therefore, it has to be divided in connected components in order to be able to study its Lie algebra structure. The four different possibilities are presented in Tab. 2.1. Among the four components, only the proper orthochronous transformations are a subgroup of the Lorentz transformations. The other three elements, together with the identity, form a discrete abelian subgroup[3].

Table 2.1: Discrete transformations of the Lorentz group components

	$\Lambda^0_0 \geq 1$ (orthochronous)	$\Lambda^0_0 \leq -1$ (non-orthochronous)
$\det\Lambda = +1$ (proper)	$\mathbb{I}$	$-\eta$
$\det\Lambda = -1$ (improper)	η	$-\mathbb{I}$

To build a Poincaré Lie algebra, it is necessary to consider the product of the group of translations and the proper orthochronous Lorentz transformations $L^{(po)}$, giving, as a result, the transformation law

$$x'^{\mu} = \Lambda^{\mu}_{\nu} x^{\nu} + a^{\mu}. \tag{2.35}$$

This algebra is going to be fundamentally governed by the Lie algebra of $L^{(po)}$, because of the abelian nature of the translation group. So, it is then convenient to focus on the $L^{(po)}$ group.

The $L^{(po)}$ group is generated by ordinary spatial rotations and Lorentz boosts under the action of Λ^{μ}_{ν}, and is usually denoted by $SO^{+}(3,1)$. As the name indicates, this is a subgroup of the special orthogonal group acting on a space with metric η and, therefore, is a 6 dimensional Lie group. Let the following group, denominated $SL(2,\mathbb{C})$, be

$$SL(2,\mathbb{C}) := \left\{ \begin{pmatrix} a & b \\ c & d \end{pmatrix} \mid \ a,b,c,d \in \mathbb{C},\ ad - bc = 1 \right\}, \tag{2.36}$$

where L refers to linear transformations in a two-dimensional complex space, and S stands for special (determinant equal to 1). It can be shown that, introducing the matrix $X = \sigma_{\mu} x^{\mu}$ (σ_{μ} is the four-vector formed by the Pauli matrices in Eq. (2.23) and the identity matrix) and applying the transformation $X' = AXA^{\dagger}$, where A is an element of the $SL(2,\mathbb{C})$ group, the Lorentz transformation condition $x'^2 = \det X' = \det X = x^2$ is recovered. The result indicates that there exist a connection between the elements of $SL(2,\mathbb{C})$ and $SO^{+}(3,1)$. In particular, it can be noticed that A and $-A$ define the same transformation $X' \longrightarrow X$, thus it is said that $SL(2,\mathbb{C})$ double covers $SO^{+}(3,1)$. To recover the natural exponential form of Lie groups, the elements A are written as $A = \exp(B)$, transferring the condition $\det A = 1$ into the requirement $\mathbf{Tr}B = 0$. The Lie algebra of $SL(2,\mathbb{C}) \cong SO^{+}(3,1)$ results in

$$[X_a, X_b] = i\varepsilon_{abc} X_c, \qquad [Y_a, Y_b] = -i\varepsilon_{abc} X_c, \qquad [X_a, Y_b] = i\varepsilon_{abc} Y_c, \tag{2.37}$$

where $a,b,c = 1,2,3$. The 6 generators X_a and Y_a form the basis of the Lie algebra, but it is common to differentiate them in $SO^{+}(3,1)$ to indicate that the first ones generate standard

[3]Not only the continuous Poincaré symmetries are relevant for particle physics, also the discrete symmetries play an important role, being the most prominent ones, parity, time reversal, and charge conjugation [17].

space rotations and the second ones generate Lorentz boosts. Nevertheless, one can define the generators $X_a^{\pm} := \frac{1}{2}(X_a \pm iY_a)$, and Eq. (2.37) becomes

$$[X_a^+, X_b^+] = i\varepsilon_{abc}X_c^+, \qquad [X_a^-, X_b^-] = i\varepsilon_{abc}X_c^-, \qquad [X_a^+, X_b^-] = 0. \tag{2.38}$$

The above equation makes evident the presence of two independent Lie subalgebras in the algebra of $SL(2,\mathbb{C})$, and it says a little more; the two subalgebras are identical, each of them shapes a $SU(2)$ Lie algebra (Subsec. 2.2.3.1). It follows immediately that the irreps of $SL(2,\mathbb{C})$ can be labeled by the pair (j^+, j^-), where the j^+ can take values completely independent from those of j^-. The values that each $SU(2)$ component can take are $j^{\pm} = 0, \frac{1}{2}, 1\ldots$, and the dimension of the irreps are $2j^{\pm}+1$. So, the dimension of the irreps of $SL(2,\mathbb{C})$ are given by $(2j^+ + 1)(2j^- + 1)$, and they read

$$(0,0) \quad (\frac{1}{2},0) \quad (0,\frac{1}{2}) \quad (1,0) \quad (0,1) \quad (\frac{1}{2},\frac{1}{2}) \quad (\frac{3}{2},0) \quad (0,\frac{3}{2}) \quad \cdots. \tag{2.39}$$

The 1-dimensional representation $(0,0)$ is clearly the trivial representation and is commonly known as Lorentz scalar. The two 2-dimensional representations $(\frac{1}{2},0)$ and $(0,\frac{1}{2})$ are called Weyl spinor representations, and each furnishes a perfectly good representation of the Lorentz group. The 4-dimensional representation $(\frac{1}{2},\frac{1}{2})$ is but the vector representation of the Lorentz group. In Tab. 2.2, there is a summary of the most relevant cases for modern particle physics of finite-dimensional irreps of the Lorentz group. It is important to point out that also the two direct sum representations $(\frac{1}{2},0)\oplus(0,\frac{1}{2})$ and $(1,0)\oplus(0,1)$, which frequently represent the Dirac spinor and the antisymmetric electromagnetic tensor respectively, are occasionally more used than their associated irreps.

Table 2.2: Some of the smallest irreps of the $SL(2,\mathbb{C})$ group with their corresponding field

Representation	**Dimension**	**Field**	**Name**
$(0,0)$	1	ϕ	scalar
$(\frac{1}{2},0)$	2	χ_L^α	left-handed Weyl spinor
$(0,\frac{1}{2})$	2	χ_R^α	right-handed Weyl spinor
$(1,0)$	3	$+\frac{1}{2}\varepsilon_{\mu\nu\sigma\lambda}F^{\sigma\lambda}$	self-dual antisymmetric 2-tensor
$(0,1)$	3	$-\frac{1}{2}\varepsilon_{\mu\nu\sigma\lambda}F^{\sigma\lambda}$	anti-self-dual antisymmetric 2-tensor
$(\frac{1}{2},\frac{1}{2})$	4	A^μ	vector field
$(\frac{1}{2},1)$	6	$\Psi_L^{\mu\alpha}$	left-handed Rarita-Schwinger field
$(1,\frac{1}{2})$	6	$\Psi_R^{\mu\alpha}$	right-handed Rarita-Schwinger field
$(1,1)$	9	$h^{\mu\nu}$	symmetric traceless 2-index tensor

It is of relevance for physics to know the consequences of restricting the whole group to a subgroup, for instance, the rotation subgroup. The generators of rotations (in this case associated to X_a) are related to the $X_a^{\pm}$ via the formula $X_a = X_a^+ + X_a^-$, but this is essentially

the addition of two Lie algebras, represented in Eq. (2.19), which induces a multiplication (tensor product) of the elements of the group. Thus, it means that one just needs to build the tensor product of two irreps j^+ and j^- and decompose it into irreps through Eq. (2.27). Now, for instance, the $SL(2,\mathbb{C})$ irrep $(\frac{1}{2},0)$ decomposes under restriction to the rotation subgroup into $\mathbf{2} \to \mathbf{2}$, while the vector representation does it into $\mathbf{4} \to \mathbf{3} \oplus \mathbf{1}$. That is the reason why, in particle physics, spin-$\frac{1}{2}$ particles are represented by spinors, and spin-1 particles are represented by 4-vectors.

Going back to the Poincaré group; a large part of its Lie algebra has already been covered with the $L^{(po)}$ group, the remaining task is to incorporate the translation generators. In order to be able to write down a covariant form of the Lie algebra, it is convenient to define the antisymmetric tensor $M^{\mu\nu}$, with components $M^{ab} = -\varepsilon_{abc}X^c$ and $M^{0b} = Y^b$. Denoting the four remaining translation generators by P^μ, the Poincaré Lie algebra reads

$$\begin{aligned} [M^{\mu\nu}, M^{\rho\sigma}] &= -i(\eta^{\mu\rho}M^{\nu\sigma} - \eta^{\mu\sigma}M^{\nu\rho} - \eta^{\nu\rho}M^{\mu\sigma} + \eta^{\nu\sigma}M^{\mu\rho}), \\ [P^\rho, M^{\mu\nu}] &= i(\eta^{\rho\mu}P^\nu - \eta^{\rho\nu}P^\mu), \\ [P^\mu, P^\nu] &= 0. \end{aligned} \tag{2.40}$$

The task is now to construct the Casimir invariants so that the one-particle states can be labeled. Unfortunately, when one turns to the full Poincaré group, the two Casimir operators (one for each $SU(2)$ algebra) of $L^{(po)}$ do not commute with P^μ, so they are not Casimirs of the Poincaré group. In turn, the so-called Pauli-Lubanski pseudo-vector can be defined, given by $W_\mu = \frac{1}{2}\varepsilon_{\mu\nu\rho\sigma}M^{\nu\rho}P^\sigma$. The two (pseudo-)vectors P^μ and W^μ, upon contraction with themselves, will form the two possible Casimir invariants and, therefore, are going to label the irreps

$$C_2 = P_\mu P^\mu, \qquad\qquad C_4 = W_\mu W^\mu. \tag{2.41}$$

Additionally, there happens to be another difficulty, which is a feature of groups (like $SL(2,\mathbb{C})$) whose finite-dimensional representations might not be unitary. In fact, it is not difficult to prove that an element of the group $SL(2,\mathbb{C})$ can be written as the product of a unitary matrix times a hermitian matrix, thus no finite-dimensional unitary irrep exists apart from the trivial one. However, QM demands building unitary representations to preserve norms and maintain the probabilistic interpretation. It is also common in QM to associate the generators P^μ with the energy-momentum operators and the generators $M^{\mu\nu}$ with the angular momentum generator, which leads to an inevitable hermitian representation of these physical quantities. It was Wigner [38] the one who proposed a way to cope with this inconvenience, the method of induced representations. In general, one has to appeal to the theory of projective representations [39] (a collection of operators that are only defined up to multiplication by a constant) to be able to construct unitary representations of a certain symmetry group.

The eigenvalues of the two Casimir operators in Eq. (2.41) label the irreps of the Poincaré group. The approach employed by Wigner considers a subspace of the full Hilbert space on which $P_\mu P^\mu$ have a fix value m^2 that can a priori be any real number; but only the values $m^2 \geq 0$ are physically meaningful. The possible eigenvalues of $W_\mu W^\mu$ can be obtained using the Wigner trick. From Eq. (2.40), it is obvious that all the translation generators commute with each other, so it is convenient to express physical states in terms of eigenvectors of the translation generators. Secondly, the label σ is introduced to denote all other degrees of freedom. Then, a general state having the same eigenvalue p^μ of P^μ with different σ labels

is represented by $|p,\sigma\rangle$. A general unitary representation of the Poincaré group $U(\Lambda,a)$ can be written in infinitesimal ($\Lambda^\mu_\nu \approx \delta^\mu_\nu - \omega^\mu_\nu$, $a^\mu \approx \epsilon^\mu$) form as

$$U(I-\omega,\epsilon) \approx 1 + \frac{i}{2}\omega_{\mu\nu}M^{\mu\nu} - i\epsilon_\mu P^\mu, \tag{2.42}$$

where P^μ and $M^{\mu\nu}$ represent now Hermitian operators. With the help of the composition rule $U(\bar{\Lambda},\bar{a})U(\Lambda,a) = U(\bar{\Lambda}\Lambda, \bar{\Lambda}a+\bar{a})$, it can be proven that the operator P^μ transforms under $U(\Lambda,a)$ via

$$U(\Lambda,a)P^\mu U^{-1}(\Lambda,a) = \Lambda^\mu_\nu P^\nu. \tag{2.43}$$

Taking into account the operator equation $P^\mu|p,\sigma\rangle = p^\mu|p,\sigma\rangle$, a pure translation can be easily identified with the unitary operation $U(I,a)|p,\sigma\rangle = \exp(-ia_\mu P^\mu)|p,\sigma\rangle$. Given that the action of $U(I,a)$ on the states is already known, obtaining a complete Poincaré transformation only requires to find out how a pure Lorentz transformation acts on $|p,\sigma\rangle$. Immediately after applying $P^\mu U(\Lambda,0)|p,\sigma\rangle$ and using the transformation properties of the four-momentum operator (Eq. (2.43)) is found that $U(\Lambda,0)|p,\sigma\rangle$ is the eigenstate of P^μ with eigenvalue $(\Lambda p)^\mu \equiv \Lambda^\mu_\nu p^\nu$. So, $U(\Lambda,0)|p,\sigma\rangle$ can be written as a general superposition of such states

$$U(\Lambda,0)|p,\sigma\rangle = \sum_{\sigma'} C_{\sigma\sigma'}|\Lambda p,\sigma'\rangle\,. \tag{2.44}$$

The next step is to obtain the coefficients $C_{\sigma\sigma'}$ in a block diagonal basis so that they can be associated with the irreps of some symmetry group. In order to do that, the standard four-momentum k^μ and a standard proper ortochronous Lorentz transformation $(L_p)^\mu_\nu$ are defined, in such a way that $p^\mu = (L_p)^\mu_\nu k^\nu$. If $U(L_p)$ is the unitary representation of the above Lorentz transformation, the states can be represented as $|p,\sigma\rangle = N_p U(L_p)|k,\sigma\rangle$, where N_p is some normalization constant. Later, it can be observed that $\Lambda L_p = (L_{\Lambda p})(L^{-1}_{\Lambda p}\cdot\Lambda\cdot L_p)$, where the second term is known as a Wigner rotation $W^\mu_\nu := (L^{-1}_{\Lambda p}\cdot\Lambda\cdot L_p)^\mu_\nu$. The effect of this rotation on the four-momentum k^μ is to leave it invariant

$$k^\mu = W^\mu_\nu k^\nu. \tag{2.45}$$

The Eq. (2.45) defines the so-called *little group*. Translating this into the action of unitary operators yields $U(\Lambda,0)|p,\sigma\rangle = N_p U(L_{\Lambda p},0)U(W,0)|k,\sigma\rangle$, where the group composition law has been used. Since W^μ_ν are elements of a group, they can be represented by matrices, which are denoted by $D(W)$, and the final transformation becomes

$$U(\Lambda,0)|p,\sigma\rangle = \frac{N_p}{N_{\Lambda p}}\sum_{\sigma'} D_{\sigma\sigma'}(W(\Lambda,p))|\Lambda p,\sigma'\rangle\,. \tag{2.46}$$

Comparing the above equation with Eq. (2.44) allows realizing that the problem of finding a block diagonal form of $C_{\sigma\sigma'}$ has been reduced to the one of encountering the irreps $D_{\sigma\sigma'}$ of the little group. Bellow, two important cases for particle physics are distinguished.

Massive representations: For this case, the standard four-momentum k^μ in the particle's rest frame $k^\mu = (m,0,0,0)$ may be taken as reference. This choice is obviously invariant under spatial rotations generated by the $SO(3)$ group. The irreps for massive particles can thus be obtained from the irreps of $SO(3) \cong SU(2)$, which share the same Lie algebra. Then, it is easy to anticipate that the labels of such states are going to be related to the quantum

number $s = \frac{1}{2}, 1, \frac{3}{2} \cdots$. Actually, coming back to the second Casimir operator, it is observed that in this frame of reference its components are $W^0 = 0$ and $W^i = -mX^i$, being the spacial components proportional to the $SU(2)$ spin generators. Calculating the eigenvalues of C_4 conduces to the expression $-m^2 s(s+1)$, which explicitly shows that the irreps of the Poincaré group correspond to states differing in mass and spin (m, s).

Massless representations: In this case, it is convenient to choose $k^\mu = (k, 0, 0, k)$. This form of the 4-momentum is preserved by the isometries of the Euclidean (x, y) plane, which include rotations about the z axis and translations along x and y. These form the group $ISO(2)$. In this frame, the Pauli-Lubanski pseudo-vector components are given by $W^0 = kX^3$, $W^1 = -k(X^1 + Y^2)$, and $W^2 = -k(X^2 - Y^1)$, which also generate the $ISO(2)$ algebra. In this algebra, the generators W^1 and W^2 commute, so they can be simultaneously diagonalized, and their corresponding eigenvalues used to label the states. However, it can be proven that if one set of non-zero eigenvalues of W^1 and W^2 is found, then a whole continuum spectrum is necessarily present. These representations have no physical meaning since they would describe massless particles with continuous spin, and such a spectrum has not yet been seen. The only physical case is that in which both eigenvalues are zero and, therefore, the states are solely labeled by the 4-momentum and the $W^0 = kX^3$ eigenvalues. Since $\vec{k} = (0, 0, k)$ is the 3-momentum vector, X^3 is the component of the angular momentum in the direction of motion, and its eigenvalues h are called *helicity*.

2.3 Field Quantization

In this section, some of the most important aspects of field quantization will be briefly addressed. As seen in Sec. 2.1, any classical field theory can be described in terms of a Lagrangian density that has one or more fields associated with it, to which their respective canonically conjugate fields are added. The objective of field quantization is to establish certain rules of quantization, under which, a consistent theory of quantum fields can be derived. Historically, two different approaches have been prominent in the task of quantifying a given field theory: *the canonical quantization* and *the path integral formulation*. The two methods will be discussed in this section, highlighting the importance of each of them, both for the physical interpretation and for the practical realization.

2.3.1 Canonical Quantization

The quantization process that revisits the standard form of quantization using the commutator (anticommutator) between a field and its conjugate momentum is called canonical quantization [16, 18]. This procedure attempts to preserve the defining symmetries of the classical theory to the greatest extent possible. The quantization tends to be rather field-dependent, that is, each field must be treated differently at the time of quantizing it, according to the type of excitation (irreps of the Poincaré group, see Subsec. 2.2.3.3) it contains. Nevertheless, there is a fairly well-defined pattern, and it has to do with the spin-statistics theorem [40], which says that fermions and bosons must obey different statistics. This implies that all the bosonic fields must be quantized in a specific way (using commutators), whereas all the fermionic fields have to be quantized in another specific way (using anticommutators). Proceeding in any other manner would lead to rather undesired conceptual problems with

systems lacking a stable ground state. Moreover, the causality of this theory would be also facing difficulties, due to the cancellation of commutators outside the light-cone region.

The most important cases of field quantization will be reviewed in the following. Now, when dealing with identical-multi-particle systems is necessary to define the Fock space, which is basically the sum of a set of Hilbert spaces $F = \bigoplus_{k\geq 0} H_n^{\otimes k}$. In this space, the classical fields are going to be promoted to operator-valued quantum fields, assigning to each point an operator. A quantum state is an element of the Fock space with a well-defined number of particles, and the way to act on these states is through the quantum fields.

2.3.1.1 Scalar Field Quantization

The simplest example of a relativistic field theory deals with spin-0 particles described by the Klein-Gordon Lagrangian density [17]

$$\mathcal{L} = \frac{1}{2}\left(\partial_\mu \phi \partial^\mu \phi - m^2\phi^2\right). \tag{2.47}$$

The real field ϕ usually corresponds to neutral particles; for charged particles a complex field is normally used. The canonically conjugate momentum of the field $\phi(x)$ is given by $\pi(x) = \dot{\phi}(x)$. A general solution of the Klein-Gordon field can be expressed in terms of a Fourier transform

$$\phi(x) = \int \frac{d^3p}{\sqrt{2E_{\mathbf{p}}(2\pi)^3}}\left[\alpha(\mathbf{p})e^{-ipx} + \alpha^*(\mathbf{p})e^{ipx}\right], \tag{2.48}$$

where the relation $E_{\mathbf{p}} = +\sqrt{\mathbf{p}^2 + m^2}$ holds. Later, canonical quantization proceeds by replacing the coefficients $\alpha(\mathbf{p})$ and $\alpha^*(\mathbf{p})$ with operators $\hat{\alpha}(\mathbf{p})$ and $\hat{\alpha}^\dagger(\mathbf{p})$ acting on the Fock space, which converts the classical field into a function of these operators. Then, the Poisson brackets $\{\cdot,\cdot\}_{PB}$ in Eq. (2.3) are replaced by commutators (this is a bosonic field) $[\cdot,\cdot]$. The above requirements result in commutator relations between the operators $\hat{\alpha}(\mathbf{p})$ and $\hat{\alpha}^\dagger(\mathbf{p})$

$$\begin{gathered}[\hat{\alpha}(\mathbf{p}), \hat{\alpha}^\dagger(\mathbf{p}')] = \delta^3(\mathbf{p} - \mathbf{p}'), \\ [\hat{\alpha}(\mathbf{p}), \hat{\alpha}(\mathbf{p}')] = [\hat{\alpha}^\dagger(\mathbf{p}), \hat{\alpha}^\dagger(\mathbf{p}')] = 0.\end{gathered} \tag{2.49}$$

The Eq. (2.49) contains the typical canonical commutation relations of bosonic particles, therefore, the operators $\hat{\alpha}(\mathbf{p})$ and $\hat{\alpha}^\dagger(\mathbf{p})$ are identified as a set of annihilation-creation operators creating states with well defined momentum $\mathbf{p}$ out of the vacuum $|0\rangle$. The occupation numbers are determined with the help of the number operator $\hat{N}(\mathbf{p}) = \hat{\alpha}^\dagger(\mathbf{p})\hat{\alpha}(\mathbf{p})$, whose eigenvalues can be any non-negative integer $n(\mathbf{p}) = 0, 1, 2, \ldots,$. The important thing to notice is how this formalism has made the concept of particle appear as a result of the quantization of a classical field.

In QFT, taking products of operators (fields) is not only mathematically useful, but can also lead to physical interpretations. For instance, the probability amplitude for a particle to travel from one point to another follows from the multiplication of two space-time separated fields. As far as the free scalar field theory is concerned, all relevant information is encoded

in the time-ordered correlation functions

$$\mathcal{G}_n(x_1, \ldots, x_n) = \langle 0| \mathcal{T}\left[\hat{\phi}(x_1) \cdots \hat{\phi}(x_n)\right] |0\rangle, \tag{2.50}$$

where $\mathcal{T}$ represents the time-ordered product, i.e. the operators are written in chronological order with time in such a way that they "operate" in the order in which they occur in time. Among these correlated functions, the most relevant for free fields are the so-called propagators (two-point correlation functions), which are essential in perturbation theory. In the scalar field case, the propagator is

$$\Delta(x_1 - x_2) := \langle 0| \mathcal{T}\left[\hat{\phi}(x_1)\hat{\phi}(x_2)\right] |0\rangle = \int \frac{d^4p}{(2\pi)^4} \frac{ie^{-ip\cdot(x_1-x_2)}}{p^2 - m^2 + i\epsilon}. \tag{2.51}$$

The term $i\epsilon$ has to do with the poles appearing in the integration over p^0, which must be surrounded when performing the contour integral.

Some aspects of the complex scalar field case are worth mentioning. In Subsec. 2.1.2, it has been pointed out that internal symmetries can also be part of a theory. Most of the internal symmetries are related to Lie groups (Subsec. 2.2.2), in particular, the $U(1)$ symmetry is very often encountered in particle physics (electric charge, weak hypercharge, lepton number, baryon number, etc.). To describe a system of spin-0 particles subject to a $U(1)$ symmetry, one reasonable way to proceed is to write down a Lagrangian with two identical Klein-Gordon fields. However, a more effective way would be to introduce complex scalar fields, which also have two degrees of freedom. The Lagrangian density of the complex scalar field is easily obtained by replacing in Eq. (2.47) the terms $\partial_\mu\phi\partial^\mu\phi \to \partial_\mu\phi^\dagger\partial^\mu\phi$ and $\phi^2 \to \phi\phi^\dagger$, where ϕ and $\phi^\dagger$ must be thought of as independent fields. By imposing the canonical quantization on these operators, two different sets of commutator relations of type (2.49) are obtained, hence the resulting operators $\hat{\alpha}(\mathbf{p})$ ($\hat{\alpha}^\dagger(\mathbf{p})$) and $\hat{\beta}(\mathbf{p})$ ($\hat{\beta}^\dagger(\mathbf{p})$) should be interpreted as annihilation (creation) operators of two types of particles.

2.3.1.2 Dirac Field Quantization

Even though the Lorentz (Poincaré) representation theory (Subsec. 2.2.3.3) suggests that the "standard" irreps for spin-$\frac{1}{2}$ particles should be the Weyl spinors (see Tab. 2.2), one has to deal very often with parity conserving theories such as quantum electrodynamics. It is a known fact that under parity the Weyl spinor irreps are interchanged $(\frac{1}{2}, 0) \leftrightarrow (0, \frac{1}{2})$, so it would be impossible to construct such theories with only one of the Weyl spinors. In that sense, it is said that parity forces to stack two Weyl spinors together to form a Dirac spinor.

The Lagrangian proposed by Dirac to describe spin-$\frac{1}{2}$ particles is [16]

$$\mathcal{L} = \bar{\psi}(i\gamma_\mu\partial^\mu - m)\psi, \tag{2.52}$$

where γ_μ are the known 4×4 Dirac γ-matrices. The canonical conjugate momentum of the $\psi(x)$ field is $\pi(x) = i\psi^\dagger(x)$. A similar expression can be obtained for the Dirac conjugate spinor $\bar{\psi}(x)$. As it is not difficult to notice, the Dirac spinor (also known as bispinor) is a 4-dimensional representation, although a reducible one. Consequently, the equation of motion derived from the Lagrangian (2.52) is expected to have four solutions, two with helicity $s = \frac{1}{2}$, and two with helicity $s = -\frac{1}{2}$ (usually it is more convenient to divide them in positive and

negative energy solutions). Then, a general solution to the Dirac equation can be written in terms of operators as

$$\hat{\psi}_\alpha(x) = \sum_{s=\pm\frac{1}{2}} \int \frac{d^3p}{(2\pi)^{3/2}} \sqrt{\frac{m}{E_{\mathbf{p}}}} \left[u_\alpha(\mathbf{p},s)\hat{a}(\mathbf{p},s)e^{-ip\cdot x} + v_\alpha(\mathbf{p},s)\hat{b}^\dagger(\mathbf{p},s)e^{ip\cdot x} \right], \tag{2.53}$$

with $u_\alpha(\mathbf{p},s)$ being the components of a bispinor ($\alpha = 1,\ldots,4$) for a given momentum $\mathbf{p}$ and helicity s, and $E_{\mathbf{p}} = \sqrt{\mathbf{p}^2+m^2}$. Unlike the real scalar field, the Dirac field is not hermitian, so two independent annihilation (creation) operators, which have been denoted by $\hat{a}(\mathbf{p},s)$ ($\hat{a}^\dagger(\mathbf{p},s)$) and $\hat{b}(\mathbf{p},s)$ ($\hat{b}^\dagger(\mathbf{p},s)$), are needed; the operators enter the solutions of $\hat{\psi}$ and $\hat{\bar{\psi}}$. Later, imposing quantization conditions on those fields requires to take into account that they represent spin-$\frac{1}{2}$ particles, and according to the spin-statistics theorem they must be quantized using anticommutation relations. Therefore, for Dirac fields, the quantization simply proceeds by replacing the Poisson brackets $\{\cdot,\cdot\}_{PB}$ (Eq. (2.3)) with anticommutators of operators $\{\cdot,\cdot\}$ and adding a Kronecker delta $\delta_{\alpha\beta}$ to account for the different components. All this produces the following algebra

$$\{\hat{a}(\mathbf{p},s),\hat{a}^\dagger(\mathbf{p}',s')\} = \delta^3(\mathbf{p}-\mathbf{p}')\delta_{ss'}, \qquad \{\hat{b}(\mathbf{p},s),\hat{b}^\dagger(\mathbf{p}',s')\} = \delta^3(\mathbf{p}-\mathbf{p}')\delta_{ss'}, \tag{2.54}$$

$$\{\hat{a}(\mathbf{p},s),\hat{a}(\mathbf{p}',s')\} = \{\hat{a}^\dagger(\mathbf{p},s),\hat{a}^\dagger(\mathbf{p}',s')\} = \{\hat{b}(\mathbf{p},s),\hat{b}(\mathbf{p}',s')\} = \{\hat{b}^\dagger(\mathbf{p},s),\hat{b}^\dagger(\mathbf{p}',s')\} = 0.$$

The Eq. (2.54) exhibits the ordinary canonical commutation relations of fermionic particles. The two number operators are $\hat{N}(\mathbf{p},s) = \hat{a}^\dagger(\mathbf{p},s)\hat{a}(\mathbf{p},s)$ and $\hat{\bar{N}}(\mathbf{p},s) = \hat{b}^\dagger(\mathbf{p},s)\hat{b}(\mathbf{p},s)$, and because of their fermionic nature, the operators' eigenvalues can only be 0 or 1.

Analogously to the case of the real scalar field, the time-ordered correlation functions are also defined, now formed by products of both fields $\hat{\psi}(x)$ and $\hat{\bar{\psi}}(x)$. The fermionic correlation functions feature additional minus signs with respect to the bosonic ones. Those are associated with the anticommutating character of the fields, which introduces a -1 factor under the permutation of two of them. In particular, the two-point correlation function can be computed using the field expansion in terms of creation-annihilation operators ($\not{p} \equiv \gamma^\mu p_\mu$)

$$\Delta_{\alpha\beta}(x_1-x_2) := \langle 0|\,\mathcal{T}\left[\hat{\psi}_\alpha(x_1)\hat{\bar{\psi}}_\beta(x_2)\right]|0\rangle = \int \frac{d^4p}{(2\pi)^4} \left(\frac{i}{\not{p}-m+i\epsilon}\right)_{\alpha\beta} e^{-ip\cdot(x_1-x_2)}. \tag{2.55}$$

This is the fermion propagator in position space, and it completely describes the transition probabilities from point to point, as the other two-point time-ordered correlation functions vanish $\langle 0|\,\mathcal{T}\left[\hat{\psi}_\alpha(x_1)\hat{\psi}_\beta(x_2)\right]|0\rangle = \langle 0|\,\mathcal{T}\left[\hat{\bar{\psi}}_\alpha(x_1)\hat{\bar{\psi}}_\beta(x_2)\right]|0\rangle = 0$.

2.3.1.3 Vector Field Quantization

The last case of field quantization analyzed is that of a vector field. In terms of Lorentz group representations, the vector field is associated to the irrep $(\frac{1}{2},\frac{1}{2})$. In Subsec. 2.2.3.3, it was shown how this representation decomposes when restricted to the rotation group. It was found that, apart from the trivial representation, the vector irrep decomposes into a 3-dimensional irrep of the rotation group, which is basically the spin-1 representation. So,

vector fields represent spin-1 bosons, and they play a fundamental role in gauge interactions. It was also seen that the unitary representations of the Poincaré group are totally different for massive and massless particles, this fact turns out to be transferred to the quantization problem as well. The little group for a massive vector is the $SO(3)$, whose spin-1 irrep possesses three degrees of freedom, whereas for a massless vector is $ISO(2)$ (one rotational degree of freedom), which, along with the aforementioned parity invariance condition[4], provides two degrees of freedom. The above describes a small but significant difference between the two cases, which is also reflected in the treatment at the level of fields.

The first case corresponds to that of a massless vector field. The classical Lagrangian density describing Maxwell equations is

$$\mathcal{L} = -\frac{1}{4} F_{\mu\nu} F^{\mu\nu}, \tag{2.56}$$

with $F_{\mu\nu} = \partial_\mu A_\nu - \partial_\nu A_\mu$. Unlike the cases seen so far, here, the massless field A_μ is not unambiguously defined since the action and the equations of motion are invariant under the gauge transformations $A_\mu \longrightarrow A_\mu + \partial_\mu f$. An implication of this invariance is that the theory has less physical degrees of freedom than what would be expected for a vector field. Not fixing the gauge causes, for instance, that the canonical quantization can not be carried out, because the time component of the canonically conjugate momentum of the field $A_\mu(x)$ vanishes $\pi_0(x) = 0$. The way this problem can be tackled is by fixing the gauge, and this can be done in several ways. The so-called Lorentz gauge $\partial_\mu A^\mu = 0$ has the advantage that maintains covariance in the fixing condition, this to the detriment of not fixing completely the gauge freedom (still invariant under $\partial_\mu \partial^\mu f = 0$). A very elegant way to implement the Lorentz gauge is to introduce the condition as a Lagrange multiplier term $-\frac{\chi}{2}(\partial_\mu A^\mu)^2$ in Eq. (2.56). However, for simplicity, it is set $\chi = 1$ (Feynman gauge), which implies that the equation for χ should be interpreted as a constraint on the solutions of $A_\mu(x)$. This yields

$$\mathcal{L} = -\frac{1}{2} \partial_\mu A_\nu \partial^\mu A^\nu, \qquad \text{with} \qquad \partial_\mu A^\mu = 0. \tag{2.57}$$

The canonical quantization usually proceeds by putting aside for a moment the constraint. Then, after having quantized the field, a "physicality" condition is applied to eliminate the extra degrees of freedom. One approach is the well-known Gupta-Bleuler formalism [41, 42], which successfully implements a constraint at the level of operators. One can nonetheless infer the final result without having to go through the rigorous procedure. In principle, the solutions of the field $A_\mu(x)$ can be expanded on a basis of four linearly independent real polarization vectors $\varepsilon_\mu(\mathbf{p}, \lambda)$, $\lambda = 0, 1, 2, 3$. However, two of them can be eliminated. The first, by imposing the Lorentz gauge condition, which forces the polarization vectors to be transverse $\varepsilon_\mu(\mathbf{p}, \lambda) p^\mu = 0$. The second, using the conditions $p^2 = 0$ and $\partial_\mu \partial^\mu f = 0$ to eliminate time-like polarization vectors. Finally, just two physical independent transverse polarizations $\lambda = 1, 2$ are left. The solution written in terms of operators is

$$\hat{A}_\mu(x) = \int \frac{d^3 p}{\sqrt{2E_{\mathbf{p}}(2\pi)^3}} \sum_{\lambda=0}^{3} \varepsilon_\mu(\mathbf{p}, \lambda) \left[\hat{a}(\mathbf{p}, \lambda) e^{-ip\cdot x} + \hat{a}^\dagger(\mathbf{p}, \lambda) e^{ip\cdot x} \right], \tag{2.58}$$

[4]Under parity, spin remains unchanged, but helicity flips sign.

with $E_{\mathbf{p}} = |\mathbf{p}|$. The reduction to the two physical degrees of freedom ($\lambda = 1, 2$) is normally carried out with the Gupta-Bleuler procedure after quantization. For the Lagrangian in Eq. (2.57), the canonically conjugate momentum is $\pi_\mu(x) = -\dot{A}_\mu(x)$ (no vanishing components), thereby the quantization procedure for the vector boson field continues as usual, replacing the Poisson brackets $\{\cdot,\cdot\}_{PB}$ with commutators $[\cdot,\cdot]$. Apart from an extra factor $(-\eta_{\mu\nu})$ that must be added to preserve covariance, the field commutation relations are identical to those of four independent Klein-Gordon fields, thus obtaining

$$\begin{aligned}[\hat{a}(\mathbf{p},\lambda), \hat{a}^\dagger(\mathbf{p}',\lambda')] &= \delta^3(\mathbf{p}-\mathbf{p}')\delta_{\lambda\lambda'}\zeta_\lambda, \\ [\hat{a}(\mathbf{p},\lambda), \hat{a}(\mathbf{p}',\lambda')] &= [\hat{a}^\dagger(\mathbf{p},\lambda), \hat{a}^\dagger(\mathbf{p}',\lambda')] = 0,\end{aligned} \tag{2.59}$$

with $\zeta_0 = -1$ and $\zeta_1 = \zeta_2 = \zeta_3 = 1$. Again, the commutation relations of the operators $\hat{a}(\mathbf{p},\lambda)$ and $\hat{a}^\dagger(\mathbf{p},\lambda)$ are easily recognized as the canonical conditions for bosonic particles. The massless vector field propagator can also be obtained by computing the time-ordered correlation functions. In this case, the two-point correlation function is

$$\Delta_{\mu\nu}(x_1 - x_2) := \langle 0|\, \mathcal{T}\left[\hat{A}_\mu(x_1)\hat{A}_\nu(x_2)\right]|0\rangle = \int \frac{d^4p}{(2\pi)^4}\frac{-\eta_{\mu\nu}}{p^2 + i\epsilon}e^{-ip\cdot(x_1-x_2)}. \tag{2.60}$$

This equation exhibits the contributions to the propagator from transverse, longitudinal and time-like modes (more details in [17]).

On the other hand, the case of a massive vector field presents its particularities. After having discussed the massless case, it is not necessary to deepen much in the mathematics of the massive vector field, since in essence, both are very similar. However, there are core differences in their physics, which are going to be stressed. The Lagrangian that leads to the so-called Proca equation for a massive vector field is directly obtained if a mass term $\frac{1}{2}m^2 A_\mu A^\mu$ is added to Eq. (2.56). The mass term explicitly breaks gauge invariance, so it is not necessary to impose the Lorentz gauge fixing $\partial_\mu A^\mu = 0$, this naturally arises as a consequence of the equations of motion. The constraint removes one of the four initial degrees of freedom, leaving, therefore, three independent polarization modes. It can also be checked that, just like for the massless field, the zeroth component has no canonical conjugate momentum $\pi_0(x) = 0$. However, such a requirement is not needed now, as it can be proven that the $A_0(x)$ component is a dependent quantity and not a dynamical variable. The solution for the field $\hat{A}_\mu(x)$ is the same as in Eq. (2.58), with the only difference (apart from $E_{\mathbf{p}} = +\sqrt{\mathbf{p}^2 + m^2}$) that now the sum runs over three polarization states $\lambda = 1, 2, 3$. The canonical quantization is then achieved as usual. The same algebra as in Eq. (2.59) is obtained for the creation-annihilation operators associated with the three polarization components. Regarding the two-point correlation functions, the propagator of the massive vector field is a little different compared to the massless case, for more information see [17].

2.3.2 Path Integrals

The previous subsection addressed the fundamental aspects of the canonical quantization in QFT for free fields (non-interacting particles), in which the fields have been represented by non-commuting operators. However, the canonical quantization becomes difficult to apply

when dealing with non-abelian gauge theories (Subsec. 2.4.2), that is, theories in which the interaction occurs by means of non-abelian Lie group transformations of fields. In such cases, the alternative "path integral" formalism is particularly well suited. The path integral method offers a very elegant way to determine all the properties of a system using tools from functional analysis. It is also equipped with a nice physical interpretation of quantum amplitudes, as it deals with an infinity of quantum-mechanically possible trajectories, instead of a single classical trajectory. In spite of the above mentioned, it is important to point out that both formulations are equivalent.

Feynman was one of the pioneers in introducing the non-relativistic formulation of QM in terms of path integrals [43, 44]. In the non-relativistic theory, the systems have a finite number of degrees of freedom, nevertheless, the results from the finite-dimensional case can be transferred to field theory without difficulties. The standard term of the form e^{iS}, where S is the action (2.1), can be roughly viewed as a probability density function containing the different field configurations. The physical observables are then obtained by computing "expectation values" over the different operators. These computations are done employing functional integrals [45]. The quantum character of this method is intrinsically related to the fact that each of these alternative functions makes its coherent contribution to the integral, thus giving rise to interference among the various trajectories.

In Subsec. 2.3.1, the concept of time-ordered correlation functions has already been introduced. Those are basically the expected value of an operator formed by the multiplication of several fields, so it is possible to use the method of path integrals to compute them. For instance, in the case of the real scalar field $\phi(x)$, the correlation function in Eq. (2.50) can be translated into a path integral of the form

$$\mathcal{G}_n(x_1, \ \dots \ , x_n) = \frac{\int \mathcal{D}\phi \ \phi(x_1) \ \cdots \ \phi(x_n) \exp(iS[\phi])}{\int \mathcal{D}\phi \ \exp(iS[\phi])}, \tag{2.61}$$

where $\mathcal{D}\phi$ denotes integration over all possible field configurations $\phi(x)$, with a phase given by the classical action $S[\phi]$ evaluated in that field configuration. As indicated above, this is the expectation value of an operator, this time the product of n fields ϕ. So, obtaining the Green's functions (correlation functions) is reduced to the calculation of path integrals.

There exists a method able to generate in a systematic way all the relevant Green's functions, namely all the correlation functions involving an arbitrary number of fields at different space-time points. For the non-interacting field theory, all these correlation functions are encoded in one main transition amplitude, called *Generating Functional*. The idea is to introduce an arbitrary source $J(x)$, in such a way that, performing functional derivatives with respect to $J(x)$, provides access to all possible Green's functions. For the real scalar field, the expression reads

$$\mathcal{Z}[J] = \int \mathcal{D}\phi \ \exp\left\{ i \int d^4x [\mathcal{L}(\phi, \partial_\mu \phi) + J(x)\phi(x)] \right\}. \tag{2.62}$$

It is not hard to check that when applying derivatives on $\mathcal{Z}[J]$ and evaluating in $J = 0$, the operation returns the Green's functions

$$\mathcal{G}_n(x_1, \ \dots \ , x_n) = \left. \frac{i^{-n} \delta^n \mathcal{Z}[J]}{\delta J(x_1) \ \cdots \ \delta J(x_n)} \right|_{J=0}. \tag{2.63}$$

All the information is now contained in the generating functionals, which are hence the primary objects to be calculated. This method can be easily applied to the Lagrangian (2.47) for the scalar field. Proceeding with the first derivative produces a trivial result, $\mathcal{G}_1(x_1)$ vanishes, which indicates that there is no such thing as a one-point correlation function. A second-order derivative leads to exactly the same expression (up to a constant factor) as Eq. (2.51), which is the propagator obtained via the two-point Green's function $\mathcal{G}_2(x_1, x_2)$. Operating in a similar way, the rest of the higher order Green's functions can be derived. This explicitly shows that the quantization of the system can also be achieved using path integrals.

The second-order $\mathcal{G}_2(x_1, x_2)$ and all non-vanishing higher order Green's functions regularly depend on distances $x_i - x_j$, just like the propagator $\Delta(x_1 - x_2)$. Such functions are conveniently represented by lines having end points x_i and x_j, as shown in the equation bellow

$\mathcal{G}_2(x_1, x_2)$:

,

(2.64)

$\mathcal{G}_4(x_1, x_2, x_3, x_4)$:

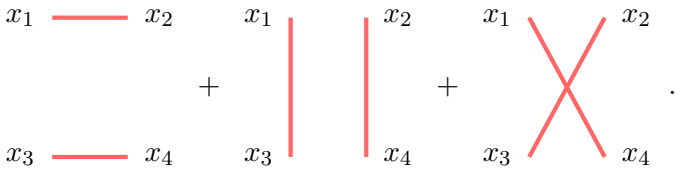

.

These pictorial representations of the underlying mathematical expressions are the well-known *Feynman graphs*. In perturbation theory, the Feynman graphs take a rich variety of forms, especially in the context of the current physical models involving many types of particles and several interactions among them. Now, it is also common to use, instead of the generic Green's functions $\mathcal{G}_n(x_1, \ldots, x_n)$, the so-called n-point connected Green's functions $\mathcal{G}_n^C(x_1, \ldots, x_n)$, which are obtained by taking derivatives $\delta/\delta J(x)$ of $\log \mathcal{Z}[J]$ rather than $\mathcal{Z}[J]$. The resulting graphs have all the n external legs connected among each other, so they are consequently called connected Feynman graphs.

So far, only the case of the real scalar field has been treated for simplicity. For other bosonic fields, the treatment is not too dissimilar, one just needs to take into account the additional degrees of freedom and any possible gauge fixing (e.g., following the Fadeev-Popov ansatz [46]). However, in the case of fermionic fields, the procedure becomes a bit peculiar. It was said that the path integral formalism is handled with classical actions, but it is known that fermion field operators are anticommuting quantum objects. Therefore, there is no way that the path integral detects that it is dealing with a different class of fields obeying the Pauli principle unless that condition is explicitly imposed on the fields. To do so, one has to resort to the machinery of anticommuting numbers, the Grassmann algebra or exterior algebra [47–49]. It is not the purpose of this subsection to delve much into the subject of Grassmann algebra, but some important properties are worth mentioning. The basic property of anticommuting numbers is, not surprisingly, that they anti-commute

$$\{\theta_i, \theta_j\} = 0. \tag{2.65}$$

As a consequence, the square and all higher powers of a generator are equal to zero $\theta_i^2 = 0$. Therefore, the most general element of a Grassmann algebra with n generators is a finite sum of the form

$$g(\Theta) = g^{(0)} + \sum_i g_i^{(1)}\theta_i + \sum_{i<j} g_{ij}^{(2)}\theta_i\theta_j + \cdots + g^{(n)}\theta_1 \ldots \theta_n. \tag{2.66}$$

This algebra also possesses the integration and differentiation operations, although these turn out to be rather odd compared to the usual differential analysis. For instance, the product rule for derivatives now appears with a "$-$" sign instead of the standard "$+$" sign, which induces an anticommutation algebra between the Grassmann variable and its corresponding derivative, similar to the one between the creation and annihilation operator of fermionic particles. But one of the most singular properties is that, for Grassmann variables, integration and differentiation are the same.

All those properties, and many others, make the treatment of the path integral method for fermionic fields a bit different from that of the bosonic fields. The Dirac field becomes a space-time function whose values are anticommuting numbers, hence the reason to introduce Grassmann-valued source fields for the construction of the generating functional. A quite detailed explanation of the path integral quantization for the Dirac field can be found in [18]. Other references that include a fairly broad explanation on Grassmann variables are [16, 17].

2.4 The Gauged Interactions

Even after Einstein expressed the need to describe the laws of physics in covariant terms, no one, not even him, had realized the role that symmetries, and therefore group theory, could play in this formulation. It was not until the concepts of mathematics were developed and deeply condensed, especially the theory of Lie groups, that physicists began to link them with the patterns that were being seen in nature. In 1954 Yang and Mills [50], inspired by Einstein's idea of covariance, included a space-time dependence in the parameters of the $SU(2)$ group to describe the conservation of isospin. Although the idea of Yang and Mills was dismissed at the time, it was the trigger for a new conception within the framework of field theories: the local gauge invariance. That formalism contained two important mathematical ingredients; the diffeomorphisms, which comprised the local symmetry transformations manifested in the principle of general covariance, and the Lie groups, which accounted for internal transformation invariance. With the help of those two pillars of modern physics, it was possible to provide a description of the interactions between elementary particles and give an explanation to some phenomena like asymptotic freedom [30]. There is no doubt that Yang-Mills' theories are very successful; nowadays, they are applied in several branches of physics, and in particular for high energy physics, they are the cornerstone. In this section, the topic of gauge field theories will be covered [51–53], its interrelation with Lie group theory, and the way they both combine to give rise to modern particle physics.

2.4.1 Abelian Gauge Invariance

In Subsec. 2.3.1.3, it was seen that the equation of motion for a vector field is not uniquely determined, indeed, the equation is said to be gauge invariant under the transformation $A_\mu \longrightarrow A'_\mu = A_\mu + \partial_\mu f$. On the other hand, it is not difficult to prove that the Dirac Lagrangian (2.52) is invariant under the internal symmetry transformation of the Dirac spinor

$$\psi(x) \longrightarrow \psi'(x) = e^{i\alpha}\psi(x), \tag{2.67}$$

where α denotes, for the time being, a constant real parameter. Such transformation is generated by one of the simplest unitary Lie group, $U(1)$, the group of 1×1 unitary complex matrices, which are basically complex numbers with norm equal to 1. This group is evidently abelian, and according to Schur's lemma, all irreducible representations are 1-dimensional. Later, the transformation (2.67) is allowed to become local $\alpha \longrightarrow \alpha(x)$, but by doing so, the Dirac Lagrangian is no longer invariant. Denoting by U the $U(1)$ group representation, the transformation of the terms with derivatives reads $\partial_\mu\psi \longrightarrow \partial_\mu\psi' = U(\partial_\mu\psi) + (\partial_\mu U)\psi$. Such a transformation helps to see that the problem arises when promoting U to be space-time dependent. To solve that issue, the following ansatz is normally proposed. Instead of ∂_μ, a modified version $D_\mu \equiv \partial_\mu - igA_\mu$ (covariant derivative) is plugged into the Lagrangian, where A_μ represents a field. The only requirement needed is that

$$\bar{\psi}\not{D}\psi = \bar{\psi}'\not{D}'\psi' \qquad \Leftrightarrow \qquad D'_\mu\psi' = U(x)D_\mu\psi. \tag{2.68}$$

If $D'_\mu = \partial_\mu - igA'_\mu$ and $\psi'(x) = e^{i\alpha(x)}\psi(x)$ are inserted in the second equality, it follows that A_μ should transform as

$$A'_\mu(x) = A_\mu(x) + \frac{1}{g}\partial_\mu\alpha(x), \tag{2.69}$$

so that Eq. (2.68) is satisfied. The previous expression is recognized right away; it is the gauge transformation of the vector field. Then, it is natural to take the vector field Lagrangian (2.56) and combine it with the one for the Dirac spinor. Since the vector field Lagrangian is invariant under the transformation (2.69), and the modified Dirac Lagrangian is already invariant under the local transformations of its field, the full theory would be invariant. In turn, besides the free-field terms, a new term in the Lagrangian of the form $ig\bar{\psi}\not{A}\psi$ pops up. This describes a sort of coupling between the fermion and boson fields, so it can be said that their interaction has been gauged. If electrons and positrons are taken as fermions, and photons as bosons, the resulting abelian gauge theory is Quantum Electrodynamics (QED) [54]

$$\mathcal{L}_{QED} = \bar{\psi}(i\not{D} - m)\psi - \frac{1}{4}F_{\mu\nu}F^{\mu\nu}. \tag{2.70}$$

The photon must be massless because a mass term like $\frac{1}{2}m_\gamma^2 A_\mu A^\mu$ would break gauge invariance. This is a very important feature of gauge theories, and one of the biggest obstacles faced by models with interactions mediated by massive gauge bosons.

Even when the above discussion was, to some extent, quite exhaustive, there is a tiny detail difficult to notice in the context of the abelian gauge theory. Therefore, it is convenient to leave the discussion for the next subsection, where the non-abelian case will be treated.

2.4.2 Non-Abelian Gauge Invariance

This case consists of a $SU(n)$ Lie group and a Dirac field with n internal degrees of freedom, the latter transforming under the fundamental representation of this group in a local way

$$\psi(x) \longrightarrow \psi'(x) = V(x)\psi(x) \equiv e^{i\alpha_a(x)T^a}\psi(x). \tag{2.71}$$

A priori, n could take any value, so the general construction comprises non-abelian Lie groups. Again, the aim is to find a way to make the theory invariant under this local transformation and thereby determining the interactions between fields that appear as a consequence of this requirement. In that sense, the standard derivative must be replaced by a new covariant derivative as for the abelian case. The inclusion of new terms in the redefinition of the derivative could be done in a very general way, but it happens that, due to renormalizability reasons, the principle of minimal substitution must be applied [55]. The incorporation of non-minimalist interactions in field theories can be addressed within the novel approach adopted by the Effective Field Theories (EFT) [56, 57]. As in Subsec. 2.4.1, the minimal term that should be added in order to construct the covariant derivative is proportional to a vector field $D_\mu \equiv \partial_\mu - igW_\mu$. Imposing now the condition in Eq. (2.68) yields

$$D'_\mu \psi'(x) = (\partial_\mu - igW'_\mu)V(x)\psi(x) = V(x)(\partial_\mu - igW_\mu)\psi(x). \tag{2.72}$$

The previous equation can be solved for W'_μ if it is multiplied on the right by $V(x)^{-1}$, which leads to the following expression

$$W'_\mu = V(x)W_\mu V(x)^{-1} - \frac{i}{g}[\partial_\mu V(x)]V(x)^{-1}. \tag{2.73}$$

If the local transformations are neglected for a moment, the only term that survives is the first one. Revisiting the topic of Lie group representations (Subsec. 2.2.2.3) allows recognizing such transformation as that of the action of the adjoint representation of the group (Eq. (2.16)). The term with derivative appears because the Lie group parameters $\alpha_a(x)$ now have a dependency on the space-time coordinates. The gauge field W_μ is in the Lie algebra, and can therefore be expanded taking the generators as basis $W_\mu = W^a_\mu T^a$, where the sum over a is implicit. The covariant derivative for $SU(n)$ finally reads

$$D_\mu = I\partial_\mu - igW^a_\mu T^a, \tag{2.74}$$

where I is the identity matrix matching the size of the generators. Since the $W^a_\mu(x)$ transform like the adjoint representation, they form themselves an n^2-1 dimensional multiplet of $SU(n)$. It is easy to check that Eq. (2.73) recovers the form of Eq. (2.69) for the abelian case, so it represents a generalization of both cases.

So far, what has been shown is that the fermionic part of the Lagrangian is locally gauge invariant if the gauge field is changed according to the adjoint representation. The missing piece is the bosonic Lagrangian that remains invariant under the gauge field transformation. The part of the QED Lagrangian corresponding to the vector field is visibly not invariant under such transformation, at least with the former definition of $F^{\mu\nu}$. To construct this new field strength tensor, the obvious fact that covariant derivatives transform covariantly is used. The covariant object resulting from the commutation of two covariant derivatives is computed, producing $[D_\mu, D_\nu] = -igG^a_{\mu\nu}T^a$. The object $G^a_{\mu\nu}$ has been extracted out to isolate the space-time transforming part

$$G^a_{\mu\nu} := \partial_\mu W^a_\nu - \partial_\nu W^a_\mu + g f^{abc} W^b_\mu W^c_\nu, \tag{2.75}$$

with f^{abc} being the structure constants. The object $G^a_{\mu\nu}T^a$ is an element of the Lie algebra since it is expressed as a linear combination of generators, which implies that $G^a_{\mu\nu}$ transforms

under the adjoint representation. What is left then is to make use of the adjoint transformation to build a trivial-transforming object, and that can be done contracting the adjoint irrep with itself. All that together produces the following locally gauge invariant Lagrangian

$$\mathcal{L} = \underbrace{-\frac{1}{4}G^a_{\mu\nu}G^{\mu\nu a}}_{\mathcal{L}_{YM}} + \underbrace{\bar{\psi}(i\not{D} - m)\psi}_{\mathcal{L}_F}. \tag{2.76}$$

As in the abelian case, the general purpose of field gauging is achieved: a theory obeying external and internal symmetry transformations, and providing interactions. However, in the non-abelian case, an additional source term appears. The $\mathcal{L}_{YM}$ depends only on the gauge fields and contains terms of second and third-order in these and their derivatives. Physically, this means that the gauge field quanta interact among themselves. The coupling constant for those self-interactions is the same g as that for the coupling between the fermionic and bosonic fields. One of those cases is the field theory involving quarks and gluons, Quantum Chromodynamics (QCD) [58], in which the $SU(3)$ symmetry is gauged in the color space.

2.4.3 Breaking of Gauged Symmetries

Two deficiencies can be recognized in the formalism described so far. The first was naively introduced when mentioning the concept of renormalizability. Despite the theory is worked out in the minimal coupling scenario, some divergences have to be sorted out. Those divergences come mainly from connected loop diagrams that lead to divergent integrals. This issue will be briefly addressed in Subsec. 2.4.4.2. The second problem arises from the gauge invariance condition, and it has already been spotted in the abelian case. It is more dramatic in the non-abelian case, there is an additional term that further prohibits mass terms for the gauge fields. It seems that there simply exists no mass term compatible with local gauge invariance, but nature insists on an explanation for massive vector bosons. Apparently, for those cases, the symmetry subject to gauging is not there, or at least it has not been there for a while, since much earlier than when physicists knew about the existence of massive gauge bosons. One way to solve this is to resort to some mechanism that breaks the symmetry, which could explain the presence of mass terms for vector fields.

There are essentially two ways to break a symmetry. The first one is called explicit breaking, and the second one is known as spontaneous symmetry breaking. The first method simply consists of adding extra terms "by hand" to the Lagrangian, like $\delta\mathcal{L} = \frac{1}{2}m_\gamma^2 A_\mu A^\mu$, to actively break the symmetry present in the theory. The addition of symmetry-breaking terms makes the dynamical equations of fields not invariant under the symmetry group considered. Nevertheless, as the breaking term gets close to zero $\delta\mathcal{L} \to 0$ (e.g. $m_\gamma \to 0$), the symmetry is restored in those equations. The second case is less trivial, since the Lagrangian remains invariant under the symmetry group $\delta\mathcal{L} = 0$ but the vacuum (ground) state does not $\hat{U}(\alpha_a)\,|0\rangle \neq |0\rangle \iff \hat{T}_a\,|0\rangle \neq 0$. This is because the dynamics of the vacuum state is degenerate, and a particular "choice" of one as the physical vacuum breaks the symmetry. Every choice for the ground state is equal, which manifests the permanence of the hidden symmetry. However, once a specific ground state is selected it gets transformed to another ground state, which makes it not invariant under the symmetry.

2.4.3.1 Goldstone's conjecture

Spontaneous symmetry breaking was introduced in QFT by Nambu [59] in analogy with the theory of superconductivity. A couple of years later Goldstone, Salam, and Weinberg [60, 61] studied the breaking of the symmetry with non vanishing vacuum expectation values of scalar fields. They detected the appearance of a massless mode out of a degenerate vacuum, corresponding to the so-called Nambu-Goldstone boson. That was then generalized becoming the well-known Goldstone's theorem. In rough terms the theorem says that: *For a quantum field system subject to an internal continuous global symmetry, when its ground state spontaneously breaks this symmetry, there are massless excitations whose number is equal to the number of broken generators of the symmetry.* A proof of the Goldstone's theorem for classical field theories can be found in [18].

This theorem can be interpreted in the context of group theory if one considers a scalar field $\phi^\alpha(x)$ with potential $V(\phi^\alpha)$ invariant under an internal symmetry generated by a representation $U^\alpha_\beta(g)$ of a Lie group G. Classically

$$V(U^\alpha_\beta(g)\phi^\beta) = V(\phi^\alpha), \qquad\qquad U^\alpha_\beta(g)\phi^\beta_0 \neq \phi^\alpha_0, \tag{2.77}$$

where ϕ^α_0 represents the state that minimizes the potential, i.e. the vacuum expectation value. One example of such a potential is the "Mexican-hat-like potential", which is given by $V(\phi^\alpha) = \mu^2\phi_\alpha\phi^\alpha + \lambda(\phi_\alpha\phi^\alpha)^2$ for $\mu^2 < 0$ and $\lambda > 0$. Later, the symmetry does not have to be broken completely, so there might exist a subgroup $H \in G$ for which the ground state is still invariant. So, the concept of little group appears again, this time referred to the transformations that leave the ground state invariant $U^\alpha_\beta(h)\phi^\beta_0 = \phi^\alpha_0$. Consequently, the Lie algebra of this little group H forms a subset with $n-k$ generators t^a of the Lie algebra of G, which contains n generators T^a. Then, by making a Taylor expansion of the potential to extract the mass matrix $M^2_{\alpha\beta}$ (second-order partial derivatives), and using the invariance of $V(\phi^\alpha)$ in Eq. (2.77), it results in

$$M^2_{\gamma\alpha}T^a_{\alpha\beta}\phi^\beta_0 = 0 \qquad\qquad \forall_a \in \{1, \ldots, n\}. \tag{2.78}$$

This relation means that, when acting with the $n-k$ generators of the little group, there is no restriction on masses since $t^a_{\alpha\beta}\phi^\beta_0 = 0$. In contrast, when acting with the remaining k "broken" generators, the only possible solution is to have k states $\chi^a_\alpha \equiv T^a_{\alpha\beta}\phi^\beta_0$, for which the mass eigenvalue vanishes. The above clearly reflects the content of the Goldstone's theorem. It is worth mentioning that the linear sigma model [62, 63] is a good example of application of this theorem, as the pion can be regarded as an approximate Nambu-Goldstone boson.

2.4.3.2 Higgs mechanism

Goldstone's conjecture did not help much in trying to get massive gauge bosons, at least at first sight. In principle, it was only applicable to global symmetries, and the only thing that supplied was massless particles. All that, added to the difficulties of Yang-Mills' theory, became a very unfavorable scenario for theoretical particle physics. Nevertheless, a physicist named Peter Higgs discovered that when one incorporates locality to the theory, the Goldstone's theorem breaks down [64]. Besides, several independent groups, among them Peter Higgs himself [65], Robert Brout and François Englert [66], and Gerald Guralnik, Carl

Richard Hagen and Tom Kibble [67], managed to develop a relativistic model obtaining the same result. This procedure describing the spontaneous breaking of a gauged continuous symmetry was called the "Brout-Englert-Higgs mechanism". Although the spontaneous symmetry breaking mechanism is essentially the same, when combined with gauge fixing, it allows the gauge bosons to consistently acquire a nonzero mass.

The new terms appearing in the Lagrangian when incorporating gauge invariance are shown in Eq. (2.79). The kinetic term of the scalar field is now accompanied by a covariant derivative like (2.74), which includes all the gauge fields contained in the theory. For any scalar field, real group representations can be used, so $T^a \to iT^a$ can be taken. The gauge-invariant kinetic term then reads

$$\frac{1}{2}(D_\mu\phi_\alpha)(D^\mu\phi^\alpha) = \frac{1}{2}(\partial_\mu\phi_\alpha)(\partial^\mu\phi^\alpha) + gW^a_\mu(\partial^\mu\phi^\alpha T^a_{\alpha\beta}\phi^\beta) + \frac{1}{2}g^2W^a_\mu W^{b,\mu}(T^a\phi)_\alpha(T^b\phi)^\alpha. \quad (2.79)$$

When the scalar potential ϕ^α is expanded around the ground state ϕ^α_0, the last term becomes $\frac{1}{2}m^{ab}W^a_\mu W^{b,\mu}$, where $m^{ab} = g^2(T^a\phi_0)_\alpha(T^b\phi_0)^\alpha$. Thus, for each broken generator, a mass term will appear for its corresponding gauge boson, contrary to the case with global symmetry. Oppositely, the gauge bosons associated with some generator of the little group will be massless. This explains very easily how the masses of the gauge bosons are generated, however, it was mentioned in Subsec. 2.3.1.3 that massive spin-1 particles have three degrees of freedom, whereas the massless ones have only two. It seems as if the vector field had obtained an additional degree of freedom for free, but certainly not. At first glance, the massless Nambu-Goldstone bosons do not seem to have anything to do with the mass of the gauge fields, as they emerge from the spontaneous symmetry breaking driven by the potential, so one would expect that they are still there. The explanation lies in the fact that the theory is now gauge-invariant and, as previously seen, a gauge fixing should be chosen. There is nothing prohibiting the implementation of the gauge fixing by conditions on distinct fields at once. Differently from the standard procedure where the conditions are only applied on W^a_μ, it is also possible to impose conditions on ϕ^α. In fact, Weinberg [68] proved that there always exists a gauge, which was called "unitary gauge", such that the scalar field components in the direction of the Goldstone states are zero

$$\tilde{\phi}^\alpha\, T^a_{\alpha\beta}\, \phi^\beta_0 = 0 \qquad\qquad \forall_a \in \{1,\dots,n\}. \quad (2.80)$$

Here the $\tilde{\phi}^\alpha$ represents a suitable transformation of the fields ϕ^α in order to make them orthogonal to the k Goldstone fields χ^a_α. This demonstrates that the Goldstone bosons are not physical particles, basically, they can be gauged away. Regardless of the chosen gauge, physical massless states will never emerge. Now it is straightforward to deduce where the additional degrees of freedom of the gauge fields came from; they are the Goldstone bosons that were "rotated" away and transformed into the longitudinal polarization of the massive spin-1 particles. The remaining $n-k$ orthonormal set of states η^a_α spanning the subspace orthogonal to the subspace generated by all χ^a_α will give rise to massive scalar particles. So, the mechanism generates massive gauge bosons and a bunch of massive scalars, the latter ones are referred to as the *Higgs bosons*. As it will be seen later, within the framework of the SM, where the symmetry breaking materializes as $SU(2)_L \times U(1)_Y \to U(1)_{EM}$, the remaining unbroken generator suggests the existence of the famous SM Higgs boson. In other models with a bigger internal symmetry group, the breaking can result in more that one Higgs boson.

2.4.4 Perturbative Methods for the Interactions

It is clear that the gauge principle provides the basis for understanding the way different types of particles interact. Such interaction is controlled by the coupling constant g introduced in the covariant derivative when implementing the minimal substitution. Aside from the interactions generated by the gauge couplings, other types of interactions might also take place, such as interactions between scalar and fermion fields, and many others. The way in which the physicists have been able to probe the existence and characteristics of these interactions is by using experiments involving many of those kinds of particles. The particles approach each other from macroscopic distances to a small area of interaction, which then abandons the products of the interaction becoming distant again. The physical particles before and after the interaction are so far from each other that they can be considered as free particles; those which are described by the previously treated free fields. What can be measured from these "scatterings" are transition probabilities between the initial and final states. The magnitude that generally quantifies these transition probabilities is called "cross-section". In this subsection, two topics concerning the interactions that occur in a field theory will be addressed; Perturbation Theory [16, 18, 19] and Renormalization [15, 20, 69, 70].

2.4.4.1 Perturbation Theory

In QM, there are three well-known pictures used to represent the evolution of states and operators. In the Schrödinger picture, the time dependence is carried by the states obeying the Schrödinger equation, while the operators remain constant in time. By means of unitary transformations, one can reach the so-called Heisenberg picture, which behaves the other way around to the Schrödinger picture; the states are time-independent, and the operators are the ones carrying the dependence. In this case, the evolution equation is a pure operator equation involving commutators. The last one is the most relevant for QFT perturbation theory since, in this context, the evolution of the free fields is well known and, therefore, the only missing piece is the interaction part. Consequently, it is called the Interaction Picture (or Dirac Picture), and it is an intermediate representation between the previous two, as both, the states and the operators evolve in time. The main idea is to split the Hamiltonian into two parts, $H = H_0 + H_I$. An unitary operator $\hat{U}_I$ governs the evolution of the states $|\psi_I(t)\rangle$ by $|\psi_I(t)\rangle = \hat{U}_I(t, t_0)\,|\psi_I(t_0)\rangle$. This operator can be expressed in terms of the interacting Hamiltonian part as

$$\hat{U}_I(t, t_0) = \mathcal{T}\left\{\exp\left[-i\int_{t_0}^{t} dt'\ \ \hat{H}_I(t')\right]\right\}, \tag{2.81}$$

with $\mathcal{T}$ denoting the time-ordered product. Now, a scattering process in which two initial particles approach each other from a large distance outside the range of their interactions is normally assumed, so, at times $t \to -\infty$, the states are time-independent and are denoted as $|\psi_{in}\rangle$. The same applies for a very long time after the scattering $t \to \infty$, the states become free and time-independent $|\psi_{out}\rangle$. As stated before, the evolution of the system from $|\psi_{in}\rangle$ to $|\psi_{out}\rangle$ is dictated by the operator $\hat{U}_I$, which then takes the form $\hat{S} := \hat{U}_I(\infty, -\infty)$. This operator is called the S-matrix.

The Green's functions defined in Sec. 2.3 can be regarded as those corresponding to the Heisenberg picture since the quantum fields (the operators) have explicit time dependence, and the states are generated by time-independent quantities (creator operators) out of the

vacuum. Then, the Green's functions can be brought to the interaction picture through unitary transformations applied over the fields and the vacuum state. After doing that, a hypothetical Green's function containing interaction among different types of fields is expressed as

$$\mathcal{G}^{\mu\dots}(w,\dots x,\dots y,\dots z,\dots) = \frac{\langle 0|\,\mathcal{T}\left\{\hat{S}\;\hat{\phi}(w)\dots\hat{A}^{\mu}(x)\dots\hat{\psi}(y)\dots\hat{\bar{\psi}}(z)\dots\right\}|0\rangle}{\langle 0|\,\hat{S}\,|0\rangle}, \tag{2.82}$$

where $\hat{S}$ refers to the S-matrix, and all quantities are considered in the interaction picture. In general, the expression (2.82) is very hard to compute analytically, so, if the interaction term $H_I = \int d^3x\mathcal{H}_I(x)$ is small enough, a power series expansion of $\hat{S}$ can be performed. This usually occurs in gauge theories when the coupling constant g is small, like for instance QED, where $g_{QED} \approx 1/137$. The power expansion is sometimes known as Dyson series [71], and it reads

$$\hat{S} = \sum_{n=0}^{\infty}\frac{(-i)^n}{n!}\int\;\dots\;\int d^4x_1\;\dots\;d^4x_n\;\;\mathcal{T}\left\{\hat{\mathcal{H}}_I(x_1)\;\dots\;\hat{\mathcal{H}}_I(x_n)\right\}, \tag{2.83}$$

with the integrations being over all space-time. The previous formula is the basis of perturbation theory in QFT. As it can be seen, evaluating very high order terms would require to compute very complicated time-ordered products. To simplify those calculations, Wick [72] developed a method that is able to express a time-ordered product of fields as a sum of several terms, each of which is a normal-ordered product [16] containing contractions of pairs of fields (Feynman propagators) and the remaining non-contracted fields. The sum accounts for all possible generalized normal products that can be formed out of contractions between two fields. Then, using the S-matrix expansion (Eq. (2.83)) in conjunction with Wick's theorem, the Green's functions can be evaluated in perturbation theory as well. The different terms in this expansion are represented by Feynman diagrams, which are drawn according to some rules that may vary depending on the interaction $\mathcal{H}_I(x)$ among fields [54, 73, 74].

The importance of the path integral treatment for non-abelian gauge theories has already been emphasized in Subsec. 2.3.2. As seen before, for those cases, it is useful to construct a single object called generating functional, in which all the information is contained. Then, it is convenient to apply the machinery of the S-matrix expansion to the generating functional of an interacting theory, and thus simplify the complicated analytic calculations. This would allow relating the interacting generating functional to the relatively easy case of the free-field generating functional via a perturbation series. The free field theory is simple to solve because only Gaussian integrals appear in the calculations. First, an interacting term $\mathcal{H}_I(x) = -\mathcal{L}_I(x)$ is considered, and then a fictitious source $\mathcal{L}_S(x)$ that augments the interaction Lagrangian density is added $\mathcal{L'}_I(x) = \mathcal{L}_I(x) + \mathcal{L}_S(x)$. The modified S-matrix associated with the augmented interaction Lagrangian $\mathcal{L'}_I(x)$ is denoted by $\hat{S}'$. Taking into account the formulas (2.82) and (2.83), the interacting generating functional can be canonically defined as

$$\mathcal{Z}[J] = \frac{\langle 0|\,\hat{S}'\,|0\rangle}{\langle 0|\,\hat{S}\,|0\rangle}, \tag{2.84}$$

where J represents all the possible types of sources needed to construct the augmented Lagrangian. The definition is constructed in such a way that, in the absence of sources, $\mathcal{Z}[J]$

becomes equal to the unity $\mathcal{Z}[0] = 1$. The expression (2.84) is already quite revealing as far as the perturbation expansion is concerned, but it is in the path integral formalism where this becomes even clearer. In order to formulate the path integral version of Eq. (2.84), one can take as example the particular case of the real scalar field, for which an expression for the free-field generating functional was already given in Subsec. 2.3.2. Next, the generating functional (2.62) is denoted by $\mathcal{Z}_0[J]$, to stress the fact that it represents the free-field case. The form of $\mathcal{Z}_0[J]$ easily reveals that the interacting generating functional is driven by the augment Lagrangian $\mathcal{L}' = \mathcal{L}_0 + \mathcal{L}'_I$, being $\mathcal{L}_0$ the free field Lagrangian. Later, since the path integral only contains classical fields, the exponential can be split into the free and the interacting parts, so $\mathcal{Z}_0[J]$ would appear as an independent factor in the integration. Furthermore, it can be checked that the external source inserts fields $\phi(x)$ inside the integral through derivatives. Hence, it is reasonable to replace $\phi(x)$ with the functional-derivative operator $\phi(x) \to i\frac{\delta}{\delta J(x)}$ wherever it enters in $\mathcal{L}_I(\phi(x))$. What is left is to set a normalization for the generating functional, then producing

$$\mathcal{Z}[J] = \frac{\exp\left[i\int d^4x \mathcal{L}_I\left(-i\frac{\delta}{\delta J(x)}\right)\right]\mathcal{Z}_0[J]}{\exp\left[i\int d^4x \mathcal{L}_I\left(-i\frac{\delta}{\delta J(x)}\right)\right]\mathcal{Z}_0[J]\Big|_{J=0}}. \tag{2.85}$$

It is evident now that if the exponential function is expanded into its power series, the perturbation expansion for the generating functional is accomplished. The price to pay is having to deal with complicated functional derivatives, but the great merit is to replace integrals by derivatives.

Before concluding this subsection, it is important to mention that perturbation theory is the basis of modern calculations in high energy physics. It sets the foundations to construct the physical observables, and it establishes a logic of the physical process that goes through the mathematical formulation, the physical interpretation, up to the final measurable quantity. Unfortunately, there exist physical systems in which this theory does not apply and other methods must be employed. That is the case of Lattice QCD [75, 76], a non-perturbative approach to solving low-energy QCD. In this regime, nonlinearity and large coupling constants predominate, which makes impossible any attempt to apply the standard perturbation expansion. In all other cases where the perturbation is appropriate, the procedure has been tremendously successful.

2.4.4.2 Renormalization of Gauge Theories

The previous subsection reviewed a feasible way to access the computation of physical observables via the perturbation expansion. However, it turns out that some of the integrals appearing in such calculations are divergent, which represents a serious threat to the applicability of the theory. Diagrammatically, these divergences are identified by graphs containing some kind of loop, as shown in Fig. 2.1. They usually emerge in the calculation of important physical quantities, such as the corrections to the coupling constants and the mass of the particles. Nevertheless, the "bare" parameters included in the Lagrangian of any field theory have no physical meaning, as they can not be measured. What is really measured is the whole contribution of the quantum corrections to a given bare parameter. On top of that, the measurement of a single "renormalized" quantity normally takes as input the values of other parameters that would have previously been measured too. Therefore, the only phys-

ically meaningful dependence is the relations between observables, which incorporates loop effects to all orders in perturbation theory. For this reason, it is imperative to know the effect that every new order in the perturbation expansion has on the value of the parameter. So, a consistent way to extract finite predictions for physically observable quantities is needed; this technique is called *Renormalization* [20,20,77]. With that method, infinities can be absorbed in a mathematically consistent manner, such that local gauge invariance remains intact. Not

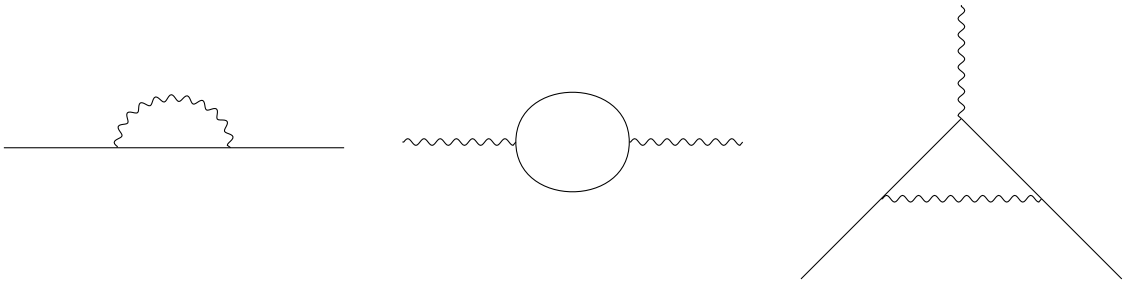

Figure 2.1: Some Feynman diagrams that lead to divergent integrals.

all field theories are renormalizable; if a Lagrangian contains combinations of field operators of high enough dimension, the number of counterterms required to cancel all divergences is infinite and, therefore, the theory would lose all predictive power [78]. In the case of the Yang-Mills theory, a work carried out by 't Hooft [79] showed that such gauge theory was renormalizable. It was essential to have absolute gauge invariance to be able to renormalize the theory. Although, the experimental results leaned towards a possible scenario of spontaneous symmetry breaking, luckily, the Higgs mechanism was already there, and that led 't Hooft to extend his findings to the case of spontaneously broken gauge theories [80]. Later, the technique of dimensional regularization was developed [81, 82], one of the most used in the field of renormalization.

It is useful to define a magnitude that quantifies the degree of divergence of certain integral. It is called superficial degree of divergence D, and it is the difference between the power of p^μ in the nominator and the power of p^μ in the denominator. Most of the divergent integrals that appear in the perturbation theory have the simplified form $\int^\infty p^{D-1}dp$, and they characterize the ultraviolet divergence produced in the internal loops. For $D > 0$, the integral will have a polynomial divergence, for $D = 0$, it will diverge logarithmically, and for $D < 0$, it will not diverge. In principle, D can be computed for each diagram if certain information is a priori known. A quite general formula is given by

$$D = 4 - \sum_f N_f^{(E)}(S_f + 1) - \sum_i N_i^{(V)}\Delta_i, \qquad \Delta_i \equiv 4 - d_i - \sum_f N_{if}^{(F)}(S_f + 1), \tag{2.86}$$

where $N_f^{(E)}$ is the number of external lines of field type f, S_f is the sum $j^+ + j^-$ of the corresponding irrep (j^+, j^-) in $SL(2,\mathbb{C})$ of the field type f (see Tab. 2.2), $N_i^{(V)}$ is the number of vertices of interaction type i, d_i is the power of the derivatives in the interaction of type i, and $N_{if}^{(F)}$ is the number of fields of type f in the interaction of type i. The parameter Δ_i has been set apart because it identifies the dimensionality (in power of mass) of the coupling constant of the interaction of type i. If a given theory has $\Delta_i \geq 0$, an upper bound can be set on D, namely $D \leq 4 - \sum_f N_f^{(E)}(S_f+1)$. This means that, for this case, only a finite number of

diagrams will yield a divergent integral. On the other hand, if $\Delta_i < 0$ the term $-\sum_i N_i^{(V)} \Delta_i$ will grow as the number of vertices increases, therefore, D will become larger and larger when including more vertices, and eventually, an infinite number of counterterms will have to be introduced to cancel those infinities. Summarizing, the degree of renormalizability can be classified as

- Super-Renormalizable: $\Delta_i > 0$
- Renormalizable: $\Delta_i = 0$
- Non-Renormalizable: $\Delta_i < 0$

These three cases can be translated as Relevant, Marginal and Irrelevant operators, respectively, within the more general classification scheme provided by the EFTs. Now, to consistently renormalize the $\Delta_i \geq 0$ cases, the procedure requires that the divergences show a well-defined pattern in all relevant orders in perturbation theory. A very simple argument that illustrates why this happens is that, in every renormalizable theory, the interaction terms in the Lagrangian obey certain symmetry principles, therefore, the form in which they appear is limited. This could suggest that symmetries also impose restrictions on the type of infinities occurring in the theory; indeed, for gauge theories, that is verified [83] under the BRST formalism [84–86].

Taking into account the different elements mentioned, a "program" dictating the steps to follow to renormalize the theories is commonly designed. It basically consists of two steps: the *Regularization* and the *Renormalization* [16, 18]. The Fig. 2.2 contains a small scheme summarizing, in a loose way, the general procedure to be carried out. Below, some of the points referred to in the figure are going to be discussed.

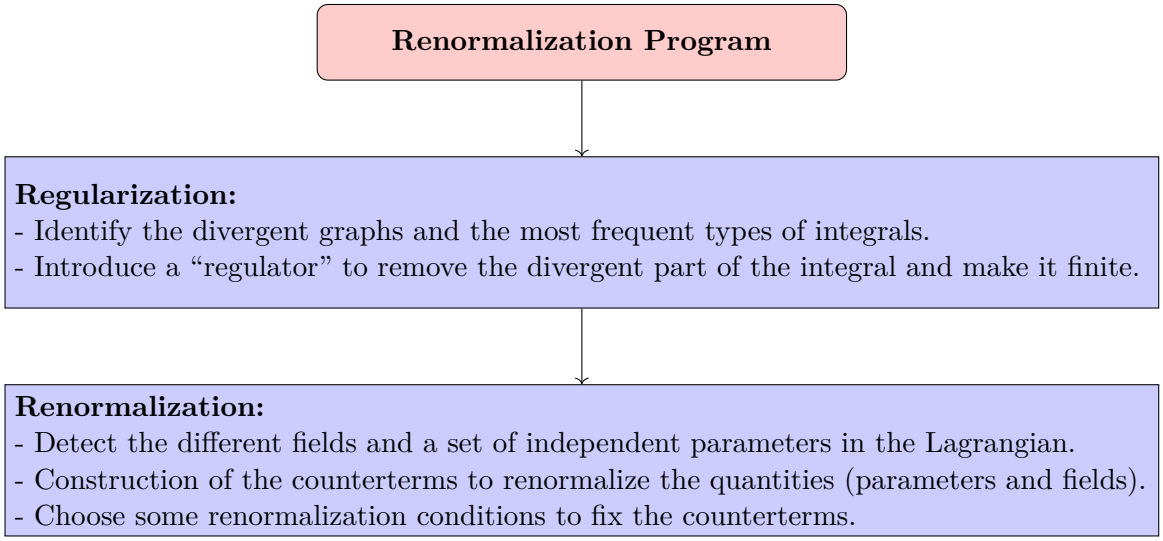

Figure 2.2: A short outline of the renormalization procedure.

Regarding regularization, with the help of the superficial degree of divergence, the common class of divergent diagrams can be identified. As illustrated in Fig. 2.1, in gauge theories, most of them tend to have cycles (loops) that are responsible for the divergent integrals. Among the regulators, perhaps the simplest one is the so-called momentum "cut-off", which

simply consists of imposing a finite upper bound Λ to the momentum running in the loop

$$\int d^4p_{_E} \longrightarrow \int_{p_{_E}^2<\Lambda^2} d^4p_{_E}, \tag{2.87}$$

where $p_{_E}$ refers to the Euclidean momenta. However, this kind of cutoff leads to some problems with unitarity. Other methods, like the lattice regularization, Pauli-Villars, and higher-derivative regulators [77], could be considered more "physical", although they entail some other practical problems. But definitely, the most known and used method is dimensional regularization. The basic idea is to take the space-time dimension $\mathfrak{d}$ to be a continuous parameter that can be modified as $\mathfrak{d} \to \mathfrak{d}-\varepsilon$. Then, the space-time dimension can be restored by taking the limit $\varepsilon \to 0$. For instance, a common integral is

$$\int \frac{d^{\mathfrak{d}}p}{(p^2-m^2+i\varepsilon)^n} = i\pi^{\mathfrak{d}/2}(-1)^n \frac{\Gamma(n-\mathfrak{d}/2)}{\Gamma(n)} \frac{1}{m^{2n-\mathfrak{d}}}, \tag{2.88}$$

which has poles for some sets of parameters n and $\mathfrak{d}$, if the latter is taken to be an integer, nevertheless, for continuous values of $\mathfrak{d}$, the integral is well defined. In four-dimensional space and for $n = 2$, the integral diverges as $\sim \frac{1}{\varepsilon}$, so this term can be removed (absorbed into a redefinition of the quantities), and the remaining finite part is kept. Physically, what a regulator does is just introduce a new energy scale Λ into the theory, so that the physics can be well established for energies far below that scale, whereas for energies above Λ the theory is not valid anymore.

As stated in the renormalization box of Fig. 2.2, first of all, the types of fields and constants appearing in a given Lagrangian need to be identified. The QED Lagrangian (2.70) can be taken as a guide. This possesses two fields (ψ and A_μ), and two parameters ($g \equiv e$ and $m \equiv m_e$). The bare quantities are denoted with a superscript (0). Later, the renormalized quantities can be defined by the following relations

$$\psi^{(0)} = \sqrt{Z_2}\psi, \quad A_\mu^{(0)} = \sqrt{Z_3}A_\mu, \quad m_e^{(0)} = m_e + \delta m, \quad e^{(0)} = \frac{Z_1}{Z_2\sqrt{Z_3}}e, \tag{2.89}$$

where $Z_1 = Z_2$ should hold in order for the covariant derivative to not change, and thus maintaining gauge invariance in the Lagrangian. The bare Lagrangian (same as Eq. (2.70) but with the bare quantities as arguments) then splits into two parts

$$\mathcal{L}_{QED}^{bare} = \mathcal{L}_{QED}^{ren} + \mathcal{L}_{QED}^{counter}, \tag{2.90}$$

where $\mathcal{L}_{QED}^{ren}$ is the renormalized Lagrangian (renormalized quantities as arguments), and $\mathcal{L}_{QED}^{counter} = \bar{\psi}(i\not{\partial}\delta_2 - \delta_m - e\not{A}\delta_1)\psi - 1/4F_{\mu\nu}F^{\mu\nu}\,\delta_3$ ($\delta_i = Z_i - 1$, for $i = 1, 2, 3$) is the counterterm Lagrangian. The counter term factors (δ_i) are not defined yet at all unless one exactly defines how much of the infinite parts of the divergent diagrams they must absorb. As seen before, there are different ways (regulators) to do that and, to choose one, means to choose a particular "renormalization scheme". One physically motivated choice is the on-shell scheme [87]. In this scheme, the pole in the exact fermion propagator (2.55) in momentum space is required to occur at the physical mass value. By using a geometric sum over the one loop diagrams, it can be proven that the propagator of the fermion is modified as $i(\not{p} - m)^{-1} \to i(\not{p} - m - \Sigma_f(p))^{-1}$, therefore, requiring the on-shell renormalization con-

ditions means $\Sigma_f(\not{p} = m) = 0$. Fixing the residue of the mass pole to the unity might also be sought, which is easily done by imposing $\partial\Sigma_f(\not{p})/\partial\not{p}|_{\not{p}=m} = 0$. Those previous requirements, plus two more conditions (photon propagator and electron charge), explicitly determine how the counter-terms have to be chosen to cancel the divergent parts. There are other quite used renormalization schemes, like the minimal subtraction (MS), or its close partner, the modified minimal subtraction ($\overline{MS}$) [87]. Unlike the on-shell scheme, they do not impose any conditions on amplitudes, they rather make use of dimensional regularization to control the divergences. In order to do that, a new energy scale parameter μ has to be introduced to ensure that the natural dimension of integrals like (2.88) does not depend on $\mathfrak{d}$. As mentioned before, these integrals diverge as $\frac{1}{\varepsilon}$, so in the case of the MS scheme, what all the counterterms do is to subtract the pole $\varepsilon = 0$. In the $\overline{MS}$ scheme, they subtract the pole plus some numerical constants that usually accompany the $\frac{1}{\varepsilon}$ term. With all that, the path to be taken to renormalize a certain gauge theory is more or less condensed. In many of the cited references, the topic is treated extensively.

Finally, mention should be made to the conceptual approach of the renormalization group. The notion in the context of QFT was first introduced in QED [88–93], but due to its general perspective, it has expanded to many modern theories. The method identifies itself through the idea that the modifications in the renormalizable quantities are changes in a physical system when viewed at different length (energy) scales. When the arbitrary renormalization scale is changed, the parameters are simultaneously altered. Then, it is said that the parameters are "running" with the scale. The way these evolve is determined by the so-called renormalization group functions (beta functions), which allow constructing the renormalization group equations [94,95]. These equations not only have great applicability in the current calculations in high energy physics, but the concept of renormalization group has also led to novel interpretations in connexion with the Conformal Field Theories (CFT) [96].

CHAPTER

3

HIGGS PHYSICS WITHIN AND BEYOND THE STANDARD MODEL

Contents

It is in the nature of a scientist to desire to understand the universe at its most fundamental level. This was what led physicists, for many years, to wonder where the mass of elementary particles came from. Some time ago, the so-called Higgs mechanism was proposed as an explanation of the phenomenon of mass acquisition of elementary particles, which in the context of particle physics responds to spontaneous breaking of the symmetry. It was not until just a few years ago, with the development of big particle accelerators and sophisticated experimental facilities, that the theory of the Higgs boson could finally be proven, to some extent. This further boosted the investigation related to the Higgs boson and the implications that it entailed. Currently, there is a broad interest in discerning all the properties of that particle, as well as ascertaining if it really is the boson that was once predicted.

This chapter is intended to make a review of some aspects of the SM, in particular, the part concerning the Higgs sector, as well as introducing new theories beyond the SM incorporating fresh and rich physics into this field of study. At the same time, that will help to motivate the analysis that is being presented in this thesis, which involves novel hypotheses concerning the Higgs sector.

The elements of theory that were reviewed in the previous chapter will be indispensable to shorten and give basis to the expositions that will emerge throughout this chapter. The first section of this chapter will be dedicated to the successful SM, and to enumerate some of its shortcomings. The second part is conceived for Higgs physics beyond the SM; here the most relevant models for the case study in this thesis will be addressed.

3.1 The Standard Model

The SM is a renormalizable gauge quantum field theory (see chapter 2) describing three of the four known fundamental forces in the universe: the electromagnetic, the weak and the strong interactions. It is responsible for giving a mathematical structure to the way in which the elementary constituents of matter interact and group. The SM Lagrangian density is constructed by assuming some basic principles that are going to be detailed below. Most aspects of this section are based on the references [97, 98].

Power Counting: According to renormalization theory (Subsec. 2.4.4.2), and in the modern view of EFT, all operators of mass dimension four or less must be included in the Lagrangian in order to ensure renormalizability. The dimension of the action $[S]$ is zero, appearing in exponentials such as e^{iS} (Subsec. 2.3.2), therefore, the mass dimension of the Lagrangian density has to be $[\mathcal{L}] = 4$ and, correspondingly, that of each term that composes it. Some examples of mass dimension of different components appearing in the SM Lagrangian are

$$[\phi] = 1, \qquad [\psi] = \frac{3}{2}, \qquad [A_\mu] = 1, \qquad [\partial_\mu] = 1, \qquad [m] = 1, \qquad [g] = 0, \tag{3.1}$$

where ϕ, ψ and A^μ are scalar, fermion (Dirac or chiral) and vector fields respectively. The other three represent partial derivatives, masses, and dimensionless couplings.

Symmetries: The complete Lagrangian must transform trivially under the whole symmetry group (Sec. 2.2), which includes internal and external (space-time) symmetries, i.e. the Lagrangian should remain invariant under the symmetry transformations. The fundamental group of space-time symmetries in the SM is the Poincaré group (Subsec. 2.2.3.3),

and the group of internal transformations is determined by $SU(3)_C \times SU(2)_L \times U(1)_Y$ (Subsecs. 2.2.3.1 and 2.2.3.2), which represent the color-, weak- and hypercharge-gauged symmetries (Sec. 2.4). The invariance associated with $SU(3)_C$ determines the physics of the QCD, and the $SU(2)_L \times U(1)_Y$ group covers the Electroweak (EW) sector.

Field content: The two above conditions impose certain restrictions on the type of fields that the theory may have and the way they can be coupled. The field content is then determined by the multiple categorizations that the irreps (Subsec. 2.2.1.2) of the symmetry group can confer to the fields involved in the theory. The fermionic representations of the Poincaré group tend to transform under the fundamental irrep of the gauged groups that act non-trivially on them, whereas the vector representations do it under the adjoint irrep. The representations of the scalar under the gauged groups are chosen in such a way to favor the spontaneous electroweak symmetry breaking (EWSB) (Subsec. 2.4.3) and to generate the fermion masses. The Tab. 3.1 shows a summary of the SM field content.

Table 3.1: Field content of the Standard Model

Name	Symbol	$SU(3)_C$	$SU(2)_L$	$U(1)_Y$	Spin
Gauge fields	G^a_μ	**8**	**1**	0	1
	W^a_μ	**1**	**3**	0	1
	B_μ	**1**	**1**	0	1
Quarks	$Q_{_L}$	**3**	**2**	$+\frac{1}{6}$	$\frac{1}{2}$
	$u_{_R}$	**3**	**1**	$+\frac{2}{3}$	$\frac{1}{2}$
	$d_{_R}$	**3**	**1**	$-\frac{1}{3}$	$\frac{1}{2}$
Leptons	$L_{_L}$	**1**	**2**	$-\frac{1}{2}$	$\frac{1}{2}$
	$e_{_R}$	**1**	**1**	-1	$\frac{1}{2}$
Higgs	H	**1**	**2**	$+\frac{1}{2}$	0

The symbol $Q_{_L}$ refers to left-handed quarks, $u_{_R}$ to up-type right-handed quarks, and $d_{_R}$ to down-type right-handed quarks. The same applies to leptons, where now $e_{_R}$ denotes the down-type right-handed leptons. Note that one lepton species is missing, the up-type right-handed leptons; those are the right-handed neutrinos, which are not present in the SM, although they could be accommodated in the model in some scenarios (see Subsec. 3.1.2.3).

There are other types of symmetries participating in the SM, such as the set of discrete symmetries given by charge conjugation (C), parity transformation (P), and time reversal (T) [17]. However, the CPT combination is the only exact symmetry observed at the fundamental level. This is connected with the CPT theorem [99], which states that all local Lorentz-covariant field theories of point particles have CPT symmetry. Other symmetries appear as a consequence of the flavor structure of the SM, in which coexist three generations of the group representations presented in Tab. 3.1. These are global symmetries explicitly broken by the Yukawa terms. This part of the Lagrangian must be there to allow the incorporation of the fermion masses into the model. The kinetic term of the SM Lagrangian has a large global

flavor symmetry given by $U(3)_q^3 \times U(3)_l^2$ [100]. This group is broken down to $U(1)_B \times U(1)_L^3$, which expresses the conservation of the baryon and lepton numbers. That kind of symmetry is conventionally referred to as "accidental symmetry" since it is simply there because one can not write down renormalizable terms that break it. Furthermore, not all of the classical symmetries also remain a symmetry at the quantum level, in that case, the symmetry is called anomalous. An anomalous symmetry is hence not a symmetry of the full quantum theory. Not only the exact symmetries are important, but there are also approximate symmetries that "protect" some parameters from acquiring large quantum corrections. That is the case of the chiral symmetry protecting the fermion masses and the custodial symmetry in the Higgs sector [98].

The most general Lagrangian[1] fulfilling the aforementioned formalities is

$$\begin{aligned}
\mathcal{L}_{SM} = &-\frac{1}{4}G^a_{\mu\nu}G^{a\mu\nu} - \frac{1}{4}W^a_{\mu\nu}W^{a\mu\nu} - \frac{1}{4}B_{\mu\nu}B^{\mu\nu} \\
&+ i\bar{Q}^n_L \not{D} Q^n_L + i\bar{d}^n_R \not{D} d^n_R + i\bar{u}^n_R \not{D} u^n_R + i\bar{L}^n_L \not{D} L^n_L + i\bar{e}^n_R \not{D} e^n_R \\
&- [Y^{mn}_{(d)}\bar{Q}^m_L H d^n_R + Y^{mn}_{(u)}\bar{Q}^m_L H^c u^n_R + Y^{mn}_{(e)}\bar{L}^m_L H e^n_R + h.c.] \\
&+ (D_\mu H)^\dagger (D^\mu H) - [-\mu^2 H^\dagger H + \lambda (H^\dagger H)^2],
\end{aligned} \tag{3.2}$$

where the covariant derivatives D_μ include as many types of gauge fields as the number of non-trivially acting groups for a given fermion field. The more general D_μ includes three coupling constants g_1, g_2 and g_3, one for each gauged group. The field strengths $X^a_{\mu\nu}$ ($X = G, W, B$) are in general defined according to Eq. (2.75), and for the abelian case, the structure constants must be set to zero. Members of successive generations are denoted by a generation index $n, m = 1, 2, 3$. It is important to point out that other indices labeling the irreps might be hidden for simplicity, or they can be encoded in the notation. For instance, the Higgs and the left-handed fermions are explicitly written in terms of $SU(2)$ doublets. The H^c represents the charge-conjugate doublet, which has hypercharge $-\frac{1}{2}$, although this still transforms under the fundamental representation of $SU(2)$. The Higgs sector will be treated more in-depth later.

The SM model Lagrangian (3.2) contains in total 18[2] physical parameters [101]. The Lagrangian may be parameterized in different ways, however, the number of physical parameters does not change. Most of those parameters come from the breaking of the flavor group. In general, on can relate the number of physical parameters to the number of broken generators of the flavor group by $N_{\text{phys}} = N_{\text{general}} - N_{\text{broken}}$. Each class of Yukawa coupling contains 18 general real parameters, while the number of generators of the $U(3)$ Lie group is 9. From this is concluded that the flavor sector contributes to $54 - (45 - 4) = 13$ physical parameters, which are often chosen to be 3 lepton masses, 6 quark masses, and 4 parameters (3 mixing angles and one phase) in the Cabibbo-Kobayashi-Maskawa (CKM) matrix [102]. The 5 remaining parameters are simply the 3 gauge couplings and the 2 parameters in the

[1] One may also include total derivatives of the form $\frac{g^2\Theta}{32\pi^2}\epsilon_{\mu\nu\rho\sigma}X^{a\mu\nu}X^{a\rho\sigma}$ for the three gauge fields, but it turns out that only one of those has physical implications.

[2] Without considering the parameter related to the strong CP problem.

Higgs sector (the Higgs mass and the strength of the self-interaction). All those 18 parameters can not be rotated away by performing phase transformations or flavor rotations, so they are said to be physical. There is an additional parameter that is often included, the strong CP angle Θ_{QCD}. This has not been included in the classical analysis above since it is a result of a quantum anomaly. As said before, the anomalous symmetries are not a real symmetry of the theory, so they should be excluded from the classical counting. In QCD, the axial symmetry $U(1)_A$ is anomalous, and that was a matter of discussion during many years turning into the strong CP problem [103–105] (see Subsec. 3.1.2.6).

3.1.1 The Standard Model Higgs Boson

Unfortunately, nature does not exhibit having all the symmetries that are often imposed on the models describing it. That forced physicists to have to resort to mechanisms that allowed to break the symmetries that were assumed a priori, and which are not present in the universe that is currently described. That is the case of the untouchable gauged symmetry in the electroweak sector of the SM, which becomes apparently broken $SU(2)_L \times U(1)_Y \to U(1)_{EM}$ by having the bosons $W^{\pm}$ and Z^0 a mass, in the same way as the fermions do. Already in the previous chapter, it was seen how the Higgs mechanism allows a spontaneous breaking of the symmetry (Subsec. 2.4.3.2) by circumventing the Goldstone's theorem with the incorporation of locality. In the SM, the scalar $SU(2)$ doublet has the exact quantum numbers to perform two fundamental functions, induce the EWSB and, as a consequence, generate masses for the fermions. But the significance of the Higgs is not limited to that only. Without the Higgs boson, perturbative unitarity would be lost at high energies [106], and the quantum corrections to the gauge boson self-energies would acquire large divergences. Moreover, with the addition of a scalar particle with a mass around the electroweak scale, the Standard Model is theoretically consistent and can be extrapolated up to very high energy.

For many years, the absence of experimental evidence of the existence of such a particle made many scientists worry. But all those concerns vanished when in July 2012 the ATLAS and CMS collaborations announced the discovery of a Higgs-like particle with a mass around 125 GeV [7, 8]. That breakthrough has been considered a historic step in the understanding of nature. Since then, many experimental results have shown that the particle behaves like the SM Higgs boson, having spin 0 and positive parity, and making it the only elementary scalar particle observed in nature [107–109]. However, more studies are needed to verify with higher precision that the discovered particle has all of the properties predicted, or whether, it is hiding some features of physics beyond the SM.

The way in which the Higgs mechanism is applied to the case of the EWSB, and the associated mass generation process in the SM context will be reviewed in the next subsection. The standard electroweak theory was first formulated in this way, independently, by Weinberg in 1967 [110] and by Salam in 1968 [111].

3.1.1.1 Breaking the $SU(2)_L \times U(1)_Y$ Symmetry

It is worth ascertaining first that the properties of the Higgs field have to be the ones shown in Tab. 3.1. In order to spontaneously break the internal symmetry without spoiling Lorentz invariance, the field can not be other than a scalar with a non-zero vacuum expectation value

(v.e.v.). Now, due to the fact that only an EWSB is present, i.e. the symmetry of the strong sector remains intact, the Higgs field must carry no color charge and therefore, transform trivially under $SU(3)$ rotations. Before the EWSB, the SM Lagrangian must be invariant under the complete gauged symmetry group. So, in order to produce invariant Yukawa terms, the fermionic $SU(2)$ doublets Q_L and L_L must be coupled to another doublet[3], which should be, in this case, the Higgs field. Furthermore, the $U(1)_Y$ invariance must be respected in the Yukawa sector as well, which along with the fact that after the EWSB the electric charge conservation ($U(1)_{EM}$ symmetry) must hold exactly, supplies the Higgs with a value of hypercharge equal to $+\frac{1}{2}$. The labeling (Y) of the $U(1)_Y$ representation is related to that of the $U(1)_{EM}$ representation (Q) through the eigenvalues of the diagonal weak isospin $SU(2)$ generator (I_3) via $Q = Y + I_3$. This allows representing the Higgs doublet as

$$H = \begin{pmatrix} h^+ \\ h^0 \end{pmatrix} = \frac{1}{\sqrt{2}} \begin{pmatrix} h_1 + ih_2 \\ h_3 + ih_4 \end{pmatrix}, \tag{3.3}$$

where each component h_i refers to a real field.

Now, the spontaneous breaking of the symmetry is caused by the Mexican-hat-like potential (second term of the last line in Eq. (3.2)), which presents a minimum at values of h_i displaced from zero, as illustrated in Fig. 3.1. Therefore, as explained in Subsecs. 2.4.3.1 and 2.4.3.2, any choice of a vacuum will break the symmetry and will generate massive modes called Higgs bosons. As it is easy to check, the breaking $SU(2)_L \times U(1)_Y \to U(1)_{EM}$ com-

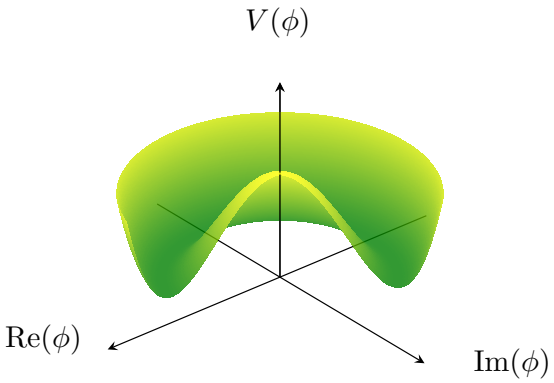

Figure 3.1: Illustration of a Mexican-hat-like potential, in this case, for a hypothetical $U(1)$ symmetry that breaks upon selection of a vacuum state.

prises $k = 3$ broken generators, so only one generator will remain unbroken giving rise to one Higgs boson: the SM Higgs boson. By choosing the unitary gauge $h_1 = h_2 = h_4 = 0$, and

[3]Rather to a conjugate doublet, but in $SU(2)$ they furnish the same irrep, see Subsec. 2.2.3.1.

writing $h_3 = v + h(x)$, the vacuum state reads

$$H_0 = \frac{1}{\sqrt{2}} \begin{pmatrix} 0 \\ v + h(x) \end{pmatrix}, \tag{3.4}$$

with v being the v.e.v.. The field $h(x)$ is part of the real component of the neutral complex scalar h^0, so it carries no electrical charge and is CP-even. It is easy to verify that the three $SU(2)$ generators (2.23), along with the hypercharge generator, rotate the vacuum state (3.4) to another non-null state. However, the combination $Q = Y + I_3$ rotates H_0 to the null state since the vacuum has been chosen to be neutral. This means that only three physical states out of the four initial gauge bosons (W_1, W_2, W_3 and B) can acquire a mass through the Higgs mechanism. The three massive gauge bosons emerge from two linear combinations of $W_1 \leftrightarrow W_2$ and one linear combination of $W_3 \leftrightarrow B$. The other component (also a mixture of $W_3 \leftrightarrow B$) remains massless, which is interpreted as a gauge boson associated with the invariance of $U(1)_{EM}$. All this can be seen explicitly if the last two lines of the Lagrangian (3.2) are expressed in terms of the vacuum state, yielding

$$\begin{aligned} \mathcal{L}_{\cancel{SU(2)_L \times U(1)_Y}} = \quad & \frac{1}{2}\partial_\mu h \partial^\mu h - \lambda v^2 h^2 - \lambda v h^3 - \frac{\lambda}{4} h^4 \\ & + \frac{1}{8}(v+h)^2 [g_2^2 (W_\mu^1 - iW_\mu^2)(W^{1\mu} + iW^{2\mu}) + (g_1 B_\mu - g_2 W_\mu^3)^2] \\ & - \frac{1}{\sqrt{2}}(v+h)[Y_{(d)}^{mn} \bar{d}_L^m d_R^n + Y_{(u)}^{mn} \bar{u}_L^m u_R^n + Y_{(e)}^{mn} \bar{e}_L^m e_R^n + h.c.]. \end{aligned} \tag{3.5}$$

The first line in the above expression contains terms involving only the Higgs boson field, namely the kinetic part, the mass term with $m_h = \sqrt{2\lambda} v$, and the Higgs self-couplings. The second line includes the Higgs couplings to gauge bosons, and the relevant mass terms for the vectors. It can be noticed there that the two components W_μ^1 and W_μ^2 do not mix with any other, so it is suitable to redefine the fields as $W_\mu^\pm \equiv \frac{1}{\sqrt{2}}(W_\mu^1 \pm iW_\mu^2)$ in order to make them match the irrep of the unbroken $U(1)_{EM}$ group. Those are the $W^\pm$ bosons, which have received a longitudinal third-polarization component thanks to the EWSB, thus becoming massive vector fields with $m_{W^\pm} = \frac{g_2 v}{2}$. The third massive vector field is the one given by the linear combination $Z_\mu^0 \equiv W_\mu^3 \cos\theta_W - B_\mu \sin\theta_W$, where θ_W is called weak-mixing (Weinberg) angle, and is defined through the relation $\tan\theta_W = \frac{g_1}{g_2}$. The mass of the Z^0 vector boson is $m_{Z^0} = \frac{v}{2}\sqrt{g_1^2 + g_2^2}$. The final mass eigenstate $A_\mu^0 \equiv W_\mu^3 \cos\theta_W + B_\mu \sin\theta_W$ is just the combination orthogonal to Z_μ^0. This field does not possess a mass term in the Lagrangian (3.5), thus becoming the massless photon field. Finally, the last line in Eq. (3.5) comprises the interaction of the Higgs boson field with the fermions, as well as the mass terms for these. The fermion mass terms induced by the Yukawa couplings are, in general, not diagonal in the generation indices m, n. Nevertheless, they may be diagonalized to $\mathrm{diag}(f_{(\cdot)}^1, f_{(\cdot)}^2, f_{(\cdot)}^3)$, with $(\cdot) = \{(d), (u), (e)\}$, and $f_{(\cdot)}^n$ being real and non-negative, which results in fermion masses of the form $m_{(\cdot)}^n = \frac{1}{\sqrt{2}} f_{(\cdot)}^n v$.

As already mentioned in the above discussion, the Lagrangian (3.5) also sheds light on

the different ways in which Higgs interacts with the rest of the particles and itself. The Higgs self-interaction comes from the cubic and quartic terms in h grouped in the first line of Eq. (3.5). The interactions of the Higgs field with the gauge bosons are generated by expanding the factor $(v+h)^2$ in the second line. The Higgs couplings to fermions is due to the last term in the Lagrangian involving the Yukawa sector. A summary of the various couplings discussed can be seen in Fig. 3.2. The figure is a diagrammatic illustration of the different types of interactions at tree-level in which the scalar particle is involved.

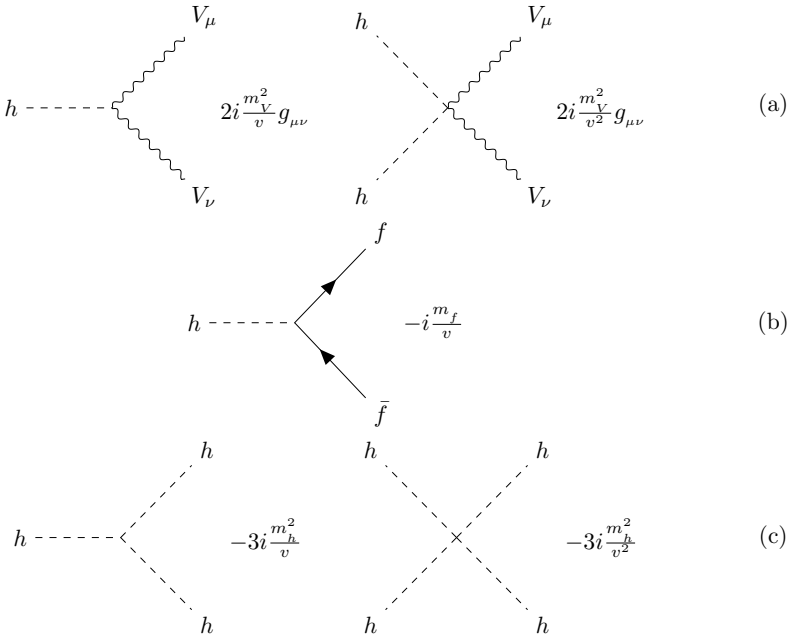

Figure 3.2: Representation in terms of single-vertex Feynman diagrams of the Higgs couplings to gauge bosons ((a), with $V_\mu = W_\mu^\pm, Z_\mu$), couplings to fermions ((b), with $f = u, d, c, s, t, b, e, \mu, \tau$), and its self-couplings (c).

3.1.1.2 Higgs Collider Phenomenology

Nowadays all the masses of the gauge bosons, the charged fermions[4], and the Higgs itself are known, so this knowledge can be exploited to detect any possible deviation from the theoretical predictions within the Higgs sector. Such hypothetical incompatibility would mean that some other effects not contained in the SM framework would be taking part in the physics, therefore, it would justify the construction of models beyond the SM (BSM). At the LHC, an extensive program intended to measure the properties of the new particle found by ATLAS and CMS has been set up. So far, all the data show consistency with the SM Higgs hypothesis, although many more collisions are needed to precisely determine whether the nature of the 125 GeV particle is SM-like or not. Among those measurements is the one of the Higgs boson mass [113–115]. The m_h parameter enters in the calculations of observables such as the production cross-section and the partial decay widths [116], and its

[4]Due to confinement [112], the masses of the quarks cannot be measured directly. However, they can be inferred from the study of hadronic properties provided that one sticks to a particular renormalization scheme (Subsec. 2.4.4.2).

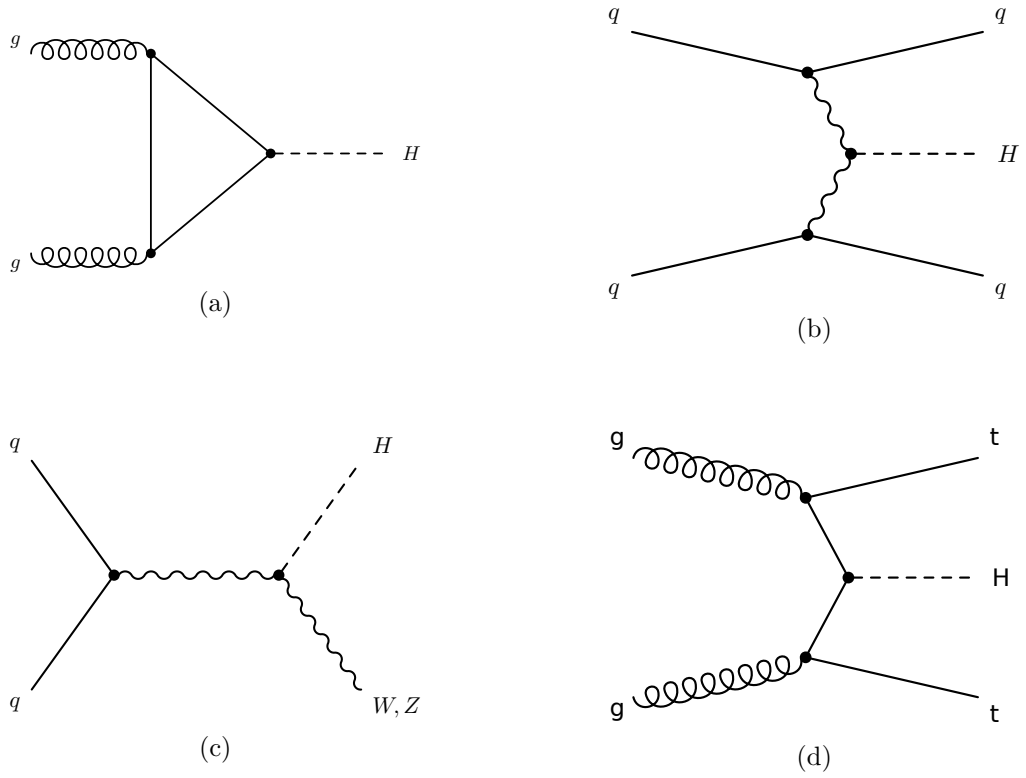

Figure 3.3: Representative diagrams for the four dominant Higgs production modes (a) ggF, (b) VBF, (c) VH and (d) ttH.

precise determination is crucial for measuring the couplings. On the other hand, constraints have been set on the Higgs boson decay width [117–119], as well as on its spin-parity nature [120, 121]. Other parameters, like the couplings of Higgs with the rest of particles, have been widely tested and all show compatibility with the SM predictions [109, 122–126]. In particular, there has recently been evidence of the Higgs-boson Yukawa couplings with the third generation of fermions [127–132].

All the previous results were obtained in the context of proton-proton collisions at the LHC, where physics is highly dominated by QCD processes. The fact that protons are bound states of quarks and gluons, together with the strong coupling being the largest one at the common energy scales in hadron colliders, drastically favors the production of color-charged particles over EW-only interacting particles at such experimental facilities. That is something that directly affects the Higgs boson production at the LHC; loosely speaking, one needs to collide 1 billion protons to produce a Higgs boson. The main production mechanisms at the LHC are gluon fusion (ggF), vector-boson fusion (VBF), associated production with a gauge boson (VH), and associated production with a pair of $t\bar{t}$ quarks (ttH). Their respective leading order Feynman diagrams can be seen in Fig. 3.3. At tree-level, the SM Higgs couples to SM particles in proportion to their masses, so there is no such coupling to gluons due to the colorless nature of the scalar. In the case of proton valence quarks u and d, their small Yukawa couplings, along with the parton distribution function suppression for anti-quarks, reduce the possibility of having a Higgs out of these. This leads to the most predominant process being the one mediated by the exchange of a virtual heavy top quark, the ggF. The cross-section

of this process has been calculated at the next-to-next-to-next-to-leading order (N^3LO) in QCD and NLO in EW corrections [116]. The next most significant production mechanism at the LHC is VBF, where quarks from both protons radiate each a vector boson that combines with the other to form a Higgs boson. The radiated-off Higgs boson is accompanied at least by two quarks that generally form back-to-back jets. The computations of the VBF cross-section have reached the precision of NNLO in QCD and NLO in EW corrections. The third most important contribution is due to the VH production mechanism, also known as Higgs-strahlung. The EW production of a W or a Z boson via the interaction of two quarks from the protons can give rise to the radiation of a Higgs with another vector boson through the interaction vertex shown in Fig. 3.2 (a). This process is in general very clean, as it is dominated by the EW physics, which decreases the probability of having agglomerated multi-jets signatures in the detectors. In recent publications, the full QCD corrections up to NNLO order and the NLO EW corrections have been taken into account to compute both the ZH and the WH cross-sections. Finally, the process with the smaller cross-section, out of the four mentioned, is the ttH, which makes use of the top-quark-Higgs coupling to produce a scalar boson in association with a $t\bar{t}$ pair. The large dependence of the cross-section on the renormalization scale for ttH makes this theoretical calculation very challenging. So far, a precision of up to NLO in both QCD and EW radiative corrections has been achieved. The Tab. 3.2 presents a summary of the cross-section values of the four main production modes, and in Fig. 3.4 (left), one can see the dependence of these on the centre-of-mass energy for $m_h = 125$ GeV. The Higgs particle is also very unstable, decaying into other particles almost

Table 3.2: The SM Higgs boson production cross-sections in pp collisions at $\sqrt{s} = 13$ TeV for the four main production processes [6].

Production cross-section (in pb) for $m_h = 125$ GeV in pp collisions at $\sqrt{s} = 13$ TeV				
ggF	VBF	WH	ZH	ttH
$48.6^{+5\%}_{-5\%}$	$3.78^{+2\%}_{-2\%}$	$1.37^{+2\%}_{-2\%}$	$0.88^{+5\%}_{-5\%}$	$0.50^{+9\%}_{-13\%}$

immediately (the average lifetime is $\tau_h \approx 16 \times 10^{-23} s$ [133]). Then, it is not only necessary to copiously produce the boson in particle accelerators to detect it, but the state must also be reconstructed from its final decay products. In order to determine the final states which the boson is more likely to decay into, the partial widths for all possible decays need to be known. Having already measured the remaining unknown parameter (m_h) of the Higgs sector, all the partial widths are exactly predicted within the SM theory. The predictions for these decay widths (or branching ratios) are very important in the analysis of the LHC Higgs data since what is measured is the multiplication of the production and decay rates in individual channels $\sigma_i \mathcal{B}_i$. The measurements of the branching ratios also constitute a way to test the SM nature of the Higgs boson. In the case of Higgs decays to fermion pairs, the ones to the heaviest kinematically allowed fermion final states will have the largest partial widths, as the Higgs-fermion interaction strength is proportional to the fermion mass. Therefore, in the SM with $m_h = 125$ GeV, the most dominant fermion final states are $b\bar{b}$, $\tau\bar{\tau}$ and $c\bar{c}$, as the decay to $t\bar{t}$ is pretty off-shell for this mass. The leading-order expression for the $h \to f\bar{f}$

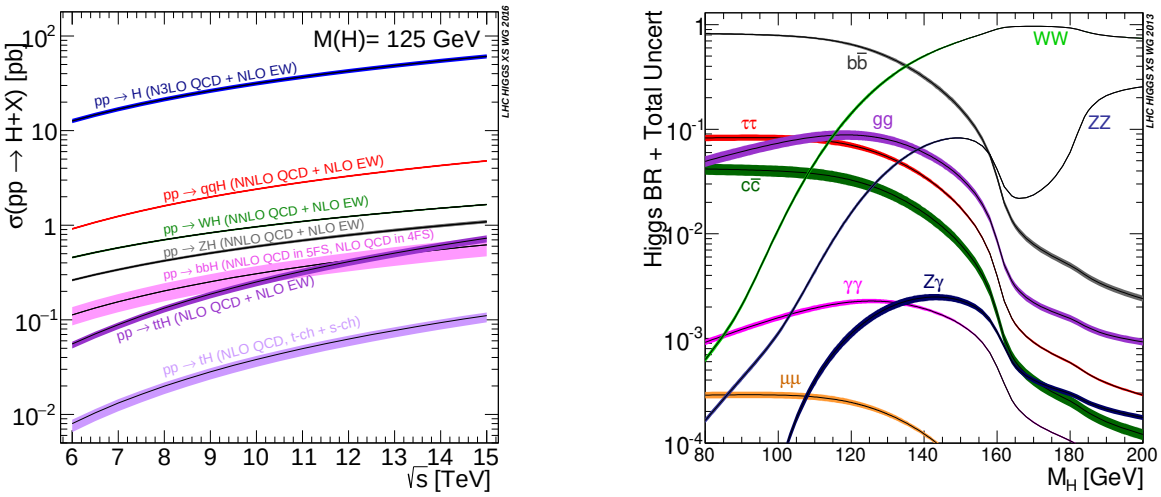

Figure 3.4: The SM Higgs boson production cross sections (left) as a function of the center-of-mass-energy [116], and the branching ratios (right) as a function of the mass [135].

partial decay width is [134]

$$\Gamma(h \to f\bar{f}) = \frac{N_c}{8\pi}\frac{m_f^2}{v^2} m_h \left[1 - \frac{4m_f^2}{m_h^2}\right]^{\frac{3}{2}}, \tag{3.6}$$

where the color factor is $N_c = 3$ for quarks and $N_c = 1$ for leptons. The current numerical predictions [135] include QCD corrections up to N^{4}LO, and NLO precision in the case of electroweak quantum effects. The decay of Higgs to gauge bosons is quite significant as well, and it is evidenced through the three-body and four-body decays, where one or both of the vector bosons are off-shell respectively. The $h \to VV \to f\bar{f}f\bar{f}$ decay is currently known up to NLO in QCD and electroweak quantum corrections including all interferences [134]. In particular, the decay of $h \to W^*W$ possesses the second largest branching fraction after the $h \to b\bar{b}$. There also exist loop-induced decays of the Higgs boson, such as $h \to gg$, $h \to \gamma\gamma$, and $h \to Z\gamma$. They are not so frequent but they have special features that make them important. For instance, the $h \to \gamma\gamma$ decay is observed with a very clean signature in the detectors, which gave it the possibility to become one of the two Higgs boson discovery channels. The $h \to gg$ decay is dominated by the top quark loop, whereas the other two are dominated by a W boson loop. The loop induced decays of the SM Higgs are known at NLO, nevertheless, some of them have been calculated beyond that order [6]. The SM predictions for the branching ratios of the different decay modes of the Higgs in a low mass interval can be observed in Fig. 3.4 (right).

Although the measurements of the Higgs properties are becoming increasingly accurate due to the amount of data delivered by the LHC, there is still room for the existence of BSM processes in the physics of the Higgs sector. The estimations of some of the parameters have reached the percentage level, however, other measurements are far from completely excluding models with more than one scalar particle, or simply with a non-SM interpretation of the 125 GeV Higgs boson. This fact, along with many other shortcomings of the SM that will be addressed in the next subsection, constitutes one of the main motivations to investigate

possible BSM scenarios comprising a new Higgs sector.

3.1.2 The Standard Model Weaknesses

Even though the SM presented above has been a remarkably successful theory, it is far from being a complete description of nature. It has been said repeatedly that there is no confirmed experimental evidence against the SM, and the recent discovery of Higgs came to reaffirm that. However, the SM is theoretically very unsatisfactory, and not only that, there are many experimental pieces of evidence that point to a post-SM theory. Even if one accepted the odd group structure it possesses, there would not still be an explanation for having at least 18 unknown parameters in a fundamental theory. Many other limitations like this will be addressed below.

3.1.2.1 Absence of Gravity

As one can easily tell, the SM does not include gravity. Trying to build a QFT of gravity [136] to incorporate it into the SM eventually leads to a non-renormalizable theory, due to the spin-2 structure of the metric tensor [137]. The interaction of the "graviton" with the stress-energy tensor of the matter fields would produce irrelevant operators, making then impossible the application of renormalization procedures (Subsec. 2.4.4.2). But the need of reconciling general relativity with quantum mechanics has pushed forward the emergence of completely new theories such as string theory [138, 139], while other theories, like loop quantum gravity [140], have taken the path of keeping the gravitational force separated from the other three. The basic idea of string theory is to put aside the concept of point-like objects (particles), and replace it with new extended one-dimensional entities called *strings*. On the other hand, loop quantum gravity attempts to give a discrete description of the space-time by imposing a quantization on it, then turning it into a network (spin network) made out of loops. One of the problems more difficult to overcome when formulating a quantum theory of gravity is that such gravitational effects occur at energies near the Planck scale ($\Lambda_P \sim 10^{19}$ GeV), energy far beyond the reach of modern accelerators, thus putting in risk the falsifiability of those theories.

3.1.2.2 Dark Matter and Dark Energy

Cosmological observations [141, 142] suggest that the SM explains only about 5% of the energy present in the universe, and about 26% should be dark matter, which is not included in the SM. There are not enough hints to provide an explanation of how this dark matter interacts, if it interacts, with the ordinary matter contained in the SM. If dark matter exists, it must barely interact with ordinary baryonic matter and radiation. Models are proposing that the dark matter is a weakly interacting massive elementary particle [143, 144] that has not yet been discovered, but anyways, this particle does not exist in the SM, so it must be part of a BSM theory. Many efforts have been done in order to provide a dark matter candidate within supersymmetric theories [145, 146], but the results from dark matter experiments, as well as the lack of supersymmetric partners in LHC searches, are destroying the last hopes.

In addition to the problem of dark matter is the dark energy mystery. Observations indicating that the universe is expanding began to be explained by the presence of a dark energy filling the space homogeneously [147, 148]. According to experiments, this energy

should make up 69% of the total energy of the universe. In particle physics terms, the dark energy is interpreted as the vacuum energy, which would imply that the non-zero vacuum provided by the SM should match the value of the effective vacuum energy, directly related to the Einstein cosmological constant [149]. It turns out that the mismatch can be as large as 120 orders of magnitude.

3.1.2.3 Neutrino Masses and Mixing

According to the standard model, neutrinos are massless particles. However, neutrino oscillation experiments [150–152] have shown that neutrinos do have mass and they mix [153, 154]. They have to be massive so that the phases propagate differently and, therefore, generate a change in the flavor eigenstate (linear combination of the mass eigenstates). They have to mix since otherwise, flavor eigenstates are also eigenstates of the Hamiltonian and do not evolve. Due to mixing, neutrino oscillations violate the flavor lepton number. If neutrinos are Dirac particles [155, 156], the SM could be easily extended by adding a right-handed neutrino that would allow generating a Dirac mass via a Yukawa-like coupling (at least 7 more parameters). However, according to upper bounds on neutrino masses [157], this Yukawa coupling must be extremely tiny compared to other fermions, which many theorists consider unsatisfactory. On the other hand, if neutrinos are Majorana particles, their masses could arise as an effective realization of a higher-energy theory, as proposed in the different models based on the well-known see-saw mechanism [158, 159].

3.1.2.4 Matter-Antimatter Asymmetry

It is evident that our universe (as far as it can be seen) consists predominantly of matter and not antimatter. There is a clear asymmetry between the number of baryons and antibaryons, which implies that something must have happened in order to generate that imbalance. Sakharov proposed [160] a set of necessary conditions that interactions must satisfy to produce such asymmetry. It should include baryon number B violation, C-symmetry and CP-symmetry violation, and be out of thermal equilibrium. In principle, all three Sakharov conditions are satisfied in the SM. The B violation can be obtained with the hypothesized Adler-Bell-Jackiw anomaly in electroweak interactions [161], the CP-violation is present in the CKM matrix, and the fact that the universe is expanding (non-zero vacuum) makes processes go out of equilibrium. However, no experimental evidence of sphalerons [162] has yet been observed [163], the amount of CP-violation in the SM is not enough to account for the measured baryon asymmetry, and the universe is not sufficiently out of equilibrium [164]. All the above said essentially means that there is no known mechanism in the SM able to generate the total amount of baryon asymmetry required, so it is mandatory to go beyond.

3.1.2.5 The Hierarchy Problem

Among the theoretical problems is the so-called hierarchy problem of the electroweak scale. From the EFT point of view, the SM is a low energy description of a more fundamental theory that is defined at some high energy scale ($\sim \Lambda_P$) and, therefore, it should be valid up to that scale [165]. If the SM is the only physics present up to such scale, the renormalization machinery should be treated accordingly, and all the parameters should get contributions up to Λ_P. But it happens that the masses of scalar fields (relevant operators) receive large

additive quantum corrections, namely corrections proportional to Λ_P [166]. So, it seems unnatural to have light scalars in the low energy effective theory, as their masses would have to be very fine-tuned. This is the case of the SM Higgs boson with an EW-scale mass, for which, at scales $\Lambda >> 1$ TeV, there must be a cancellation of several orders of magnitude to reproduce the observed mass of 125 GeV.

This was part of the great enthusiasm of being able to enter into the TeV scale since a theory like the SM based on a scalar Higgs is either correct and, there is new physics at the TeV scale that makes the small mass natural, or something more exotic than a simple scalar Higgs is responsible for EWSB. Several theories are proposing a solution to the hierarchy problem such as supersymmetry [167], composite Higgs models [168], the anthropic principle [169], and the relaxation mechanism [170], just to mention a few. Some of those will be treated in more detail in the next section.

3.1.2.6 The Strong CP Problem

Another problem related to fine-tuning is the already mentioned strong CP problem [171]. Historically, this problem appeared as a consequence of a solution to the $U(1)_A$ problem [172]. The dilemma was given to the impossibility to explain the physical absence of the η' meson; a Goldstone boson (Subsec. 2.4.3.1) engendered from the spontaneous breaking of the global $U(1)_A$ symmetry by the quark condensate. One of the solutions to this problem was the introduction of "instantons" [173, 174], but this allowed the presence of an additional term in the Lagrangian ($\sim \Theta_{QCD}\tilde{F}^a_{\mu\nu}F^{a\mu\nu}$) that violated CP. The CP-violating term raised another issue, the observed tiny value of Θ_{QCD}. The term contributes to observables such as the neutron electric dipole moment, whose measurements imposed an upper limit of $\Theta_{QCD} \lesssim 10^{-10}$ [104, 175]. The unnaturalness of Θ_{QCD} afflicts QCD, as there is no plausible theoretical explanation within the SM framework to the fact that the strong sector preserves the CP-symmetry. The most well-known solution to the problem is the Peccei-Quinn theory [176]. In this model, Θ_{QCD} is replaced by a dynamical field that can relax to zero giving rise to a very light pseudoscalar particle called the "axion" [177, 178].

3.2 Higgs Beyond the Standard Model

It is clear from the last section that the SM is not enough to describe all the physical phenomena occurring in the universe. The SM is also far from being a "theory of everything", where, in some way, the interactions known can be unified and described under the same formalism. There are countless new models that partly modify the SM structure or completely change its theoretical basis in order to get closer to a more faithful description of reality. Some of those trying to solve part of the problems encountered in the SM were mentioned in Subsec. 3.1.2. The Higgs sector gets particularly impacted in some of the BSM theories, typically in those addressing the hierarchy problem (Subsec. 3.1.2.5). Other models propose that the Higgs field could provide a portal to dark matter [179], or may help to generate electroweak baryogenesis of sufficient amount to explain the baryon asymmetry [180]. These assumptions would be reflected as either a modification in the interactions and properties of the 125 GeV Higgs boson or in the existence of additional scalars in the theory. All that constitutes a huge motivation to look for new physics in the Higgs sector. In this section, the

most interesting models that provide an incentive for searches such as the one presented in this thesis will be reviewed.

3.2.1 Supersymmetric Models

In chapter 2, the relevance of symmetries when labeling particles and determining the interactions among them was stressed. In the second half of the 20th century, scientists started to wonder whether it was possible to add new fashions to the symmetry group of a QFT. However, a very restrictive theorem derived by Coleman and Mandula [181] came up to prove that it was only possible to combine external and internal symmetries in a trivial manner, Poincaré $\otimes$ Internal, i.e. without mixing them. So, no new extravagant symmetry could be imposed on a system unless the Poincaré or the internal Lie groups were individually redefined. Then, physicists realized that a way around the theorem would be to "augment" the Lie algebra of some of the components. Indeed, that was what Golfand and Likhtman proposed for the external component of the symmetry group [182], a gradation of its Lie algebra to also include fermionic generators. In mathematical terms, this is understood through the formalism called graded Lie algebras [183], and the particular case concerning supersymmetry (Z_2 gradation) is known as Lie superalgebra. The above means that the Lie algebra (Subsec. 2.2.2.2) is no longer necessarily commutative, but it can also have anticommutation relations between generators. This powerful tool led Wess and Zumino to formulate the first 4-dimensional supersymmetric field theory (SUSY) in 1974 [184]. The following subsection, meant to review some basic aspects of SUSY, is mainly based on the references [11, 185–189].

3.2.1.1 The Supersymmetric Algebra

In standard supersymmetry, there are two fermionic generators Q_α and $\bar{Q}_{\dot{\alpha}}$, corresponding to the two irreps $(\frac{1}{2}, 0)$ and $(0, \frac{1}{2})$ of $SL(2, \mathbb{C})$[5] in Tab. 2.2, being $\alpha = 1, 2$ ($\dot{\alpha} = 1, 2$) spinor indices. The graded Lie algebra of the Poincaré group in SUSY is obtained by complementing the algebra in Eq. (2.40) with

$$\begin{aligned} [Q_\alpha, M^{\mu\nu}] &= i(\sigma^{\mu\nu})^\beta_\alpha Q_\beta, & [Q_\alpha, P^\mu] &= [\bar{Q}_{\dot{\alpha}}, P^\mu] = 0, \\ \{Q_\alpha, Q_\beta\} &= \{\bar{Q}_{\dot{\alpha}}, \bar{Q}_{\dot{\beta}}\} = 0, & \{Q_\alpha, \bar{Q}_{\dot{\beta}}\} &= 2(\sigma^\mu)_{\alpha\dot{\beta}} P_\mu, \end{aligned} \tag{3.7}$$

where $\sigma^\mu = (I_2, \sigma^i)$, and $\sigma^{\mu\nu} = \frac{1}{4}(\sigma^\mu \bar{\sigma}^\nu - \sigma^\nu \bar{\sigma}^\mu)$. Now, since the Coleman-Mandula theorem alludes only to bosonic generators commuting with internal symmetry generators, there is no restriction on possible non-vanishing relations between Q_α ($\bar{Q}_{\dot{\alpha}}$) and the internal generators. It turns out that there exists one symmetry, called R-symmetry ($U(1)$), whose generator has a non-trivial commutation with the fermionic generators, namely $[Q_\alpha, R] = Q_\alpha$ and $[\bar{Q}_{\dot{\alpha}}, R] = \bar{Q}_{\dot{\alpha}}$.

Later, the new graded algebra should, in general, generate different Casimir operators compared to the ones in the nominal Poincaré group. In fact, the second Casimir (C_4) in Eq. (2.41) is not a Casmir operator of the SUSY algebra[6], which means that the irreps of the superalgebra are in principle different from the irreps of the standard Poincaré group.

[5] Note the analogy with $P_\mu \leftrightarrow (\frac{1}{2}, \frac{1}{2})$ and $M_{\mu\nu} \leftrightarrow (1, 1)_A$.

[6] The new Casimir is given by $\tilde{C}_4 = C_{\mu\nu} C^{\mu\nu}$, with $C_{\mu\nu} = O_\mu P_\nu - O_\nu P_\mu$ and $O_\mu = W_\mu - 1/4 \bar{Q}_{\dot{\alpha}} (\bar{\sigma_\mu})^{\dot{\alpha}\beta} Q_\beta$.

The quantum number associated with the new Casimir invariant is called superspin, which along with the other Casimir operator, allows labeling the SUSY irreps, the supermultiplets. It can be proven that in those multiplets the number of bosons and fermions must be the same. In order to construct unitary representations of the super Poincaré group, it is necessary to proceed similarly to the way Wigner did, that is, making use of the induced representation method (Subsec. 2.2.3.3). As in the standard case of the Poincaré group, two concrete types of representations make up the spectrum, the massless and the massive representations. For the massless multiplet, both Casimir invariants vanish, so the supermultiplet is represented by $\{|p^\mu, \pm\lambda\rangle\,; |p^\mu, \pm(\lambda + \frac{1}{2}\rangle\}$, where λ is the helicity. The two more relevant supermultiplets are the chiral multiplet with $\lambda = 0$, containing the scalars and helicity-$\frac{1}{2}$ fermions, and the vector multiplet $\lambda = \frac{1}{2}$, including helicity-$\frac{1}{2}$ fermions and helicity-1 bosons. In the massive case, the multiplets are labeled by $|m, y\rangle$, and comprise the states $\{2 \times |m, j = y, p^\mu, j_3\rangle\,; 1 \times |m, j = y + \frac{1}{2}, p^\mu, j_3\rangle\,; 1 \times |m, j = y - \frac{1}{2}, p^\mu, j_3\rangle\}$ for $y \neq 0$, where j denotes the spin. The case with $y = 0$ is a bit different but follows the same logic.

3.2.1.2 Constructing Superfields

Identically to the non-supersymmetric case, the construction of fields that later undergo quantization and generate the field quanta is essential. According to the exponential mapping (Subsec. 2.2.2.1), the most general element of the super Poincaré group will be determined by an exponentiation of a linear combination of the group generators accompanied by continuous parameters. Therefore, the new generators Q_α ($\bar{Q}_{\dot{\alpha}}$) must also have parameters associated with them. However, these parameters have to behave like Grassmann variables θ_α ($\bar{\theta}_{\dot{\beta}}$), due to the fermionic nature of the supersymmetry generators. The space generated by the space-time coordinates plus the additional Grassmann variables is known as superspace. Superfields are then constructed as entities depending on the coordinates of the superspace. Having functions depending on Grassmann variables provides the ease that they can be expanded in powers of θ_α and $\bar{\theta}_{\dot{\beta}}$, as showed in Eq. (2.66). Then, the most general superfield $\Phi(x, \theta, \bar{\theta})$ has a finite number of $\theta/\bar{\theta}$ terms, and can be written as

$$\begin{aligned}\Phi(x,\theta,\bar{\theta}) \;=\; & C(x) + \theta\psi(x) + \bar{\theta}\bar{\psi}'(x) + (\theta\theta)M(x) + (\bar{\theta}\bar{\theta})M'(x) \\ & + (\theta\sigma^\mu\bar{\theta})V_\mu(x) + (\theta\theta)\bar{\theta}\bar{\lambda}'(x) + (\bar{\theta}\bar{\theta})\theta\lambda(x) + (\theta\theta)(\bar{\theta}\bar{\theta})D(x),\end{aligned} \tag{3.8}$$

where $[\psi,\ \bar{\psi}',\ \lambda,\ \bar{\lambda}']$ are two-component spinor fields, $[C,\ M,\ M',\ D]$ are scalar fields, and V is a vector field. Due to the fact that the expression (3.8) has been obtained by applying an expansion in $\theta/\bar{\theta}$ only, it is clear that $\Phi(x, \theta, \bar{\theta})$ does not have necessarily to be an irreducible representation of SUSY. The way to decompose $\Phi(x, \theta, \bar{\theta})$ into irreducible parts is to impose supersymmetric invariant constraints on it. By doing so, one gets a group of superfields that can be used to construct Lagrangian superfield theories. One of those is the so-called chiral superfield, which is obtained by imposing $\bar{\mathcal{D}}_{\dot{\alpha}}\Psi = 0$, where $\bar{\mathcal{D}}_{\dot{\alpha}} \equiv \bar{\partial}_{\dot{\alpha}} + i\theta^\beta\sigma^\mu_{\beta\dot{\alpha}}\partial_\mu$; analogously, the anti-chiral superfield $\mathcal{D}_\alpha\Psi' = 0$. These two are commonly reserved to represent the SM fermions and their associated scalar supersymmetric partners, sfermions. Another important superfield is the real (vector) superfield, obtained by the restriction $\mathcal{V} = \mathcal{V}^\dagger$, and which typically incorporates SM gauge bosons and their superpartners, gauginos.

The above-mentioned superfields can serve to build renormalizable (mind $\int d^4x d^4\theta$) gauge

theories, in a pretty similar way to the non-supersymmetric case. SUSY is just an extension of the external symmetry group, so for a supersymmetric realization of a gauge theory, the internal symmetry group subject to gauging remains intact. One of the most cumbersome parts when building such theories is the breaking of supersymmetry. Until the present day, no experiment has observed the presence of the equally massive superpartners of the SM particles, which requires a breaking of the assumed SUSY. That makes these theories even more crowded in terms of unpredicted parameters. Nevertheless, SUSY gives an elegant solution to some of the problems attached to the SM.

3.2.1.3 The Minimal Supersymmetric Standard Model

The Minimal Supersymmetric Standard Model (MSSM) is a supersymmetric extension of the SM that incorporates the minimum number of new particles in the theory keeping the same internal group. All the fermionic fields of the SM are promoted to a chiral superfield transforming under the same irreps of the group $SU(3)_C \times SU(2)_L \times U(1)_Y$. As mentioned before, the chiral superfield also incorporates the superpartner of the quarks and leptons, which are respectively called squarks and sleptons. Accordingly, each gauge boson field of the SM is promoted to a vector superfield containing the gauge bosons and the gauginos. The three types of gauginos are the gluinos ($SU(3)_C$), the winos ($SU(2)_L$) and the bino ($U(1)_Y$). But the biggest change is observed in the Higgs sector, since now the scalar doublet field is replaced by two chiral superfields. The presence of a second Higgs doublet increases the number of physical states to 5, as they comprise 8 degrees of freedoms instead of 4 like in the SM.

Before briefly discussing the Higgs sector in the MSSM, it is worth mentioning the impact of the R-parity on this. It was seen how in the SM the conservation of the baryon and lepton numbers arises naturally. However, in the MSSM one must enforce this conservation by imposing the R-parity symmetry ($R = (-1)^{L+3B+2S}$), which basically confers to the SM particles the quantum number $R = 1$, and to their superpartners the value $R = -1$. This brings an important phenomenological feature, namely that sparticles are always produced in pairs, thus ensuring that the lightest one (called LSP and a good dark matter candidate) is stable. Typically, the LSP is neutral, a property that makes it pass through the detector materials undetected. This is reflected as a "missing energy" signature, which is one of the common ways to search for SUSY.

There are mainly two reasons for having two $SU(2)$ Higgs doublets in SUSY. The first one has to do with the fact that SUSY requires the presence of holomorphy in the Lagrangian, due to some non-renormalization theorems [190], which precludes the presence of a chiral complex conjugate field. The presence of a complex conjugated Higgs field was what made possible to give mass to both up-type and down-type quarks in the SM Lagrangian employing only one scalar field. However, now in the framework of SUSY, an additional chiral superfield must be added, if the aim is to provide a mass term for both types of fermions via Yukawa couplings. The distinction between the two doublets would be given by the hypercharge quantum number, one would be charged under $Y = \frac{1}{2}$, whereas the other would have $Y = -\frac{1}{2}$. The second argument comes from the triangular Feynman diagram anomalies [191], the ones that are driven by a chiral fermion running in the loop. In the SM, this type of anomalies cancel, as the inclusion of a scalar field like the Higgs does not contribute to the anomaly. In the MSSM, they also cancel in the gauge sector, but since chiral superfields are now the

field entity, the inclusion of a Higgs superfield would bring a new fermion (higgsino) to the particle content, thus causing some troubles. One way to annihilates its effect is to include another fermion with opposite hypercharge value, as would happen with the inclusion of a second chiral superfield. In order to generate the EWSB, both Higgs doublets will get a v.e.v. (v_1 and v_2), whose values are going to be constrained by the relation $v = \sqrt{v_1^2 + v_2^2} \simeq 246$ GeV. The five physical states consist of two charged particles, two neutral CP-even particles, and a neutral CP-odd particle. More details of this type of Higgs sector will be given in the subsection addressing the two Higgs doublet models, which generalize the MSSM case.

Finally, it is important to highlight the elegant way in which SUSY solves the hierarchy problem concerning the Higgs boson (Subsec. 3.1.2.5). It was mentioned before that a type of custodial symmetry, called chiral symmetry, protects the masses of the fermions form getting large quantum corrections. Due to the fact that SUSY provides a link between bosons and fermions, it is expected that some of the features involving fermions (like chiral symmetry) be transferred to the bosons. This is what explains the cancellation of the large corrections to the Higgs mass. Technically, what happens is that fermions also start to run in the loop, generating opposite sign terms (with respect to bosons), which makes the quadratic divergences cancel. The result is that the new physics scale Λ only enters logarithmically. However, to avoid a considerably large fine-tuning, the masses of some sparticles should be around the TeV scale. Such particles have not been found yet.

3.2.2 Models with Additional Singlet Scalars

These models are mainly motivated by dark matter considerations, as well as by baryogenesis in the electroweak sector [12, 192–194]. In general, one can consider the SM being extended by the addition of N scalars transforming trivially under the SM internal symmetry group. Imposing the scalars to transform under the fundamental representation of $O(N)$, and to have an odd Z_2 symmetry $\vec{\phi} = -\vec{\phi}$ among them, produces the potential [192]

$$V(H, \vec{\phi}) = -\mu_H^2 H^\dagger H + \lambda_H (H^\dagger H)^2 + \frac{1}{2}\mu_\phi^2 \vec{\phi}^2 + \frac{1}{4!}\lambda_\phi (\vec{\phi}^2)^2 + \lambda_x H^\dagger H \vec{\phi}^2, \tag{3.9}$$

where H is the SM $SU(2)$ doublet. If $\langle\vec{\phi}\rangle = 0$, there is no mixing between $\vec{\phi}$ and H, so the mass of the 125 GeV particle (h_{125}) remains unaltered, and its couplings to SM particles are not modified. However, it turns more interesting for collider physics if the v.e.v. is different from zero, for which it is necessary to dispense with the global $O(N)$ symmetry to evade the emergence of massless Goldstone bosons (Subsec. 2.4.3.1).

The above is easily done by promoting the parameters μ_ϕ^2, λ_ϕ and λ_x to tensors with indices differing for each component of $\vec{\phi}$ while keeping the discrete Z_2 symmetry, or imposing a bigger one to reduce the number of free parameters of the theory; for instance [194]

$$V(H, \vec{\phi}) = -\mu_H^2 H^\dagger H + \lambda_H (H^\dagger H)^2 + \lambda_{ij}\phi_i\phi_j + \lambda_{ijkl}\phi_i\phi_j\phi_k\phi_l + \lambda_{ijHH}\phi_i\phi_j H^\dagger H. \tag{3.10}$$

The non-zero v.e.v. makes possible the occurrence of mixing and, therefore, of new mass eigenstates, being identified one of them with h_{125}. In the literature, one can find the two simplest cases, namely $N = 1$ [193] and $N = 2$ [194]. In both models, the presence of mixing gives rise to changes in the couplings of h_{125}, which tend to be reduced by the mixing angles. In the scenario where one of the particles is light enough, the h_{125} scalar can decay to other

scalar particles, materializing a non-zero $\mathcal{B}(h_{125} \to BSM)$ via the decay $h_{125} \to h_s h_s$. In general, the phenomenology of both cases can be regarded as very similar. However, in the case of $N = 2$, apart from the $h_{125} \to h_s h_s$ decay, there also are asymmetric decays, where the h_{125} decay products differ from one another $h_s \neq h_{s'}$.

That being so, it is clear that the precision studies at the LHC provide an excellent way to test these models [195]. The production rates of h_{125} are affected by the mixing of the $SU(2)$ doublet with the singlet components, and the possibility of a $h_{125} \to h_s h_s$ decay could be highly constrained by refined measurements of the h_{125} couplings. Nevertheless, a very effective approach is the search for additional light bosons within all possible scenarios, including also the potential $h_{125} \to h_s h_s$ exotic decay.

3.2.3 Adding a Vector Field

As seen in Subsec. 3.1.2.2, by today, there has not been a measurement that accounts for a sizable interaction between the ordinary SM matter and the dark matter. This has motivated the idea that the dark matter sector could be blind to the SM interactions, without excluding the possible interaction of dark matter with itself [196,197]. A rather inclusive class of theories with a hidden sector is the so-called "hidden valley" [198–201], in which models are distinguished by a confining gauge interaction that creates a mass gap into the theory. In such theories, a very rich phenomenology with regard to the Higgs sector can be integrated, in particular, the one that has to do with exotic decays of h_{125}.

Perhaps one of the simplest alternatives is to add an extra $U(1)_D$ (D refers to dark) in the gauged group of the SM, allowing a renormalizable kinematic mixing term between the hypercharge gauge boson B_μ and a new vector field X_μ [202,203]. The mixing does not break gauge invariance, and its coupling is presumably small to have escaped detection thus far. The smallness of the coupling would also be beneficial for some freeze-in scenarios of dark matter [204]. Furthermore, adding the vector field X_μ implies a new contribution to the anomalous magnetic moment of a lepton. That could potentially help to clarify the observed discrepancy for the muon [205].

One of the models considers a spontaneously broken $U(1)_D$ symmetry, having an additional Higgs field H_D in the hidden sector that couples to the SM Higgs. That is achieved by including the following Lagrangian to the SM one [206]

$$\begin{aligned}\mathcal{L}_D = &-\frac{1}{4}X_{\mu\nu}X^{\mu\nu} + \frac{\chi}{2}X_{\mu\nu}B^{\mu\nu} \\ &+ (D_\mu H_D)^\dagger (D^\mu H_D) + \mu_D^2 H_D^\dagger H_D - \lambda_D (H_D^\dagger H_D)^2 - \kappa H^\dagger H H_D^\dagger H_D.\end{aligned} \tag{3.11}$$

In the above equation, the SM Higgs is a singlet under $U(1)_D$, and the dark Higgs transforms as the $(\mathbf{1}, 0, q_D)$[7] representation under the augmented EW group $SU(2)_L \times U(1)_Y \times U(1)_D$. The $U(1)_D$ is spontaneously broken by $\langle H_D \rangle = \xi/\sqrt{2}$. Due to the tiny value of χ, the mass of the SM Z boson is nearly unaffected by the kinematic mixing. Besides, the SM photon remains massless, and the dark photon (dark-Z) Z' gets a mass by "eating" the Goldstone boson associated to the pseudoscalar component of H_D (Subsec. 2.4.3.2). In the Higgs sector, both fields mix because of the coupling through the κ term, producing two massive bosons, one of them being h_{125}. The $H - H_D$ mixing enables the $h_{125} \to Z'Z'$ decay, when kinematically

[7] Note that B_μ does not have to be $U(1)_D$ charged, as the group is abelian (see Sec. 2.4).

allowed, followed by the consequent decay of Z' to SM fermions, if Z' is the lightest state in the dark sector.

The exotic $h_{125} \to Z'Z'$ decay competes with the asymmetric one $h_{125} \to ZZ'$ according to the amount of mixing in the gauge and in the Higgs sector [12]. The mixings are respectively driven by the coupling parameters χ and κ. If $\kappa \gg \chi$, the $h_{125} \to Z'Z'$ tends to dominate over $h_{125} \to ZZ'$. However, if the spectrum of the dark sector is such that the dark massive boson is below half the h_{125} mass, the decays of the SM Higgs boson into pairs of light scalars become highly competitive. On the other hand, the decay of Z' to SM fermions is uniquely governed by the kinematic mixing parameter χ. The interaction term is $\mathcal{L}_I \supset g_{Z'ff} Z'^{\mu} \bar{f} \gamma_\mu f$ [12], with $g_{Z'ff}$ being proportional to χ and to the gauge couplings. This means that the leptonic branching ratios are nearly the same in the entire kinematic region where Z' can decay to all leptons. Furthermore, the leptonic branching ratios prove to be not negligible at all in comparison to those of the hadronic modes. For that reason, the exotic Higgs decays $h_{125} \to Z'Z' \to 4l$, especially those involving muons in the final state, constitute a very interesting signature for searches at the LHC.

In this context and, despite not being the ideal leptonic decay modes for the model here discussed (for experimental reasons), the decay channels on which the current thesis focuses represent an additional possibility for testing the physics behind the dark sector.

3.2.4 Little Higgs Models

The introduction of scalar fields in a Lagrangian is always problematic since its relevant operators, like those involved in the fields' masses, always get corrections from the largest scale in the theory (Subsec. 3.1.2.5). Because of that, some proposals are questioning the point-like structure of the discovered scalar boson; they are known as composite Higgs models [166, 207, 208]. Those models represent extensions of the technicolor theories [209–211]. It is very well known from the chiral theory of QCD [212, 213] that the approximate chiral symmetry $SU(3)_L \times SU(3)_R$ (explicitly broken by quark masses) is spontaneously broken down to $SU(3)_V$ via the quark condensate. This gives rise to Goldstone bosons (Subsec. 2.4.3.1) with small masses called pseudo-Nambu-Goldstone bosons, the eight light pseudoscalar mesons. In analogy with the QCD case, the composite Higgs models attempt to explain the small mass of the Higgs by associating it with a pseudo-Nambu-Goldstone boson coming from a spontaneously broken global symmetry of a new strongly interacting sector. Similarly to the pion decay constant $f_\pi \approx 93$ MeV, in the chiral theory, the electroweak scale $v \approx 246$ GeV would be the parameter of interest in the theory, so the Higgs would reveal itself to be composite at $\Lambda \simeq 4\pi v$. In this scenario, the mass of the scalar would not be sensitive to virtual effects above the $\Lambda \simeq 4\pi v$ scale, hence the reason why the model would not be subject to the annoying naturalness problem.

To construct such composite models, it is necessary to require the unbroken subgroup $\mathcal{H}$ of the global symmetry group $\mathcal{G}$ to contain the SM electroweak group $SU(2)_L \times U(1)_Y$ [166]. However, if that condition is fulfilled, $\mathcal{H}$ is an unbroken symmetry, so the EWSB cannot be accomplished at tree-level. On the other hand, the global symmetry $\mathcal{G}$ has to be only approximate to generate a massive pseudo-Nambu-Goldstone boson, therefore, an explicit breaking has to be introduced through gauge and Yukawa couplings. The quantum effects involving the symmetry-breaking interactions produce a non-vanishing Higgs effective potential, which in turn breaks the electroweak symmetry. All this fancy machinery starts to wobble when

put under test with precision electroweak studies [214], originating a significant splitting between the compositeness and the EW scale. This little hierarchy problem is overcome within the framework of the Little Higgs models [215], which introduce the mechanism of collective breaking [216].

There is a construction called the littlest Higgs model [217] that is considered the smallest extension of the SM in the context of composite Higgs. In this model, the spontaneous symmetry is generated via the Lie groups $SU(5)/SO(5)$, which have 24 and 10 generators respectively. Such breaking structure then provides 14 Goldstone bosons. The explicitly breaking of the global $SU(5)$ is achieved by gauging (Sec. 2.4) a $[SU(2) \times U(1)]^2$ subgroup, which is then broken down by the condensate to the SM electroweak group. The subsequent breaking $SU(2)_L \times U(1)_Y \to U(1)_{EM}$ occurs by means of a radiative-induced Higgs potential.

Now, due to extrapolations from electroweak precision observables, one of the $U(1)$ gauged groups has been identified as problematic, so new ideas proposing just to keep the $U(1)_Y$ gauged have shown up [218, 219]. The unwanted extra $U(1)$ group has been conveniently treated as an explicitly broken global symmetry, thus generating a massive (pseudo-)scalar a particle [220]. The particle field can be perfectly coupled to the SM Higgs boson ($\sim \phi_a^2 H^\dagger H$), by means of which there would be Higgs decays of the form $h_{125} \to a\, a$ for masses of a below 62.5 GeV. The decays of a to SM fermions have been studied in [219] for a particular model. For some other scenarios with Yukawa-like couplings, a non-negligible fraction to the $a \to \tau\tau$ decay mode in the very-low-m_a region is conferred.

Although these types of models tend to be extremely complex in terms of new interactions and parameters, they represent another possible alternative to solve the unnaturalness mystery of the scalar sector. The kind of search carried out in this thesis constitutes one more chance to detect any potential hint of compositeness in the structure of the Higgs boson.

3.2.5 Two Higgs Doublet Models Plus a Scalar Singlet

Without a doubt, one of the classes of models on which this work has more impact is the extension of the standard two Higgs doublet model (2HDM) by an additional scalar singlet. The 2HDMs are a very simple prolongation of the scalar structure of the SM, adding an extra $SU(2)$ multiplet in the fundamental irrep (Subsec. 2.2.3.1). Such extension is allowed since it respects the custodial symmetry [6]. The 2HDMs are commonly found in SUSY (Subsec. 3.2.1), like the already seen MSSM, which is a particular case of a more general formulation for these models. It was seen in the review of SUSY how adding an extra $SU(2)$ doublet could solve two problems at once, namely maintaining holomorphy and canceling anomalies. Another two motivations for 2HDMs come from axion models (Subsec. 3.1.2.6), which sometimes require at least two Higgs doublets in their field content, and from baryogenesis (Subsec. 3.1.2.4), which could be fairly well triggered within the context of these models [221].

The most general CP conserving scalar potential for two doublets H_1 and H_2 is [221]

$$\begin{aligned} V_{2HDM} = {} & m_{11}^2 H_1^\dagger H_1 + m_{22}^2 H_2^\dagger H_2 - m_{12}^2 (H_1^\dagger H_2 + H_2^\dagger H_1) + \frac{\lambda_1}{2}(H_1^\dagger H_1)^2 + \frac{\lambda_2}{2}(H_2^\dagger H_2)^2 \\ & + \lambda_3 H_1^\dagger H_1 H_2^\dagger H_2 + \lambda_4 H_1^\dagger H_2 H_2^\dagger H_1 + \frac{\lambda_5}{2}[(H_1^\dagger H_2)^2 + (H_2^\dagger H_1)^2], \end{aligned} \tag{3.12}$$

where m_{11}, m_{22}, m_{12}, λ_1, λ_2, λ_3, λ_4, and λ_5 are real parameters. After minimization, the

two doublets $H_{1,2}$ get a v.e.v. $v_{1,2}$, thus propitiating the EWSB. That results in five physical degrees of freedom (eight in total, minus the three broken generators): two charged mass eigenstates $H^{\pm}$, one neutral pseudoscalar mass eigenstates A, and two neutral scalar mass eigenstates, H^0 and h_{125}. One of the parameters of the model can be taken to be the rotation angle $\tan\beta = v_2/v_1$ that diagonalizes the charged scalar matrix. The neutral scalar matrix is diagonalized by another angle denoted as α. These two parameters basically describe the phenomenology of the 2HDMs in terms of couplings of the neutral Higgses with the other SM particles (the charged scalars are sometimes ignored since they are assumed to be heavy). Without flavor changing neutral currents (FCNC)[8], there are four types of fermion couplings [12]; those are summarized in Tab. 3.3. Once a type of fermion coupling is given, the

Table 3.3: The four standard types of fermion couplings in 2HDMs without FCNC [12]. Some of the most used terminologies in the literature have been included.

2HDM	up-type quarks	down-type quarks	charged leptons
Type-I	H_2	H_2	H_2
Type-II (MSSM-like)	H_2	H_1	H_1
Type-III (lepton-specific)	H_2	H_2	H_1
Type-IV (flipped)	H_2	H_1	H_2

couplings of the neutral mass eigenstates to SM fermions and gauge bosons are determined in a two-dimensional phase-space spanned by the parameters α and β. Therefore, the couplings at tree-level of those interactions relative to the SM values can be expressed as a function of α and β. In the case of the gauge bosons, the three states couple with a relative strength equal to $\sin(\beta-\alpha)$ for h_{125}, $\cos(\beta-\alpha)$ for H^0, and 0 for A, independently of the 2HDM type. For fermions, the pattern is more complex, as there is an explicit dependence on both the type of 2HDM coupling and the type of fermion. A summary based on [12, 221, 223] is provided in Tab. 3.4.

It turns out that, by now, the 2HDMs are strongly constraint from experimental data [224–228]. In particular, there is vast evidence suggesting that these variety of models should be near to the so-called decoupling limit $\alpha \to \beta - \pi/2$ [229], where the lightest CP-even scalar h_{125} becomes very SM-like, depending all its properties on the parameters α and β for a given 2HDM type [12]. In this limit, the other massive eigenstates tend to be quite heavy and decouple from the physics at the lower scale [230]. One can notice in Tab. 3.4, for instance, how the heavier CP-even scalar H^0 decouples from the gauge bosons in that limit, while the SM-like Higgs boson gets couplings close to the unity. Despite the stringent restrictions on the 2HDM, there is still enough parameter space to be viable near the decoupling limit. However, there is another way to provide this class of models with larger flexibility: adding a complex scalar singlet to the 2HDM

$$S = \frac{1}{\sqrt{2}}(S_R + iS_I). \tag{3.13}$$

[8]Normally, this is achieved by imposing Z_2 symmetries in the model [222].

Table 3.4: Fermionic couplings (up/down-type quarks (u/d) and charged leptons (l)) of the three neutral mass eigenstates (h_{125}, H^0 and A) normalized to those of the SM Higgs in the four types of 2HDMs [221, 223].

Eigenstate	Coupling	Type-I	Type-II	Type-III	Type-IV
h_{125}	$\xi^u_{h_{125}}$	$\cos\alpha/\sin\beta$	$\cos\alpha/\sin\beta$	$\cos\alpha/\sin\beta$	$\cos\alpha/\sin\beta$
	$\xi^d_{h_{125}}$	$\cos\alpha/\sin\beta$	$-\sin\alpha/\cos\beta$	$\cos\alpha/\sin\beta$	$-\sin\alpha/\cos\beta$
	$\xi^l_{h_{125}}$	$\cos\alpha/\sin\beta$	$-\sin\alpha/\cos\beta$	$-\sin\alpha/\cos\beta$	$\cos\alpha/\sin\beta$
H^0	$\xi^u_{H^0}$	$\sin\alpha/\sin\beta$	$\sin\alpha/\sin\beta$	$\sin\alpha/\sin\beta$	$\sin\alpha/\sin\beta$
	$\xi^d_{H^0}$	$\sin\alpha/\sin\beta$	$\cos\alpha/\cos\beta$	$\sin\alpha/\sin\beta$	$\cos\alpha/\cos\beta$
	$\xi^l_{H^0}$	$\sin\alpha/\sin\beta$	$\cos\alpha/\cos\beta$	$\cos\alpha/\cos\beta$	$\sin\alpha/\sin\beta$
A	ξ^u_A	$\cot\beta$	$\cot\beta$	$\cot\beta$	$\cot\beta$
	ξ^d_A	$-\cot\beta$	$\tan\beta$	$-\cot\beta$	$\tan\beta$
	ξ^l_A	$-\cot\beta$	$\tan\beta$	$\tan\beta$	$-\cot\beta$

This singlet is only allowed to couple to the $H_{1,2}$ fields and to itself, then it has no direct fermionic couplings, acquiring all of them through the mixing with the doublets. The resulting model is known as the two Higgs doublet model plus a scalar singlet (2HDM+S) [231–233], and it features seven physical states (one more CP-even H^0_S and one more CP-odd a with respect to the 2HDM). Thanks to the incorporation of a new possible mixing among the components of the singlet and the doublets, the 2HDM+S can comfortably accommodate an SM-like Higgs boson that easily satisfies all the experimental constraints[9]. Besides, the requirement that the mixing has to be small, in order not to destroy the SM-like nature of h_{125}, allows for the existence of mostly-singlet-like light states whose production cross-section would be suppressed by the tiny mixing angle, hence the reason why they would have remained undetected thus far. In supersymmetric theories, there are also realizations of the 2HDM+S that address problems of preexisting versions. That is the case of the Next-to-Minimal Supersymmetric Model (NMSSM), a type-II 2HDM+S intended to solve the "μ-problem" of the MSSM [234–236].

With the addition of the singlet, two more mass eigenstates are candidates to be the lightest one, either a light scalar or pseudoscalar. The case of a light scalar is more difficult to conciliate with the constraints giving rise to the decoupling limit since the mixing of the three CP-even suggests that H^0 and H^0_S should be heavier than h_{125} [236]. This, however, does not completely exclude the possibility of having an alignment without a decoupling limit, which results in relatively light additional Higgs boson [233]. But the most interesting scenario is the one with a mostly-singlet-like light pseudoscalar [12]

$$a = \cos\theta_a S_I + \sin\theta_a A \tag{3.14}$$

[9] In general, the larger the number of parameters, the easier to avoid the constraints.

where $\theta_a \ll 1$, indicating the smallness of the mixing. For masses $m_a < 62.5$ GeV, decays of the SM-like Higgs to a pair of a will take place. Searching for light pseudoscalars in decays of the h_{125}, with their consequent decay to SM fermions, is one of the more suitable approaches to detect those particles, as the direct production of the boson would be diminished by its reduced couplings to the SM fermions (proportional to $\sin\theta_a$). The insertion of the mixing angle θ_a makes the phenomenology of decays $h_{125} \to aa \to f\bar{f}f'\bar{f}'$ depend on three independent parameters, aside from the type of 2HDM fermion coupling. A very comprehensive analysis of such types of decays, including the values of the $\mathcal{B}(a \to f\bar{f})$ for different scenarios, can be found in [12].

The leptonic decay $a \to \tau\tau$ is highly favored for a considerable region of the parameter phase-space in the 2HDM+S. Depending on the specific type of model, decays to pairs of τ leptons could even exceed those to pairs of b-quarks for pseudoscalar masses above the b-quark pair threshold. More details about this will be given in Sec. 6.2. This is the main reason why, despite the experimentally challenging decay topology, it is worth looking for pseudoscalars in the final states involving τ leptons.

CHAPTER

4

EXPERIMENTAL SETUP

Contents

The research presented in this thesis was carried out using the experimental data that was delivered by the Large Hadron Collider and collected by the Compact Muon Solenoid detector during the period of data taking corresponding to the year 2016. The purpose of this chapter is to provide an overview of the experimental apparatus used to carry out this work.

In the following, a relatively detailed description of the complex process that goes from the generation of a collision to the point in which the experimental data becomes available and ready to be analyzed can be found. The first section of this chapter is dedicated to the description of the Large Hadron Collider and to the way it manages to achieve such high-energy collisions and huge amounts of data. The other two sections are meant to outline the main characteristics of the Compact Muon Solenoid detector and the main mechanisms involved in the processing of the data originated by the collisions, as well as the fundamental aspects of the modeling of the various physical processes derived from the theories.

4.1 The Large Hadron Collider

The Large Hadron Collider (LHC) [237] is the largest and most powerful particle accelerator built to this day. The LHC is situated at the European Organization for Nuclear Research (CERN), Geneva, across the border between Switzerland and France. The collider is contained in a circular tunnel that previously hosted the Large Electron Positron Collider (LEP) [238], with a circumference of 27 km and located 100 m underground. As its name suggests, the LHC collides hadrons, accelerating them in opposite directions to near the speed of light and then smashing the particles together; in practice, it accelerates protons or heavy ions. The machine has already managed to collide protons at a nominal center-of-mass energy of 13 TeV, but after an upgrade, it is expected to reach the design value of 14 TeV in the coming years. The purpose of the construction of the LHC and the surrounding experimental facilities is to test the physics of the fundamental constituents described by the SM (Sec. 3.1) and help to answer some of the open questions, which might require a new theory (Subsec. 3.1.2). So far, one of the major contributions of the LHC was to the discovery of a Higgs-like particle at CERN in 2012 (Subsec. 3.1.1).

4.1.1 The Accelerator Complex

To produce beams containing those high-energy hadrons, a large acceleration complex capable of boosting the hadrons from near rest to speeds close to that of light is needed. Since in this work only proton-proton collisions are considered, the following brief description of the CERN accelerator complex is focused on the group of machines operated to accelerate such particles.

The protons that later undergo the acceleration process are extracted from standard molecular hydrogen, whose electrons are stripped away to produce an ionized gas feasible to accelerate with electric fields. The first stage of acceleration takes place at LINAC 2 [240], a linear accelerator equipped with radiofrequency cavities that are used to charge the cylindrical conductors, through which the protons are going to get energies up to 50 MeV. After the LINAC 2, the protons are injected into the Proton Synchrotron Booster (PSB) [241], which raises their energy to about 1.4 GeV. The PSB feeds a larger circular accelerator with 628 m

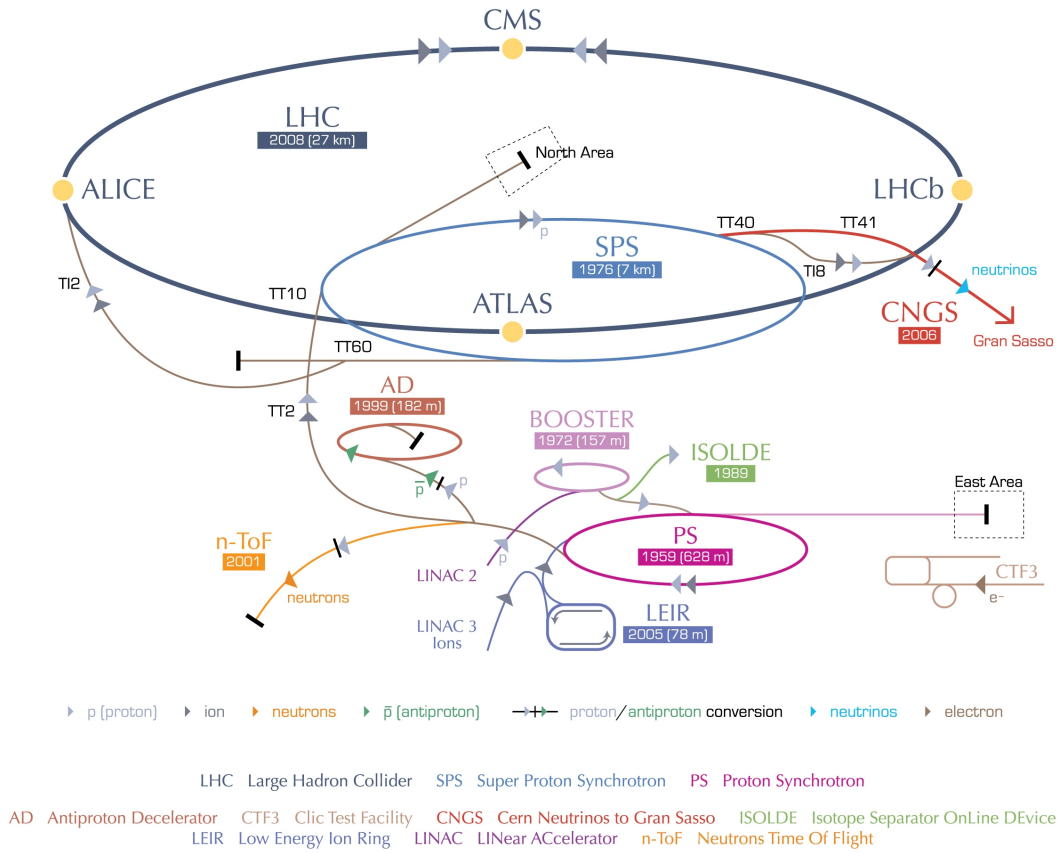

Figure 4.1: Accelerator complex at CERN [239]

simply called Proton Synchrotron (PS) [242], provided with 277 electromagnets that ensure the circular movement of the protons, as well as a maximum energy of roughly 25 times the rest mass of the proton. The Super Proton Synchrotron (SPS) [243] is the next accelerator in the chain and the last step before injection to the LHC. The SPS is the second largest machine in the CERN accelerator complex with a circumference of nearly 7 km, which makes it capable of reaching the respectable value of 450 GeV. In Fig. 4.1, a comprehensive sketch of the previous description of the accelerator chain, as well as of the various experiments present at CERN can be found.

Once the two proton beams reach the LHC, they can be accelerated to a maximum design energy of 7 TeV each one. Rather than having continuous beams, during the acceleration process, the protons are bunched together into up to 2808 packets containing a hundred billion protons that are separated in time by 25 ns. At 6.5 TeV (the operating energy in the main period of 2016-2018), the protons give around 11245 turns in one second along the 27 km ring. This is possible due to radiofrequency cavities (8 per beam) inside the LHC that are cooled down to 4.5 K using liquid Helium, being able to provide an alternating electric field with a frequency of 400 MHz [244]. But it is also crucial to keep the beams on their circular path and, in order to achieve that, the LCH requires 1232 dipole magnets of 15 m long and 30 tons each [245] together with 392 quadrupole magnets used to keep the beams

focused. The dipole magnets are superconductors that can be operated at a temperature of 1.9 K and can reach a magnetic field of 8.33 T. Magnets of higher multipole orders are used to correct smaller imperfections in the field configuration.

At the moment a stable condition is accomplished for the two beams, they are made collide at four interaction points along the ring. In each interaction point is located one of the "big" experiments at CERN. ATLAS [246] (A Toroidal LHC ApparatuS) and CMS [247] (Compact Muon Solenoid) are general-purpose detectors designed to perform precision tests within the SM and searches for BSM physics studying proton-proton collisions. Although they both have the same scientific goal, there are some technical features that differentiate them; for instance, ATLAS has larger dimensions, while CMS has a higher weight condensed in a smaller volume. The ALICE [248] (A Large Ion Collider Experiment) collaboration studies heavy ion (Pb-Pb nuclei) collisions to gain knowledge about the very strong interacting environments subject to high energy and density. The LHCb [249] (Large Hadron Collider beauty) experiment was designed to investigate the b-quark physics via the production and decay of B-mesons, which plays an important role in the phenomenon of CP violation.

4.1.2 Beam Parameters and Data Taking

A parameter of most importance when operating a collider is the instantaneous luminosity $\mathcal{L}$ [250]. The number of events per unit time taking place (dN/dt), corresponding to a certain physics process, is proportional to the cross-section σ of such process. The proportionality constant in that relation is the instantaneous luminosity

$$\frac{dN}{dt} = \mathcal{L} \cdot \sigma. \tag{4.1}$$

The expression for the instantaneous luminosity of two head-on colliding Gaussian beams (Gaussian profile in all dimensions) that contain roughly the same number of protons per bunches and that are regularly spaced is [251]

$$\mathcal{L} = \frac{N^2 n_b f}{4\pi\sigma_x\sigma_y}, \tag{4.2}$$

where N is the number of protons per bunch, n_b is the number of bunches per beam, f is the revolution frequency, and σ_x/σ_y characterizes the rms transverse beam size in the x/y direction. However, the formula (4.2) assumes only ideal collisions with uncorrelated particle densities; in practice it has to be modified to account for corrections. Some of the effects that have to be included are non-zero crossing angles, longitudinal dependence of the transverse beam sizes, collision offsets, non-Gaussian beam profiles, and optical imperfections [251]. For the LHC, the formula reads [252]

$$\mathcal{L} = \frac{N^2 n_b f \gamma_r}{4\pi\varepsilon_n\beta^*} F, \tag{4.3}$$

where the modifications F (geometric luminosity reduction factor), ε_n (normalized transverse beam emittance), β^* (beta function at the collision point), and γ_r (relativistic gamma factor) account for different corrections to the ideal case. The peak design LHC instantaneous luminosity is $\mathcal{L} = 10^{34}$ cm^{-2}s^{-1}, which was first reached and later surpassed.

One is often interested in the total number of events that a collider produces over a period, for which the term integrated luminosity is used

$$L = \int dt\mathcal{L}. \tag{4.4}$$

The first phase of the LHC operation, usually referred to as Run 1, started in March 2010 with a center-of-mass energy of $\sqrt{s} = 7$ TeV; value that was afterward raised to $\sqrt{s} = 8$ TeV in 2012. The LHC delivered around 6.1 fb^{-1} and 23.3 fb^{-1} of integrated luminosity in proton-proton collisions at 7 and 8 TeV respectively [253]. That was enough for the ATLAS and the CMS collaborations to discovery the Higgs boson. After 3 years of operation in Run 1, the machine was stopped for a first long shutdown for 2 years (2013 to 2015). After receiving an upgrade that made it capable of reaching the $\sqrt{s} = 13$ TeV, the machine was recommissioned in 2015 and started the second period (Run 2) of data taking. This run continued until the end of 2018 delivering more than 162 fb^{-1} of data, and after that, the LHC is in shutdown complying with a second period (2019 to 2020) of upgrades. The LHC Run 3 should start in 2021 with collisions at $\sqrt{s} = 14$ TeV and a goal of 300 fb^{-1}. In the future high luminosity run of the LHC that is foreseen for 2027 [254], the total recorded luminosity is expected to reach the 3000 fb^{-1} [255].

The analysis presented in this work uses data from pp collisions at $\sqrt{s} = 13$ TeV, recorded during the 2016 data taking period and corresponding to an integrated luminosity of 35.9 fb^{-1}.

4.2 The Compact Muon Solenoid

As it was mentioned above, the Compact Muon Solenoid (CMS) [247, 256] is one of the two general-purpose detectors at the LHC located in a cavern near Cessy in France. The detector is operated by the CMS collaboration, a group of around 4000 people representing 200 scientific institutes from more than 40 countries [257]. The CMS detector is 21 m long, 15 m in diameter, and weighs about 14000 tonnes.

4.2.1 Overview of the CMS Detector

Among the distinctive features of CMS is to have a great performance detecting and measuring muons; partly from that derives its name. But muons are not the only objects that need to be measured accurately, in general, good particle identification and momentum reconstruction are required to precisely test the theory of the SM, and to detect (in case of being within reach) any elusive evidence of new physics. Moreover, since most of the visible byproducts of the collisions are either hadrons or particles subject to electromagnetic interaction, it is important to have good calorimeters capable to provide a high energy resolution. All this is achieved with a series of sub-detectors organized in the form of layers, each one with a specific function. The CMS detector has a cylindrical structure, symmetric around the beam pipe and centered at the interaction point. The innermost layer is a silicon-based tracker surrounded by a scintillating crystal electromagnetic calorimeter. Next, there is a hadron calorimeter followed by the outermost layer, consisting of systems designed for the detection of muons called muon chambers. A schematic representation of the CMS detector and its various components can be found in Fig. 4.2.

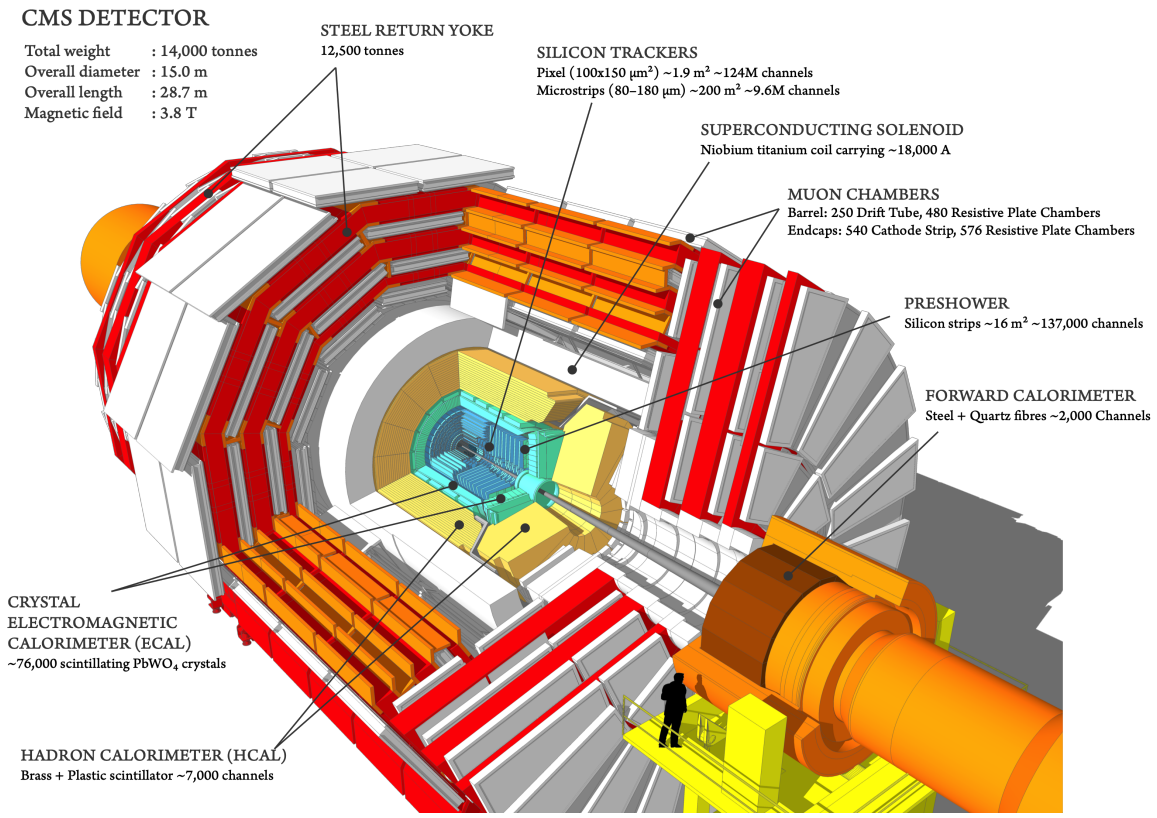

Figure 4.2: General view of the CMS detector structure. [258]

Regarding the coordinate system used by CMS, its origin is selected as the nominal collision point. The z-axis points in the anticlockwise direction of the proton beam, the x-axis is placed radially towards the center of the LHC, and the y-axis is so that the cartesian coordinate system is dextrogyral. The equivalent polar coordinate system is defined accordingly, with the φ angle measured from the x-axis and the radius r being the radius in the x-y plane. The angle θ identifies the polar angle in the r-z plane. Due to the fact that collisions suffer from boosts in z-axis direction (longitudinal momentum fractions of partons), the use of invariant quantities under Lorentz boosts along the z-axis is crucial. The quantity called rapidity y has the property that the difference Δy is invariant with respect to such Lorentz boosts [259]. The rapidity is given by

$$y = \frac{1}{2} \ln \left(\frac{E + p_z}{E - p_z} \right), \tag{4.5}$$

with p_z being the z-component of the three-momentum $\vec{p}$ and E the energy. The high energy nature of the collisions taking place at the LHC implies that the particles involved are typically in the ultrarelativistic approximation ($E \approx |\vec{p}|$), so it is convenient to use, instead, the pseudorapidity

$$\eta = -\ln \tan \frac{\theta}{2}. \tag{4.6}$$

The pseudorapidity becomes almost equal to the rapidity in the ultrarelativistic limit and is much easier to measure for highly energetic particles.

4.2.2 Superconducting Magnet

To a large degree, the high efficiency that CMS exhibits in reconstructing tracks of charged particles is due to its powerful magnet [247, 260]. The magnet, with an inner radius of 6 m and a length of 13 m, is a superconducting solenoid providing a magnetic field of 3.8 T. Such a field is generated by a complex structure of niobium-titanium coils capable of carrying a nominal current of 19500 A and cooled down by liquid helium. The large inner radius allows for the tracker and calorimeters to be fully contained within the solenoid. The magnet system also includes a return yoke of 14 m surrounding the magnet coils.

4.2.3 Inner Tracking System

The inner tracking system [247,261] of CMS is meant to precisely determine the trajectory of charged particles in association with the magnetic field, and to identify the primary and secondary vertices of the event. The tracker consists of two subsystems; a pixel detector that extends radially from 4.4 cm to 10.2 cm away from the beamline, and a silicon strip tracker that covers the radii between 20 cm and 116 cm. The silicon modules take up a total active area of more than 200 m^2 and cover a pseudorapidity range $|\eta| < 2.5$.

The pixel detector is the closest component of the tracking system to the interaction point and consists of 3 barrel layers and 2 end-cap disks on each side of the barrel. The barrel layers (BPIX) are located at radial distances of 4.4 cm, 7.3 cm and 10.2 cm from the beamline, and have a length of 53 cm. The endcap disks (FPIX) extend from 6 to 15 cm in radius and are located at points $z = \pm 34.5$ cm and $z = \pm 46.5$ cm. The size of a pixel cell is 100×150 μm^2, and they are arranged in modules; there are 768 of those modules in the PBIX and 672 in FPIX. The intrinsic spatial resolution of the pixel detector is about 20 μm along the z-axis and up to 10 μm in the r-φ direction.

The silicon strip tracker is located surrounding the pixel tracker. It is divided into two parts: the inner strip tracker, formed by its respective tracker inner barrel (TIB) and tracker inner disks (TID), and the outer strip tracker consisting of the tracker outer barrel (TOB) and the tracker end-caps (TEC). The four different subsystems contain in total 15148 detector modules carrying either one thin (320 μm) or two thick (500 μm) silicon sensors. The TIB contains four concentric cylinders placed at radii of 25.5 cm, 33.9 cm, 41.9 cm and 49.8 cm respectively covering the range $|z| < 70$ cm. The TID comprises 3 identical disks placed within the segments 80 cm $< |z| <$ 90 cm on each side of TIB, and spanning a radial region from 20 cm to 50 cm. The TOB is a 218 cm long single mechanical structure with inner and outer radii of 55.5 cm and 116 cm respectively, composed by four identical disks joined by three outer and three inner cylinders. The TEC includes 18 disks (9 on each side) extended radially from 22 cm to 113.5 cm and placed from ± 124 cm to ± 280 cm along the z-direction.

4.2.4 Electromagnetic Calorimeter

The electromagnetic calorimeter (ECAL) is designed to measure with high accuracy the energies of electrons and photons [247, 262]. The ECAL is a hermetic, homogeneous, fine-grained scintillating calorimeter consisting of 75848 lead tungstate ($PbWO_2$) crystals. Most of those crystals (61200) form part of the central ECAL barrel, which covers the pseudorapidity range $|\eta| < 1.48$; the rest are mounted in the two end-cap regions reaching up to $|\eta| = 3.0$.

In the barrel section, the crystals are organized into 36 supermodules, each containing 1700 crystals with a length of 23 cm and an area of 2.2×2.2 cm^2 and 2.6×2.6 cm^2 at the front and the rear face respectively. Each end-cap is divided into 2 halves containing 3662 crystals with rear face cross-section 3.0×3.0 cm^2, front face cross-section 2.86×2.86 cm^2 and length 22 cm.

The short-lived π^0 mesons are particles that appear quite often during pp collisions and they generally decay into two photons. Being so light, they tend to be very boosted (especially in the high $|\eta|$ regions), therefore, producing highly collimated γ-γ pairs, which turn difficult to resolve by the ECAL. In order to improve the resolution for such processes, there is a preshower detector with finer granularity in front of the ECAL end-caps. The preshower detector is based on lead absorber and silicon strips sensors, and spans the fiducial region of $1.65 < |\eta| < 2.6$.

4.2.5 Hadronic Calorimeter

The hadron calorimeter (HCAL) [247,263] is essential for measuring the energy of hadrons and the missing transverse energy in an event. They exploit the nuclear interactions of hadrons, like the case of inelastic collisions with atomic nuclei, which can produce the hadronic showers. Hadron calorimeters are able to fully contain those low-energy particles, providing then a hermetic coverage and also a detectable signal through an active medium.

The HCAL is located between the ECAL and the magnet coil (1.77 m $< r < 2.95$ m), which restricts the amount of stopping material in the detector. To ensure the adequate thickness in the central region ($|\eta| < 1.3$), an outer hadron calorimeter (HO) is placed outside the solenoid. The remaining three components of the HCAL system are the inner barrel (HB), the end-caps (HE), and the forward calorimeter (HF).

The HB covers the region with $|\eta| < 1.3$, its absorber material consists of thick tiles of brass, and the active medium consists of thinner tiles of scintillating plastic with wavelength-shifting readout fibers. The HO uses the same plastic scintillator as HB but also takes advantage of the solenoid coil as an additional absorber. The HE covers the $1.3 < |\eta| < 3.0$ range and utilizes the same materials as HB. Unlike the three other parts of HCAL, HF uses quartz core and acrylic clad fibers as active medium, due to the fact that it is exposed to high radiation doses coming from the large particle fluxes in this part of the detector ($3.0 < |\eta| < 5.0$). The absorber chosen for HF is steel.

4.2.6 Muon Systems

The detection of muons is of great importance in high energy physics, as they provide feasible access to the second generation of particles in the SM, and they also might be the evidence of the decay of a potential new particle. Being the muons about 200 times heavier than the electrons, they turn very difficult to be disturbed by electromagnetic fields when passing through the materials, which makes the detection of these particles very hard. Because of that, the subdetector dedicated to the detection of muons in CMS is the outermost system [247, 264]. In this region, muons are the only particles likely to have penetrated through the calorimeters and, therefore, the only ones able to produce a signal.

The muon system consists of three kinds of gaseous ionization detectors, whose modules are commonly referred to as chambers: drift tubes (DT), cathode strip chambers (CSC), and

resistive plate chambers (RPC). Similarly to the subdetector systems described above, the muon systems contain a barrel and two end-caps, where the barrel is interleaved with layers of the steel flux-return yoke.

In the barrel region where the magnetic residual flux and the muon rate are low, there are 250 drift tube chambers grouped into 4 stations forming concentric cylinders around the beamline and extending radially from 4.0 m $< r <$ 7.0 m. The DT chambers cover the pseudorapidity region $|\eta| < 1.2$, and their arrangement is so that it provides a good time resolution and a high efficiency in reconstructing the muon track from its hits in the stations. Each cell contains a gas mixture of 85% Ar + 15% of CO_2 surrounding a gold-plated stainless-steel anode wire, which results in a drift time of 380 ns.

The muon system end-caps cover a region of $0.9 < |\eta| < 2.4$, where the expected rate of muons and neutron background is much higher than that in the barrel, requiring then the use of CSC. The 468 trapezoidal CSC chambers are organized in 4 stations (rings) in each end-cap. Each chamber consists of 6 anode planes interleaved among 7 cathode panels with wires running azimuthally. The chambers are filled with a gas mixture of 50% CO_2 + 40% Ar + 10% CF_4.

In addition to the DT and CSC detectors, RPC are interspersed in the barrel and end-cap layers to complement the other two systems in the region $|\eta| < 1.6$. They are used to provide a fast response with good time resolution (less than 25 ns) and an independent triggering system for muons. The RPC chambers consist of two resistive Bakelite plates separated by a gas volume.

4.2.7 Trigger System

The LHC provides a collision rate of about 100 MHz producing an enormous amount of data, most of which is irrelevant for the CMS physics program and practically impossible to store. The trigger system is responsible for selecting the small fraction of collision events that are interesting for CMS. The CMS trigger system [247] consists of two stages: the Level-1 trigger (L1) [265], which is entirely hardware-based and filters events to an output rate of $\sim$ 100 kHz, and the software-based high-level trigger (HLT) [266] that reduces the rate further down to $\sim$ 1 kHz.

The L1 trigger decision occurs with a latency of few microseconds using a simplified readout of the calorimeter and muon subdetectors. The L1 trigger is organized into local, regional and global components. The local components are based on energy deposits in ECAL and HCAL, and hits and segments in the muon system. The regional components rank the trigger candidate objects (muons, electrons, jets, photons, etc) in small regions, combining the information from the local components using pattern recognition and track finding. The next step is the determination by the global components of the highest-rank objects, which are then transferred to the global trigger to make the decision of accepting or not the event. Later, the information is passed to the HLT software (implemented in a computing farm), which has access to more detailed information of the event. At a much lower rate, the algorithm is able to perform more dedicated calculations to accept events with the most interesting physics content.

4.3 Event Reconstruction and Simulation in CMS

Once all the information provided by the different subdetectors in CMS for a given pp collision is gathered, the next step is to proceed with the reconstruction and identification of all the stable particles (electrons, muons, photons, charged hadrons, and neutral hadrons) that make up the event. Other physics objects like jets, missing transverse energy, taus and primary (secondary) vertices are built, identified or reconstructed from individual elements that compose them.

On the other hand, a set of general-purpose event generators that possess implementations of the various theoretical models are used with the objective of simulating pp collisions. The generated events are subjected to a process of modeling within the CMS framework that goes from basic detector simulation to total event reconstruction.

4.3.1 Physics Objects Reconstruction

The first stage of the event reconstruction is carried out by the particle flow algorithm [267–269], which uses a combination of charged-particle hits, calorimeter clusters, and muon tracks to identify each final-state particle. The reconstructed particle candidates are used to build the physics objects and related quantities through specific high-level algorithms, thus permitting to give a proper structure to the event information and facilitating the task of performing a physics analysis. An illustration of different types of particles registering signals in the subdetectors can be seen in Fig. 4.3.

4.3.1.1 The Particle Flow Algorithm

In CMS the particle flow (PF) algorithm can be arranged in a three-step process as described in [270, 271].

First, the fundamental elements, namely charged-particle tracks and calorimetric clusters, are reconstructed using sophisticated techniques designed for each type of object. Finding the trajectories of the charged particles mostly relies on the tracker system of CMS, as it allows for a very good momentum resolution. The tracking algorithm of CMS is based on an iterative approach [272], which has proven to be more efficient than the global combinatorial track finder method [273]. The process starts by generating a seed that is generally related to three hits in the pixel detector. Then, a track finding strategy based on the combinatorial Kalman filter method is used [274] to reconstruct trajectories with certain quality criteria. Finally, the trajectory is refitted using a least-squares method, with the peculiarity that it has a smoother complementing the Kalman filtering. On the other hand, the measurements of the energy deposits in the calorimeters are combined in a clustering algorithm that is applied separately in the barrels and end-caps (including the preshower detectors) of ECAL and HCAL [271]. Analogously to the iterative tracking, the calorimetric clustering is seeded by imposing some initial conditions, in this case, calorimeter-cell energies above a given threshold. Subsequently, topological clusters are built out of the seeds by adding cells with a minimum amount of energy and at least one corner in common with the seed. The last step reduces the identification of single clusters within each topological cluster with the help of a mixture of Gaussian distributions as model.

Second, the linking algorithm is applied. This is conceived to link the elements of a single particle throughout its trajectory inside the detector. It can be seen in the sketch of

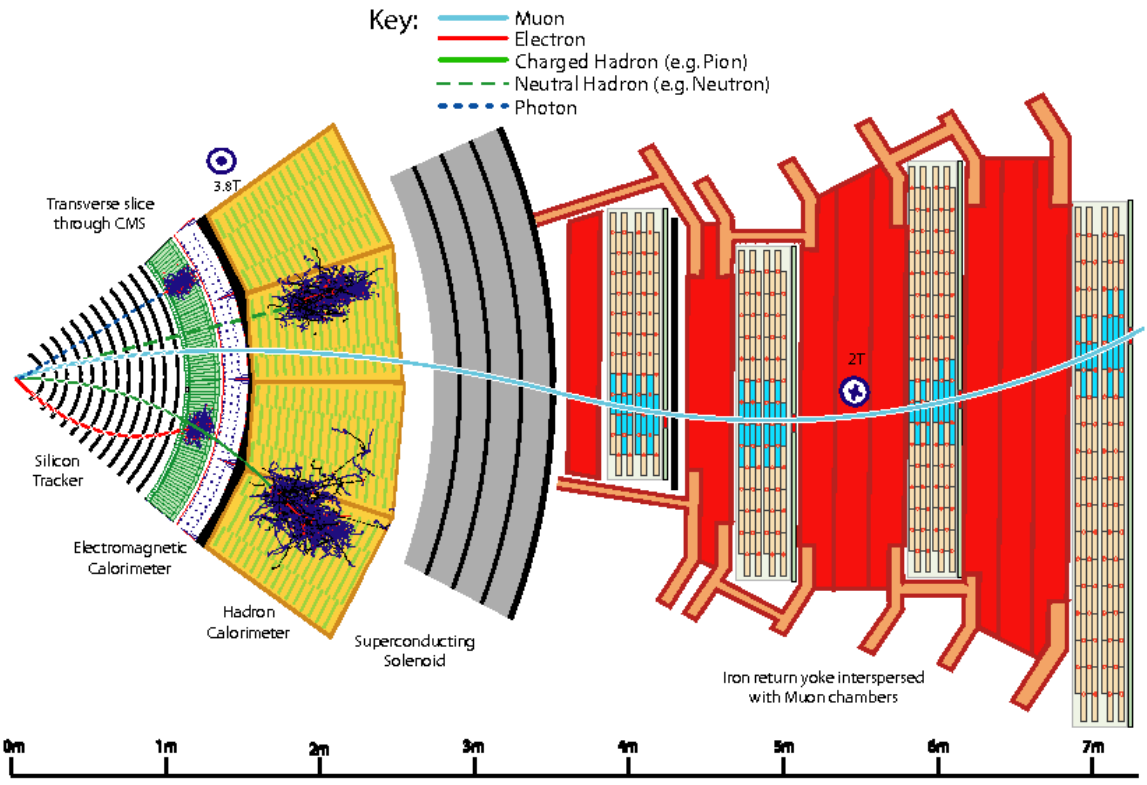

Figure 4.3: Sketch of a CMS transverse slice showing physics objects interacting with different subdetectors. [271]

Fig. 4.3 how each particle gives rise to several PF elements in the various CMS subdetectors. Starting from a pair of elements in the event, the link algorithm defines a distance between them (typically is the distance in the (η, φ) or the (x, y) plane) and evaluates the quality of the link itself; those linked elements are then grouped into blocks. Different kinds of links can be established, according to the parts of the detector that they are connecting. A link between a track in the central tracker and a calorimeter cluster is obtained via an extrapolation from its last measured hit to any given cluster in the calorimeters. The energy of Bremsstrahlung photons emitted by electrons is calculated employing the extrapolation of tangent lines to the electron trajectory to the ECAL. Cluster-to-cluster links are formed if the cluster position in the more granular calorimeter is within the cluster envelope in the less granular calorimeter. Other types of configurations are also possible as shown in [271].

Third, the particle reconstruction and identification is carried out. This final stage is the core part of the PF algorithm. It is the point at which a list of all the particles that have been recognized by the PF algorithm is produced [270]. Global muons (track obtained from the combination of hits in the inner tracker and the muon systems) with a momentum compatible with the tracker-only measurement are identified as PF muons; the corresponding track is removed from the block. Electrons are identified by their characteristic short tracks and by the loss of energy when crossing the tracker due to the Bremsstrahlung; the associated tracks and ECAL clusters are then eliminated. Charged hadrons are formed by the remaining tracks in the block, using the track momentum to directly determine their energy and momentum.

The remaining ECAL and HCAL clusters, either not linked to any track or with a link incompatibility, are identified as PF photons and PF neutral hadrons respectively.

4.3.1.2 Primary Vertices

The primary vertex (PV) reconstruction aims at determining the position of every individual pp interaction in each event using the available information about the reconstructed particle tracks. Due to the large number of protons per bunch at the LHC (Sec. 4.1), multiple pp interactions can take place in each bunch crossing, giving rise to a phenomenon called pile-up (PU). The PV reconstruction is a three-step procedure [272]. The first is the selection of the tracks. Those are chosen by imposing requirements on the transverse impact parameter, the position with respect to the beam spot, the number of pixel and strip hits, and the χ^2 of the track fit. Then, the deterministic annealing algorithm [275] is used to cluster the set of selected tracks to primary vertex candidates. Finally, the candidate vertices with at least two tracks are refitted using the adaptive vertex fitter [276]. The one with the largest value of the p_T^2 sum of jets clustered with the anti-k_T algorithm (Subsec. 4.3.1.5) is regarded as the hard-scattering vertex, whereas the others are considered as PU [277].

4.3.1.3 Muons

In CMS the muons can be reconstructed by both the tracker and the muon systems with the help of the PF algorithm (Subsec. 4.3.1.1). This leads to the existence of three possible ways in which a muon can be reconstructed [278]:

- Standalone muon tracks are reconstructed exploiting only the information provided by the muon subdetectors and using the Kalman filter method.
- Tracker muon tracks are built from the inner tracker trajectory reconstruction with additional loose matching to DT or CSC segments.
- Global muon tracks are reconstructed by matching standalone-muon tracks with tracker tracks.

Since each specific analysis might need a different balance of efficiency and purity, a number of identification variables are incorporated to provide a way of tuning such quantities. Some of those variables are the number of hits in the tracker and the muon chambers, the χ^2 of the muon track fit and the track impact parameters. They are introduced in an algorithm that returns values ranging from 0 to 1, with 1 representing the highest degree of compatibility. This results in three main types of identification (ID) for muons, refereed to as loose muon ID, medium muon ID and tight muon ID. Each working point is optimized to identify muons having some specific characteristics (low or high p_T, prompt or non-prompt muon, etc.), as described in [278].

4.3.1.4 Electrons and Photons

The electrons are reconstructed using the silicon tracker and the ECAL, taking advantage of combined procedure based on the PF algorithm (Subsec. 4.3.1.1) and a stand-alone reconstruction method [279,280]. To carry out the clustering in the ECAL two different algorithms are implemented, the so-called hybrid algorithm in the barrel and the multi-5×5 algorithm in

the end-caps; both techniques are described in [279]. For the track reconstruction, due to the losses of energy by Bremsstrahlung, a modification of the Kalman filtering is employed. The method is called gaussian sum filter [281] and makes use of a Gaussian mixture rather than a single Gaussian distribution for the energy losses. In order to link the track and the ECAL superclusters, a combination of ECAL-based and tracker-based seeding algorithms is applied. Moreover, a set of variables is introduced into a boosted decision tree (BDT) classifier (see Sec. 5.1 and Subsec. 6.1.3) to achieve the maximum possible performance in the identification of electrons.

Photons, especially isolated ones, are of particular interest for some kind of signals or signatures in CMS; for instance, the Higgs diphoton decay channel, which has significantly contributed to the discovery and measurement of the properties of the scalar boson [282]. In CMS, electrons and photons are intrinsically linked to each other due to the presence of processes like the Bremsstrahlung and the photon conversion. So, the fundamental aspects of the reconstruction procedure, as well as the measurement of the energies for these two particles are quite similar. Some differences come from the isolation applied for photons with respect to tracks and calorimetric clusters, and from the presence of distinctive energy patterns in ECAL and HCAL. A fairly detailed description can be found in [283], with special emphasis on the selection made for photons in $H \to \gamma\gamma$ decays.

4.3.1.5 Jets and Missing Transverse Energy

It is well known that only color singlet states are allowed to exist at relatively low energies because of the phenomenon of QCD confinement. At the LHC, when a colorful object is produced as a consequence of a collision, it creates out of the vacuum other color-charged states and combines with them to form colorless particles in a process called hadronization. All these hadrons tend to travel in the same direction in which the initial parton was produced, forming collimated streams of particles called *jets*. The main goal of the procedure used in CMS to reconstruct jets is to provide a good estimate of the initial energy and direction of the particle that produced the jet. The jets are reconstructed by putting their components together with the help of an algorithm that obeys the principles of collinear and infrared safety [284]. This is because the reconstruction should not be sensitive to processes that can not be resolved, such as the emission of a soft or a collinear parton.

Using different combinations of subdetectors leads to a variety of possible types of reconstructed jets. The so-called "Calo jets" are obtained by using solely the calorimeter information; analogously, the "Track jets" are clustered using only the inner tracker. A combined version of the previous two has also been implemented, however, the best performance is attributed to the method that reconstructs jets by clustering PF particles together, the "PF jets". The most widely used technique to reconstruct the PF jets is the anti-k_T sequential algorithm [285]. The anti-k_T method is based on the clustering of pairs of particles (protojets) defining a certain metric under which it is decided whether the two objects should be paired or not. The metric makes use of two quantities: the distance d_{ij} between two protojets i and j, and the distance d_{iB} between any entity i and the beamline; their expressions are

$$d_{iB} = (p_{ti})^{-2}, \qquad d_{ij} = \min\{(p_{ti})^{-2}, (p_{tj})^{-2}\}\frac{R_{ij}^2}{R^2}, \tag{4.7}$$

where p_{ti} is the transverse momentum of the object i, $R_{ij} = \sqrt{(y_i - y_j)^2 + (\phi_i - \phi_j)^2}$, and R is a parameter that controls the radius of the jet in the y-ϕ plane. All possible values of d_{iB} and d_{ij} are calculated, then the smallest one is used to start the algorithm. If $d_{ij} < d_{iB}$, the objects are recombined into a single object, while if $d_{ij} > d_{iB}$ the object i is identified as a jet and removed from the list of objects to be clustered. The procedure is repeated until all PF candidates are clustered into jets.

Despite the good functionality of these algorithms, other effects, both in the real detector and in its simulation, cause inconsistencies between the energy of the parton and that of the clustered jet. This leads to the application of procedures for the correction of the energies, such as those described in [284, 286].

It might happen that, after all the PF candidates have been processed, a momentum imbalance in the transverse plane shows up[1]. This is because the detector is not able to detect a certain class of particles that possess very low interaction cross-section, such as neutrinos and other BSM hypothetical neutral weakly interacting particles. So, the magnitude that quantifies this imbalance is the missing transverse momentum $\vec{E}_T^{miss}$, defined as the negative vectorial sum of the transverse momentum of all reconstructed PF objects in the event. More information about its reconstruction and performance in CMS can be found in [287, 288].

4.3.1.6 Taus

The τ lepton is a charged lepton belonging to the third generation, with a lifetime of 2.9×10^{-13} s and a mass of $m_\tau = 1776.86 \pm 0.12$ MeV [289]. Unlike the other leptons, the τ lepton features an extended list of possible decay modes, including decays to hadrons; the most likely ones are shown in Tab. 4.1.

Table 4.1: Decay modes of the τ lepton (only τ^- is shown for simplicity) and their corresponding branching ratios ($\mathcal{B}$) [289–291].

Decay mode	Meson resonance	$\mathcal{B}$ [%]
$\tau^- \to e^- \bar{\nu}_e \nu_\tau$		17.8
$\tau^- \to \mu^- \bar{\nu}_\mu \nu_\tau$		17.4
$\tau^- \to h^- \nu_\tau$		11.5
$\tau^- \to h^- \pi^0 \nu_\tau$	$\rho(770)$	25.9
$\tau^- \to h^- \pi^0 \pi^0 \nu_\tau$	$a_1(1260)$	9.5
$\tau^- \to h^- h^+ h^- \nu_\tau$	$a_1(1260)$	9.8
$\tau^- \to h^- h^+ h^- \pi^0 \nu_\tau$		4.8
Other hadronic modes		3.3

Due to the short lifetime of the τ, electrons and muons originating from τ decays are difficult to distinguish from those produced in the primary proton-proton interaction, thus having

[1]The total transverse momentum of the colliding protons is supposed to be zero.

to be identified via the standard techniques developed for each lepton. For the hadronic decay modes τ_h, the CMS collaboration has designed a dedicated identification technique, which has been named as the hadron plus strips (HPS) algorithm [290, 291]. This procedure uses information from PF charged hadron tracks and from photons coming from π^0 decays to reconstruct the τ_h candidates. The π^0 tends to convert to e^-e^+ pairs, which are bent in opposite directions by the magnetic field, leaving a distinctive strip-like signature in the η-ϕ plane. The HPS algorithm also exploits the relevant attributes of the various τ_h decay modes to increase its effectiveness.

The next step is the adequate identification of τ_h leptons, which is related to procedures capable of suppressing as much as possible the fake reconstructed taus emerging from different physical processes. The major challenge of the τ_h identification is the discrimination between true taus and QCD jets arising from quark and gluons. To reduce this huge background, one uses the fact that taus tend to be more collimated, have lower track multiplicity, and are more isolated than jets [292]. The fundamental isolation criterion has been implemented using both cut-based and multivariate analysis (MVA) approaches (see Sec. 5.1); the MVA discriminator has evidenced better performance. Not only jets but also isolated leptons have a sizable, though smaller, misidentification rate in τ decays involving one charged hadron. Two different anti-lepton multivariate BDT discriminators [293], one against electrons and one against muons, have been developed to suppress the respective fake backgrounds.

In Run 1, the HPS algorithm maintained a τ_h identification efficiency in the range 50-60 %, while keeping the misidentification rates between the per mille and the percent level. For Run 2, some improvements with respect to Run 1 have already been achieved, as it can be seen in [291].

4.3.2 Simulation

Testing theoretical models in high energy physics, or simply the interpretation of the data provided by particle colliders, relies on the appropriate modeling of all involved physical processes. Both in the extraction of the relevant parameters of a theoretical model and in the inference from data of the existence of new physics, the simulation plays a fundamental role. The process of event generation is based on the general-purpose Monte Carlo (MC) event generators [294], which use numerical MC techniques [295] to produce collisions as those obtained in particle accelerators. Once the physical events are generated with the information primarily coming from the theoretical models integrated into the generator, the effects that a detector, as in this case CMS, incorporates into the bare theory, must be taken into account.

The MC event generators provide a complete picture of the collision process from the initial to the final state, which comprises the strongly inelastic interaction, the radiation process, the hadronization of partons, and the description of the underlying event. All this is guaranteed on an event-by-event basis with the complete information regarding the particle types and their momenta, as well as the values of the differential and integral cross sections for a given process. The Fig. 4.4 shows an illustration of a pp collision event simulated with a MC event generator.

When colliding protons (hadrons) at very high energies, there are at least two energy scales mediating in the process: the hard scale Q and the proton scale $m_p \sim 1$ GeV, with $Q \gg m_p$. This allows to separate into two different regimes the dynamics of the process

occurring at each scale, which is commonly called "factorization" [296]. The two domains are referred to as the perturbative and the non-perturbative regime, for obvious reasons. The dynamics happening at m_p is encoded in non-perturbative objects, the so called collinear parton distribution functions (PDFs) [297–299]. On the other hand, the hard scale Q interaction is described by perturbation theory (Subsec. 2.4.4.1). Using the factorization theorem, the cross-section of a hard scattering process $p_1 p_2 \to n$ can be written as [18, 300]

$$\sigma = \sum_{a,b} \int_0^1 \int_0^1 dx_a dx_b \, f_{a/p_1}(x_a, \mu_f) f_{b/p_2}(x_b, \mu_f) \, \hat{\sigma}_{ab\to n}(\mu_f, \alpha_s(\mu_r)), \tag{4.8}$$

where x_a and x_b are the longitudinal momentum fractions of the respective proton momentum, μ_f is the factorization energy scale, $f_{a(b)/p_{1(2)}}(x_{a(b)}, \mu_f)$ are the PDFs, $\alpha_s(\mu_r)$ is the QCD running coupling constant implicitly depending on the renormalization scale μ_r, and $\hat{\sigma}_{ab\to n}$ is the partonic cross-section of the process $ab \to n$.

Both the initial interacting partons and the ones produced as a consequence of the hard scattering can produce QCD radiation, resulting in dozens of additional partons in the event. These branchings of the partons are known as parton showers [303], and can be regarded as approximate higher-order corrections to the hard scattering via real emissions of radiation. The radiation emission chain, i.e. the shower, is triggered by the fact that gluons interact among themselves, so once a gluon is irradiated it will propagate emitting radiation itself. As it is not feasible to compute all the higher-order contributions with the parton showers, a simplified procedure including only dominant corrections through collinear or soft emissions is carried out. These leading contributions can be written in such a way as to express the probability for an emission [300]

$$d\mathcal{P} = \frac{\alpha_s(Q^2)}{2\pi} \frac{dQ^2}{Q^2} P_{a\to bc}(z) dz. \tag{4.9}$$

The Eq. (4.9) expresses the probability that parton a will split into partons b and c at a scale Q^2 and with b carrying a fraction z of the momentum of parton a. In order to avoid the divergences for $z = 0, 1$ (too soft) and $Q = 0$ (too collinear), one usually introduces a cutoff scale, which is physically justified, as such emissions are not resolvable for the detectors. The unresolvable and virtual contributions are combined in the Sudakov form factor [301,304] included in $P_{a\to bc}(z)$, which orders the emissions with respect to the evolution variable in such a way that it gives the probability that no emissions occur from a given Q'^2 to Q^2. The most commonly used evolution variables are the transverse momentum of the parton $b(c)$ relative to the direction of a, the virtuality of the splitting, and the angle between b and c. The showering scheme has the advantage that it can be applied to both initial state and final state partons. In modern MC generators, the initial state evolution starts at the scale of the process and evolves backward to the proton, thereby being called "backward evolution" [305]. The final state radiation concerns the outgoing partons of the hard subprocess. The parton starts at high energy and evolves losing it because of the radiation until it reaches the resolvable scale, then, giving way to the process of hadronization of partons.

Due to the renormalization scale dependence of α_s (Subsec. 2.4.4.2), at some scale of the order ~ 1 GeV, the evolution perturbation theory becomes invalid. The evolution of the event enters the non-perturbative regime and hadrons start to be formed as a consequence of color confinement. The current non-perturbative techniques are not easy enough to handle to be

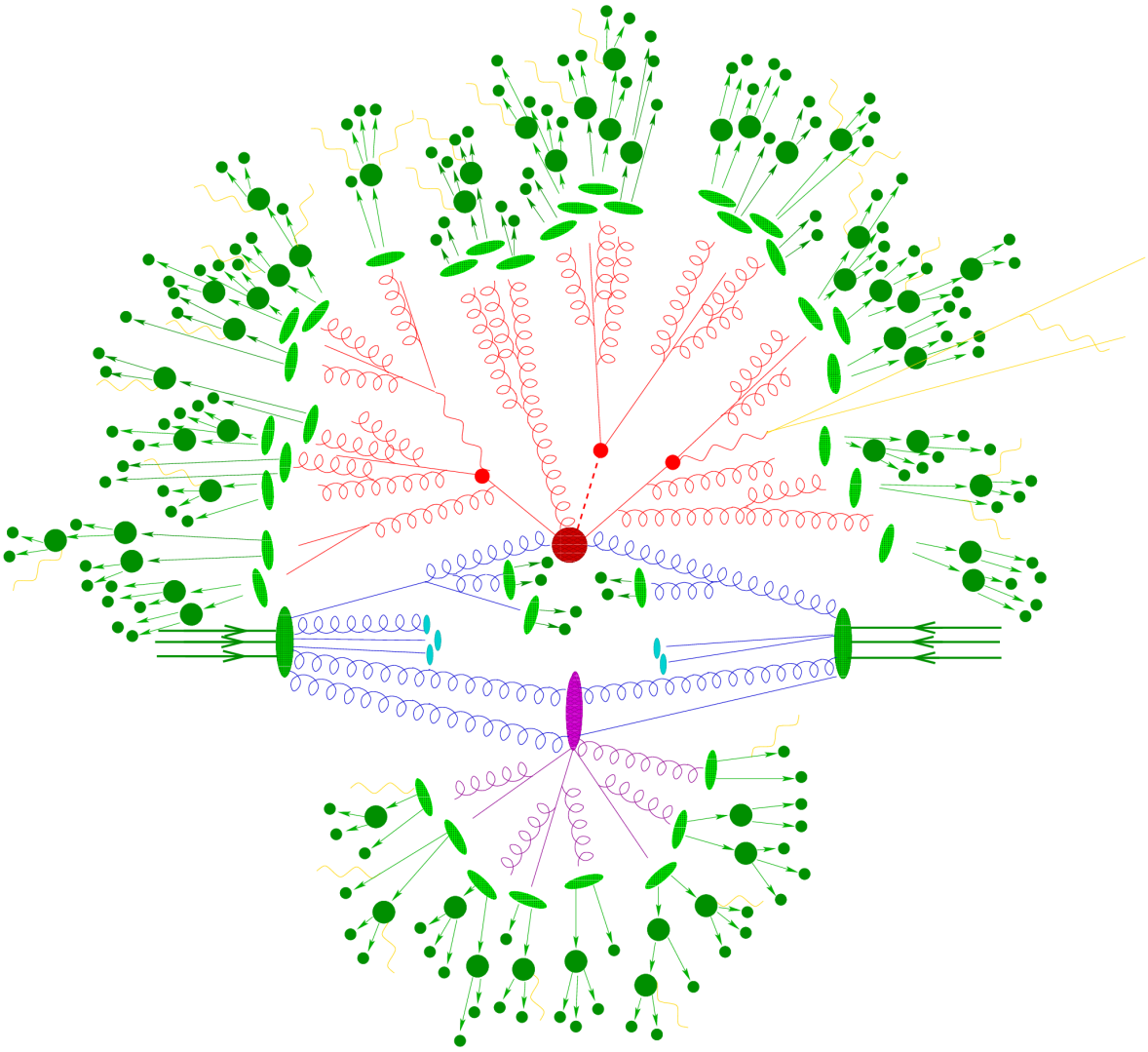

Figure 4.4: Sketch of a proton-proton collision as simulated by a MC event generator. The red blob in the center represents the hard collision, with red curly and straight lines representing the final state parton showers; the analogous objects in blue are the initial state parton showers. The purple blob and lines symbolize the underlying event. The hadronization process and its consequent decays are illustrated by light and dark green blobs [301, 302].

used for calculations, so the hadronization process is mostly described by phenomenological models. One of the available models is the so-called "string model" [306], which makes use of the linearity manifested (observed in lattice QCD simulations [307]) by the potential energy of two color charges with respect to their separation. The string is thought to be generated by a gluonic tube configuration that makes, for instance, that a quark and an antiquark attract each other. As the quark and antiquark move apart, the energy stored in the string grows, thus making favorable for the string to break at some point along its length. The string breaking can be regarded as the creation out of the vacuum of a new quark-antiquark pair, each one now connected to the respective original charged conjugated. This results in the continued fragmentation of the new strings into smaller pieces as long as they have enough energy, which brings about the emergence of multiple hadrons in the final state.

Another model used is the "cluster model" [308, 309], a model that is based primarily on the preconfinement properties of the QCD [310]. In the preconfinement stage, the partons can be clustered into color singlet proto-hadrons $q\bar{q}$ with masses independent of the scale of the hard process the partons underwent, being only sensitive to the fundamental QCD scale. Later, the clusters can be decayed isotropically into pairs of hadrons according to the corresponding density of states. After the hadrons have been formed in the event, they undergo subsequently decays into their possible decay channels.

The underlying event modeling is based on the need for characterizing the existence of an extra hadron activity that can not be described by the above-mentioned methods. It is formed by collisions that do not yield any relevant hard subprocess, such as multiple parton interactions and beam-beam remnants. The existence of such phenomena is one of the main causes of the enhancement of jet multiplicity in the event. For a more detailed description see [301].

The MC generators that currently exist tend to focus on one or a few of the elements described above. Some of them are listed below:

- PYTHIA [311] is a generator designed to handle a wide variety of processes within the SM and beyond. The program includes all the main elements of the event generation process that go from the hard scattering to the modeling of hadronization and the respective decays. It provides matrix element calculations for the hard subprocess at the basic LO precision. PYTHIA mostly relies on its powerful radiation model that is currently implemented on a p_T ordered dipole showering and includes initial and final state radiation. It incorporates a highly developed simulation of the multiple parton interactions as well as a model of hadronization using the Lund string approach.

- MADGRAPH5_AMC@NLO [312] is a generator mainly designed to automatically compute the matrix elements of multi-partonic final states, such as $2 \to n$ scatterings. The showering, the hadronization and the multi-parton interaction are not implemented in MADGRAPH5, therefore, it is commonly interfaced with PYTHIA for such purposes. The additional package AMC@NLO [313] allows for matrix element calculations at NLO accuracy and provides a method to match them to the parton showering.

- POWHEG [314,315] is a generator designed to produce calculations of the hard scattering subprocess at NLO accuracy. It employs a method to match the matrix element to the parton showers producing events with positive weights, a feature not present in other approaches such as that of AMC@NLO.

Finally, the last step in the process of event modeling within CMS is to make the generated processes (including the PU overlapping) pass through the detector response simulation. This constitutes a transition from the description of the events at generator level to the desired physical observables at detector level. The simulation of the CMS detector is carried out using the GEANT4 software [316]. The detector simulation comprises the detector geometry, the interaction of particles with the various materials, the effects of the magnetic field, the real conditions during the detector operation, the electronic readout, etc. With the detector response at hand, the events are reconstructed using the same algorithms used for real data, allowing for a consistent comparison between the data and the simulation.

Most of the aspects of the event reconstruction and simulation are generally integrated into a common framework called the CMS software (CMSSW) [317].

CHAPTER

5

STATISTICAL TREATMENT OF THE DATA AND PHYSICS ANALYSIS

Contents

Many of the reasons that motivate the existence of theories beyond the SM were already discussed in chapter 3. In particular, emphasis was placed on theories that partly or completely modify the Higgs sector, which is almost always accompanied by the inclusion of additional scalars in the field content of the theory. Among those, models containing a light boson (a) in the spectrum that can couple to the SM-like Higgs boson (h_{125}), arouse great

interest. If the a boson is light enough, decays of the form $h_{125} \to aa$ could take place, providing the model with a rich phenomenology in exotic Higgs decays. Searching for such possible exotic decays is the main objective of the work presented in this thesis.

After having gathered most of the necessary experimental and theoretical elements in previous chapters, this chapter is intended to describe the part concerning the analysis of the data obtained from the experiment. The first section focus on the main aspects of the statistical apparatus utilized to carry out the data analysis. All the concepts and methods that are reviewed throughout this section form an indispensable basis for extracting meaningful information out of the data. The second section comprises a general overview of the physics analysis, as well as a brief discussion on the impact that might have on some of the theoretical models introduced in Sec. 3.2. The third section is designed to give a detailed explanation of the search performed with the experimental data available. The section focus on the first approach adopted for the physics analysis, which primarily targets boosted event topologies, occurring for very light bosons. This analysis uses a set of selection cuts that maximize the signal-to-background ratio and exploits a 2D distribution of observables to extract the signal from the data. The analysis described in this last section has been published in the journal Physics Letters B [318].

5.1 Statistical Methods

5.1.1 Fundamental Concepts

There are various types of processes in physics that reveal an uncertain nature, that is, they cannot be predicted with complete certainty. This could be due to several reasons, such as the inaccurate reproduction of the phenomenon upon repetition, or because of intrinsic randomness of the process (like in QM). The degree of randomness that such processes evidence can be quantified with the concept of probability. An axiomatic definition of probability can be found in [319], where a real number $P(E)$ (called probability) is assigned to every subset of elements of a given sample space S. Three axioms define all the properties of probability [320]: $P(E)$ is non-negative, $P(\cup_{i=1}^{n} E_i) = \sum_{i=1}^{n} P(E_i)$, with E_i being disjoint subsets ($E_i \cap E_j = \emptyset$ for $i \neq j$), and $P(S) = 1$. The variable that represents each of the elements of the set S is called a random variable.

One of the most important theorems in probability theory is the Bayes' theorem, which makes use of the concept of conditional probability between to subsets A and B to formulate the following relation [321]

$$P(A|B) = \frac{P(B|A)P(A)}{P(B)}, \tag{5.1}$$

where $P(A|B)$ is the probability of A given B (conditional probability), and analogously for $P(B|A)$. It is often convenient to express $P(B)$ (or $P(A)$) as a linear combination of probabilities of disjoint subsets A_i that cover the whole S, giving then $P(B) = \sum_i P(B|A_i)P(A_i)$. That is called the law of total probability.

There are two main different interpretations of the concept of probability resulting in two distinct schools of thought: the frequentist and the Bayesian probabilities. The frequentist approach defines the probability as the fraction of the number of occurrences of an event over the total number of possible events, taking for granted that the experiment is repeatable and so is performed a large number of times [322, 323]. On the other hand, the Bayesian school

associates the elements of S with hypotheses that are either true or false, conferring to the concept of probability the capability of measuring the degree of belief that certain hypothesis is true [324–326]. In high energy physics, the most commonly used is the frequentist interpretation.

The elements of the set S can be discretely or continuously distributed, so the random variable x that represents them can take on both possible type of values. If a variable x only takes on discrete values x_i, for $i = 1, \ldots, N$, the probability to observe the outcome x_i can be expressed as

$$P(x_i) = f_i, \tag{5.2}$$

with $\sum_{i=1}^{N} f_i = 1$. This can be generalized for multidimensional continuous variables $\{\vec{x} = (x_1, \ldots, x_n) \in V \subseteq R^n\}$ by associating to each point $\vec{x}$ a real non-negative probability density function (p.d.f.) $f(\vec{x}) = f(x_1, \ldots, x_n)$. The probability to observe $\vec{x}$ in the region $A \subseteq V$ is

$$P(A) = \int_A d^n x f(x_1, \ldots, x_n). \tag{5.3}$$

The transition from the continuous to the discrete case can be done using Dirac's delta functions $\delta(\vec{x} - \vec{x}_0)$. The discussion of some other important concepts associated with probability distributions, such as cumulative distribution, quantile, marginal p.d.f., expectation value, variance, moment, covariance and correlation, skew and kurtosis, and many others can be obtain from the references [327–329].

5.1.2 Elements of Parameter Estimation

One of the most common situations that appear when dealing with statistical problems is that of having to estimate the defining parameters of a certain probability density function. Inferring the properties of an unknown p.d.f. by sampling the values of the random variables that obey such distribution is considered one of the central problems of statistics. The idea is to take a set of independent observations of the random variables (sample) and construct functions of the outcomes to estimate the parameters of the p.d.f. via the best fit [328]. Such a function of the data sample that returns the estimated value of the parameters is called an estimator.

There are several properties that are relevant to determine if an estimator is suitable for a specific problem. The consistency reflects the capability of the estimators to converge to the true unknown parameter values as the sample size tends to infinity. For the case of a one-parameter p.d.f., the above can be written as $\lim_{n\to\infty} P(|\hat{\theta}_n - \theta| < \varepsilon) = 1$, where n is the size of the sample, $\hat{\theta}_n$ is the estimator value of the parameter θ for a given sample, and ε is an infinitesimal. Being an estimator a function of the measured values, it is also a random variable, so it has an associated p.d.f. $g(\hat{\theta}, \theta)$ that, in principle, depends on θ [328]. From that, another important property of the estimators arises, the bias, which is defined by $b(\theta) = \langle\hat{\theta}\rangle - \theta$, with $\langle\hat{\theta}\rangle$ denoting the expected value of $\hat{\theta}$ obtained from $g(\hat{\theta}, \theta)$. The variance is also an important quality criterion for an estimator, and specifically, for consistent estimators, it gets a lower bound [330]. Some fairly well-known methods to obtain estimators are the sample mean, the sample variance, the least-squares method, and the method of moments [328]. But in particular, in high energy physics, the most frequently used is the method of maximum-likelihood.

The maximum-likelihood method is based on finding the estimators of the parameters

by maximizing the value of the likelihood function [331]. This method possesses very good statistical properties with regard to the indicators mentioned above [329]. Let $f(\vec{x};\vec{\theta})$ be the p.d.f. describing certain statistical model, depending on n random variables $(x_1,\ldots,x_n)$, and being parametrized by m parameters $(\theta_1,\ldots,\theta_m)$. Let N be the number of repeated measurements of the n random variables, yielding the sample $\mathbf{x} = \{(x_1^1,\ldots,x_n^1),\ldots,(x_1^N,\ldots,x_n^N)\}$. Assuming independent measurements, the likelihood function of the sample can be written as

$$L(\mathbf{x}|\vec{\theta}) = \prod_{i=1}^{N} f(x_1^i,\ldots,x_n^i;\theta_1,\ldots,\theta_m). \tag{5.4}$$

Then, the maximum-likelihood estimators $(\hat{\theta}_1,\ldots,\hat{\theta}_m)$ are defined as those values of the parameters which maximize the likelihood function [328]

$$\frac{L(\mathbf{x}|\theta_1,\ldots,\theta_m)}{\partial\theta_i} = 0, \;\; \{i=1,\ldots,m\} \qquad \Rightarrow \qquad (\hat{\theta}_1,\ldots,\hat{\theta}_m). \tag{5.5}$$

It is often practical to perform the maximization process through the logarithm of the likelihood function, as it greatly facilitates the calculations. That strategy is employed by the computer tool MINUIT [332], one of the most widely used numerical algorithms in high energy physics.

A peculiarity of dealing with physical events in the context of high energy physics is that sometimes the rate of the processes that produce such events is not known. This makes the total number of events (normalization) N behave as a random variable too, with distribution $p(N;\nu)$, so an additional term must be included in the likelihood function to estimate the parameter ν. The resulting likelihood function is known as the extended likelihood function $L(\mathbf{N},\mathbf{x}|\nu,\vec{\theta}) = p(N;\nu)L(\mathbf{x}|\vec{\theta})$ [333], where the sample has also been extended, being now the number $\mathbf{N}$ plus the N values $\mathbf{x}$. In most cases, the p.d.f. $p(N;\nu)$ is a Poisson distribution, whose parameter ν might or might not depend on the m unknown parameters $\vec{\theta}$. If the expected number of events ν is independent of the parameters $\vec{\theta}$, the estimated value is identical to the observed value $\hat{\nu} = N$. Otherwise, the extended likelihood only depends on the parameters $\vec{\theta}$, therefore, their estimators are going to be able to exploit the information from the augmented sample rather than merely the measurements $\mathbf{x}$, thus providing a more efficient estimation.

Very often, one faces the case where the data sample consists of two types of events, namely signal and background. On these occasions, the p.d.f. of the model is a linear combination of two distributions, one describing the signal events, and the other describing the background events

$$f(\vec{x};\nu_s,\nu_b,\vec{\theta}_s,\vec{\theta}_b) = \frac{\nu_s}{\nu_s+\nu_b} f_s(\vec{x};\vec{\theta}_s) + \frac{\nu_b}{\nu_s+\nu_b} f_b(\vec{x};\vec{\theta}_b), \tag{5.6}$$

where f_s and f_b are normalized to the unity. The number of signal (N_s) and background (N_b) events obey Poisson distributions with means ν_s and ν_b respectively. Having $N = N_s + N_b$ events, multiple situations can occur regarding the knowledge of the parameter values of both the signal and the background components, as well as of their corresponding normalizations.

So far, the discussion of the maximum-likelihood method has focused on continuous (referred to as unbinned or parametric) distributions only. However, in the case of a very large sample, the numerical calculation of the likelihood function may become unpractical. More-

over, the construction of multidimensional parametric p.d.f. models is really non-trivial when dealing with correlated random variables. That is the reason why it is often convenient to use binned distributions of the random variables, realized in histograms [334] containing information of the number of entries in each single bin. The expected number of entries in each bin ν_i is obtained by means of Eq. (5.3), performing the integration in a region A formed by a hyperrectangle (bin), and multiplying that probability by the expected number of total events ν. The resulting p.d.f. is given by

$$f(\vec{n};\vec{\nu}) = \prod_{i=1}^{B} \frac{\nu_i^{n_i}}{n_i!} e^{-\nu_i}, \tag{5.7}$$

where B is the total number of bins, and n_i is the observed number of entries for the bin i. The total number of events is $N = \sum_{i=1}^{B} n_i$, and the expected number of total events is $\nu = \sum_{i=1}^{B} \nu_i$. The histogram obtained is then considered as a single measurement of the B-dimensional random vector $\vec{n}$ [328], therefore, the extended likelihood function is the p.d.f. (5.7) itself.

Finally, and to make way to the next subsection, it is worth mentioning the topic of systematic and statistical uncertainties. It happens from time to time that the model introduced to estimate the values of the parameters $\vec{\theta}$ can not provide an accurate description of the measurements $\mathbf{x}$, not even using the best possible estimator. In practical situations, that may occur due to imperfections of the model caused by systematic effects, such as miscalibrations, inefficiencies, incompatibilities, and many others. A very straightforward way to improve the fitting is to introduce more parameters in the model, although these new parameters are not going to be of intrinsic interest. The name given to such elements is *nuisance parameters* $\vec{\mu}$ [329], and their incorporation into the likelihood function results in $L(\mathbf{x}|\vec{\theta},\vec{\mu})$. The inclusion of these new parameters may improve the fitting, but since they tend to be correlated with the parameters of interest $\vec{\theta}$, aside from increasing the parameter phase space, their presence can lead to larger statistical uncertainties for the estimates of $\vec{\theta}$. The statistical uncertainties are closely associated with the relation between the amount of data and the number of parameters. One way to reduce the impact of the nuisance parameters is to construct subsidiary measurements $\mathbf{y}$ (increase information about $\vec{\mu}$) that allow to constraint the nuisance parameter values [289]. If such a measurement is completely independent from the nominal one $\mathbf{x}$, the augmented likelihood function can be written as $L(\mathbf{x},\mathbf{y}|\vec{\theta},\vec{\mu}) = L_x(\mathbf{x}|\vec{\theta})L_y(\mathbf{y}|\vec{\mu})$. The augmented likelihood function is then profiled with respect to the nuisance parameters $\vec{\mu}$ [335], namely $L(\mathbf{x}|\vec{\theta}) = L(\mathbf{x}|\vec{\theta},\hat{\hat{\vec{\mu}}}(\vec{\theta}))$, where $\hat{\hat{\vec{\mu}}}(\vec{\theta})$ indicates the values of the nuisance parameters $\vec{\mu}$ that maximize the likelihood function for the specified $\vec{\theta}$. In high energy physics, the profile likelihood is widely used in the branch of statistical tests.

5.1.3 Confidence Level of Statistical Errors

In the previous subsection, the maximum-likelihood method was presented as a very effective way to estimate the parameters of a certain model. Once the parameters have been estimated, the next natural step would be to give some measure of the statistical uncertainty of the estimates. The reason behind it is that the estimators themselves also obey a certain distribution, that is, repeating the experiment many times would give different values for the estimates. So, in order to adequately report the estimated values for the parameters,

one should take into account the level of uncertainty (error) when taking the fitted values as reference.

One simple way of reporting the error of a given estimate is with the variance of the corresponding estimator [328]. Depending on the complexity of the case in question, the computation of the variance of estimators can be performed analytically, or using other methods like MC. In very complicated scenarios, the Rao-Cramér-Frechet inequality [330] can be used to provide a lower bound on the variance of the estimator. Another common method is the one that carries out a local Gaussian approximation of the likelihood function [329], based on the fact that $L(\mathbf{x}|\vec{\theta})$ can be approximated to a multivariate Gaussian distribution in the limit of large number of events [336]. In this approximation, the estimator of the covariance matrix takes the form

$$(\widehat{C^{-1}})_{ij} = -\frac{\partial^2 \ln L(\mathbf{x}|\vec{\theta})}{\partial\theta_i \partial\theta_j}\bigg|_{\vec{\theta}=\hat{\vec{\theta}}}, \tag{5.8}$$

so the estimated variance for the parameter estimate $\hat{\theta}_i$ would be given by $\hat{\sigma}_{\hat{\theta}_i} = \sqrt{\widehat{C}_{ii}}$. An equivalent approach is to expand the log-likelihood function in Taylor series about the estimates $\hat{\vec{\theta}}$ up to second order (a parabola, as in the Gaussian case), and estimate the variances from the contour formed by values of $\vec{\theta}$ fulfilling [329]

$$\ln L_{\max} - \ln L(\vec{\theta}) = \frac{1}{2}. \tag{5.9}$$

This last procedure provides for a given estimate, in general, asymmetric errors $\theta = \hat{\theta}\,{}^{+\Delta\hat{\theta}_+}_{-\Delta\hat{\theta}_-}$, called negative and positive uncertainties respectively, whereas the local Gaussian approximation gives symmetric errors $\theta = \hat{\theta} \pm \hat{\sigma}_{\hat{\theta}}$.

The above suggests that, in this context, the statistical errors are interpreted (independently of the p.d.f.) as the standard deviation of the distribution of the estimates. However, none of those methods guarantees an exact coverage of the statistical errors. A more appropriate treatment of the statistical uncertainties lies within the framework of confidence intervals [337]. The method relies on the knowledge of the distributions of the estimators $g(\hat{\vec{\theta}}; \vec{\theta})$, which depends on the true parameter values $\vec{\theta}$. As already mentioned, the p.d.f. of $\hat{\vec{\theta}}$ can be obtained in simple cases by means of analytic calculations or MC studies, but the real advantage lies in the fact that knowing the values of $\vec{\theta}$ allows knowing the p.d.f. of $\hat{\vec{\theta}}$. For a single-parameter distribution $g(\hat{\theta}; \theta)$ (for simplicity), one can construct the probabilities α and β to observe $\hat{\theta} \geq u_\alpha$ and $\hat{\theta} \leq v_\beta$ for a fixed value of θ respectively, where u_α and v_β are functions of the true parameter θ defined as [328]

$$\alpha = P(\hat{\theta} \geq u_\alpha(\theta)) = \int_{u_\alpha(\theta)}^{\infty} d\hat{\theta}\; g(\hat{\theta}; \theta), \qquad \beta = P(\hat{\theta} \leq v_\beta(\theta)) = \int_{-\infty}^{v_\beta(\theta)} d\hat{\theta}\; g(\hat{\theta}; \theta). \tag{5.10}$$

For fixed α and β, one can determine the behavior of the two functions $u_\alpha(\theta)$ and $v_\beta(\theta)$ by scanning the parameter space allowed for θ. These two curves form a region in the $\hat{\theta} - \theta$ plane called the confidence belt. Regardless of the value of θ, the probability of $\hat{\theta}$ to be inside the belt is $P(v_\beta(\theta) \leq \hat{\theta} \leq u_\alpha(\theta)) = 1 - \alpha - \beta$, which, inverting the functions $u_\alpha(\theta)$ and $v_\beta(\theta)$,

yields

$$P(a(\hat{\theta}) \leq \theta \leq b(\hat{\theta})) = 1 - \alpha - \beta, \tag{5.11}$$

where the functions $a(\hat{\theta})$ and $b(\hat{\theta})$ can now be evaluated with the value of the estimate. The resulting two values determine the so-called confidence interval $[a, b]$ at the confidence level $1 - \alpha - \beta$. Such interval would contain the true parameter value θ in a fraction $1 - \alpha - \beta$ of the total number of times the experiment is repeated. The choice of the probability pair α and β is in accordance with the type of confidence interval desired; for instance, central intervals, one-sided intervals, or two-sided intervals [328]. One particular case is that of the upper limits, for which one takes the probability $P(\theta \leq \theta_{up}) = 1 - \beta$. The most commonly used confidence level value in high energy physics is 95%.

Probably the greatest difficulty of using this method is the fact that the p.d.f. $g(\hat{\theta}; \theta)$ has to be known, which is only plausible in very few cases. Nevertheless, in many ordinary cases, the approximation of a Gaussian distribution perfectly works, which leads to very straightforward estimations of the confidence intervals (e.g., at 68% confidence level, the interval $\theta = \hat{\theta} \pm \hat{\sigma}_{\hat{\theta}}$ is covered). On other occasions, where the approximation is not good enough in the first instance, a process of gaussianization is carried out with the help of a new estimator [328]. Even in the case of a non-Gaussian estimator, under fairly general conditions and in the large sample limit, the maximum-likelihood estimators are going to obey a multivariate Gaussian distribution, transferring to the likelihood function the Gaussian shape. Then, it can be shown [289], analogously to Eq. (5.9), that a multivariate confidence region can be formed by values of $\vec{\theta}$ (m-dimensional) defining the contour

$$\ln L_{\max} - \ln L(\vec{\theta}) = \frac{F^{-1}_{\chi^2_m}(1 - \alpha)}{2}, \tag{5.12}$$

with $F^{-1}_{\chi^2_m}(1 - \alpha)$ being the chi-square quantile of order $1 - \alpha$ for m degrees of freedom, and $1 - \alpha$ representing the confidence level that the true vector $\vec{\theta}$ is contained within that region. In addition to those methods, there is another procedure [338] based on a statistical test called likelihood ratio (see Subsec. 5.1.4), which assumes that the true parameters' values are $\vec{\theta}$. The values of $\vec{\theta}$ for which the hypothesis is rejected with size α or less are excluded, while the remaining values make up the confidence region at level $1 - \alpha$.

5.1.4 Testing Statistical Hypotheses

A key task in most of the physics measurements is to discriminate between two or more hypotheses, basing the judgment on the agreement of the observed experimental data with one of them. The objective of a statistical test is to provide a quantitative way to help make the decision and draw conclusions. One example of testing the validity of certain hypotheses is to check whether the observed data originate only from SM background processes, or if they also contain events coming from physics beyond the SM, as it happens in the context of this thesis.

When performing a statistical test, the hypothesis under consideration is traditionally called the null hypothesis H_0, which can be assigned, for instance, a p.d.f. $f(\vec{x})$ of the random variables $\vec{x}$. Testing the hypothesis H_0 and drawing conclusions on it usually involves a comparison with one or more alternative hypotheses $H_1, H_2, \ldots$ [327], specified by probability density functions $f(\vec{x}|H_i)$, for a given H_i. In order to quantify the level of agreement of

a certain hypothesis with the data, a test statistic $t(\vec{x})$ that obeys the p.d.f. $g(t|H_i)$ is constructed and evaluated in the observed data $\vec{x}_{\rm obs}$. This test statistic could be given as a multidimensional quantity, however, due to the frequently limited amount of data, defining a scalar function turns out to be more convenient. The decision whether to accept or reject the null hypothesis H_0 is made by defining the so-called critical region for t, chosen in such a way that the probability to observe t there is α, where α is defined as the significance level of the test. But even so, the critical region is not uniquely defined, so its selection is based on the possible alternative hypotheses. Considering only one alternative hypothesis H_1, the decision boundary of the critical region could simply be a cut $t_{\rm cut}$ applied to the test statistic. Then, the value $\alpha = \int_{t_{\rm cut}}^{\infty} dt\, g(t|H_0)$ gives the probability to reject H_0 if H_0 is true, whereas $\beta = \int_{-\infty}^{t_{\rm cut}} dt\, g(t|H_1)$ is the probability to accept H_0 if H_1 is true [289]. The magnitude $1-\beta$ quantifies the power of the test with respect to the alternative H_1 for a given significance level α. In principle, the optimal test statistic would be the one that achieves the best possible separation of the distributions of t for H_0 and H_1. A lemma due to Neyman and Pearson [320, 339] states that the maximum power for a given probability α is provided by the likelihood ratio

$$t(\vec{x}) = \frac{f(\vec{x}|H_1)}{f(\vec{x}|H_0)}, \tag{5.13}$$

with the critical region defined as $t(\vec{x}) > c$, where c is a constant whose value is determined by α. If the observed data $\vec{x}_{\rm obs}$ falls into the critical region, the hypothesis H_0 is rejected. In high energy physics, the value of c (or $t_{\rm cut}$) is sometimes not completely fixed to allow for a large flexibility in the selection criterion. This allows meeting certain particular needs according to the required proportion of the so-called true and false positive rates, rather known in this field as selection efficiency and misidentification probability respectively.

The most problematic aspect of Eq. (5.13) is that it can be really difficult in practice to know the form of the multidimensional p.d.f.s $f(\vec{x}|H_0)$ and $f(\vec{x}|H_1)$, as they might depend on hundreds of discriminating variables. Then, one has to resort to MC methods to generate events that follow the p.d.f.s, and perhaps use multidimensional histograms to represent such distributions [328]. However, as the number of dimensions gets larger, the number of bins needed to construct the multidimensional histograms increases dramatically. For instance, having b bins for each of the n variables will lead to b^n total bins, which, for large n and relatively reasonable b, requires a huge amount of data in order to fill each of them. This exponential growth for the amount of the data needed with respect to the number of dimensions is associated with the phenomenon known as the curse of dimensionality [340]. So, in practice, the most common approach is to proceed by applying multiple cuts (cut-based) on some components of $\vec{x}$, and use one or a few powerful discriminating variables to construct the test statistic. But nowadays, more powerful and sophisticated classification methods in comparison to the rectangular cut selection have been developed: the so-called multivariate classification algorithms (MVA) [341]. From the statistical point of view, these methods consist in making an ansatz for $t(\vec{x})$ (e.g., linear function), so that it depends on fewer parameters, and then adjust the parameters to obtain the best possible separation between $g(t|H_0)$ and $g(t|H_1)$. The way to achieve so is closely related to what is called pattern recognition [342], which uses information from the statistical distributions to optimally assign a definite class type to the events. For instance, in experimental particle physics, two assignments could be used for events depending on whether they belong to signal events or background events.

The performance of the classification algorithm carrying out the task of deciding whether the event is signal-like or background-like can be estimated from the receiver operating characteristic (ROC) curve, which basically encodes the relation between the signal efficiency and the background rejection. Similarly to t_{cut}, choosing a particular point on the ROC curve corresponds to a definite selection of the proportion of signal and background events. In order to efficiently determine such decision boundary, a large variety of existing algorithms are subject to training using events known to pertain to specific classes. This supervised training is known as machine learning [343, 344]. Several algorithms are currently available: projective likelihood estimation, k-nearest neighbor, Fisher linear discriminant, artificial neural networks, support vector machines, (boosted) decision trees, and many more [329]. In this thesis, the method of boosted decision trees (BDT) implemented in the TMVA package [345] of ROOT [346] is utilized.

Often one is interested in tests that reflect the level of agreement between the data and H_0 without specific reference to any H_1. To quantify this level of agreement, a significance test (goodness-of-fit) of the hypothesis H_0 is constructed [289, 347]. The significance of a possible discrepancy is measured with the p-value, defined as the probability to find the statistic t in the region of equal or lesser compatibility with H_0 than the level observed with the data

$$p = \int_{t_{\text{obs}}}^{\infty} dt\; g(t|H_0), \tag{5.14}$$

where t_{obs} is the observed value of the statistic. Saying that a given data have less compatibility with H_0 implies that it has more compatibility with some alternative hypothesis. So, in this context, the hypothesis H_0 is rejected if the data are found in the critical region $p \leq \alpha$. One of the most common practices is to convert the p-value into an equivalent significance $Z = \Phi^{-1}(1-p)$, where Φ is the cumulative standard Gaussian distribution; then, a significance of $Z = 5$ (i.e. a 5σ effect) corresponds to a p-value of 2.87×10^{-7}. The previous definition is frequently used to quantify the expected sensitivity one would obtain with certain measurements under the assumption of different hypotheses.

In particle physics, most of the time, the parameter of interest is the cross-section of the signal process (or other proportional to this, denoted as μ), but almost always its measurement has associated nuisance parameters $\vec{\nu}$, whose values are unknown and have to be obtained from a fit[1] to the data [348]. In order to overcome that difficulty, the test statistic $t(\mu)$ is defined in such a way that its p.d.f. is independent of the nuisance parameters. A very good approximation to accomplish that goal is obtained from the so-called profile likelihood ratio

$$\lambda(\mu) = \frac{L(\mu, \hat{\hat{\vec{\nu}}})}{L(\hat{\mu}, \hat{\vec{\nu}})}, \tag{5.15}$$

where $L(\mu, \hat{\hat{\vec{\nu}}})$ is the profile likelihood (Subsec. 5.1.2), and $L(\hat{\mu}, \hat{\vec{\nu}})$ is the global maximum-likelihood, with $\hat{\mu}$ and $\hat{\vec{\nu}}$ being its estimators. The quantity $\lambda(\mu)$ is defined so that it can take values $0 \leq \lambda(\mu) \leq 1$, with higher values indicating greater compatibility between the data and the hypothesized value of μ. It is convenient to use instead the statistic $t(\mu) = -2\ln\lambda(\mu)$, which, according to a theorem from Wilks [349], approaches a χ^2 distribution in the large

[1] The increased flexibility offered to the model by the introduction of nuisance parameters leads to a loss of sensitivity.

sample limit under certain conditions. The advantage of this statistic is that its asymptotic distribution is independent of $\vec{\nu}$. However, in practice, the amount of data is limited, so the asymptotic behavior is not exact and, therefore, there exits a small dependence. For models where μ has to be necessarily non-negative, an alternative definition of $t(\mu)$ can be used [348]

$$\tilde{t}(\mu) = \begin{cases} -2\ln\frac{L(\mu,\hat{\hat{\vec{\nu}}}(\mu))}{L(0,\hat{\hat{\vec{\nu}}}(0))} & \hat{\mu} < 0 \\ -2\ln\frac{L(\mu,\hat{\hat{\vec{\nu}}}(\mu))}{L(\hat{\mu},\hat{\hat{\vec{\nu}}}(\mu))} & \hat{\mu} \geq 0 \end{cases}, \tag{5.16}$$

where a explicit dependence of the nuisance parameters with respect to μ has been emphasized. After having constructed the test statistic $\tilde{t}(\mu)$, the level of disagreement of the hypothesized value of μ can be quantified with the p-value of its distribution.

Two important special cases of the previous statistic $\tilde{t}(\mu)$ can be identified. The first instance is when aiming for the discovery of a positive signal, for which the hypothesis that undergo testing is $\mu = 0$ (background-only hypothesis). If the $\mu = 0$ hypothesis is rejected, a new signal might have been discovered. The test statistic for this case then reads ($q_0 \equiv \tilde{t}(0)$)

$$q_0 = \begin{cases} 0 & \hat{\mu} < 0 \\ -2\ln\frac{L(0,\hat{\hat{\vec{\nu}}})}{L(\hat{\mu},\hat{\vec{\nu}})} & \hat{\mu} \geq 0 \end{cases}. \tag{5.17}$$

Large q_0 means increasing incompatibility between the data and the $\mu = 0$ hypothesis, and the significance of such discrepancy is given by the approximate asymptotic equation $Z_0 = \Phi^{-1}(1 - p_0) = \sqrt{q_0}$ [348]. An apparently statistically significant observation may arise when looking for a signal in a very broad region without specifying in advance the location of the signal. This phenomenon is known as the look-elsewhere effect and must be treated carefully [350]. The second relevant case is the one dedicated to establishing an upper limit on the strength parameter μ. The hypothesis to test is that of a signal with a given μ (signal-plus-background hypothesis), and the corresponding test statistic $\tilde{q}_\mu \equiv \tilde{t}(\mu)$ (for $\mu \geq 0$) is [348]

$$\tilde{q}_\mu = \begin{cases} 0 & \hat{\mu} > \mu \\ -2\ln\frac{L(\mu,\hat{\hat{\vec{\nu}}}(\mu))}{L(\hat{\mu},\hat{\hat{\vec{\nu}}}(\mu))} & 0 \leq \hat{\mu} \leq \mu \\ -2\ln\frac{L(\mu,\hat{\hat{\vec{\nu}}}(\mu))}{L(0,\hat{\hat{\vec{\nu}}}(0))} & \hat{\mu} < 0 \end{cases}, \tag{5.18}$$

where the occurrence of data fluctuating upward ($\hat{\mu} > \mu$) is dismissed. As with the case of discovery, the level of agreement between the data and the supposed value of μ is measured with the p-value. The values of μ not rejected during such a test of size α ($p_\mu > \alpha$) constitute a confidence interval (upper limit) with confidence level $1 - \alpha$. However, there are some regions of the parameter space, specially those with small μ, where the distribution of the statistic being used is almost identical under the signal-plus-background hypothesis and the background-only hypothesis. This type of situation corresponds to cases to which one has little or no sensitivity, so it is questionable whether such parameter values should be regarded

as disfavored. By construction, the probability to reject μ if μ is true is α and, since both statistic distributions are very similar, the probability to reject μ if $\mu = 0$ is true (the power $1 - \beta$) is only slightly greater than α. So, there is a probability of value just above α to exclude models that should not be excluded. One way of avoiding this spurious exclusion is by using the $\mathrm{CL_s}$ procedure [351], which is based on the quantity

$$CL_s = \frac{p_\mu}{1 - p_b}, \tag{5.19}$$

where p_b is the p-value of the background-only hypothesis. The signal-plus-background hypothesis is then rejected if $CL_s \leq \alpha$. Apart form this observed upper limit on the parameter μ, it is common to provide as well the expected exclusion limit, i.e. the values of μ that can be excluded if the signal is in fact absent. The procedure is very similar to that of the observed limit, but instead of the actual data, an Asimov dataset generated with the MC toy method under the background-only hypothesis is used [348, 352]. By means of this, the median and the uncertainty bands ($\pm 1\sigma$ and $\pm 2\sigma$) for the expected signal strength are computed. The actual data might contain statistical fluctuations, hence the reason why, in general, the observed median will not be equal to the expected median.

Most of the statistical calculations presented in the context of this thesis were performed with the Combine Tool package, developed by the LHC Higgs combination group [352, 353]. Other excellent implementations of the different statistical methods, like the RooStats toolkit [354], are also available.

5.2 Search for Light Bosons in Exotic Decays of the 125 GeV Higgs Boson

As discussed in Sec. 3.2, there is a wide variety of models that predict an extended scalar sector, which certainly has the 125 GeV state h_{125} included in its mass spectrum. In such context, there exist scenarios where a light boson a, namely with $2m_a < 125$ GeV, can be produced from decays of the SM-like Higgs. Exploring the existence of such light bosons using direct production modes tends to be highly limited, as in most models the couplings of a to SM fermions are significantly reduced by a small parameter so that the SM-nature of the particles involved is not spoiled. For instance, in the case of the "dark-photon" model (Subsec. 3.2.3), the parameter of reference is χ, whose smallness guarantees that the mass of the SM Z boson remains almost unaffected. On the other hand, in the 2HDM+S (Subsec. 3.2.5), the parameter θ_a controlling the amount of mixing must be tiny in order to keep the SM Higgs couplings nearly untouched. The same happens in models with additional singlets, where the mixing parameter is preferred to be small to maintain the alignment limit (Subsec. 3.2.2), and also in the case of little Higgs, where the symmetry breaking scale parameter suppresses the couplings of the light bosons to fermions (Subsec. 3.2.4). For this reason, searches for the a boson via the decay of the 125 GeV Higgs become immensely favored, as the relevant quantities in the decays $a \to f\bar{f}$ are the branching ratios ($\mathcal{B}$), which do not depend on the tiny parameters[2], unlike the production cross-section. That is additionally motivated by the fact that the current upper limit for the $\mathcal{B}$ of h_{125} decaying into non-SM particles is about 34% [355], undoubtedly a non-negligible value for the presumed $h_{125} \to aa$ exotic decay.

[2]The given parameter is common for all the partial decay widths, so it does not appear in the $\mathcal{B}$s.

For the scenarios where the a boson is very light ($m_a \lesssim 20$ GeV), the leptonic channels $a \to l\bar{l}$, to which are attributed very clean signatures in the detectors, become of special importance when searching for possible a decays. Furthermore, the leptonic $\mathcal{B}$s may be also considerably large for $m_a > 20$ GeV in some regions of the parameter phase-space of the models. There are models in which a specific leptonic mode could even dominate over other types of decays. That is the case, for example, of the Type-III 2HDM+S for large $\tan\beta$, where the $a \to \tau\tau$ dominates across the entire (kinematically allowed) mass range of the a boson [12]. The study presented in this thesis primarily focuses on a search for very light bosons in the decay channel $h_{125} \to aa \to 4\tau$, supplemented with possible events coming from the $h_{125} \to aa \to 2\mu 2\tau$ channel that enter the selection. The study is an update of a similar search performed by the CMS collaboration in the Run 1 phase [356]. It also complements several searches for light bosons performed by the CMS and ATLAS collaborations in different final states ($2\tau 2b$, $2\mu 2b$, $2\tau 2\mu$, 4μ, $2\gamma 2g$, 4γ, $4b$, $4e$ and $2e2\mu$) and covering distinct mass ranges during the Run 1 and Run 2 phases [357–369].

The results from this search could be interpreted in the context of several models, as it was discussed in Sec. 3.2. However, the $h_{125} \to aa \to 4\tau$ channel offers much greater potential for the 2HDM+S, compared to the rest of the mentioned possibilities. Models like the dark photon benefits more from other decay channels (4μ, $2e2\mu$ and $4e$) possessing almost identical $\mathcal{B}$s, and with a spectacular reconstruction at detector level, thus being way more sensitive to this model than the 4τ channel [362, 368, 370]. In the case of both the model with extra scalars and the little Higgs model, for m_a above the b-quark pair threshold, the $4b$ and the $2\tau 2b$ channels can easily surpass the 4τ channel, and for masses below that limit, decay modes like the $4c$ and the $2\tau 2c$ are way more promising [12, 219]. On top of that, the combination of experimental results from precision tests and other types of searches applied to those models allows excluding regions of the parameter space far beyond the reach of this work. That is the reason why this analysis mainly examines the case of the 2HDM+S, which has not been sufficiently probed yet. Having said that, it is necessary to clarify that the final results that are going to be presented will be fundamentally linked to this particular model. This is because, in order to perform the combination of the two channels, some assumptions are made regarding the relation of their decay widths (see Eq. (5.20)), which are not always true for all types of models. Aside from that, the search is performed on a completely model-independent basis. Henceforth, the notation a_1 refers to the mostly-singlet-like-pseudoscalar of the 2HDM+S.

5.2.1 Analysis Strategy

In decays of the form $h_{125} \to a_1 a_1$ with relatively light pseudoscalars, the a_1 are produced with a large Lorentz boost, given the mass difference between these particles and the 125 GeV state. The smaller the mass of the light boson, the larger the velocity of the two a_1 particles in the rest frame associated with h_{125}. In addition to this boosting, related to the decay of the h_{125}, there might be other sources that generate a large momentum for the h_{125} itself, this time taking the laboratory system as reference. For the dominant ggF process (Subsec. 3.1.1.2), an unbalanced momentum along the z-axis induced by a big difference in the momentum fractions of the colliding partons can lead to a very high p_z for the Higgs. Besides, an event of initial state radiation triggering a hard gluon splitting on one of the partons could produce a Higgs with a large transverse momentum p_T. All these sources of

boosting cause the decay products of the a_1 bosons to be highly collimated, giving rise to nearly overlapped fermion signatures in the CMS detector. The very high performance of the reconstruction of muons in CMS allows resolving such complicated topologies for the case of the $a_1 \to \mu\mu$ decay mode. However, for the case of $a_1 \to \tau\tau$ decays, the situation is more complicated since the HPS algorithm (Subsec. 4.3.1.6) would not be able to efficiently identify individual hadronic taus, due to the presence of additional components belonging to the second τ lepton. That would also require the development and use of special triggers to select those events, which becomes highly impractical within the current CMS program and context. That is why, in this analysis, a special strategy meant to identify such collimated di-tau topologies is designed.

The main idea is to consider the τ decay modes involving only one charged particle and any number of neutral particles. These decay modes account in total for a larger branching fraction compared to the purely hadronic decays that the reconstruction algorithm uses, as it can be seen in Tab. 4.1. Then, one of the τs coming from the pseudoscalars can be identified by its muonic decay, while the other can be identified via its one-prong (charged lepton or one-prong charged hadron) decay, yielding the signature $a_1 \to \tau_\mu \tau_{\text{one-prong}}$. Such decays can be recognized in the detector by the presence of one reconstructed muon surrounded by an opposite-charge reconstructed track. That choice also allows identifying the $a_1 \to \mu\mu$ decay without any trouble. The above-described topology is illustrated in Fig. 5.1. The figure shows a_1 bosons well separated in the η-ϕ plane, a case that corresponds to the main production mechanism (ggF), in which the h_{125} tends to be produced with relatively small p_T. The analysis mainly targets the ggF process but also includes contributions from VBF, VH (WH and ZH), and ttH. Besides, in the sketch of Fig. 5.1, the presence of two same-charge muons originating from different a_1 bosons is observed, which constitutes an essential requirement in the selection, as it is one of the most effective ways to suppress background events.

5.3 Analysis Using Cut-Based Approach

This analysis covers the mass range corresponding to $4 \leq m_{a_1} \leq 15$ GeV, for which the pseudoscalars are expected to be produced with a large boosting, especially for the lower masses. The lower limit of the mass interval is selected to account for masses near the τ pair threshold occurring at $m_{a_1} \approx 3.6$ GeV, whereas the upper limit is based on the substantial loss of signal acceptance for higher mass values. In this first approach, a selection of rectangular cuts applied to the various variables, and optimized for the mass range probed has been used. Most of the adopted values for these cuts are due to exclusive studies to maximize the sensitivity of the analysis. The final discriminant in the final selected sample of events consists of a 2D distribution of variables with strong separation power between the signal and the background. These and other aspects of the analysis will be discussed in detail below.

5.3.1 Simulated Samples

The signal ggF production process is modeled with the general-purpose MC event generators (Subsec. 4.3.2) Pythia (v.8.212) and MadGraph5_aMC@NLO (v.2.2.2) for the decay channels $h_{125} \to a_1 a_1 \to 4\tau$ and $h_{125} \to a_1 a_1 \to 2\mu 2\tau$ respectively. In both channels, the p_T distribution of the h_{125} is corrected with the help of the program HqT (v.2.0) [371] interfaced with the NNLO NNPDF3.0 parton distribution functions [297], which accounts for

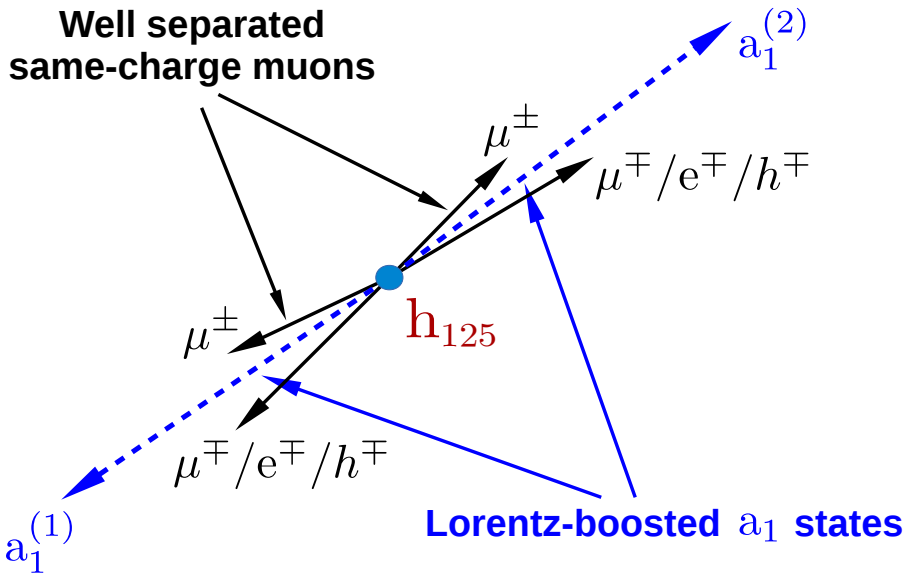

Figure 5.1: Sketch representing the signal topology. The 125 GeV Higgs boson decays into two a_1 pseudoscalar bosons, with the consequent decay of one of the pseudoscalars into a pair of τ leptons, and the decay of the second a_1 into a pair of τ leptons or a pair of muons. The final state considered is formed by one muon and an oppositely charged particle (μ, e or h) in each a_1 leg.

higher precision by means of resummation techniques at next-to-next-to-leading logarithmic order. The contributions from the rest of subdominant processes (VBF, VH, and ttH) are estimated using Pythia. For each signal process, samples corresponding to mass points from 4 to 15 GeV with a step of 1 GeV have been produced.

The main SM background processes have also been modeled with general-purpose MC generators. In the case of multi-jet events coming from QCD processes, event samples containing at least one muon have been generated with the Pythia generator. The background events arising from $t\bar{t}$ and single-top production are simulated at NLO using the PowHeg (v.2.0) event generator interfaced to Pythia. The inclusive production of Z and W vector bosons (W/Z+Jets) is simulated with MadGraph5_aMC@NLO interfaced to Pythia. Events from electroweak di-boson production (WW, WZ, and ZZ) are generated using Pythia as well.

5.3.2 Event Selection

The main objective of the event selection is to efficiently identify the four final objects (two muons and tow charged particles) while keeping low the background rate. That is achieved by an appropriate choice of the online (trigger) and offline event selection strategies. As explained in Subsec. 4.2.7, triggers are designed to keep as many events of interest as possible, reducing at the same time the background contribution, and keeping the rate at an acceptable level. According to the discussion on the signal topology (Subsec. 5.2.1), the

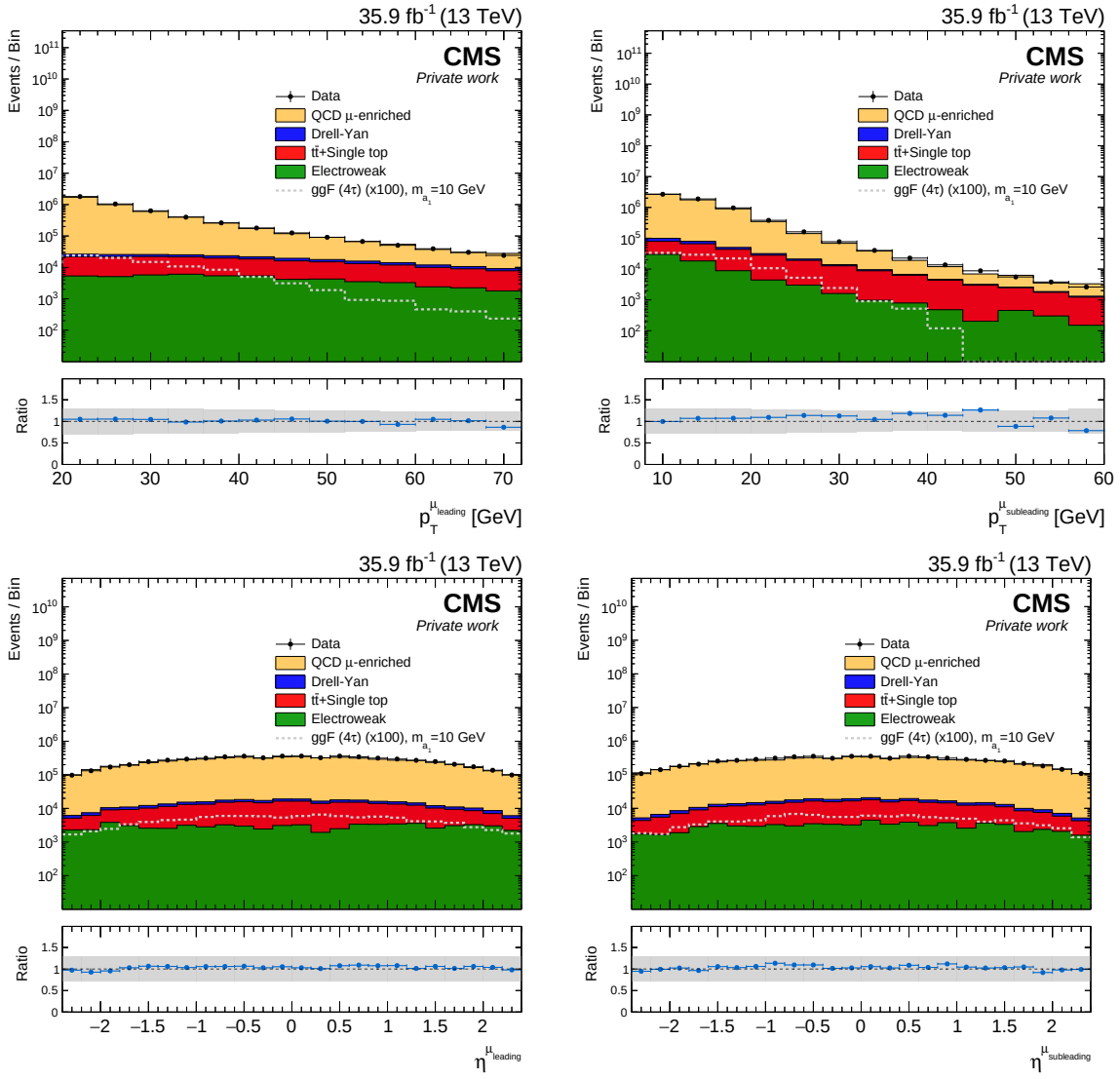

Figure 5.2: Distributions of p_T (upper) and η (lower) in the same-charge di-muon sample for both leading (left) and subleading (right) muons. The data (dots) is compared with the SM background expectation obtained from simulation (histograms). The contributions from inclusive production of Z and W vector bosons (W/Z+Jets) and electroweak di-boson production (WW, WZ, and ZZ) have been summed up into a single category ("Electroweak"). The dashed histogram is the distribution of the signal in the $h_{125} \to a_1 a_1 \to 4\tau$ channel for $m_{a_1} = 10$ GeV, which is normalized according to the benchmark scenario described in the text. The signal has further been scaled ($\times 100$) to better see the full distribution.

signal events of the main 4τ channel are expected to have relatively soft muons since they emerge from τ decays. Muonic τ decays always involve two neutrinos (Tab. 4.1), which tend to carry away most of the τ momentum. On the other hand, the boosting of a_1 pseudoscalars leads to great proximity between the muon and the one-prong candidate. So, the standard triggers using isolated leptons with relatively large p_T thresholds would not be able to keep a considerably good acceptance of signal-like events. In order to overcome that difficulty, a

same-charge di-muon trigger without isolation requirements on muons, and with p_T thresholds of 17 GeV and 8 GeV for the leading (higher p_T) and the subleading muon respectively, is used to select the events. Additionally, the trigger only selects pairs of muons that have the same charge, which collaborates suppressing background events coming from $t\bar{t}$, Drell-Yan and di-boson productions. On top of that, the HLT requires the tracks of the two muons to have points of closest approach to the beam axis within 2 mm of each other along the longitudinal direction.

Regarding the offline selection, the analysis uses well-reconstructed muons and high purity reconstructed tracks (charged PF candidates) as main physics objects (Subsec. 4.3.1). In correspondence with the trigger choice, the events must contain at least two same-charge muons fulfilling the following requirements:

- The p_T of the leading (subleading) muon must exceed 18 (10) GeV.
- The pseudorapidity of both muons must be $|\eta| < 2.4$.
- The transverse (longitudinal) impact parameters of the muons with respect to the PV must be $|d_\perp| < 0.05$ ($|d_z| < 0.1$) cm.
- The distance between the muons in the η-ϕ plane must be $\Delta R = \sqrt{(\Delta\eta)^2 + (\Delta\phi)^2} > 2$.

The first requirement is intrinsically related to the trigger p_T thresholds, which have to be exceeded in a reasonable amount (close to the efficiency curve plateau) to maintain a good trigger efficiency. The second condition is due to the pseudorapidity coverage of the CMS detector, which, for some subdetectors like the tracker and muon system, is about $|\eta| \sim 2.4$ (Subsecs. 4.2.3 and 4.2.6). The cuts on the impact parameters of the muons are designed to suppress those background events in which a heavy-flavor hadron decays into a muon and several charged particles, resulting in a displaced secondary vertex. The last requirement has to do with the already mentioned fact that, in the ggF process, the h_{125} is produced with relatively small p_T, thus having the decay products of the pseudoscalars large angular separation. After imposing those requirements, if more than one same-charge muon pair in the event is found to satisfy them, the pair with the largest $p_T^{\text{Sum}} = p_T^{\mu_1} + p_T^{\mu_2}$ is chosen. Some of the kinematic distributions (p_T and η) of the two muons after this selection can be seen in Fig. 5.2. For the drawing of these plots, and throughout this section, a benchmark value of the branching fraction $\mathcal{B}(h_{125} \to a_1 a_1)\mathcal{B}^2(a_1 \to \tau\tau) = 0.2$ is assumed, as well as that the h_{125} production cross-section is the one predicted in the SM. As seen from the plots, in this di-muon sample the dominant contribution is that from QCD multi-jets, which constitutes $\sim 95\%$ of the total background. A simulation-based study, designed to identify the flavor of the partons generating jets with muons inside, showed that the QCD multi-jet background is dominated by events containing b-quarks. The above suggests that the same-charge di-muon pairs would be being generated mainly from muonic decays of B-mesons in one b-quark jet, and muonic decays of quarkonia or B-mesons in a second heavy-flavor jet.

The analysis also uses information about tracks, which serve to identify the $\tau_{\text{one-prong}}$ and to construct an isolation criterion for the muon-track pair of each leg. Imposing isolation requirements happens to be one of the most effective ways of reducing background events that contain jets with muons inside, as the jets tend to have higher track multiplicity compared to the chosen $a_1 \to \tau_\mu \tau_{\text{one-prong}}$ candidates. The following definitions of track types are used:

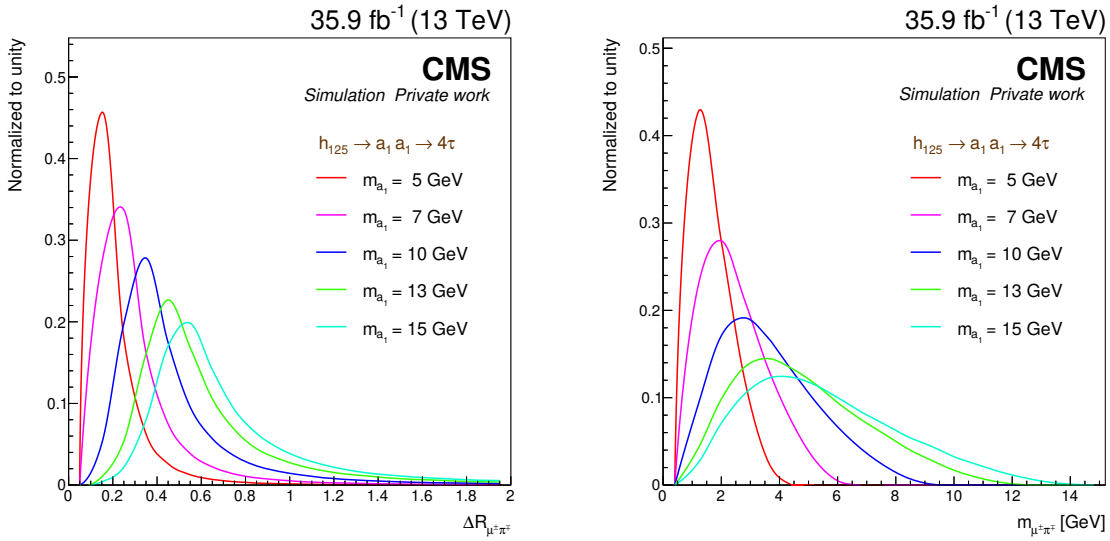

Figure 5.3: Distributions of ΔR (left) and invariant mass m (right) of the muon-track pairs for different mass points of the $h_{125} \to a_1 a_1 \to 4\tau$ channel in the ggF process. The distributions are obtained using generator-level information by selecting $\mu^{\pm}\pi^{\mp}$ pairs that emerge from the $a_1 \to \tau_\mu \tau_{\text{one-prong}}$ decay.

- The "isolation" tracks are utilized to construct the isolation criterion for the a_1 candidate. They are defined by the following criteria: $p_T > 1$ GeV, $|\eta| < 2.4$, $|d_\perp| < 1$ cm, $|d_z| < 1$ cm.

- The "signal" tracks are a subset of the "isolation" tracks meant to represent the $\tau_{\text{one-prong}}$ particles. They are defined by the following criteria: $p_T > 2.5$ GeV, $|\eta| < 2.4$, $|d_\perp| < 0.02$ cm, $|d_z| < 0.04$ cm.

- The "soft" tracks are a subset of "isolation" tracks designed to construct one of the sideband regions used in the background modeling. They are defined by the following criteria: $1 < p_T < 2.5$ GeV, $|\eta| < 2.4$, $|d_\perp| < 1$ cm, $|d_z| < 1$ cm.

In this approach (cut-based), a track is regarded as being nearby a muon if the angular separation ΔR between them is less than some specified value. In Fig. 5.3, the distributions of ΔR and invariant mass m of τ_μ-$\tau_{\text{one-prong}}$ pairs obtained through a generator-level study on the simulated signal samples can be observed. In this study, $\mu^{\pm}\pi^{\mp}$ pairs have been selected to mimic the reconstructed τ_μ-$\tau_{\text{one-prong}}$ candidates. The figure clearly shows the effect that the boosting has on the lighter resonances. For the mass range $4 \leq m_{a_1} \leq 15$ GeV, an optimized cut of $\Delta R = 0.5$ was found, so a track is considered close to a muon if the distance in the η-ϕ plane is $\Delta R < 0.5$. This ΔR value is optimal for intermediate masses, while it can maintain a good signal-to-background ratio for low masses and a reasonable signal acceptance for higher masses. Other possible cut values were probed, but that resulted in a deterioration of the overall performance. The track multiplicity distributions for each of the muons, using nearby "isolation" tracks, and for a cone of $\Delta R = 0.5$ with axis along the muon momentum direction, are shown in Fig. 5.4. It can be seen how the background components, specially QCD multi-jets, tend to have a higher track multiplicity with respect to the signal;

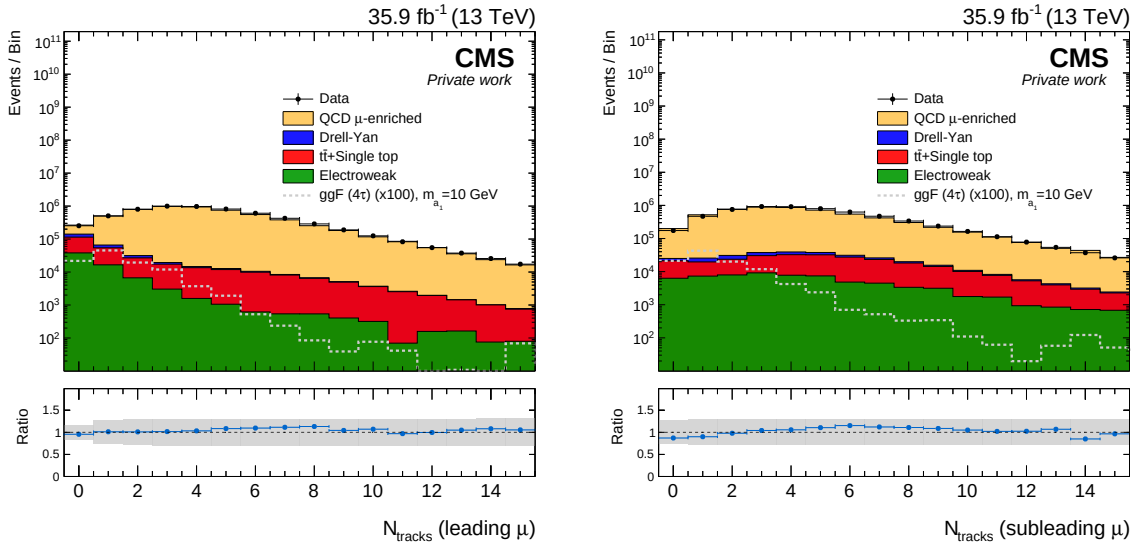

Figure 5.4: Distributions of track multiplicity (number of nearby "isolation" tracks) associated to the leading (left) and subleading (right) muons using a cone of $\Delta R = 0.5$.

the latter gets the maximum value for $N_{\text{tracks}} = 1$, as expected. Then, the selection further proceeds by requiring each muon to have one nearby "signal" track with a charge opposite to its charge. This muon-track system is accepted as a a_1 candidate if it has no additional "isolation" tracks within the cone of $\Delta R = 0.5$. The signal region (SR) of the selection is defined as that possessing two a_1 candidates. The event sample that this region comprises is the one used to carry out the statistical inference procedure.

The number of events observed in data that are selected in the SR is 2035. The number of expected background events obtained from simulation is compatible with that number, though its uncertainty is very large due to limited size in the QCD multi-jet sample. That is the main reason why the estimation of the background is addressed using a data-driven approach, as described in Subsec. 5.3.4. The rest of the background components are known with relative good accuracy from the simulation, and they amount to just a $\sim 1\%$ of the total background. In the case of the signal, the expected yield and signal acceptance values for a few representative mass points are reported in Tab. 5.1. The yield contributions from different production mechanisms (ggF, VBH, VH and ttH) of h_{125} have been summed up for each of the two channels ($h_{125} \to a_1 a_1 \to 4\tau$ and $h_{125} \to a_1 a_1 \to 2\mu 2\tau$). Now, since the couplings at tree level of the neutral scalar sector to fermions in the 2HDM+S (Subsec. 3.2.5) are proportional to the SM Higgs couplings, the equivalent expression to Eq. (3.6), for the case of a pseudoscalar ($3/2 \to 1/2$), can be used to relate the $a_1 \to \tau\tau$ and $a_1 \to \mu\mu$ partial decay widths. Then, the ratio of the branching fractions of the $a_1 a_1 \to 2\mu 2\tau$ and $a_1 a_1 \to 4\tau$ decay modes can be obtained via the ratio of the partial decay widths $\Gamma(a_1 \to \mu\mu)$ and $\Gamma(a_1 \to \tau\tau)$ as

$$\frac{\mathcal{B}(a_1 a_1 \to 2\mu 2\tau)}{\mathcal{B}(a_1 a_1 \to 4\tau)} = 2\frac{\mathcal{B}(a_1 \to \mu\mu)}{\mathcal{B}(a_1 \to \tau\tau)} = 2\frac{\Gamma(a_1 \to \mu\mu)}{\Gamma(a_1 \to \tau\tau)} = 2\frac{m_\mu^2\sqrt{1-\left(\frac{2m_\mu}{m_{a_1}}\right)^2}}{m_\tau^2\sqrt{1-\left(\frac{2m_\tau}{m_{a_1}}\right)^2}}, \tag{5.20}$$

Table 5.1: Signal acceptance (fraction of accepted events for ggF process) and yield (number of expected signal events including all processes) in the SR for some reference mass points. The yields are computed using the chosen benchmark value ($\mathcal{B}(h_{125} \to a_1 a_1)\mathcal{B}^2(a_1 \to \tau\tau) = 0.2$) for the 4τ channel, and by means of the relation (5.20) for the $2\mu 2\tau$ channel.

m_{a_1} [GeV]	Acceptance $\times 10^4$		Number of events	
	4τ	$2\mu 2\tau$	4τ	$2\mu 2\tau$
4	3.29 ± 0.16	89.3 ± 1.4	129.9 ± 6.2	54.7 ± 0.9
7	2.50 ± 0.14	69.0 ± 1.4	98.8 ± 5.5	22.5 ± 0.5
10	1.46 ± 0.11	47.1 ± 1.2	57.8 ± 4.2	14.2 ± 0.4
15	0.21 ± 0.04	3.5 ± 0.3	8.5 ± 1.1	1.0 ± 0.1

where the factor of 2 arises from the two possibilities $a_1^{(1)}a_1^{(2)} \to 2\mu 2\tau$ and $a_1^{(1)}a_1^{(2)} \to 2\tau 2\mu$. The formula (5.20) is employed to compute the expected signal yields in the $2\mu 2\tau$ channel. The partial decay width ratios were also used to estimate the possible contribution from the $h_{125} \to a_1 a_1 \to 4\mu$ decay channel. The latter was found to represent between a 0.4% and a 2% of the total signal yield (taking into account the $2\mu 2\tau$ and the 4τ channels) depending on the pseudoscalar mass, therefore, it was neglected in this analysis. In regard to the reported values of acceptance in Tab. 5.1, it can be noticed how these decrease quite abruptly for the samples corresponding to large m_{a_1}. That is because, for those masses, the angular distance of the muon-track system tends to be greater than the prescribed maximum value of $\Delta R = 0.5$ (see Fig. 5.3 (left)), thus existing a large number of events failing to fulfill the requirement of having one "signal" track nearby the muon. This is the main reason why this first approach is limited in sensitivity for relatively large masses of the a_1 boson.

5.3.3 Final Discriminant

In this cut-based approach, the chosen distribution to discriminate between signal and background is that formed by the two variables corresponding to the invariant masses of both muon-track systems (a_1 candidates). Due to the presence of neutrinos in both legs ($a_1 \to \tau\tau$) of the 4τ channel, the a_1 resonances are poorly reconstructed, as it can be inferred from Fig. 5.3 (right). This makes the construction of an analytic parametric model for the signal infeasible, so the 2D distribution has been binned. For simplicity, the 2D histogram has been filled for ordered values of the two invariant masses (m_1, m_2), so that $m_2 > m_1$. The binning layout taken is illustrated in Fig. 5.5, where it is indicated that only bins (i, j) with $j \geq i$ are filled, being j identified with m_2 and i identified with m_1. The bins $(i, 6)$, for $i = 1, \ldots, 5$, comprise all the events with $m_2 > 6$ GeV, while the bin $(6, 6)$ includes all events with $m_{1,2} > 6$ GeV. This 2D template is then translated (unrolled) into a 1D template containing the $6(6+1)/2 = 21$ bins in order to facilitate the work with the distributions and to better illustrate them.

To carry out the statistical analysis, the binned likelihood function is constructed according to Eq. (5.7) with $\nu_i \to \mu s_i + b_i$, where s_i and b_i represents the expected signal

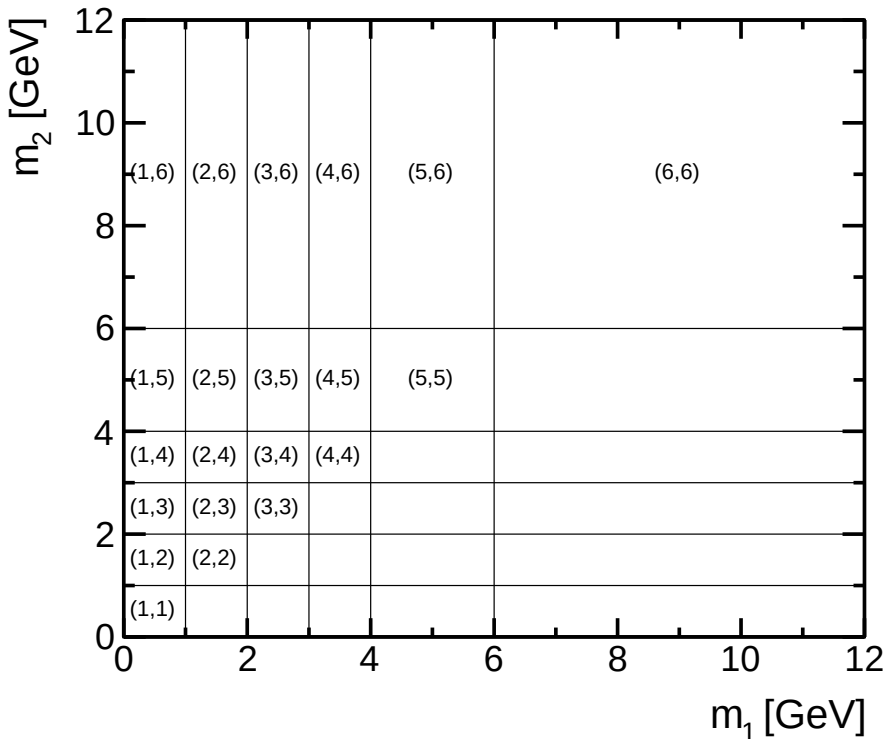

Figure 5.5: Adopted binning scheme for the 2D distribution of invariance masses (m_1, m_2) used as discriminant to extract the signal. The resulting 21 bins are labeled with the pairs (i, j), for $i, j = 1, \ldots, 6$ and with $j \geq i$.

and background event yields for a given bin. Both s_i and b_i are subject to multiple uncertainties that are handled by introducing nuisance parameters; those are treated in more detail in Subsec. 5.3.6. The compatibility of the data with the background-only and signal-plus-background hypotheses is tested with the profile likelihood ratio test, as described in Subsec. 5.1.4. The parameter of interest μ (signal strength modifier), in this case, is the product of the cross-section and branching fraction relative to the SM inclusive production cross-section of h_{125}, $\mu = \sigma(pp \to h_{125} + X)/\sigma_{SM}\,\mathcal{B}(h_{125} \to a_1 a_1)\mathcal{B}^2(a_1 \to \tau\tau)$. More details about the construction of the model and its individual components will be given in the following subsections.

5.3.4 Background Modeling

The estimation of both the shape and normalization of the background distribution from the MC simulation becomes almost impossible due to the small size of the MC sample corresponding to the largely dominating QCD multi-jet background. Therefore, a data-driven method based on several sideband (control) regions has been designed to estimate the shape (normalized 2D (m_1, m_2)) of the total background contribution in the SR. The construction of the sideband regions focuses on both the derivation of the normalized 2D distribution and on the validation of the data-driven estimation of the background shape. The definitions of the full set of control regions utilized are shown in Tab. 5.2, with their corresponding number

of observed events. All the control regions are built in such a way that their associated sample subset has null interception with that of the SR. This relies on the fact that the control regions are constructed by relaxing the isolation requirement of either one or both of the $a_1 \to \tau_\mu \tau_{\text{one-prong}}$ candidates. The purpose of each of the sideband regions will be discussed as progress is made in the description of the background model.

Table 5.2: Sideband regions used to construct and validate the background model. The symbols N_{sig}, N_{iso} and N_{soft} denote the number of "signal", "isolation" and "soft" tracks, respectively, contained in a cone of $\Delta R = 0.5$ around the muon momentum direction.

Sideband region	First μ	Second μ	Observed events
N_{23}	$N_{\text{iso}} = 1,\ N_{\text{sig}} = 1$	$N_{\text{iso}} = 2, 3$	62 438
$N_{\text{iso},2} = 1$	$N_{\text{iso}} > 1,\ N_{\text{sig}} \geq 1$	$N_{\text{iso}} = 1,\ N_{\text{sig}} = 1$	472 570
$N_{\text{iso},2} = 2, 3$	$N_{\text{iso}} > 1,\ N_{\text{sig}} \geq 1$	$N_{\text{iso}} = 2, 3$	1 766 790
N_{45}	$N_{\text{iso}} = 1,\ N_{\text{sig}} = 1$	$N_{\text{iso}} = 4, 5$	52 437
Loose-Iso	$N_{\text{sig}} = 1,\ N_{\text{soft}} = 1, 2$	$N_{\text{sig}} = 1,\ N_{\text{soft}} = 1, 2$	35 824

The normalized binned 2D distribution $f_{\text{2D}}(i, j)$ for the background is constructed as

$$f_{\text{2D}}(i,j) = \begin{cases} C(i,i) f_{\text{1D}}(i) f_{\text{1D}}(i) & i = j \\ C(i,j)(f_{\text{1D}}(i) f_{\text{1D}}(j) + f_{\text{1D}}(j) f_{\text{1D}}(i)) & j > i \end{cases}, \tag{5.21}$$

where f_{1D} represents a 1D normalized distribution of the muon-track invariant mass, and $C(i, j)$ are factors that account for possible correlation between the variables m_1 and m_2. The elements $C(i, j)$ are referred to as "correlation factors" since a hypothetical consistency of their values with the unity would imply the absence of correlation between m_1 and m_2. The addition of the contents of the non-diagonal bins (i, j) and (j, i) is attributed to the fact that each event enters the 2D distribution with ordered values of (m_1, m_2). The two components of the background distribution f_{1D} and $C(i, j)$ are determined in two different control regions as explained below.

The f_{1D} distribution is derived in the sideband region N_{23}. As seen in Tab. 5.2, the events falling in this region only contain one a_1 candidate, which is associated with a "first μ". The other muon ("second μ") is required to be accompanied by either two or three nearby "isolation" tracks. The f_{1D} distribution is derived from the invariant mass of the muon-track system corresponding to the a_1 candidate. According to the MC simulation, the control region N_{23} is dominated by QCD multi-jet events, making up more than 95% of the total background. The signal contamination in bins of the f_{1D} histogram is estimated to be less than 0.7%. The basic assumption in constructing f_{1D} from this control region is that the invariant mass distribution of the a_1 candidate is nearly unaffected by the isolation requirement imposed on the second muon. This allows extrapolating the distribution f_{1D} derived in this region to the SR. In order to verify the above stated, two additional control regions named $N_{\text{iso},2} = 1$ and $N_{\text{iso},2} = 2, 3$ are constructed. In both control regions, a

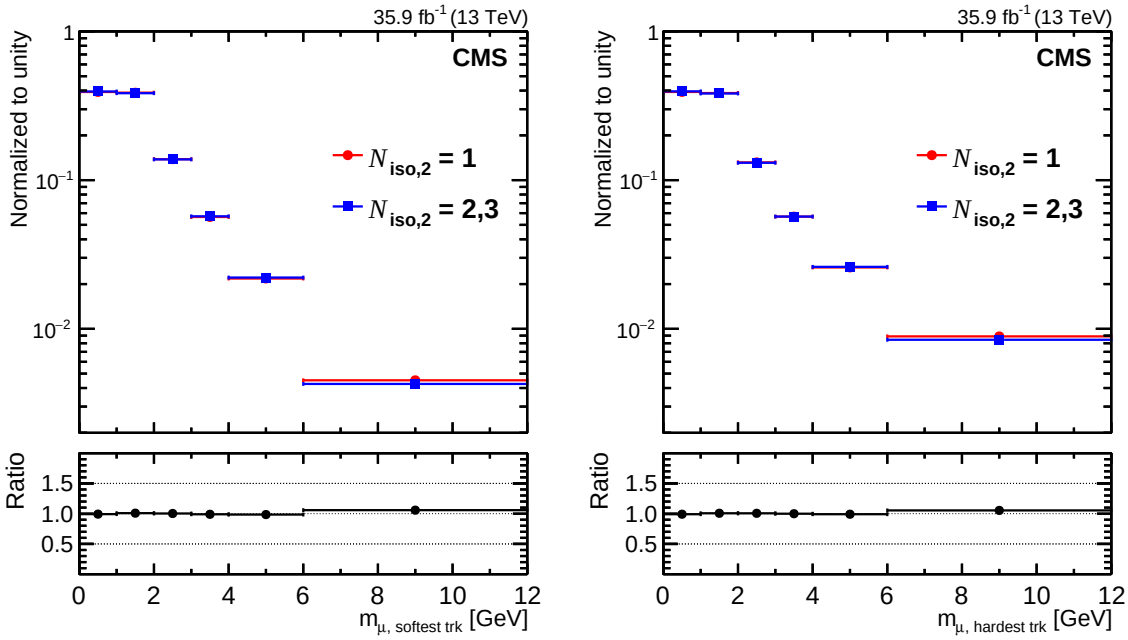

Figure 5.6: The observed normalized invariant mass distributions of the first muon and the softest (left) or hardest (right) "signal" track in control regions $N_{\mathrm{iso},2} = 1$ (red circles) and $N_{\mathrm{iso},2} = 2, 3$ (blue squares).

first muon is allowed to have more than one "isolation" track ($N_{\mathrm{iso}} > 1$), of which, at least one, must be a "signal" track. For the second muon, two types of isolation requirements are considered; the isolation condition corresponding to a a_1 candidate in the SR (sideband region $N_{\mathrm{iso},2} = 1$), and the isolation specifications introduced for the second muon in N_{23} (sideband region $N_{\mathrm{iso},2} = 2, 3$). The next step is to compare the invariant mass distributions obtained from the first muon-track pair in both control regions, and thereby assess the impact that the type of isolation has on the kinematics of the other leg. Additionally, and due to the fact that for the first muon more than one of the selected "isolation" tracks can be a "signal" track, two scenarios have been studied. That is to say, the muon-track invariant mass is calculated using both the lowest and the highest p_T "signal" tracks ("softest" and "hardest"). If only one "signal" track is found, this is regarded as both the hardest and the softest "signal" track. The comparison between the sideband regions $N_{\mathrm{iso},2} = 1$ and $N_{\mathrm{iso},2} = 2, 3$ for both scenarios is illustrated in Fig. 5.6. The results of this test show that the muon-track invariant mass distributions in the control regions $N_{\mathrm{iso},2} = 1$ and $N_{\mathrm{iso},2} = 2, 3$ are compatible, differing by less than 6% in each bin of the histogram. This serves, to some extent, to validate the assumption that the $f_{1\mathrm{D}}$ distribution can be extrapolated from the sideband region N_{23} to the SR. However, the existence of possible bias when considering N_{23} instead of any other isolation type must be taken into account too. One way to avoid such potential effects is to consider systematic errors upon the choice of the sideband region. Those uncertainties would be transferred to the final discriminant ($f_{2\mathrm{D}}(i, j)$) and taken into account as nuisance parameters in the likelihood function. The possible dependence on the isolation type imposed on the second muon is studied with a direct comparison between N_{23} and the analogous control region N_{45} (see Tab. 5.2). The results of this study are shown in Fig. 5.7 (left). A slight deviation can be clearly seen, although an overall good agreement. The small

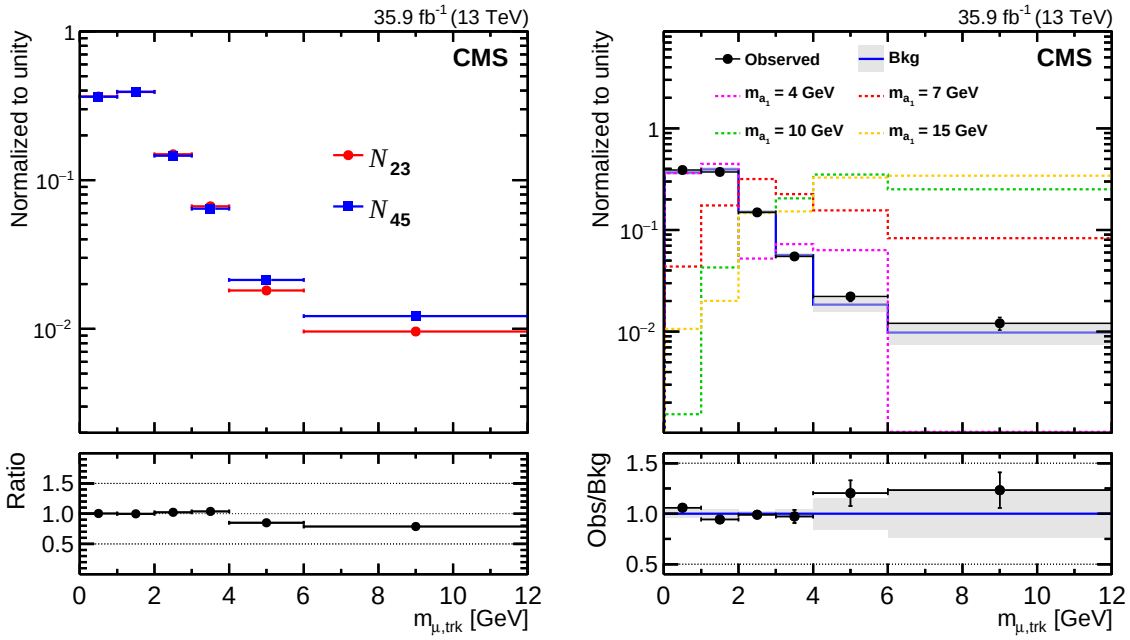

Figure 5.7: The left plot shows the observed normalized invariant mass distributions of the muon-track pair in control regions N_{23} (red circles) and N_{45} (blue squares). The right plot shows the observed normalized invariant mass distribution of the muon-track pairs in the SR (points with error bars), along with the background distribution obtained from N_{23} (blue line with error bands), and a few signal (including 4τ and $2\mu2\tau$) distributions (dashed histograms) obtained from simulation.

difference is taken as a shape uncertainty in the f_{1D} distribution, which is then propagated to the final discriminant. The shape of the f_{1D} distribution in the SR is superimposed to that of the background model (N_{23}) for comparison, as illustrated in Fig. 5.7 (right). The level of agreement between the observed data and the background model is good within their statistical uncertainties. At this point, the f_{1D} distribution could also have served as a discriminant between signal and background, nevertheless, exploiting the 2D distribution obviously results in a better discriminating power. As can be observed from Fig. 5.7 (right), for very low mass points (e.g. $m_{a_1} = 4$ GeV), the separation power of f_{1D} is still poor. This is given to the fact that the lower the pseudoscalar mass, the greater the resemblance between a muon-track pair produced from a a_1 and one produced from a QCD jet.

In order to finally obtain the $f_{2D}(i,j)$ distribution, the elements $C(i,j)$ have to be calculated. The correlation factor $C(i,j)$ are derived in the Loose-Iso sideband region, in which at least one of the muons is allowed to have one or two extra nearby "soft" tracks, apart from the accompanying "signal" track. This region comprises about 36k data events, of which nearly 99% are expected to come from QCD multi-jet background, according to MC simulation. The signal contamination is also estimated to be low, with an overall background-to-signal ratio of one order of magnitude larger than in the SR. The event sample selected in Loose-Iso is utilized to construct the $f_{2D}(i,j)$ distribution, and by means of Eq. (5.21), the $C(i,j)$ factors are calculated in this region. The values of the correlation factor obtained with this data-driven procedure are shown in Fig. 5.8, along with their statistical uncertainty. The higher-mass bins possess large uncertainties because only a few events fall in this region.

Similarly to the case of f_{1D}, the extrapolation of considering the $C(i,j)$ in the Loose-Iso

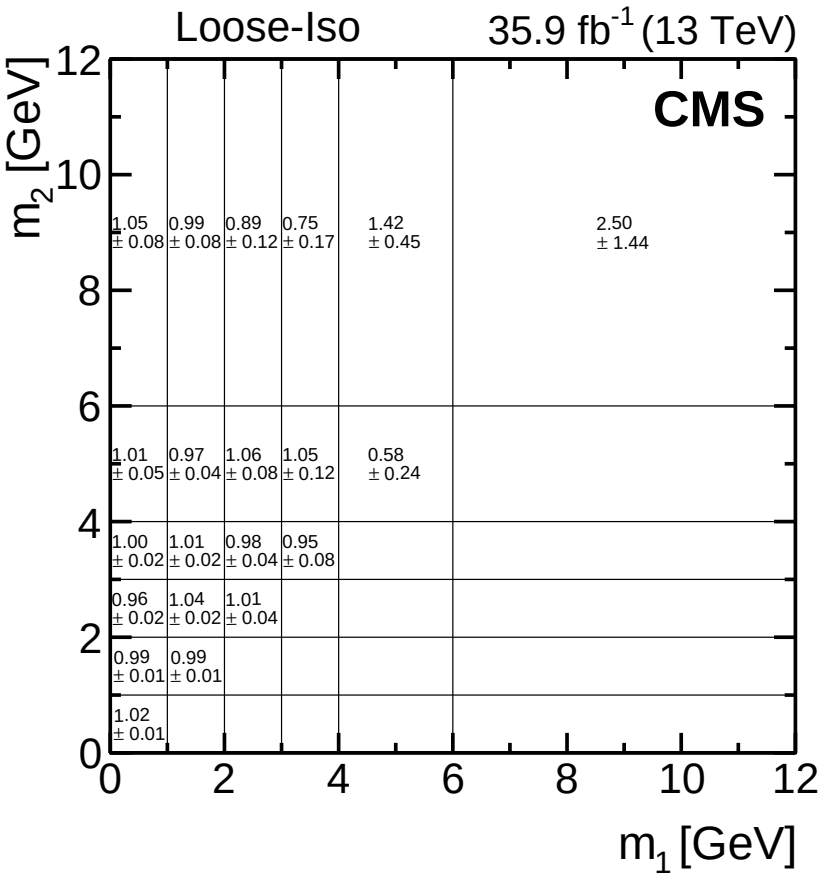

Figure 5.8: The observed values of the correlation factors $C(i,j)$ (with statistical uncertainties) obtained in the control region Loose-Iso.

sideband region identical to those in the SR must be validated. Now, in order to assess such possible difference in $C(i,j)$, rather than making the comparison in additional sideband regions, a dedicated MC study has been performed. Since the QCD multi-jet background largely dominates in the Loose-Iso control region, the QCD multi-jet MC sample has been used to conduct that study. The main objective of the study is to provide a proper comparison between the $C(i,j)$ in Loose-Iso and in the SR, overcoming somehow the problem of the limited size of the QCD multi-jet sample. The idea is to derive the probabilities of having muon-track pairs with distinct level of isolation (Loose-Iso or SR) as function of a bunch of parameters that control the dynamics of the pairs inside the jet. The probabilities are constructed as $P(p_{\text{parton}}, p_\mu/p_{\text{parton}}, f_{\text{parton}}, q_\mu \cdot q_{\text{parton}}, m_{\mu,\text{trk}})$, where p_{parton} is the parton momentum, p_μ/p_{parton} is the ratio of the muon and parton momentum, f_{parton} is the flavor of parton, $q_\mu \cdot q_{\text{parton}}$ is the muon-parton (quark) charge product, and $m_{\mu,\text{trk}}$ is the invariant mass of the muon-track pair in the jet. The evaluation is made for muons matching final state partons within a cone of $\Delta R = 0.5$. Since the derivation is made in the presence of only one muon-track pair, the size of the selected sample is reasonably good. Once this procedure was carried out and validated, the next step was to employ the derived probabilities to generate the $f_{2D}(i,j)$ and f_{1D} distributions from the same-charge di-muon sample (good size in the

QCD multi-jet simulation) mentioned in Subsec. 5.3.2. The distributions are obtained for both the SR and the control region Loose-Iso. Then, by making use of Eq. (5.21) again, the correlation factors $C(i,j)$ can be derived for both regions. The results of this simulation study are shown in Fig. 5.9. The figure shows that the correlation factors obtained in the two control regions are indeed quite similar. Nevertheless, in order to minimize any possible

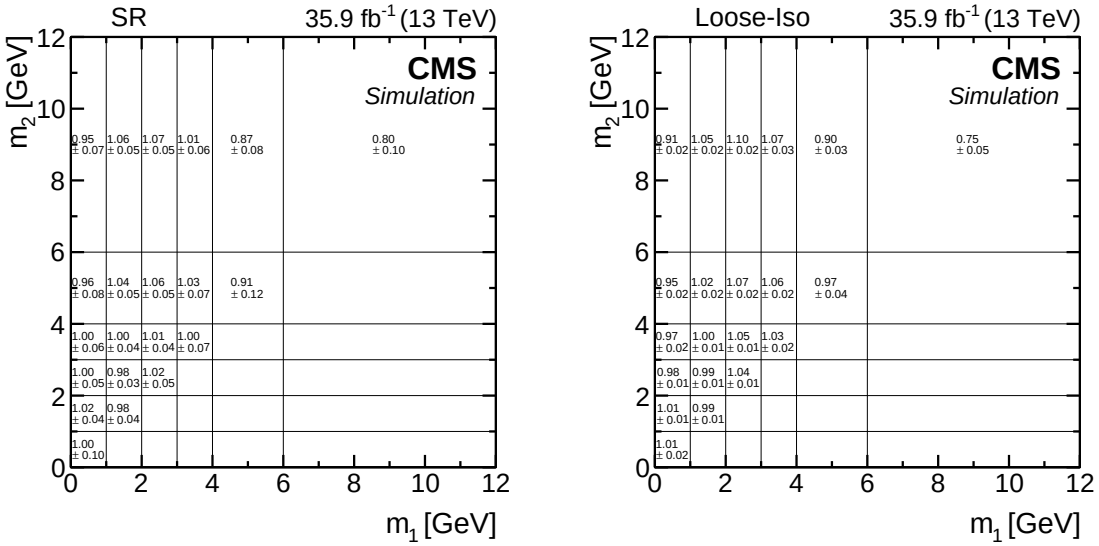

Figure 5.9: The values of the correlation factors $C(i,j)$ (with statistical uncertainties) obtained with the dedicated simulation study for the SR (left) and for the control region Loose-Iso (right).

bias, the data-driven extrapolation from Loose-Iso to SR is compensated by applying transfer factors via the relation

$$C(i,j)^{\text{SR}}_{\text{data}} = C(i,j)^{\text{Loose-Iso}}_{\text{data}} \cdot \frac{C(i,j)^{\text{SR}}_{\text{MC}}}{C(i,j)^{\text{Loose-Iso}}_{\text{MC}}}, \tag{5.22}$$

where $C(i,j)^{\text{Loose-Iso}}_{\text{data}}$ are the correlation factors derived for the control region Loose-Iso in data (Fig. 5.8), $C(i,j)^{\text{SR}}_{\text{MC}}$ are the ones derived for the SR in the simulated QCD multi-jet sample (Fig. 5.9 (left)), and $C(i,j)^{\text{Loose-Iso}}_{\text{MC}}$ are the ones derived for the Loose-Iso in the simulated QCD multi-jet sample (Fig. 5.9 (right)). Analogously to f_{1D}, the small difference observed from simulation between the $C(i,j)$ in the SR and in the control region Loose-Iso is taken as a systematic uncertainty to be propagated to the final discriminant.

5.3.5 Signal Modeling and Monte Carlo Corrections

The signal $f_{\text{2D}}(i,j)$ distributions are derived from the simulated samples of the $h_{125} \to aa \to 4\tau$ and the $h_{125} \to aa \to 2\mu 2\tau$ channels. As mentioned before, the cross sections of the various production mechanisms of h_{125} are taken as those of the SM, and the addition of the contributions of the 4τ and $2\mu 2\tau$ channels obeys the relation (5.20). The Fig. 5.10 illustrates the unrolled $f_{\text{2D}}(i,j)$ distribution for the two signal channels obtained for two representative mass points. The distributions of the two signal channels are normalized to their respective event yields (see Tab. 5.1). The shapes of the two channels differ considerably due the peak

structure of the $a_1 \to \mu\mu$ decay, in which one of the μ is identified with a reconstructed muon in the detector and the other is associated with the reconstructed "signal" track.

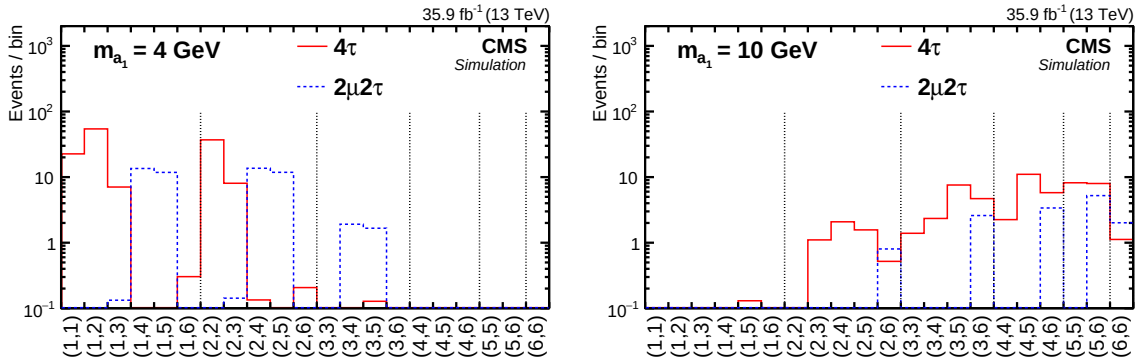

Figure 5.10: The unrolled $f_{2D}(i,j)$ distribution of both signal channels 4τ (red histogram) and $2\mu 2\tau$ (blue histogram) for two representative mass pints $m_{a_1} = 4$ GeV (left) and $m_{a_1} = 10$ GeV (right). The notation of the bins follows that of Fig. 5.5.

It is clear that one has to rely on MC simulation to describe most of the features of the signal model. However, the MC simulation is not able to fully reproduce all physical aspects of the real data, so it is necessary to make use of some corrections. In general, all the processes that are described by the MC simulation, whether signal or background, are affected by these imperfections. Since in this particular case, the background modeling in the SR was mostly carried out with a data-driven method, the signal modeling is the most impacted. There are many factors that influence the deficient modeling of MC samples. Those could be related to limitations of the MC generators (theoretical accuracy, computing power, etc.), or to imperfections in the detector simulation (detector response, detector operation, beam conditions, etc.). In this analysis, the handling of the first class of imperfections can be reflected in the aforementioned corrections to the p_T spectrum of h_{125} (Subsec. 5.3.1). The signal acceptance is moderately dependent on the p_T of h_{125} since a change in this magnitude can lead to less or more boosted a_1 bosons, thus modifying the angular distance ΔR of the muon-track pairs. To account for this, the simulated signal samples have been subject to an event-by-event reweighting to match the higher-order predictions obtained for the p_T distribution of h_{125} in all production modes. Now, regarding the second class of effects coming from the detector simulation, various corrections have been applied. One of those corrections is due to the impossibility of exactly emulate the constantly changing pile-up (Subsec. 4.3.1.2) conditions in real data taking. Although some estimates of the average number of PU are usually made[3], the exact distribution is very difficult to reproduce when generating the MC samples. Hence, a PU reweighting on an event-by-event basis is applied to the MC samples, so that the exact matching of the MC profile to the data is achieved. Besides that, muon (Subsec. 4.3.1.3) reconstruction and identification efficiencies (in general, most of the physics objects) also suffer from discrepancies between data and MC. So, weights corresponding to the efficiency ratios, with p_T and $|\eta|$ dependence, are applied to the events of the MC samples. On the same basis, the physics objects and quantities forming part of the selection of the trigger (Subsec. 4.2.7) also introduce dissimilarities between the efficiencies of the data and MC. The trigger efficiencies are measured relative to the offline selection

[3]In 2016, the average number of PU interactions per bunch crossing in data for pp collisions was about 27.

in data and MC with the tag-and-probe technique [372], and their ratio in bins of p_T and $|\eta|$ is used to reweight the MC samples. Another issue, more related to the context of this analysis, is the inexact simulation of the isolation criteria imposed on the muon-track pairs. The isolation might be affected by the presence of more (less) charged particles originating from PU interactions or from the underlying event, so the profiles could slightly differ in MC and data. To asses such potential inconsistency, a dedicated study performed on a sample of $Z \to \tau\tau$ was carried out. The selection exploits the $Z \to \tau_\mu \tau_{\text{one-prong}}$ decay mode, while trying to mimic the same aspects of the selection of the one-prong track candidate (Subsec. 5.3.2). The isolation efficiency is extracted as a function of the transverse momentum of the track in four bins of p_T through a maximum-likelihood fit (Subsec. 5.1.2) applied to the muon-track invariant mass distribution. The study showed that, indeed, the isolation must be corrected in MC. The results are shown in Fig. 5.11, which also includes the dependence obtained after a linear fit applied to the measured values. The linear function was applied as a weight on the events entering the SR of the signal sample.

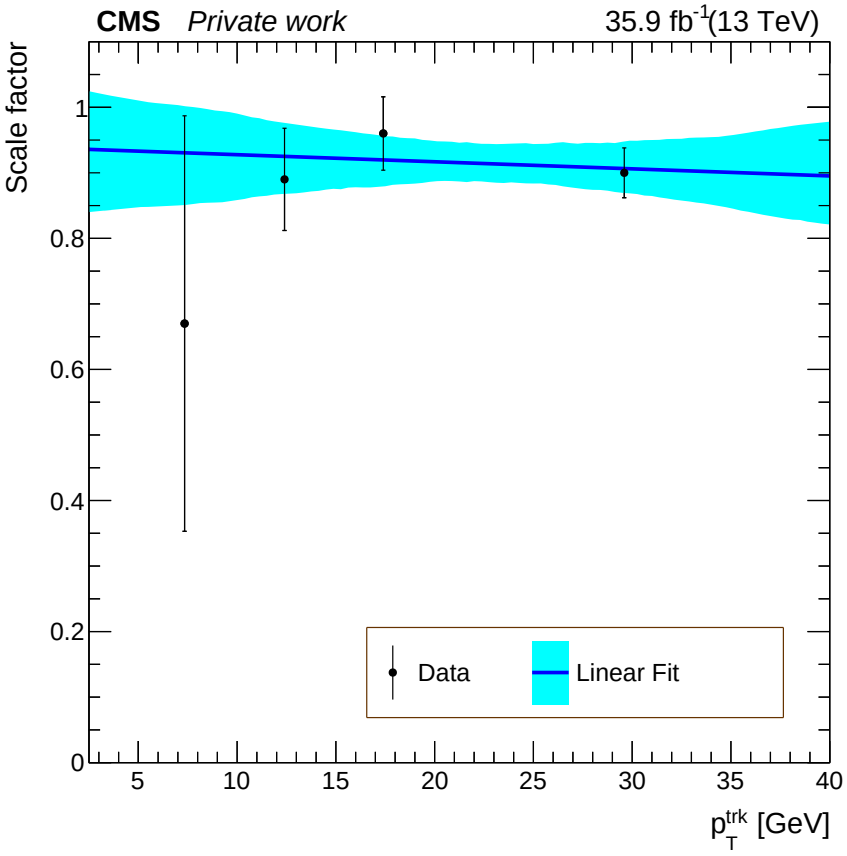

Figure 5.11: Scale factor associated with the isolation efficiency of muon-track pairs. The measured values (points with error bars) in bins of track p_T were fitted with a linear function (blue line with cyan error band). The linear dependence was applied as a weight to the signal sample on an event-by-event basis.

5.3.6 Systematic Uncertainties

In Subsec. 5.1.2, the role that the nuisance parameters play when estimating the parameters of interest in the presence of imperfect models was mentioned. They are basically introduced in the likelihood function to account for systematic biases in the model under consideration, but in turn, that decreases the accuracy in the estimation of the parameters of interest. To help constraint the nuisance parameters, auxiliary measurements are carried out when possible. However, on certain occasions, this is not possible or results very difficult. In this analysis, there are various sources of systematic uncertainties affecting both the signal and the background distributions. One of the fundamental pieces of the background model

Table 5.3: Summary of the systematic uncertainties considered in the analysis and their effect on the background and signal distributions.

Affected Distribution	Source	Value	Type
Background	Stat. unc. in $C(i,j)$	$3-60\%$	bin-by-bin
	Syst. unc. in $C(i,j)$	-	shape
	Syst. unc. in $f_{1\mathrm{D}}(i)$	-	shape
Signal	Integrated luminosity	2.5%	norm.
	Muon id. and trigger effic. (per μ)	2%	norm.
	Track id. effic. (per track)	$4-12\%$	shape & norm.
	MC stat. unc.	$8-100\%$	bin-by-bin
	$\mu_{\mathrm{R,F}}$ variations (acceptance)	$0.8-2\%$	norm.
	PDF (acceptance)	$1-2\%$	norm.
	$\mu_{\mathrm{R,F}}$ variations (ggF xsec.)	$5-7\%$	norm.
	$\mu_{\mathrm{R,F}}$ variations (others xsec.)	$0.4-9\%$	norm.
	PDF (ggF xsec.)	3.1%	norm.
	PDF (others xsec.)	$2.1-3.6\%$	norm.

is its normalization. But as it happens, due to the very limited size of the MC samples in the SR, this parameter is unconstrained, and therefore it is assigned a flat distribution. Fortunately, the modeling of the shape of the background is based on data, which makes it less vulnerable to simulation effects, hence the reason why the background model requires fewer nuisance parameters to properly describe it. The other few sources of uncertainties come from the shape modeling itself, as discussed in Subsec. 5.3.4. A first uncertainty related to the estimation of the $f_{1\mathrm{D}}(i)$ distribution, as well as another one associated with the estimation of $C(i,j)$ are incorporated into the background model. Additionally, the statistical uncertainties of the correlation factors $C(i,j)$ (ranging from 3 to 60%), which are influenced by the size of the observed Loose-Iso sample and the simulated QCD samples, are also included. The full

set of systematic uncertainties considered in the analysis, along with their values and effect on the distributions, is listed in Tab. 5.3; this also includes the signal uncertainties discussed below. The most common choices of the p.d.f. (Gaussian, Log-normal, Gamma) describing the various types of nuisance parameters listed in the table can be seen in [352].

The signal distribution is affected by various experimental and theoretical uncertainties. Part of the uncertainty in the normalization of the signal distribution comes from the precision in the measurement of the integrated luminosity, which for CMS reached a value of 2.5% [373] for the 2016 data taking period. The applied corrections to the signal MC sample targeting the imperfections on physics objects reconstruction also yield uncertainties. The estimated value for the muon identification and trigger efficiency is 2% per muon, which is accounted for via a nuisance parameter affecting the normalization of the signal. The study carried out for the track isolation efficiency produced an uncertainty of $4-12\%$ per track, depending on the track p_T, so effects on both the normalization and the shape of the distribution were taken into account. The overall small value of the signal acceptance (see Tab. 5.1) combined with the limited sizes of the signal samples cause some bins of the distribution to have very few events, provoking uncertainties as large as 100% in individual bins, and of up to 20% in the total normalization. On the other hand, the theoretical uncertainties that are reflected in the signal normalization are also taken into account by means of constrained nuisance parameters. The corrections applied in the p_T distribution of the h_{125} produce uncertainties of about 2% in the acceptance upon changes in the PDFs and variations on the renormalization (μ_{R}) and factorization (μ_{F}) scales. But the largest impact of these variations is on the cross-sections of the h_{125} production processes, reaching uncertainty values of up to 9%, as observed in Tab. 5.3.

5.3.7 Results

All the elements above discussed constitute the statistical model of this analysis, so the remaining task is to carry out the procedure of statistical inference. The first step was to subject the model to a maximum likelihood fit with the normalization of the signal and the background freely floating. The signal normalization is left unconstrained to detect any possible excess that can be described by the signal-plus-background model, whereas the background normalization is unknown because of the explained reasons. The results of the fit indicate that the background normalization tends to adjust to the number of observed events, and the signal contribution for any mass hypothesis acquires a very low estimated value. That allows promoting the fitting to the scenario where no signal is present. Accordingly, the ability of the background-only model to fit the data is tested with a similar maximum likelihood procedure. An illustration of the result of the background-only fit is shown in Fig. 5.12, where the obtained post-fit distribution is compared to the data. One can observe with a naked eye that there does not seem to be significant deviations of the data from the background prediction, neither can be described the small fluctuations by any of the signal components (normalized to their yields) that have been included in the figure. However, a simple look at the plot can not provide a rigorous assessment of what the data is really describing, therefore, it is prudent to resort to the analysis of test statistics.

As noted in Subsec. 5.1.4, one of the simplest options to test a given hypothesis without having to reference any alternative proposition is to use a goodness-of-fit test. There are many possibles types of goodness-of-fit measures that can be used. But in high-energy physics, the

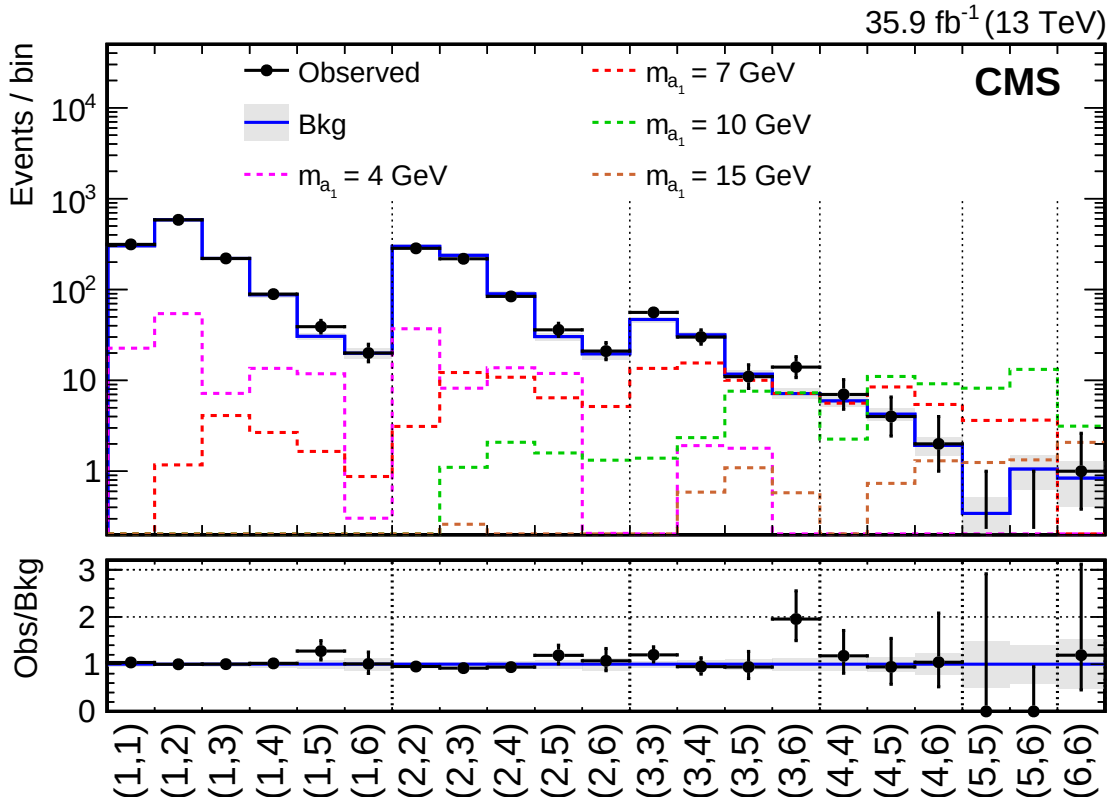

Figure 5.12: The final discriminant of the analysis. The observed number of events in each bin is represented by data points with error bars. The background distribution (blue histogram with shaded error bands) shown in the plot has been obtained after a background-only fit to the data. The representative signal distributions (dashed histograms) include both the 4τ and the $2\mu2\tau$ channels, and they have been normalized using the event yield information contained in Tab. 5.1. The notation of the bins follows that of Fig. 5.5.

"saturated" (Sat.) [374], the Kolmogorov-Smirnov (KS) [375], and the Anderson-Darling (AD) [376] models are more commonly used, due to the fact that they very well suit the problem of binned fits. First, the signal-plus-background model of this analysis with the strength modifier (μ) floating in the fit (unspecified) was tested using those methods. The results of the tests have been specified by their p-value, which corresponds to the probability of obtaining a value of the test as high as the one observed, and where the corresponding distribution of the test has been determined by Asimov data sets generated with toys. The Fig. 5.13 illustrates the result using the saturated model for a mass hypothesis of $m_{a_1} = 10$ GeV. The corresponding p-values of this and of all the other tests are summarized in Tab. 5.4 for some representative mass points. All the tests show that the signal-plus-background model is compatible with the observed data. Based on the results of the maximum likelihood fit, the model is further restricted to the background-only hypothesis ($\mu = 0$) to test the robustness of this distribution when trying to describe the data. The results of the three methods are also shown in Tab. 5.4. It can be observed that the background-only model describes very well the data, reaching p-values close to 0.5 for all tests. The above suggests that when confronting the background-only hypothesis with an alternative signal-plus-background hypothesis by means of standard

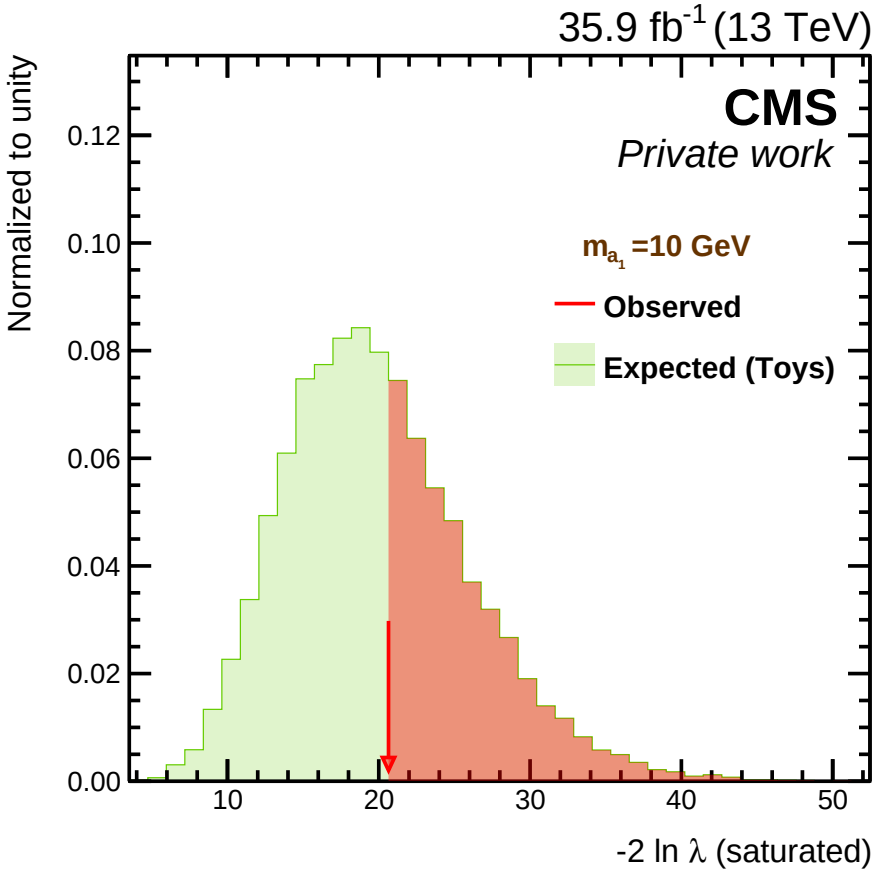

Figure 5.13: The result of the "saturated" test (based on a likelihood ratio) under the signal-plus-background hypothesis for the mass point of $m_{a_1} = 10$ GeV. The green histogram represents the distribution of the statistic obtained by means of toys. The arrow points to the observed value of the statistic, and the red shaded area represents the p-value.

Table 5.4: Results of the three goodness-of-fit tests for both hypotheses expressed in terms of p-values. In the case of the signal-plus-background hypothesis, representative mass points were considered.

	p-value			
Hypothesis H_0	signal-plus-background			background-only
m_{a_1}	5 GeV	10 GeV	15 GeV	-
Sat.	0.427	0.441	0.436	0.409
KS	0.480	0.486	0.481	0.478
AD	0.423	0.468	0.444	0.413

procedures (Subsec. 5.1.4), for relatively large values of μ, the tendency is to accept the null hypothesis. Therefore, no evidence of signal-like events is observed from the data, and upper limits on the signal strength modifier can be set.

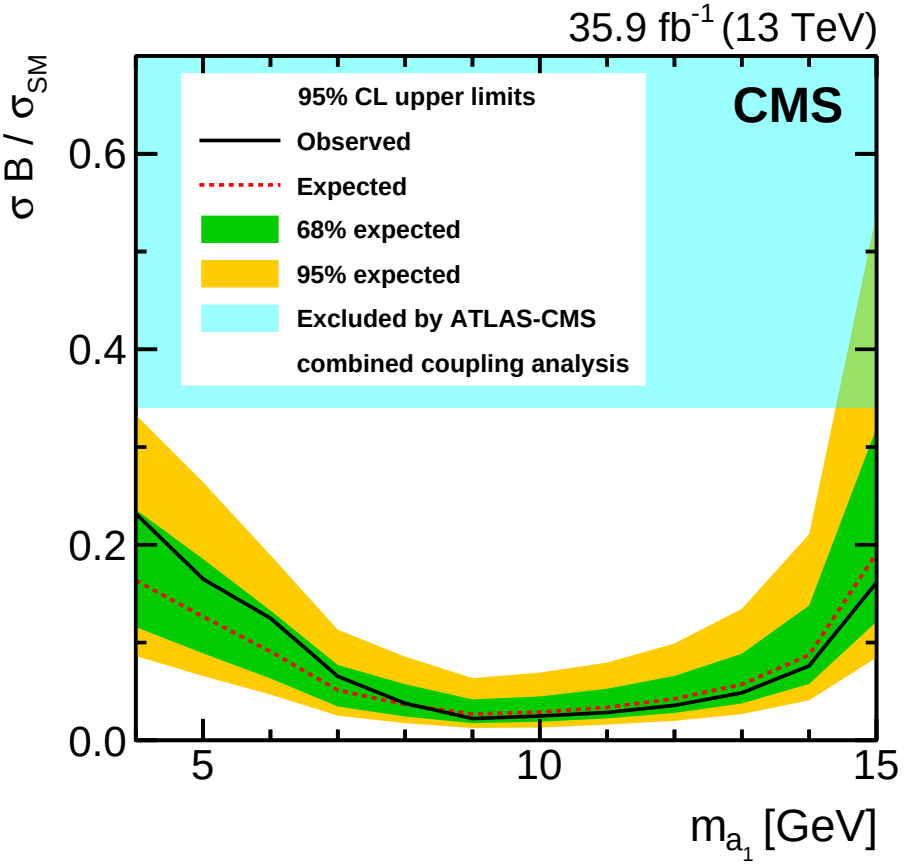

Figure 5.14: The observed and expected upper limits at 95% confidence level on the signal strength modifier $\mu = \sigma(pp \to h_{125} + X)/\sigma_{SM}\,\mathcal{B}(h_{125} \to a_1 a_1)\mathcal{B}^2(a_1 \to \tau\tau)$. The green and yellow bands indicate the central intervals that contain 68% and 95% of the distribution of expected limits. The shaded area in blue ($> 34\%$) indicates the excluded region for the branching ratio of h_{125} decaying into non-SM particles [355].

The limit setting procedure follows the modified frequentist $\mathrm{CL_s}$ criterion (Subsec. 5.1.4), for a confidence level of 95%. The hypothesis under consideration is the signal-plus-background for a given value of μ, and those values of the strength modifier that lead to a rejection of the hypothesis are considered an excluded interval at 95% confidence level (Subsec. 5.1.3). The observed upper limits for different mass points are compared with the expected limit median and intervals ($\pm 1\sigma$ and $\pm 2\sigma$) obtained with the MC toy method. The results are shown in Fig. 5.14. As seen in the figure, the observed limits are compatible with the expected limits within one standard deviation, which reaffirms the previous indication of the absence of a signal, up to certain bound. The observed upper limits range from 0.022 at $m_{a_1} = 9$ GeV to 0.230 at $m_{a_1} = 4$ GeV, whereas the median expected upper limits range from 0.027 at $m_{a_1} = 9$ GeV to 0.190 at $m_{a_1} = 15$ GeV. The lower bounds for low and high mass regions with respect to intermediate-mass points correspond to two different physical

effects in the analysis. For very low masses, as was noted before, the similarity between the invariant masses of signal muon-track candidates and those originating from a QCD jet is quite large. This results in a poor discriminating power of the 2D (m_1, m_2) distribution for the low mass hypotheses. In Fig. 5.12, the case of $m_{a_1} = 4$ GeV is exemplified. One can clearly see how this distribution and the background are more alike in shape than the rest representing higher mass values. The fall in sensitivity for high masses is related to the decrease in signal acceptance (Tab. 5.1) for these signal samples. The imposed cut of $\Delta R < 0.5$ on the muon-track pair angular separation highly limits the selection of events with less boosted $a_1 \to \tau_\mu \tau_{\text{one-prong}}$ candidates (see Fig. 5.3), like those emerging from more massive a_1 pseudoscalars. The mass points that benefit most with the selection adopted in this analysis are the ones in the intermediate region of the probed range since they possess a good balance of discriminating power and event acceptance. The above motivated the design of a new analysis strategy to improve the sensitivity of the analysis for low and high pseudoscalars masses. This treatment can be found in the next chapter.

CHAPTER

6

DATA ANALYSIS WITH MACHINE LEARNING

Contents

In recent years, machine learning has become one of the most used tools to process data containing a large number of variables as observable. In high energy physics, the use of multivariate techniques has been increasingly growing as physical processes with a lower production rate in the experimental facilities are explored. Previously, in the section dedicated to the statistical methods (Sec. 5.1), some of the aspects of multivariate discriminants that are derived from the statistical analysis were mentioned. And the fact is that, although machine learning is built on the basis of very advanced algorithms and the most modern technologies, in reality, the fundamentals of this methodology are purely statistical.

In this chapter, multivariate analysis techniques are put into practice, with the objective to improve the results obtained for the search presented in the previous chapter. This will be the main topic of the first section of this chapter, in which a second strategy attempting to overcome some of the sensitivity limitations of the first approach are going to be presented.

The principal ingredient of the new method is a multivariate classification algorithm as the final discriminant combined with a more inclusive event selection intended to stabilize the signal acceptance in the entire mass region. The second section is conceived to provide an interpretation of the experimental results and to assess the impact of those on a specific theoretical model. Here, the results obtained with this second experimental approach are translated into constraints on the parameter space of the 2HDM+S.

6.1 Analysis Using MVA-Based Approach

This approach targets the same event topology discussed in Subsec. 5.2.1, but it extends the pseudoscalar mass range up to $4 \leq m_{a_1} \leq 21$ GeV. The signal events belonging to pseudoscalars with larger masses do not enter the selection used in the previous analysis (Sec. 5.3), as the bosons tend to be less boosted, which makes their decay products fail the requirement imposed on the ΔR between muons and tracks. This is now avoided with some changes in the preselection cuts and type of isolation imposed on the various objects. As a complement to the new selection, an MVA classifier (BDT) is employed to better separate the signal and background events in the final sample (SR). The incorporation of new variables into the final discriminant tackles the inconvenience of having relatively low sensitivity for very light a_1 bosons. Given the fact that many aspects of this approach coincide with those of the previous one, the discussion here will be limited to mainly address the characteristics that distinguish them.

6.1.1 Simulated Samples

In addition to the set of MC samples listed in Subsec. 5.3.1, a group of signal samples corresponding to higher mass points was produced. Three mass points corresponding to 17, 19 and 21 GeV have been generated for all production processes and both decay channels. The event samples for the $h_{125} \to a_1 a_1 \to 4\tau$ channel were generated with the general-purpose MC generator Pythia, whereas those for the $h_{125} \to a_1 a_1 \to 2\mu 2\tau$ channel were produced with MadGraph5_aMC@NLO.

Furthermore, a complete set $(4, 5, 6, \ldots, 15, 17, 19, 21$ GeV) of same-charge di-muon enriched samples were produced for the 4τ decay channel in the ggF production mode, because of the reasons explained in Subsec. 6.1.3. The samples were filtered at generator level by requiring the presence of two same-charge muons with $p_T > 10\,(20)$ GeV and separation $\Delta R_{\mu_1,\mu_2} > 1.5$. The MC event generator used for this task was also Pythia.

6.1.2 Event Selection

This analysis uses the same trigger strategy as the cut-based approach (Subsec. 5.3.2), as it exploits the same $a_1 \to \tau_\mu \tau_{\text{one-prong}}$ decay mode. The physics objects utilized are good reconstructed muons and tracks as well. The only difference in the offline selection of same-charge muons with respect to the cut-based approach is that the angular distance between them is relaxed up to $\Delta R_{\mu_1,\mu_2} > 1.5$ since this variable is used in the MVA classification. The distributions of this observable for a few signal samples are shown in Fig. 6.1 (right). Concerning the tracks identifying the $\tau_{\text{one-prong}}$ candidate, the same classification of types of tracks ("isolation", "signal", and "soft") is used. The main difference appears in the selection

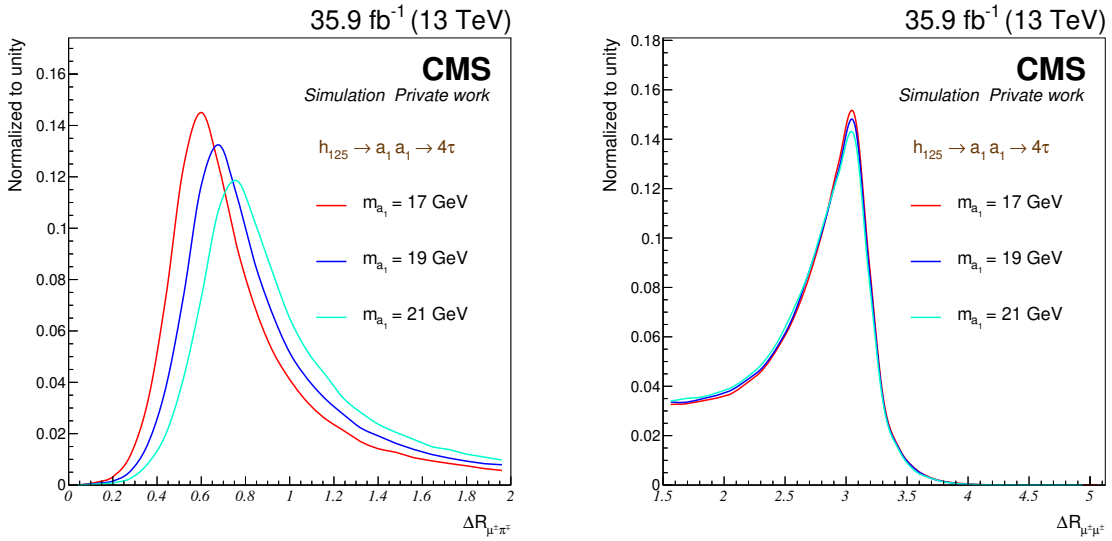

Figure 6.1: Distributions of ΔR for muon-track pairs (left) and same-charge muon-muon pairs (right) corresponding to high-mass points of the $h_{125} \to a_1 a_1 \to 4\tau$ channel in the ggF process. The distributions are obtained using generator-level information by selecting $\mu^{\pm}\pi^{\mp}$ and $\mu^{\pm}\mu^{\pm}$ pairs.

of muon-track pairs, which now tries to include events with less boosted a_1 bosons while keeping, at the same time, those of very boosted pseudoscalars. A "signal" track is chosen to accompany its muon partner (opposite charge) if the angular separation between them is $\Delta R_{\mu,trk} < 1.5$, and the reconstructed p_T of the muon-track pair is $p_T^{\text{Reco}} = |\vec{p}_\mu + \vec{p}_{\text{trk}}|_T > 10$ GeV, so that they can represent a $a_1 \to \tau_\mu \tau_{\text{one-prong}}$ decay of a_1 masses up to ~ 21 GeV, see Fig. 6.1 (left). If more than one muon-track pair is found to fulfill the requirements, the pair with the highest p_T^{Reco} is selected. That selection results in four objects; the leading muon μ_L and its associated track trk_L, and the subleading muon μ_S and its associated track trk_S. Then, additional cuts on the invariant mass of each muon-track pair ($m_{\mu_{L(S)},trk_{L(S)}} < 22$ GeV) and on the total reconstructed invariant mass of the four objects ($m_{\mu_L,trk_L,\mu_S,trk_S} < 125$ GeV) are applied. The implementation of the previous cuts is quite self-explanatory. Once these four objects are identified, a cone of $\Delta R = 0.5$ with axis along the object's momentum direction is constructed around each of them. The number of tracks (track multiplicity) nearby ($\Delta R < 0.5$) to each of the objects is counted, with the condition that the four objects are excluded from that counting. Discarding the object's tracks from being counted avoids including the own object's track or the surrounding partner's track in the multiplicity associated with a given object. This is fundamental upon establishing an isolation criterion for each of the four objects. The four resulting distributions are shown in Fig. 6.2, where the prediction from MC simulation is compared to the data. For the signal, the previous benchmark value ($\mathcal{B}(h_{125} \to a_1 a_1)\mathcal{B}^2(a_1 \to \tau\tau) = 0.2$) is assumed here and throughout this section. Then, a muon-track system is accepted as an a_1 candidate if both the muon and the track have no "isolation" tracks (zero track multiplicity) within the cone of $\Delta R = 0.5$. That is to say, the SR is defined as that having four isolated objects (two a_1 candidates). In this way, it is expected that the signal acceptance remain reasonably good in the entire mass range $4 \leq m_{a_1} \leq 21$ GeV, while the background is kept at a very low rate.

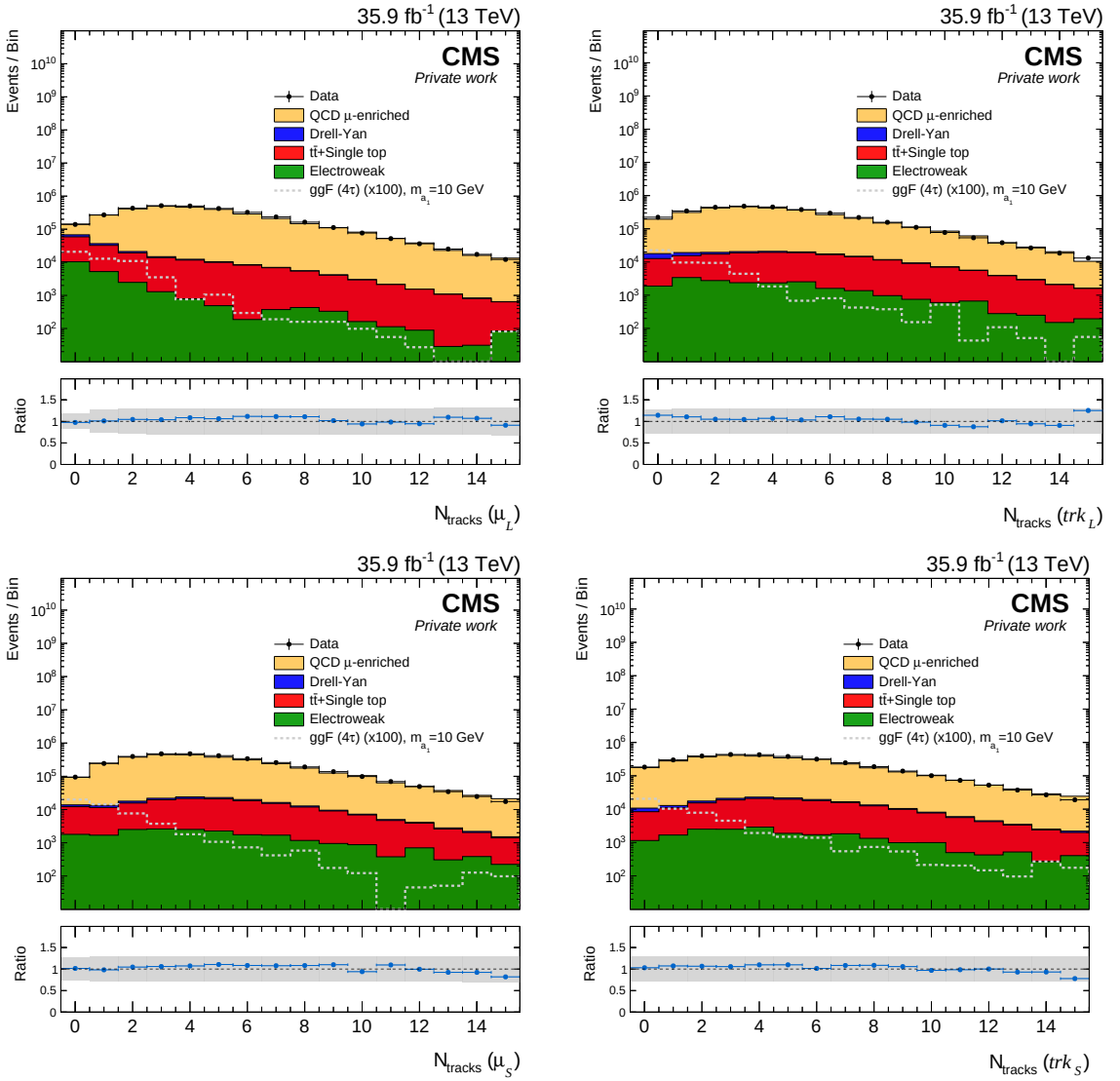

Figure 6.2: Distributions of track multiplicity (N_{tracks}) associated to each of the four selected objects; μ_L (upper left), trk_L (upper right), μ_S (lower left), and trk_S (lower right).

The number of observed events with this selection in the SR is 1979. The number of expected background events obtained from simulation is compatible with that number, but the uncertainty is again large due the limited size of the QCD multi-jet sample. The QCD multi-jet background is the dominant one, but the composition of the total background is different compared to the previous selection. The Drell-Yan process now contributes to roughly $\sim 8\%$ of the total background, and the top-quark ($t\bar{t}$ + Single top) and vector boson (electroweak) production processes are estimated to represent $\sim 1\%$ each. The values of the signal acceptance with the new selection are reported in Tab. 6.1 for a few representative mass points. These values are compared with those obtained with the previous selection. It can be seen that the new selection tends to provide more uniform values of acceptance while maintaining comparable performance for low and intermediate masses. Even so, the acceptance in the 4τ channel for the mass point $m_{a_1} = 21$ GeV is a factor ~ 2.5 less than for

$m_{a_1} = 4$ GeV. This difference is expected to be compensated by better discrimination against the background in terms of distributions, so that the sensitivity remains on an approximately same level.

Table 6.1: Comparison between the signal acceptances (for ggF) obtained using the two selection strategies employed for the cut-based and for the MVA-based approach respectively.

m_{a_1} [GeV]	Acceptance $\times 10^4$			
	"This selection" (Subsec. 6.1.2)		"Previous selection" (Subsec. 5.3.2)	
	4τ	$2\mu 2\tau$	4τ	$2\mu 2\tau$
4	2.64 ± 0.16	65.5 ± 1.2	3.29 ± 0.16	89.3 ± 1.4
10	1.63 ± 0.12	42.4 ± 1.1	1.46 ± 0.11	47.1 ± 1.2
15	1.49 ± 0.12	36.5 ± 1.0	0.21 ± 0.04	3.5 ± 0.3
21	1.09 ± 0.10	30.0 ± 0.9	-	-

The new selection partially solves the problem for large masses, however, the low mass points seem to have seen their acceptance reduced with respect to the previous selection. This could potentially result in an even worse performance of the analysis for very low pseudoscalar masses. The strategy to tackle this problem is to exploit a larger variable space, which, with proper use, should produce greater discriminating power. In the next subsection, the implementation of this scheme by means of MVA techniques is discussed.

6.1.3 Final Discriminant

Certainly, one of the most currently used techniques (MVA) to classify data with tremendous efficiency relies on machine learning algorithms. The underlying reason is that the way to optimize the parameters of the function $t(\vec{x})$ (see Subsec. 5.1.4) is, in general, extremely complicated. So, resorting to computational algorithms seems to be the best option to achieve good performance. One of the simplest algorithms is the decision tree, a binary classifier based on consecutive splits (yes/no) on one variable x_i at time. The task is to determine the best possible decision boundary between signal-like and background-like events using event samples of known class (signal or background). First, a cut is applied on the variable with the best separation between signal and background, then a second variable (can be the same) is used to further separate the resulting regions into two sectors, similarly with a third variable, and so on. The process stops when some predefined criteria are met. By then, the variable space will be already divided into sectors that are classified as signal or background, depending on the majority of training events encountered in that region; sometimes just a sort of weight is given to each sector (leaf node). In Fig. 6.3, a simplified illustration of a decision tree can be observed. The figure outlines the mechanism to grow a decision tree from cuts in the discriminant variables. The foremost shortcoming of this simple algorithm is that it tends to be unstable with respect to fluctuations in the training sample (overtraining), so an improved version employing several decision trees (forest) has been de-

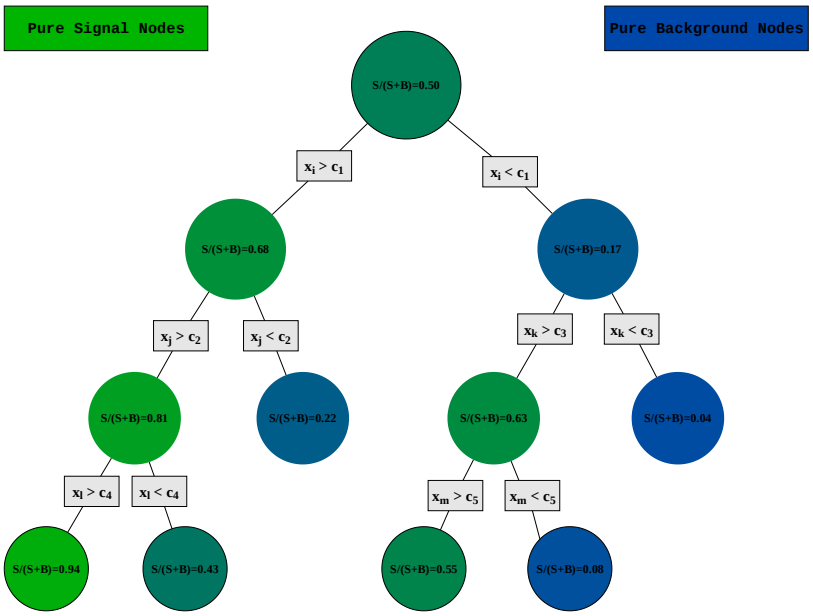

Figure 6.3: Sketch representing the structure of a decision tree. The discriminating variables $x_{i,j,k,l,m}$ are used to create nodes via decision cuts c_n. The nodes are classified as more-signal-like (green) or more-background-like (blue) depending on the proportion of training events of each type that fall into them.

veloped [377]. The method is called boosted decision trees (BDT), and the main idea is to classify an event according to the majority of individual tree "votes" in the forest. The BDT method uses the so-called "boosting algorithms" to combine the response of the individual trees, which turns it into a more powerful and stable classifier compared to a single tree. The BDT method has received lately quite a bit of attention in particle physics due to its great performance, sometimes even equating or surpassing that of the neural networks. The main core of this MVA-based approach is the use of the BDT response as the final discriminant in the statistical analysis.

First of all, upon increasing the dimension of the variable space, much more data is needed in order to have a decent description of the multidimensional distribution. In the cut-based approach, the $\sim 50 - 300$ simulated events falling in the SR for the signal samples (ggF-4τ) were just enough to describe the 2D (m_1, m_2) distribution of the signal processes. However, it is clear that this sample size is not sufficient to carry out a multivariate analysis in higher dimensional spaces. The situation is not very different with the new selection, for which the acceptance values remain of the same order of those in the previous selection. Although the di-muon trigger was found to be the best option for the complicated signal topology, already at the trigger level, the values of the acceptance are of the order of 10^{-3} for the 4τ channel. This, along with the offline selection, means that signal samples with approximately 10^8 events would be required in order to have a reasonable number of events in the SR. Submitting that huge amount of events to the lengthy simulation process (Subsec. 4.3.2) turns out to be rather impractical. The solution was to utilize an event filtering method at

generation level to mimic the selection of the same-charge di-muon trigger (Subsec. 6.1.1), thereby managing to simulate samples of approximately the same size as the nominal ones (without any filtering), but with much higher overall trigger efficiency. The same-charge di-muon enriched samples have an overall trigger efficiency greater than 85%, and acceptance values in the SR increased by a factor $\sim 250 - 300$ with respect to the nominal samples. The resulting SR sample (25k-70k events, depending on the mass point) of the signal processes would serve to train the BDT against the sample describing the background (derived from data in a control region, see Subsec. 6.1.4).

Unlike the training procedure, the event classification can still be done using the nominal signal samples, as the relevant distribution to describe is the binned 1D BDT response. For the training, rather than building separate categories for each process or channel, all of them are combined into a single signal category that contains weighted events from all components. The events from each production mode or decay channel are weighted according to its relative yield contribution in the SR with respect to that of the 4τ channel for the ggF process. The training is individualized for each mass point, i.e. the combined event sample in the SR for a particular mass point is used to train the BDT against the background sample (same for all mass hypotheses), and the resulting classifier is only used to obtain the BDT responses corresponding to that mass point. The above guarantees the maximum possible discriminating power since a BDT training based on a combination of signal mass hypotheses would lead to a complete loss of sensitivity.

The group of variables used for classification are common to all regions (SR and sideband regions), and they are formed by kinematic quantities involving a few or all the four objects $(\mu_L, trk_L, \mu_S, trk_S)$ representing the a_1 candidates. The SR was defined in Subsec. 6.1.2, while definitions for the other control regions used for background modeling can be found in Subsec. 6.1.4. In total 10 variables were used:

- $\Delta R_{\mu_L,\mu_S}$: distance in η-ϕ plane between the leading and the subleading muon.
- m_{μ_L,trk_L}: reconstructed invariant mass of the leading muon and associated track.
- m_{μ_S,trk_S}: reconstructed invariant mass of the subleading muon and associated track.
- $p^{\text{Reco}}_{T_{\mu_L,trk_L}}$: reconstructed p_T of the leading muon and associated track.
- $p^{\text{Reco}}_{T_{\mu_S,trk_S}}$: reconstructed p_T of the subleading muon and associated track.
- $\Delta R_{\mu_L,trk_L}$: distance in η-ϕ plane between the leading muon and associated track.
- $\Delta R_{\mu_S,trk_S}$: distance in η-ϕ plane between the subleading muon and associated track.
- $\Delta\phi_{\vec{p}_{T_{\mu_S,trk_S}}^{\text{Reco}},\vec{E}_T^{miss}}$: difference in azimuthal angle ϕ between the reconstructed $\vec{p}^{\,\text{Reco}}_{T_{\mu_S,trk_S}}$ (subleading muon and associated track) and the transverse vector of the missing momentum $\vec{E}_T^{miss}$.
- $m_{\mu_L,trk_L,\mu_S,trk_S}$: reconstructed invariant mass of the four objects.
- $m_{\mu_L,trk_L,\mu_S,trk_S,E_T^{miss}}$: reconstructed invariant mass of the four objects plus the missing four-momentum (assuming zero mass and zero z component).

From the previous group of variables, some pairs would seem to have a high correlation, which would worsen the performance of the BDT. But in reality, the linear Pearson correlation coefficients remain with absolute value below 20% for most pairs, and for those which exceed that value in a given class (signal or background), the corresponding coefficients in the other class acquire a low value. The most discriminating variables tend to be m_{μ_L,trk_L} and m_{μ_S,trk_S} for large a_1 masses, and $\Delta R_{\mu_L,trk_L}$ and $\Delta R_{\mu_S,trk_S}$ for low a_1 masses. An example of the signal and background distributions for $m_{a_1} = 10$ GeV is shown in Fig. 6.4. The background

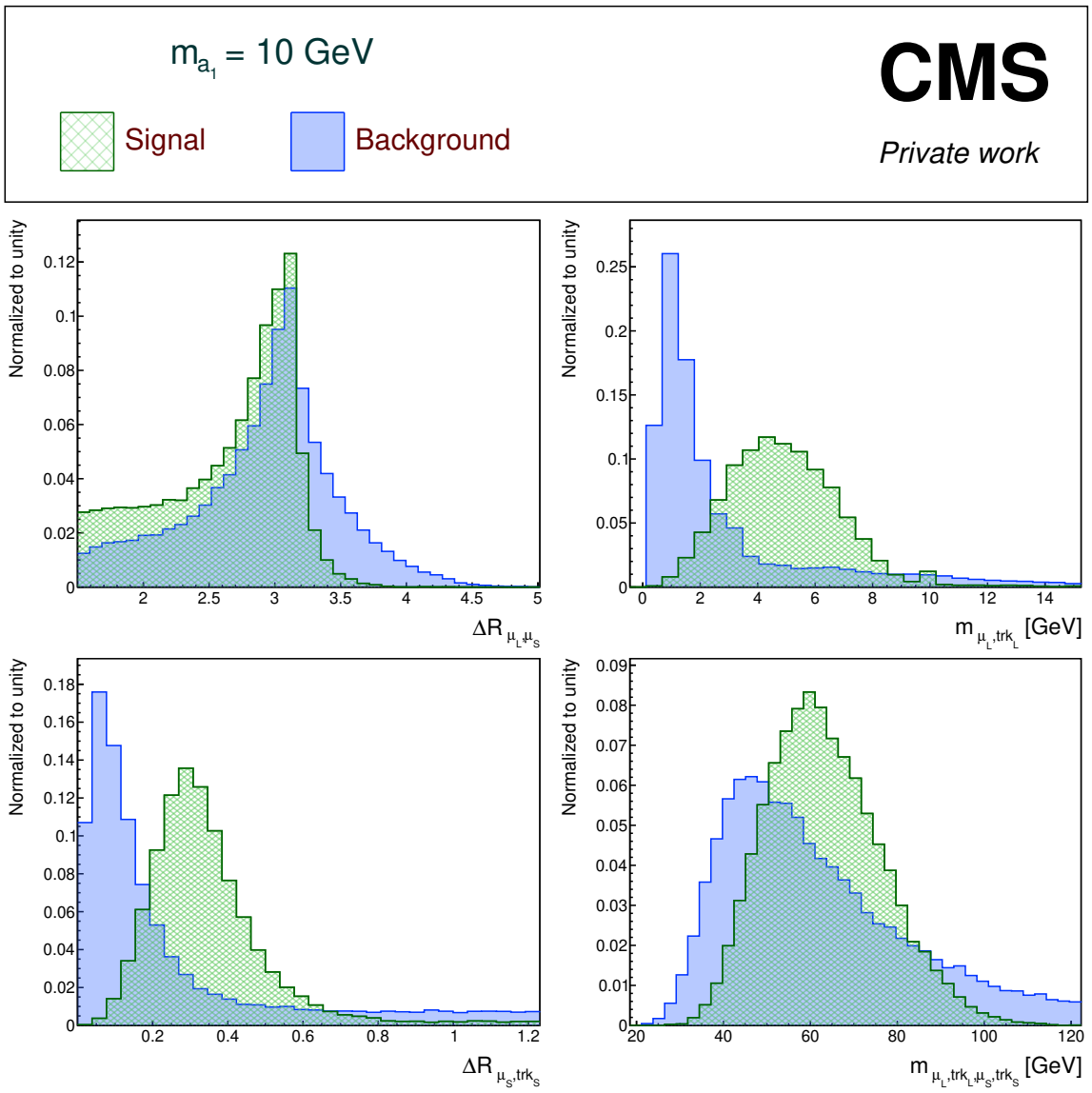

Figure 6.4: Four of the distributions used in the BDT to discriminate between signal and background. The normalized signal distributions (green) correspond to the combined event sample in the SR for the mass hypothesis $m_{a_1} = 10$ GeV. The normalized background distributions (blue) correspond to that of the control sample designed to model the background in the SR, independently of the mass point (see Subsec. 6.1.4).

distribution used for training is the same for all mass hypotheses. However, the BDT response

for the background is mass-point dependent since it is based on the algorithm resulting from the training and, as already mentioned, in this analysis the training has been executed individually for each signal hypothesis. That is the reason why the BDT output distribution of the background model might differ quite a bit for distinct mass points.

The final discriminant of this analysis simply consists of the BDT output distribution (real values between -1 and 1). The closer the BDT response to -1, the more likely it is that the event belongs to the background class, and vice versa. The Fig. 6.5 is an example of the above stated, and, at the same time, it represents an illustration of a standard overtraining check of the classifier. The figure shows a comparison between the BDT response obtained for the training and testing samples in both the signal class and the background class; the BDT classifier is that corresponding to the mass hypothesis $m_{a_1} = 10$ GeV. For the rest of the classifiers, the same procedure was performed and the results were satisfactory as well. The

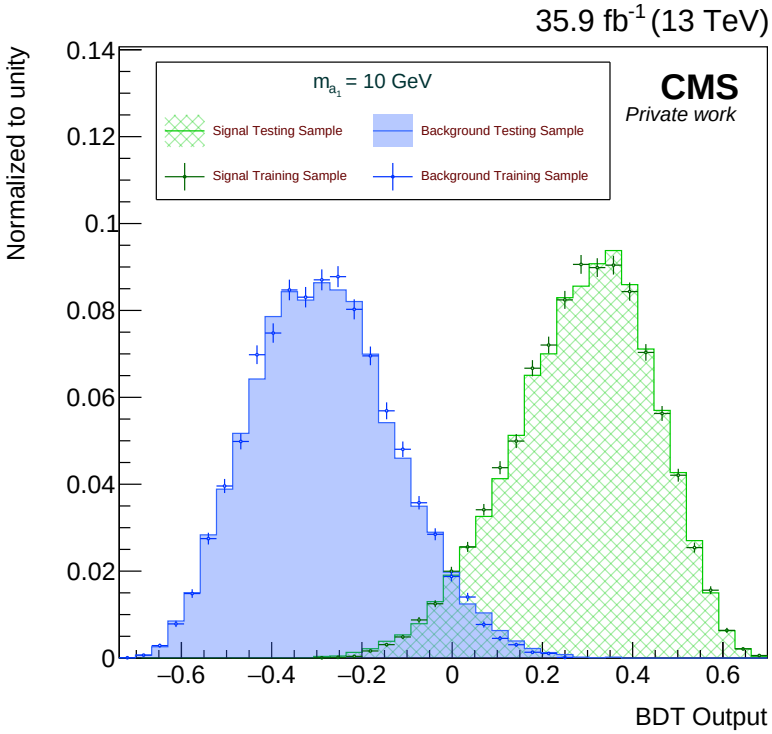

Figure 6.5: Overtraining check of the BDT classifier. The BDT responses on the testing (histograms) and training (points with error bars) samples are compared for both classes. The classifier corresponds to the mass point $m_{a_1} = 10$ GeV.

binning of the BDT output distribution is individually optimized for each mass hypothesis so that the final discriminant provides the best possible separation. For a given mass hypothesis, the signal distribution is completely determined by the simulation, with the normalization adjusting to the value of the parameter of interest μ. In contrast, only the shape of the background distribution can be known from the data-driven estimation, the normalization remains unknown.

6.1.4 Background Modeling

Similarly to the cut-based approach, the estimation of the background in the SR via MC turns out to be impossible due to the lack of simulated data. Therefore, it has been necessary to resort to data-driven methods to model the background shape without any assumption on its normalization. Again, the construction of control regions for both the estimation and the validation of the background model is based on the relaxation of the isolation criteria imposed on the four selected objects. The definitions of these sideband regions exclude any intersection with the SR. That can be checked by looking at Tab. 6.2, which reports the way the different sideband regions are constructed and their respective sizes. Any comparison of the data-

Table 6.2: Sideband regions used to construct and validate the background model. The symbols N_{sig}, N_{iso} and N_{soft} denote the number of "signal", "isolation", and "soft" tracks, respectively, contained in a cone of $\Delta R = 0.5$ around a given object. The notation "μ_L and trk_L" ("μ_S and trk_S") means that both objects must satisfy the requirement.

Sideband region	μ_L and trk_L	μ_S and trk_S	Observed events
Semi-Iso	$N_{\text{iso}} = 0$	$N_{\text{iso}} > 0$, $N_{\text{sig}} > 0$	106 592
	or		
	$N_{\text{iso}} > 0$, $N_{\text{sig}} > 0$	$N_{\text{iso}} = 0$	
Leading-Iso	$N_{\text{iso}} = 0$	$N_{\text{iso}} > 0$, $N_{\text{sig}} > 0$	62 324
Loose-Semi-Iso	$N_{\text{iso}} = 0$	$N_{\text{iso}} > 0$, $N_{\text{sig}} = 0$	13 998
	or		
	$N_{\text{iso}} > 0$, $N_{\text{sig}} = 0$	$N_{\text{iso}} = 0$	
Loose-Leading-Iso	$N_{\text{iso}} = 0$	$N_{\text{iso}} > 0$, $N_{\text{sig}} = 0$	7 707

driven background modeling with MC simulation, beyond a simple check of the background composition of the various control region with respect to the SR, is almost impossible due to the lack of MC events and the complexity of the multidimensional distribution. In fact, it was verified from simulation that the composition of the background in all the control regions defined in Tab. 6.2 is similar to that of the SR (dominated by QCD-multi-jets) within the large statistical uncertainties of the latter, as well as that the signal contamination is less than 0.5% in all of them. In this case, the adopted strategy to validate the background modeling is based on successive closure tests. In the above table, it can be noticed that as one moves down in rows, the corresponding sideband region is closer to the SR (without ever reaching it). So, the premise is that the background distribution shape must remain the same as one gets closer to the SR, in order for the chosen region (the background model) to be a faithful model of the background in the SR.

The control region designated to be a representation of the background shape in the SR is the Semi-Iso. In this region, events are selected if they have one pair of objects (muon and associated track) completely isolated, while the other two objects can have any non-zero

number and type of tracks around them. The observed sample consists of 106 592 events, which represent a rather good size for the multivariate analysis. The Semi-Iso control region is employed both for BDT training in each mass scenario and for event classification, which eventually serves to build the BDT output distribution for the background model. This BDT response on the Semi-Iso sample is normalized to the unity and its normalization is kept as unknown throughout the whole statistical inference procedure.

A first attempt to carry out the closure tests could be to compare the shape of individual distributions in the Semi-Iso control region with those of the rest of the control regions. However, this would not yield any conclusive assertion about the similarity of the multidimensional distributions since the simple comparison of marginal distributions overlooks any possible difference in the correlation pattern that might exist between the distributions representing the two compared regions. That is the reason why a direct comparison of the BDT output distributions for the Semi-Iso and any other validation region is chosen to perform the validation test.

The first comparison is done with the Leading-Iso control region. In this region, the isolation conditions are restricted a bit more compared to the Semi-Iso, as only the leading muon and associated track can be fully isolated. The subleading muon and associated track must be completely anti-isolated. The events of this sample are classified using the BDTs obtained through the individualized training specified in Subsec. 6.1.3, which uses the Semi-Iso as background training sample and the SR for a particular mass point as training signal sample. The result of the comparison between the Leading-Iso and the Semi-Iso control regions is illustrated in Fig. 6.6 for two representative mass points. The figure shows a very

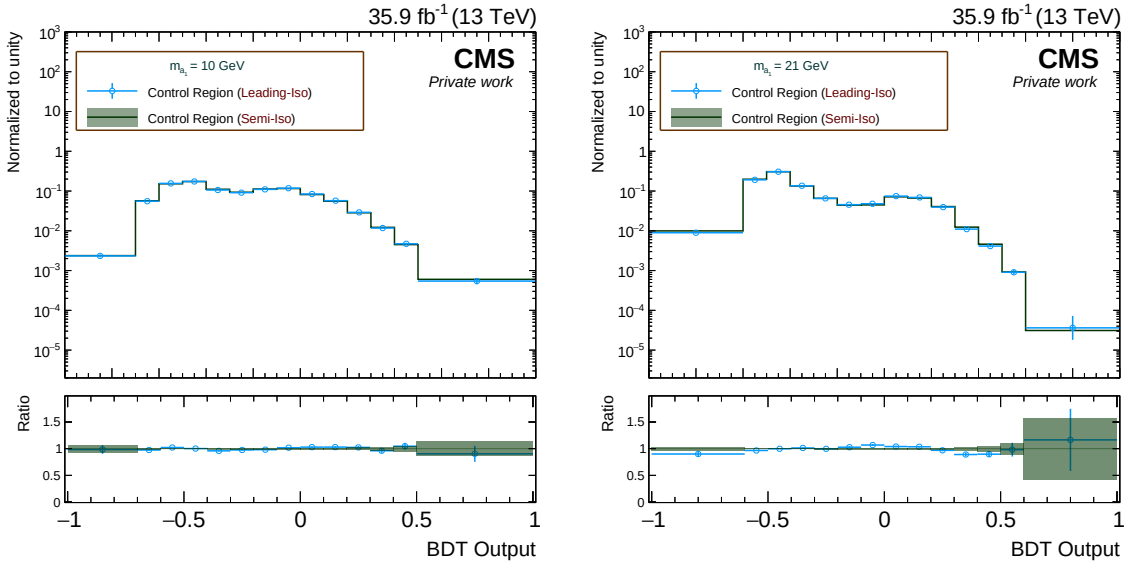

Figure 6.6: Comparison between the BDT output distributions for the background model (Semi-Iso) and the validation (Leading-Iso) control regions. The Semi-Iso (green) and the Leading-Iso (blue) distributions are shown for two illustrative signal mass scenarios $m_{a_1} = 10$ GeV (left) and $m_{a_1} = 21$ GeV (right).

nice agreement between both distributions (Semi-Iso vs Leading-Iso), thus suggesting that the relaxation condition weakly affects the distribution when applied on a muon-track pair solely. A similar result is obtained for the rest of the mass points.

The next comparison is then performed in the Loose-Semi-Iso control region. The region comprises events that feature one pair of objects completely isolated, and a second pair having any non-zero number of "soft" tracks, while the number of "signal" tracks is kept equal to zero for all objects. The definition of this region is similar to that of the Semi-Iso control region, but now the relaxation in the isolation only involves "soft" tracks rather than any kind of them. The shape comparison is shown in Fig. 6.7. The agreement is still good, however,

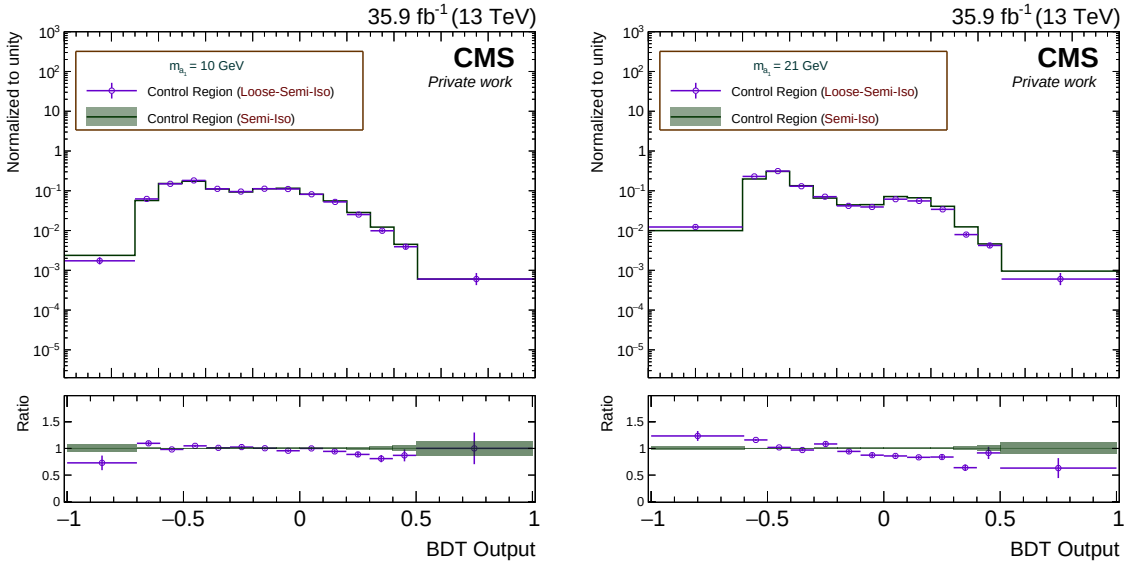

Figure 6.7: Comparison between the BDT output distributions for the background model (Semi-Iso) and the validation (Loose-Semi-Iso) control regions. The Semi-Iso (green) and the Loose-Semi-Iso (purple) distributions are shown for two illustrative signal mass scenarios $m_{a_1} = 10$ GeV (left) and $m_{a_1} = 21$ GeV (right).

for some bins, one can notice a larger discrepancy compared to the previous case. The result might be indicating that the choice on the type of tracks utilized in the relaxation condition has a bigger impact on the distribution than the number of fully isolated muon-track pairs. For the other mass scenarios, the observed tendency is the same.

The last comparison is done in a control region that incorporates the two above-mentioned effects; the region is called Loose-Leading-Iso. The events are selected in this control region if they possess a leading muon and associated track completely isolated, and a subleading muon and associated track loosely isolated (i.e. with any number of "soft" tracks around them). This region is analogous to the Leading-Iso, but now only "soft" tracks are permitted to enter in the relaxation condition. It is also important to point out that the region comprises a rather small sample (see Tab. 6.2) and is regarded as the "closest" (with regard to the definition) to the SR. The result of the comparison is shown in Fig. 6.8. Similarly to the previous case, a small discrepancy can be observed between the two distributions, although larger bin errors are also present. The overall matching of the distributions is acceptable over the whole mass range.

The previous set of results allows validating, to some extent, the choice of the control region for the background modeling, which is primarily based on relaxation conditions in the isolation criteria. The small variations observed in the distributions as the isolation criteria are tightened allow concluding that the multivariate distribution is weakly affected by the

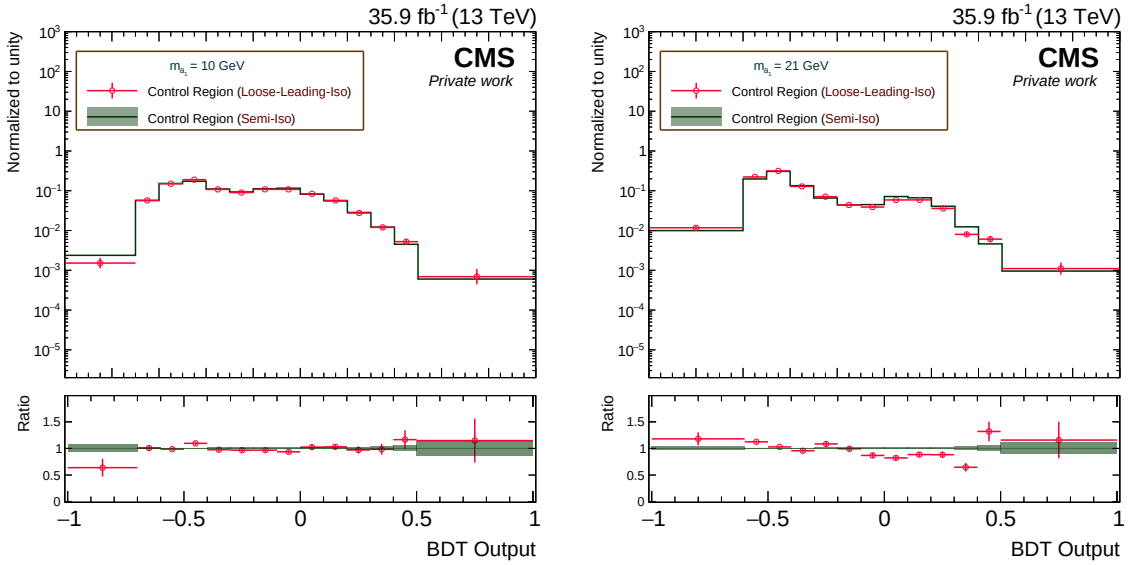

Figure 6.8: Comparison between the BDT output distributions for the background model (Semi-Iso) and the validation (Loose-Leading-Iso) control regions. The Semi-Iso (green) and the Loose-Leading-Iso (red) distributions are shown for two illustrative signal mass scenarios $m_{a_1} = 10$ GeV (left) and $m_{a_1} = 21$ GeV (right).

type of isolation imposed on the muon-track pairs. However, the agreement is not perfect across the set of control regions considered, so a criterion to avoid any possible bias in the selection of the background model must be taken into account. Analogously to the modeling of the background in the cut-based approach (Subsec. 5.3.4), a shape uncertainty is assumed for this distribution. The uncertainty is chosen to be that of the obtained difference between the nominal background control region (Semi-Iso) and the "closest" validation region to the SR (Loose-Leading-Iso), so that it covers the largest possible bin-by-bin deviation in the BDT output distribution. This systematic uncertainty is individually derived for each mass scenario, in accordance with the BDT training procedure adopted.

6.1.5 Signal Modeling

The signal BDT output distributions are derived using the simulated samples of the $h_{125} \to aa \to 4\tau$ and the $h_{125} \to aa \to 2\mu 2\tau$ channel. Similarly to the cut-based approach, the SM production cross-sections of h_{125} are assumed, and the relative contribution of $2\mu 2\tau$ channel is given by the relation (5.20). All the MC corrections mentioned in Subsec. 5.3.5 are applied to the simulated signal samples, and those affecting the shape of the BDT output are consistently transferred to such distribution.

6.1.6 Systematic Uncertainties

In this approach, most of the sources of systematic uncertainties affecting the signal model coincide with those of the cut-based approach (Subsec. 5.3.6). The only tiny difference comes from the propagation of the uncertainty in the track isolation efficiency (see Tab. 5.3) to the multivariate distribution, which is easily done with the help of an event-by-event reweighting on the BDT classification process.

In the case of the background model, the situation is a bit different since before several uncertainties were considered when deriving the 2D distribution. However, all biases related to the shape of the distribution are now integrated into the uncertainty derived with the Loose-Leading-Iso control region (Subsec. 6.1.4). The difference between this region and the Semi-Iso control region is meant to cover the largest possible bias in the selection of Semi-Iso as the shape of the background model. The other relevant aspect of the background model is the parameter associated with its normalization, which is kept unconstrained, identically to the cut-based case.

6.1.7 Results

To carry out the procedure of statistical inference, a similar procedure as before is adopted. First, the model for each mass scenario was subject to a maximum likelihood fit with the normalization of the signal and the background freely floating. The results of these fits are in accordance with the cut-based case, indicating that, if exists at all, the signal contribution for all mass hypotheses is expected to be very low. The maximum likelihood fit is then applied for the background-only scenario. The results for two representative mass points are shown in Fig. 6.9, which is also a pictorial representation of the final discriminant used for this approach. The better performance of the 4τ channel with respect to the $2\mu 2\tau$ can be noticed

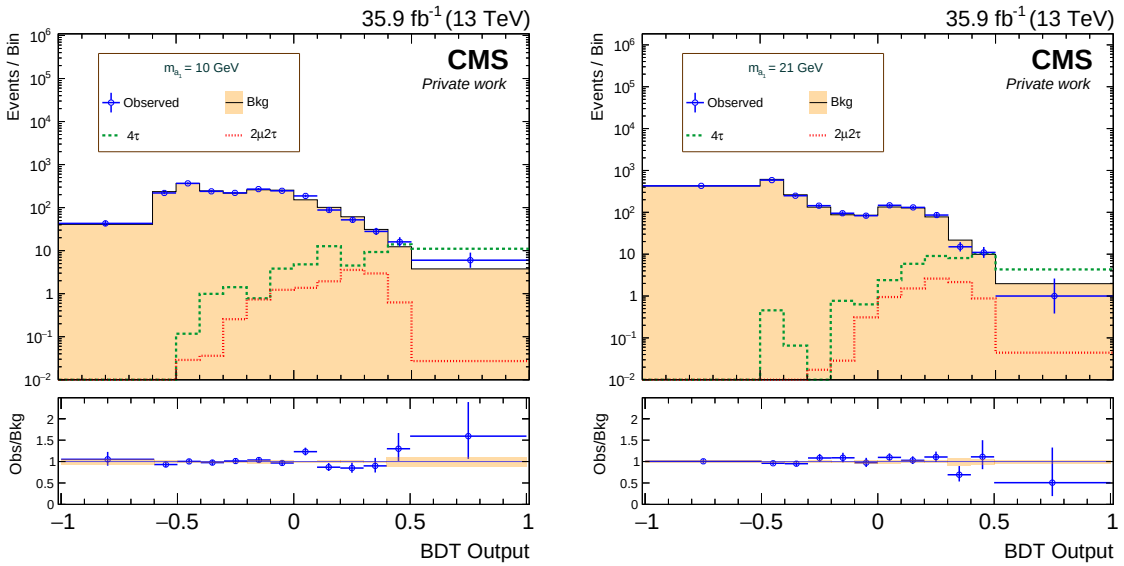

Figure 6.9: The final discriminant of the analysis for two mass scenarios $m_{a_1} = 10$ GeV (left) and $m_{a_1} = 21$ GeV (right). The observed number of events in each bin is represented by data points (blue) with error bars. The background distribution (black histogram with shaded error bands) shown in the plots has been obtained after a background-only fit to the data. The representative signal distributions (dashed histograms) include both the 4τ (green) and the $2\mu 2\tau$ (red) channels, and have been normalized to their corresponding event yields.

in the plots, something expected since the training has been performed mainly focusing on the 4τ channel. The comparison of the post-fit background distribution with the observed data does not reveal any significant excess that can be explained by the addition of the signal to the model. Then, to confirm the apparent absence of signal, the standard procedures of

hypothesis testing are used.

Goodness-of-fit tests were firstly used to check if the null hypothesis is favored by the data. The background-only hypothesis ($\mu = 0$) was tested for different mass scenarios with the help of the "saturated" model. The results of the tests for some mass points are presented in Tab. 6.3, where the p-values corresponding to each scenario have been reported. The

Table 6.3: Results of the goodness-of-fit test for the background-only hypothesis expressed in terms of p-values. Representative mass points were considered.

	p-value			
Hypothesis H_0	background-only			
m_{a_1}	4 GeV	9 GeV	15 GeV	21 GeV
Sat.	0.137	0.240	0.571	0.707

background-only model seems to describe well the data, so when confronting this hypothesis with the signal-plus-background hypothesis, the null hypothesis would likely be favored. The above is consistent with the results obtained with the cut-based analysis.

Later, upper limits on the signal strength modifier are set following the same procedure described in Subsec. 5.3.7. The upper limits are shown in Fig. 6.10. From the figure, it can be seen that, for this analysis, the observed limits are also compatible with the expected limits within one standard deviation. That is in agreement with the results obtained in Subsec. 5.3.7. The observed upper limits range from 0.059 at $m_{a_1} = 8$ GeV to 0.111 at $m_{a_1} = 6$ GeV, whereas the median expected upper limits range from 0.057 at $m_{a_1} = 9$ GeV to 0.119 at $m_{a_1} = 5$ GeV.

The MVA-based approach improves the limits for very low masses and relative high masses, while allows reaching with good sensitivity mass hypotheses of up to $m_{a_1} = 21$ GeV. Clearly, in the intermediate-mass range, for which the cut-based analysis has been optimized, the new strategy slightly worsens the constraints imposed on the strength modifier. This happens because, by increasing the maximum $\Delta R_{\mu,trk}$ between muons and tracks up to 1.5, background elements of larger invariant mass (e.g. bottomonia) are allowed to enter in the selection, thus leading to a poorer discriminating power for moderately heavy a_1 bosons (~ 9 GeV). On the contrary, for very light pseudoscalars the incorporation of new variables in the discrimination process seems to be the key to the improvement in performance, whereas for heavy bosons the increase in signal acceptance plays a decisive role. Either way, both analyses could be used as complementary to set the most stringent limits possible throughout the entire analyzed mass range.

6.2 Interpretation of the Results in the 2HDM+S Context

As was seen in Subsec. 3.2.5, the phenomenology of the 2HDM+S is very rich, comprising a great variety of possible scenarios. To a large extent, such a diversity is due to the existing four types of fermion couplings (see Tab. 3.3), which primarily dictate the phenomenology of $h_{125} \to a_1 a_1 \to f\bar{f}f'\bar{f}'$ decays. In the decoupling limit, once the type of fermion coupling has

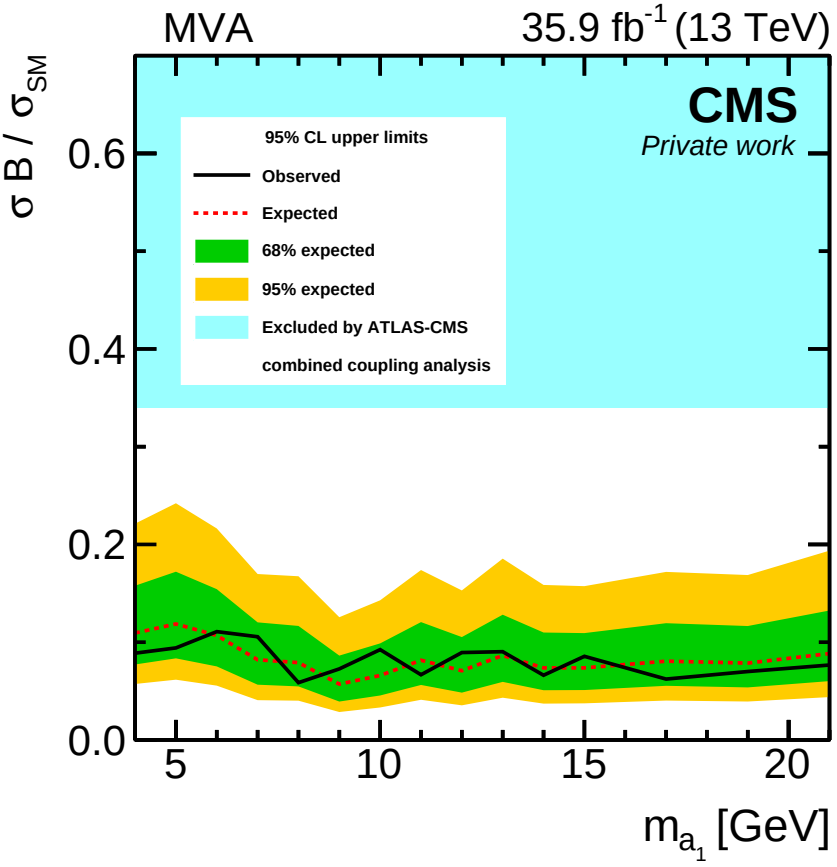

Figure 6.10: The observed and expected upper limits at 95% confidence level on the signal strength modifier for this MVA-based analysis. The shaded area in blue ($> 34\%$) indicates the excluded region for the branching ratio of h_{125} decaying into non-SM particles [355]. This result can be compared with the one shown in Fig. 5.14

been specified, the rest is determined by three independent parameters, which can be taken to be $\mathcal{B}(h_{125} \to a_1 a_1)$, $\tan\beta$, and m_{a_1}. Along this section, as the different scenarios of the model being used for interpretation are introduced, some details regarding their phenomenology are going to be added. For more information, the references [12, 378] provide a quite exhaustive discussion on the topic, including various decay width formulas at tree-level, and several calculations for the respective branching ratios.

The search described throughout these last two chapters, given the fact that it did not yield any concrete evidence of $h_{125} \to a_1 a_1$ decays, is used to constrain the parameter phase-space of the different types of 2HDM+S. The upper limits imposed on the normalized production cross-section times branching ratio (μ) of the process $h_{125} \to a_1 a_1 \to 4\tau$ are translated into restrictions for the model's free parameters. The above relies on dedicated calculations for the $\mathcal{B}(a_1 \to \tau\tau)$, a quantity that depends on the type of fermion coupling, and on the free independent parameters $\tan\beta$ and m_{a_1}. The remaining component of the total cross-section, i.e. $\sigma/\sigma_{SM}\,\mathcal{B}(h_{125} \to a_1 a_1)$, is consequently considered a free parameter as well. The scans corresponding to the values of $\mathcal{B}(a_1 \to \tau\tau)$ for different points in the phase-space are taken from [379], which are based on the calculations performed in the reference [378]. Those com-

putations include QCD corrections, possible mixing of the pseudoscalar with quarkonia, and threshold effects. In principle, both approaches discussed in the analysis could be taken to perform the interpretation of the experimental results, but for the purposes of this subsection, only the MVA-based approach will be considered. The upper limits shown in Fig. 6.10 were obtained for a series of generated mass points with a step of 1 or 2 GeV, so, for the purpose of this section, the trend is interpolated to calculate the corresponding limits for a larger number of mass points. That procedure is valid since the arrangement of generated mass points was chosen in such a way that none of the distributions used for the statistical inference is possible to resolve with a finer mass interval (< 1 GeV), that is, there is no possibility that any signal coming from a hypothetical intermediate-mass point would have escaped detection.

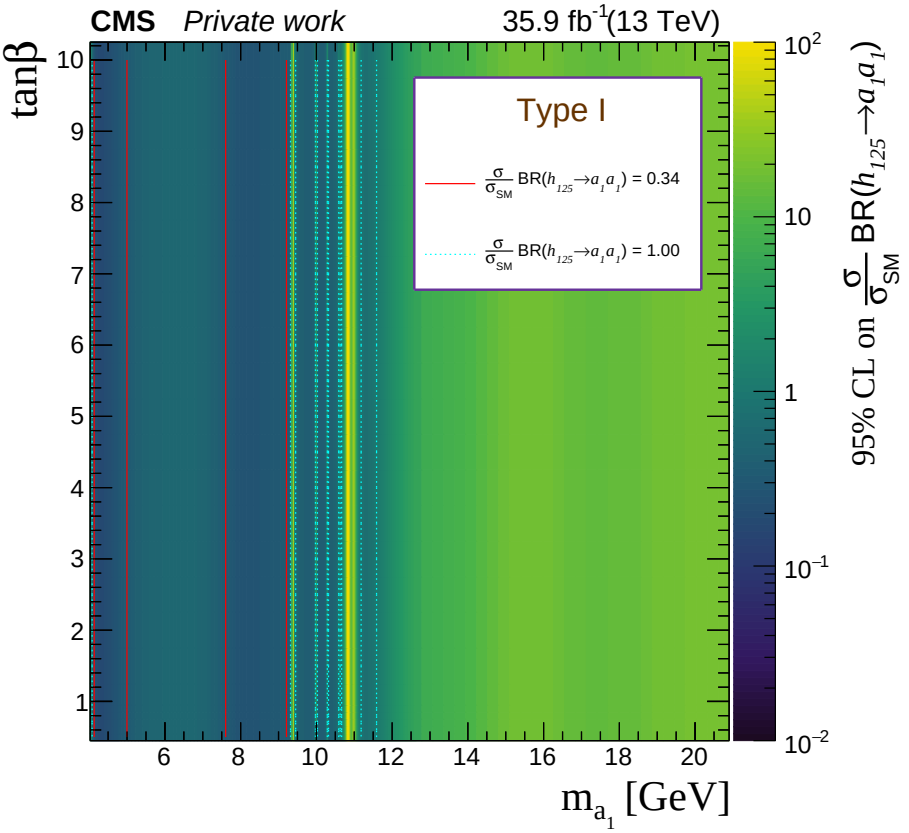

Figure 6.11: The observed upper limits at 95% CL on the parameter phase-space of the Type-I 2HDM+S. The contours corresponding to $\sigma/\sigma_{SM}\,\mathcal{B}(h_{125} \to a_1 a_1) = 1.00$ (cyan dashed line) and to $\sigma/\sigma_{SM}\,\mathcal{B}(h_{125} \to a_1 a_1) = 0.34$ (red solid line) are drawn in the plot as benchmarks.

The first type of 2HDM+S to consider is the simplest of all, the Type-I. As can be observed in Tab. 3.3, in this scenario all fermions couple only to H_2, so the couplings of the pseudoscalar to fermions are uniquely determined by the couplings of those to h_{125} in the SM multiplied by a common factor that is partially controlled by the mixing angle θ_a. That causes the $\mathcal{B}$s to be independent of $\tan\beta$, something easily deductible from Tab. 3.4, where a common coupling to A ($\pm\cot\beta$) is observed for all fermions. For this type of model, the 4τ and the $2\mu 2\tau$

channels are not particularly sensitive for a_1 masses above the b-quark pair threshold (~ 9 GeV), due to the already mentioned SM-like proportionality of the pseudoscalar couplings to the square of fermion masses (see Eqs. (3.6) and (5.20)). Above this threshold, the decays of a_1 to b-quark pairs largely dominate. That is clearly reflected in the results obtained for this type of model, which are shown in Fig. 6.11. The figure illustrates the observed limits converted into constraints of the 3D phase-space for the Type-I case. The ranges of the parameters $\tan\beta$ and m_{a_1} shown in this, and in the following figures, correspond to $[0.5, 10]$[1] and $[4, 21]$ GeV respectively. Note that for this case (Type-I), the axis associated to the parameter $\tan\beta$ is also present in the plot for the sake of uniformity, but it plays no role. Two benchmark scenarios for the parameter $\sigma/\sigma_{SM}\,\mathcal{B}(h_{125} \to a_1 a_1)$ have been added to the plot to facilitate the interpretation of the results. It can be seen in Fig. 6.11 that, for $\sigma/\sigma_{SM}\,\mathcal{B}(h_{125} \to a_1 a_1) = 1.00$ (if $\sigma = \sigma_{SM}$ this possibility is excluded by [355]), almost all m_{a_1} in the interval $[4, 9]$ GeV are excluded, whereas for $\sigma/\sigma_{SM}\,\mathcal{B}(h_{125} \to a_1 a_1) = 0.34$, only two subintervals in that range ($\sim [4, 5]$ GeV and $\sim [7.5, 9]$ GeV) are excluded; for the first case, there are other small intervals excluded above 9 GeV too. Despite having the experimental analysis (MVA-based approach) a very good sensitivity throughout the entire mass range, the model-type-dependent constraints are weakened above ~ 9 GeV, due to the suppression of the $a_1 \to \tau\tau$ decays with the opening of the $b\bar{b}$ channel.

The second model of interest is the so-called NMSSM-like version, namely, the Type-II 2HDM+S. According to Tab. 3.3, in this model, up-type fermions couple to H_2, whereas down-type fermions couple to H_1. This kind of specific coupling introduces an explicit dependence of the $\mathcal{B}$s on the parameter $\tan\beta$, as now fermions couple with a different proportionality factor to the pseudoscalar. For high values of $\tan\beta$ (> 1) the decays of a_1 to up-type fermions are suppressed, and for low values of $\tan\beta$ (< 1) these decays are enhanced; the other way around for down-type fermions. This makes the decay channels used in this analysis relatively sensitive for values of $\tan\beta > 1$ since otherwise, decays such as $a_1 \to cc$ tend to dominate over a wide range of masses. For a given value of $\tan\beta > 1$, the a_1 decays involving τ leptons must also compete with those yielding a pair of τ's down-type partners, so, for a_1 masses above the b-quark pair threshold, the leptonic decays are rarely produced, similarly to the Type-I case. The above is manifested in the limits illustrated in Fig. 6.12. As expected, for this model, the exclusion pattern is more complicated with respect to the previous one, although it is quite clear what has been stated above, namely, that the analysis is not able to constraints phase-space points with low $\tan\beta$. For $\tan\beta > 1$, the exclusion region is somewhat similar to that of the Type-I model, with the difference that now the excluded sector, for the benchmark scenarios considered $\sigma/\sigma_{SM}\,\mathcal{B}(h_{125} \to a_1 a_1) = 0.34\,(1.00)$, depends on $\tan\beta$. That gives rise to the peak-like shape of the contours in the mass regions where quarkonium states are supposed to be located. In the vicinity of these resonances, the a_1-quarkonium mixing begins to play a fundamental role, which traduces into an abrupt increase of the hadronic decay width. Such an increase for the hadronic modes via non-perturbative effects leads to the reduction of the $\mathcal{B}$s associated with decays to unbound systems, which evidently affects the $\tau\tau$ decays. That is the reason why the limits are less stringent in the regions comprising the $q\bar{q}$ resonances. The same explanation applies to the band-type exclusion pattern observed in Fig. 6.11 in these regions. Searches for a_1 particles in channels involving, for instance,

[1] Since $\tan\beta$ directly enters into the fermion couplings of the neutral scalars, its value must be bounded from below ($\tan\beta > 0.28$) and from above ($\tan\beta < 140\,(350)$) to avoid conflicts with perturbative unitarity [380].

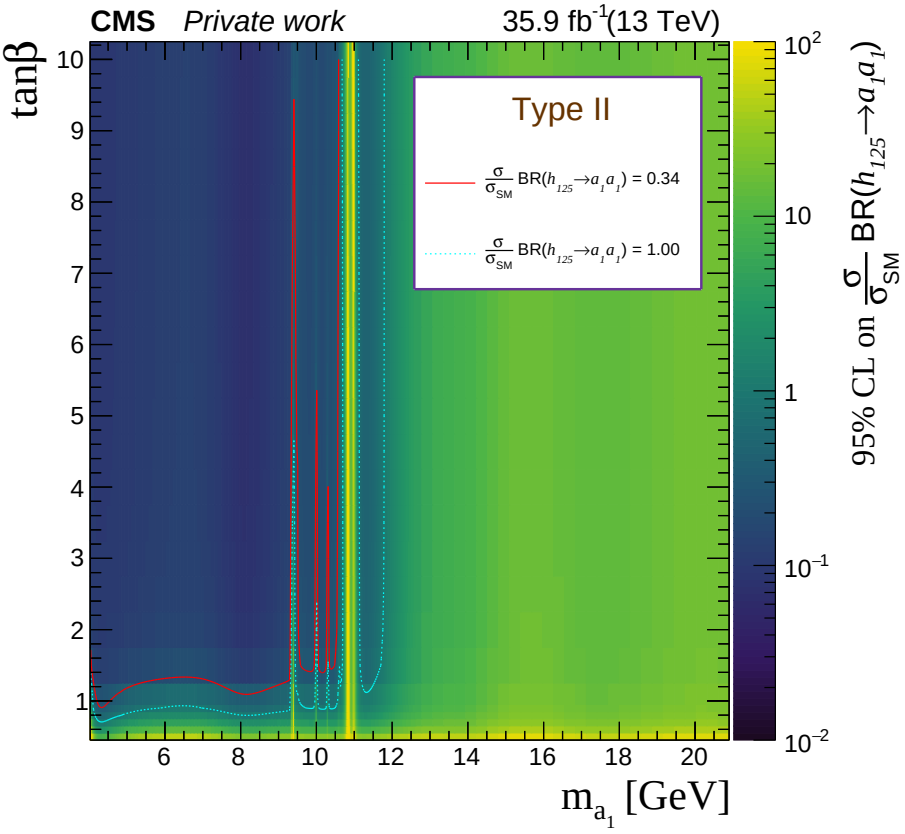

Figure 6.12: The observed upper limits at 95% CL on the parameter phase-space of the Type-II 2HDM+S. The contours corresponding to $\sigma/\sigma_{SM}\,\mathcal{B}(h_{125} \to a_1 a_1) = 1.00$ (cyan dashed line) and to $\sigma/\sigma_{SM}\,\mathcal{B}(h_{125} \to a_1 a_1) = 0.34$ (red solid line) are drawn in the plot as benchmarks.

$a_1 \to cc$ decays, would complement the results presented here for the Type-II model, as they are able to probe the region of low values of $\tan\beta$. Other alternatives using the $a_1 \to bb$ decay mode would serve as complementary for $m_{a_1} \gtrsim 10$ GeV.

Without doubt, the most interesting case for the search presented in this work is the Type-III model. As its nickname suggests, in this model, leptons couple to one of the $SU(2)$ doublets (H_1), whereas quarks are coupled to the other (H_2). This introduces a nice feature in this model, namely that, for relatively high values of $\tan\beta$, decays of a_1 to leptons can dominate over decays to quarks in the entire allowed mass range. This makes the $a_1 \to \tau\tau$ decay mode highly sensitive to this model, even for pseudoscalar masses above the b-quark pair threshold. That is evidenced in the results shown in Fig. 6.13. It can be clearly observed how, depending on the value set for $\sigma/\sigma_{SM}\,\mathcal{B}(h_{125} \to a_1 a_1)$, sectors of the phase-space with $\tan\beta > 1 - 2$ could be excluded for any value probed of the parameter m_{a_1}. Besides, the results for a_1 masses greater than 15 GeV are competitive in comparison with those of other dedicated analyses focusing on non-boosted topologies [359, 360]. However, for low values of $\tan\beta$, the analysis is not able to provide good constraints since, in this case, decays of a_1 to $b\bar{b}$ and $c\bar{c}$ are the ones that largely predominate. The above serves to motivate, despite the experimentally challenging environment, searches in boosted heavy-flavor di-jet topologies.

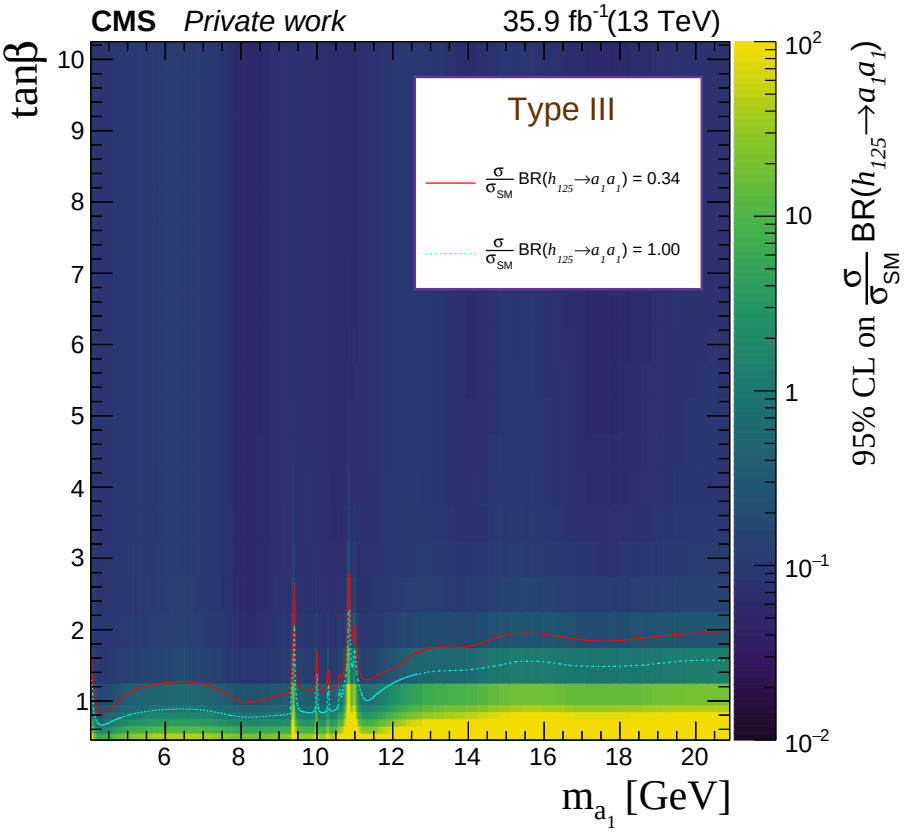

Figure 6.13: The observed upper limits at 95% CL on the parameter phase-space of the Type-III 2HDM+S. The contours corresponding to $\sigma/\sigma_{SM}\,\mathcal{B}(h_{125} \to a_1 a_1) = 1.00$ (cyan dashed line) and to $\sigma/\sigma_{SM}\,\mathcal{B}(h_{125} \to a_1 a_1) = 0.34$ (red solid line) are drawn in the plot as benchmarks.

While the Type-III happens to be the model to which the analysis is most sensitive, the Type-IV turns out to be totally the opposite. In this last scenario, up-type quarks and charged leptons couple to H_2, whereas down-type quarks couple to H_1. This means that, for $\tan\beta > 1$, decays to down-type quarks are enhanced with respect to the rest of fermions (see Tab. 3.4), so it is necessary to resort to decay modes such as $d\bar{d}$ or $s\bar{s}$ to be able to effectively probe a_1 masses below the b-quark pair threshold. Searches in channels involving decays to leptons can barely explore the region with $\tan\beta < 1$, although the $\tau\tau$ decay mode may be as sensitive as the $b\bar{b}$ for high a_1 masses. The results for this analysis are shown in Fig. 6.14. It can be noticed how the sensitivity to this model is in general quite low for high values of the parameter $\tan\beta$. Even for $\tan\beta < 1$, with relatively low values of the parameter $\sigma/\sigma_{SM}\,\mathcal{B}(h_{125} \to a_1 a_1)$, it would be practically impossible to exclude any region throughout the probed mass interval. This encourages to continue improving the results obtained in the 4τ and the $2\mu 2\tau$ channels with the design of more efficient signal-vs-background discrimination techniques, and with the addition of more experimental data in the future.

All results shown so far are only based on the observed upper limits and, although they

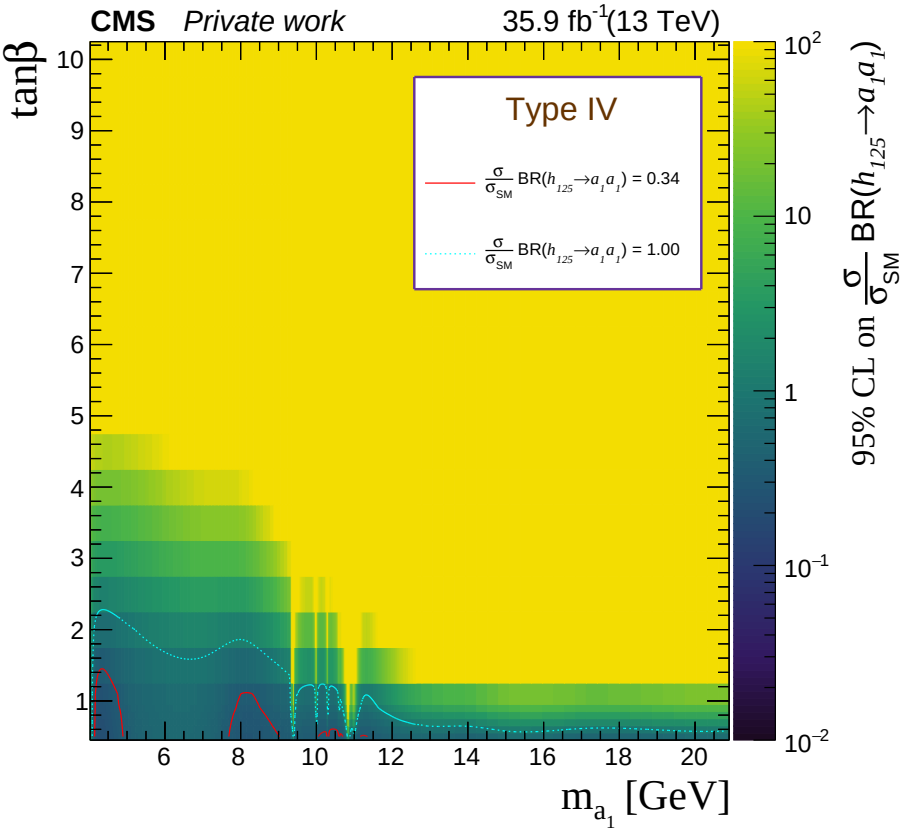

Figure 6.14: The observed upper limits at 95% CL on the parameter phase-space of the Type-IV 2HDM+S. The contours corresponding to $\sigma/\sigma_{SM}\,\mathcal{B}(h_{125} \rightarrow a_1a_1) = 1.00$ (cyan dashed line) and to $\sigma/\sigma_{SM}\,\mathcal{B}(h_{125} \rightarrow a_1a_1) = 0.34$ (red solid line) are drawn in the plot as benchmarks.

are illustrated in the most general way possible (3D template), sometimes the plots become a bit difficult to interpret. It is worth adding the expected limits to the results since they somehow reflect the impact of uncertainties in a better way. Including the expected limits in the previous figures seems to be rather impractical, as it would turn the plots too crowded. On the other hand, to ease the interpretation of the 3D templates, constant benchmark values have been assigned to the parameter $\sigma/\sigma_{SM}\,\mathcal{B}(h_{125} \rightarrow a_1a_1)$, but the same could have been applied to any other parameter. That is what has been implemented in the next set of plots, some benchmark values have been set for $\tan\beta$ depending on the model type, while the corresponding expected values of the parameter $\sigma/\sigma_{SM}\,\mathcal{B}(h_{125} \rightarrow a_1a_1)$ have been included. The Fig. 6.15 summarizes the results for all types of 2HDM+S considered. Now, the area above the observed (expected) limits is regarded as excluded for a given type of model with the corresponding fixed value of $\tan\beta$. It can be seen from the figure that the expected exclusion bands can vary the observed (expected) limit values for a given mass up to 100%.

Before concluding this section, it is pertinent to add some additional remarks. It is a known fact that the constraints on 2HDM+S are becoming increasingly stringent as more data is added. But the diversity presented by these types of models protects them from being

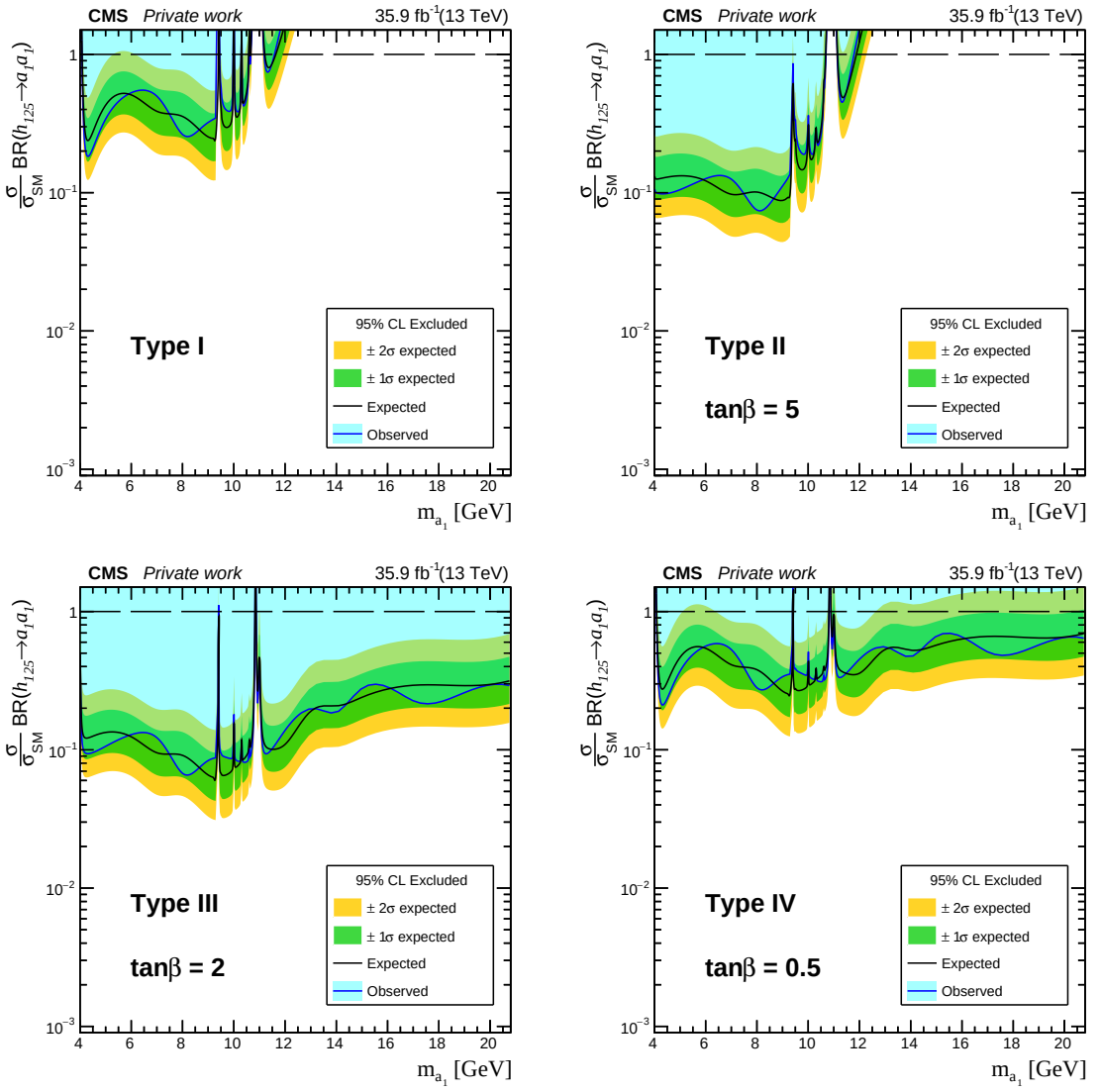

Figure 6.15: The observed and expected upper limits at 95% CL projected on the 2D parameter phase-space ($\sigma/\sigma_{SM}\,\mathcal{B}(h_{125} \to a_1 a_1)$ vs m_{a_1}) for fixed benchmark values of $\tan\beta$. The constraints for the four types of 2HDM+S considered are shown: Type-I (upper left), Type-II (upper right), Type-III (lower left), and Type-IV (lower right). The shaded area in light blue corresponds to the region excluded by the observed limits.

completely excluded by only a few physical analyses. The inclusion of many decay channels probing the entire possible mass range is required in order to further constraint the parameter phase-space. The CMS and ATLAS collaborations have an extensive program dedicated to the search for light pseudoscalars that comprises a wide spectrum of decay channels and analysis strategies. However, this is still not sufficient to reach each point of the parameter space, partly because the development of new experimental techniques is needed to discern complicated signatures, such as those involving multiple overlapped jets. Hopefully, that will motivate the emergence of fresh ideas and new efforts that help increase the variety and effectiveness of these searches.

CHAPTER

7

SUMMARY AND OUTLOOK

Over the years, the SM has proven to be a fabulous theory of the subnuclear scale, capable of demonstrating its validity in all types of experimental tests. However, it is still a model with serious drawbacks, which prevents it from being considered a complete description of nature. In an attempt to solve some of the limitations of the SM, many new theories have emerged with elegant proposals to replace it as the standard theory of fundamental interactions. One class of models simply modifies the symmetries or the field content of the theory in terms of new group representations, whereas another class completely abandons the concept of point-like particle and promotes it to another mathematically better-behaved entity. To this day, no strong evidence supporting new theories beyond the SM have been found in the countless measurements performed at the Large Hadron Collider.

Among the models preserving the concept of elementary particles, there is a group that suggests changes in the relatively under-explored scalar sector of the SM. Those changes generally result in an increased number of scalars in the theory, or in modifications of the properties of SM-like Higgs boson. So, one way of probing the viability of those models is looking for additional Higgs bosons through production or decay mechanisms induced by the presence of other particles. This thesis has focused on an search for light bosons produced in decays of the 125 GeV scalar, exploiting experimental signatures left by the decay of these to leptons. The search has been optimized to target the light boson mass region where decays to τ leptons could be enhanced, according to different models and scenarios.

Two different approaches have been considered to be able to experimentally resolve boosted and semi-boosted topologies. The first analysis has been optimized for very light bosons with masses between 4 and 15 GeV, for which a special technique for the identification of decay products coming from highly collimated τ pairs has been used. This analysis makes use of a 2D final discriminant to assess the possible presence of signal events in the observed data. The two observables utilized correspond to the invariant mass of the two light bosons, which is very well reconstructed in the case of muonic decays, and poorly reconstructed for decays into pairs of τ leptons. The statistical inference procedure reveled no compelling rea-

sons to discard the background-only hypothesis, therefore, limits were set on the production cross-section times branching ratio at 95% of confidence level. The highest sensitivity of this approach was reached for mass hypotheses around ~ 9 GeV, for which a good balance between signal acceptance and discriminating power was obtained. These results have been published in [318]. The second analysis was motivated by the decrease in sensitivity of the previous approach for masses outside the central region of the probed interval. It was determined that a combination of improved selection and better statistical discriminant could stabilize the sensitivity throughout the entire mass range, and that the latter could even be extended up to 21 GeV. In this approach, the event selection was made more inclusive, being now able to efficiently select events with boosted and not that boosted light bosons. To increase the separation power between hypotheses, a multivariate discriminant was utilized in this case. An individualized training was performed for each mass hypothesis, which resulted in a algorithm specially optimized for each instance. Once again, the results favored the background-only hypothesis and limits were imposed, thus reaffirming the absence of evidence of exotic Higgs decays into light bosons. This second approach managed to improve the limits obtained in the first analysis for very low and high masses. Both analyses used data from pp collisions at $\sqrt{s} = 13$ TeV, recorded by the CMS detector during the 2016 data taking period and corresponding to an integrated luminosity of 35.9 fb^{-1}.

The experimental results were further translated into constraints on the parameter phase-space of the 2HDM+S. The four types of fermion couplings covered by this model were analyzed. It was possible to corroborate the importance of the decay modes used in this work for the interval of masses studied. In particular, for the Type-III model, the analysis can exclude, depending on the benchmark scenario considered, regions of the parameter space with $\tan\beta > 1 - 2$ for any value probed of the boson mass. For other cases, the analysis is mainly sensitive for masses below 10 GeV.

Despite having found no sign of exotic Higgs decays into light bosons, there is still a lot of data to be analyzed and to be collected. Until this moment, the LHC has already delivered more than 150 fb^{-1} of data, and in the next few years, this figure will be doubled. In the future, the total amount of available data is expected to be about 3000 fb^{-1}. Furthermore, the implementation of new experimental particle identification techniques could considerably improve the results. In particular, the design of an algorithm able to identify pairs of (semi)collimated τ leptons could certainly boost the performance of the analysis since it would provide a better reconstructed invariant mass for the light boson. Moreover, the relevant theoretical models possessing a light boson in its spectrum still have enough parameter phase-space to be explored. That is the case of the 2HDM+S, which demands a large number of studies in various decay modes to be totally excluded. For other models, like the dark photon, it would be beneficial to include searches in the 4μ channel spanning the whole mass range up to 62.5 GeV. The $4b$ channel and others decay modes involving jets turn out to be of particular interest for the other two introduced models.

To conclude, it is essential to continue looking for new strategies and methods capable of intensifying the hunting of light bosons. That seems to be a promising approach to search for physics beyond the SM.

BIBLIOGRAPHY

[1] A. Einstein, "Zur Elektrodynamik bewegter Körper", *Annalen der Physik* **322** (1905), no. 10, 891–921, doi:10.1002/andp.19053221004. 1

[2] M. Born, "Über Quantenmechanik", *Zeitschrift für Physik* **26** (Dec, 1924) 379–395, doi:10.1007/BF01327341. 1

[3] J. Mnich, "Overview of standard model results from LEP and Tevatron", *Czech. J. Phys.* **54** (2004) A193–A205. 1

[4] CMS Collaboration, "Summaries of CMS cross section measurements". https://twiki.cern.ch/twiki/bin/view/CMSPublic/PhysicsResultsCombined. Accessed: 2020-01-24. 1

[5] ATLAS Collaboration, "Standard Model Summary Plots Summer 2019", Technical Report ATL-PHYS-PUB-2019-024, CERN, Geneva, Jul, 2019. 1

[6] Particle Data Group Collaboration, "Review of Particle Physics", *Phys. Rev.* **D98** (2018), no. 3, 030001, doi:10.1103/PhysRevD.98.030001. 1, 52, 53, 63

[7] G. Aad et al., "Observation of a new particle in the search for the Standard Model Higgs boson with the ATLAS detector at the LHC", *Physics Letters B* **716** (Sep, 2012) 1–29, doi:10.1016/j.physletb.2012.08.020. 1, 47

[8] S. Chatrchyan et al., "Observation of a new boson at a mass of 125 GeV with the CMS experiment at the LHC", *Physics Letters B* **716** (Sep, 2012) 30–61, doi:10.1016/j.physletb.2012.08.021. 1, 47

[9] J. D. Lykken, "Beyond the Standard Model", in *CERN Yellow Report CERN-2010-002, 101-109*. 2010. arXiv:1005.1676. 2

[10] J. D. Wells, "The Once and Present Standard Model of Elementary Particle Physics", arXiv:1911.04604. 2

[11] F. Quevedo, S. Krippendorf, and O. Schlotterer, "Cambridge Lectures on Supersymmetry and Extra Dimensions", arXiv:1011.1491. 2, 57

[12] D. Curtin et al., "Exotic decays of the 125 GeV Higgs boson", *Phys. Rev.* **D90** (2014), no. 7, 075004, doi:10.1103/PhysRevD.90.075004, arXiv:1312.4992. 2, 60, 62, 64, 65, 66, 96, 134

[13] W. Heisenberg, "Über den anschaulichen Inhalt der quantentheoretischen Kinematik und Mechanik", *Zeitschrift für Physik* **43** (Mar, 1927) 172–198, doi:10.1007/BF01397280. 4

[14] E. Schrödinger, "An Undulatory Theory of the Mechanics of Atoms and Molecules", *Phys. Rev.* **28** (Dec, 1926) 1049–1070, doi:10.1103/PhysRev.28.1049. 4

[15] L. Alvarez-Gaumé and M. A. Vázquez-Mozo, "An invitation to quantum field theory". Lecture Notes in Physics. Springer, Berlin, 2011. 4, 36

[16] F. Mandl and G. G. Shaw, "Quantum field theory; 2nd ed.". Wiley, New York, NY, 2010. 4, 5, 22, 24, 30, 36, 37, 40

[17] W. Greiner and J. Reinhardt, "Field quantization". Springer, Berlin, 1996. 4, 5, 18, 23, 27, 30, 45

[18] M. E. Peskin and D. V. Schroeder, "An Introduction to quantum field theory". Addison-Wesley, Reading, USA, 1995. 4, 22, 30, 34, 36, 40, 82

[19] H. Kleinert, "Particles and Quantum Fields". World Scientific, 2016. 4, 36

[20] S. Weinberg, "The Quantum Theory of Fields", volume 1. Cambridge University Press, 1995. 4, 36, 39

[21] L. D. Landau and E. M. Lifschits, "The Classical Theory of Fields", volume 2 of *Course of Theoretical Physics*. Pergamon Press, Oxford, 1975. 4

[22] E. Noether, "Invariante Variationsprobleme", *Nachrichten von der Gesellschaft der Wissenschaften zu Göttingen, Mathematisch-Physikalische Klasse* **1918** (1918) 235–257. 5

[23] A. C. Esq., "On the theory of groups, as depending on the symbolic equation $\theta^n = 1$", *The London, Edinburgh, and Dublin Philosophical Magazine and Journal of Science* **7** (1854), no. 42, 40–47, doi:10.1080/14786445408647421. 7

[24] A. G. Kurosh and K. Hirsch, "Theory of Groups, Volume 2". Ams Chelsea Publishing. Chelsea Publishing Company, 1960. 7

[25] J. G. Belinfante, B. Kolman, and H. A. Smith, "An Introduction to Lie Groups and Lie Algebras, with Applications", *SIAM Review* **8** (1966), no. 1, 11–46. 7, 15

[26] D. W. Robinson, "The differential and integral structure of representations of Lie groups", *Journal of Operator Theory* **19** (1988), no. 1, 95–128. 7

[27] R. N. Cahn, "Semisimple Lie algebras and their representations". 1985. 7

[28] B. Hall, "Lie Groups, Lie Algebras, and Representations: An Elementary Introduction". Graduate Texts in Mathematics. Springer, 2003. 7, 9, 12, 14

[29] M. Hamermesh, "Group theory and its application to physical problems". Dover, New York, NY, 1989. 10

[30] G. 't Hooft, "50 Years of Yang-Mills theory". World Scientific, Singapore, 2005. 10, 30

[31] A. Barut and R. Raczka, "Theory of Group Representations and Applications". World Scientific, 1986. 13

[32] H. R. Karadayi and M. Gungormez, "An explicit construction of Casimir operators and eigenvalues. I", *Journal of Mathematical Physics* **38** (1997), no. 11, 5976–5990, doi:10.1063/1.532175. 13

[33] C. Dodson and T. Poston, "Tensor Geometry: The Geometric Viewpoint and Its Uses". Graduate Texts in Mathematics. Springer-Verlag, 1991. 13

[34] W. Greiner and B. Müller, "Representations of the Permutation Group and Young Tableaux". Springer Berlin Heidelberg, Berlin, Heidelberg, 1994. 14, 15

[35] T. Ohlsson, "Relativistic Quantum Physics: From Advanced Quantum Mechanics to Introductory Quantum Field Theory". Cambridge University Press, 2011. 14

[36] W. Greiner and B. Müller, "The SU(3) Symmetry". Springer Berlin Heidelberg, Berlin, Heidelberg, 1994. 16

[37] M. Grigorescu, "SU(3) Clebsch-Gordan coefficients", *Stud. Cercetari Fiz.* **36** (1984) 3, arXiv:math-ph/0007033. 17

[38] E. Wigner, "On Unitary Representations of the Inhomogeneous Lorentz Group", *Annals of Mathematics* **40** (1939), no. 1, 149–204. 20

[39] "Projective Representations", volume 168, pp. 171–188. North-Holland, 1992. doi:10.1016/S0304-0208(08)70125-7. 20

[40] W. Pauli, "The Connection Between Spin and Statistics", *Phys. Rev.* **58** (Oct, 1940) 716–722, doi:10.1103/PhysRev.58.716. 22

[41] S. N. Gupta, "Theory of Longitudinal Photons in Quantum Electrodynamics", *Proceedings of the Physical Society. Section A* **63** (jul, 1950) 681–691, doi:10.1088/0370-1298/63/7/301. 26

[42] K. Bleuler, "Eine neue Methode zur Behandlung der longitudinalen und skalaren Photonen.", *Helv. Phys. Acta* **23** (1950) 567–586. 26

[43] R. P. Feynman, "Space-Time Approach to Non-Relativistic Quantum Mechanics", *Rev. Mod. Phys.* **20** (Apr, 1948) 367–387, doi:10.1103/RevModPhys.20.367. 28

[44] R. Feynman and A. Hibbs, "Quantum mechanics and path integrals". International series in pure and applied physics. McGraw-Hill, 1965. 28

[45] V. N. Popov, "Functional Integrals in Quantum Field Theory and Statistical Physics". 1984. 28

[46] L. Faddeev and V. Popov, "Feynman diagrams for the Yang-Mills field", *Physics Letters B* **25** (1967), no. 1, 29–30, doi:10.1016/0370-2693(67)90067-6. 29

[47] H. Grassmann, "Die Ausdehnungslehre von 1844 oder die lineale Ausdehnungslehre". Wigand, Leipzig, 1878. 29

[48] P. Clifford, "Applications of Grassmann's Extensive Algebra", *American Journal of Mathematics* **1** (1878), no. 4, 350–358. 29

[49] A. N. Whitehead, "A Treatise on Universal Algebra: With Applications". Cambridge Library Collection - Mathematics. Cambridge University Press, 2009. 29

[50] C. N. Yang and R. L. Mills, "Conservation of Isotopic Spin and Isotopic Gauge Invariance", *Phys. Rev.* **96** (Oct, 1954) 191–195, doi:10.1103/PhysRev.96.191. 30

[51] P. H. Frampton, "Gauge field theories; 3rd ed.". Wiley, Weinheim, 2008. 30

[52] C. Becchi, "Introduction to gauge theories", in *2nd Triangle Graduate School in Particle Physics Prague, Czech Republic, September 2-10, 1996*. 1996. arXiv:hep-ph/9705211. 30

[53] G. 't Hooft, "Under the Spell of the Gauge Principle". World Scientific, 1994. 30

[54] W. Greiner and J. Reinhardt, "Quantum electrodynamics; 4th ed.". Springer, Berlin, 2009. 31, 37

[55] E. E. Jenkins, A. V. Manohar, and M. Trott, "On Gauge Invariance and Minimal Coupling", *JHEP* **09** (2013) 063, doi:10.1007/JHEP09(2013)063, arXiv:1305.0017. 32

[56] A. V. Manohar, "Effective field theories", *Lect. Notes Phys.* **479** (1997) 311–362, doi:10.1007/BFb0104294, arXiv:hep-ph/9606222. 32

[57] H. Georgi, "Effective field theory", *Ann. Rev. Nucl. Part. Sci.* **43** (1993) 209–252, doi:10.1146/annurev.ns.43.120193.001233. 32

[58] R. K. Ellis, W. J. Stirling, and B. R. Webber, "QCD and Collider Physics". Cambridge Monographs on Particle Physics, Nuclear Physics and Cosmology. Cambridge University Press, 1996. 33

[59] Y. Nambu, "Quasi-Particles and Gauge Invariance in the Theory of Superconductivity", *Phys. Rev.* **117** (Feb, 1960) 648–663, doi:10.1103/PhysRev.117.648. 34

[60] J. Goldstone, "Field theories with Superconductor solutions", *Il Nuovo Cimento (1955-1965)* **19** (Jan, 1961) 154–164, doi:10.1007/BF02812722. 34

[61] J. Goldstone, A. Salam, and S. Weinberg, "Broken Symmetries", *Phys. Rev.* **127** (Aug, 1962) 965–970, doi:10.1103/PhysRev.127.965. 34

[62] M. Gell-Mann and M. Lévy, "The axial vector current in beta decay", *Il Nuovo Cimento (1955-1965)* **16** (May, 1960) 705–726, doi:10.1007/BF02859738. 34

[63] Y. Nambu and G. Jona-Lasinio, "Dynamical Model of Elementary Particles Based on an Analogy with Superconductivity. I", *Phys. Rev.* **122** (Apr, 1961) 345–358, doi:10.1103/PhysRev.122.345. 34

[64] P. Higgs, "Broken symmetries, massless particles and gauge fields", *Physics Letters* **12** (1964), no. 2, 132–133, doi:10.1016/0031-9163(64)91136-9. 34

[65] P. W. Higgs, "Broken Symmetries and the Masses of Gauge Bosons", *Phys. Rev. Lett.* **13** (Oct, 1964) 508–509, doi:10.1103/PhysRevLett.13.508. 34

[66] F. Englert and R. Brout, "Broken Symmetry and the Mass of Gauge Vector Mesons", *Phys. Rev. Lett.* **13** (Aug, 1964) 321–323, doi:10.1103/PhysRevLett.13.321. 34

[67] G. S. Guralnik, C. R. Hagen, and T. W. B. Kibble, "Global Conservation Laws and Massless Particles", *Phys. Rev. Lett.* **13** (Nov, 1964) 585–587, doi:10.1103/PhysRevLett.13.585. 35

[68] S. Weinberg, "General Theory of Broken Local Symmetries", *Phys. Rev. D* **7** (Feb, 1973) 1068–1082, doi:10.1103/PhysRevD.7.1068. 35

[69] S. Weinberg, "The Quantum Theory of Fields", volume 2. Cambridge University Press, 1996. 36

[70] G. 't Hooft, "The Glorious days of physics: Renormalization of gauge theories", arXiv:hep-th/9812203. 36

[71] F. J. Dyson, "The S Matrix in Quantum Electrodynamics", *Phys. Rev.* **75** (Jun, 1949) 1736–1755, doi:10.1103/PhysRev.75.1736. 37

[72] G. C. Wick, "The Evaluation of the Collision Matrix", *Phys. Rev.* **80** (Oct, 1950) 268–272, doi:10.1103/PhysRev.80.268. 37

[73] W. Greiner, S. Schramm, and E. Stein, "Quantum chromodynamics; 3rd ed.". Springer, Berlin, 2007. 37

[74] W. Greiner and B. Müller, "Gauge theory of weak interactions; 3rd rev. ed.". Springer, Berlin, 2000. 37

[75] T. DeGrand and C. DeTar, "Lattice Methods for Quantum Chromodynamics". World Scientific, Singapore, 2006. 38

[76] J. Smit, "Introduction to Quantum Fields on a Lattice". Cambridge Lecture Notes in Physics. Cambridge University Press, 2002. 38

[77] J. C. Collins, "Renormalization: An Introduction to Renormalization, the Renormalization Group and the Operator-Product Expansion". Cambridge University Press, 1984. 39, 41

[78] J. Bain, "Effective field theories", in *The Oxford Handbook of Philosophy of Physics*, R. Batterman, ed., pp. 224–254. 2013. doi:10.1093/oxfordhb/9780195392043.013.0007. 39

[79] G. 't Hooft, "Renormalization of massless Yang-Mills fields", *Nuclear Physics B* **33** (1971), no. 1, 173–199, doi:10.1016/0550-3213(71)90395-6. 39

[80] G. 't Hooft, "Renormalizable Lagrangians for massive Yang-Mills fields", *Nuclear Physics B* **35** (1971), no. 1, 167–188, doi:10.1016/0550-3213(71)90139-8. 39

[81] C. G. Bollini and J. J. Giambiagi, "Dimensional renorinalization : The number of dimensions as a regularizing parameter", *Il Nuovo Cimento B (1971-1996)* **12** (Nov, 1972) 20–26, doi:10.1007/BF02895558. 39

[82] G. 't Hooft and M. Veltman, "Regularization and renormalization of gauge fields", *Nuclear Physics B* **44** (1972), no. 1, 189–213, doi:10.1016/0550-3213(72)90279-9. 39

[83] G. Barnich, F. Brandt, and M. Henneaux, "Local BRST cohomology in gauge theories", *Physics Reports* **338** (2000), no. 5, 439–569, doi:10.1016/S0370-1573(00)00049-1. 40

[84] C. Becchi, A. Rouet, and R. Stora, "The abelian Higgs Kibble model, unitarity of the S-operator", *Physics Letters B* **52** (1974), no. 3, 344–346, doi:10.1016/0370-2693(74)90058-6. 40

[85] C. Becchi, A. Rouet, and R. Stora, "Renormalization of gauge theories", *Annals of Physics* **98** (1976), no. 2, 287–321, doi:10.1016/0003-4916(76)90156-1. 40

[86] I. V. Tyutin, "Gauge Invariance in Field Theory and Statistical Physics in Operator Formalism", arXiv:0812.0580. 40

[87] R. Coquereaux, "Renormalization schemes in QED", *Annals of Physics* **125** (1980), no. 2, 401–428, doi:10.1016/0003-4916(80)90139-6. 41, 42

[88] E. C. G. Stueckelberg de Breidenbach and A. Petermann, "La normalisation des constantes dans la théorie des quanta", *Helv. Phys. Acta* **26** (1953) 499–520, doi:10.5169/seals-112426. 42

[89] M. Gell-Mann and F. E. Low, "Quantum Electrodynamics at Small Distances", *Phys. Rev.* **95** (Sep, 1954) 1300–1312, doi:10.1103/PhysRev.95.1300. 42

[90] K. Symanzik, "Small distance behaviour in field theory and power counting", *Communications in Mathematical Physics* **18** (Sep, 1970) 227–246, doi:10.1007/BF01649434. 42

[91] F. J. Dyson, "Introduction to the Theory of Quantized Fields. N. N. Bogoliubov and D. V. Shirkov.", *Science* **132** (1960), no. 3419, 84–84, doi:10.1126/science.132.3419.84. 42

[92] K. G. Wilson, "The renormalization group: Critical phenomena and the Kondo problem", *Rev. Mod. Phys.* **47** (Oct, 1975) 773–840, doi:10.1103/RevModPhys.47.773. 42

[93] K. G. Wilson and M. E. Fisher, "Critical Exponents in 3.99 Dimensions", *Phys. Rev. Lett.* **28** (Jan, 1972) 240–243, doi:10.1103/PhysRevLett.28.240. 42

[94] C. Bagnuls and C. Bervillier, "Exact renormalization group equations: an introductory review", *Physics Reports* **348** (2001), no. 1, 91–157, doi:10.1016/S0370-1573(00)00137-X. 42

[95] J. Berges, N. Tetradis, and C. Wetterich, "Nonperturbative renormalization flow in quantum field theory and statistical physics", *Phys. Rept.* **363** (2002) 223–386, doi:10.1016/S0370-1573(01)00098-9, arXiv:hep-ph/0005122. 42

[96] J. M. Lizana and M. Pérez-Victoria, "Wilsonian renormalisation of CFT correlation functions: field theory", *Journal of High Energy Physics* **2017** (Jun, 2017) 139, doi:10.1007/JHEP06(2017)139. 42

[97] C. P. Burgess and G. D. Moore, "The Standard Model: A Primer". Cambridge Univ. Press, Cambridge, 2007. 44

[98] M. D. Schwartz, "Quantum Field Theory and the Standard Model". Cambridge University Press, 2014. 44, 46

[99] P. K. Kabir, "The Physics of Time Reversal", *Science* **240** (1988), no. 4855, 1068–1069, doi:10.1126/science.240.4855.1068. 45

[100] O. Gedalia and G. Perez, "Flavor Physics", pp. 309–382. 2011. arXiv:1005.3106. doi:10.1142/9789814327183_0006. 46

[101] R. N. Cahn, "The eighteen arbitrary parameters of the standard model in your everyday life", *Rev. Mod. Phys.* **68** (Jul, 1996) 951–959, doi:10.1103/RevModPhys.68.951. 46

[102] L.-L. Chau and W.-Y. Keung, "Comments on the Parametrization of the Kobayashi-Maskawa Matrix", *Phys. Rev. Lett.* **53** (Nov, 1984) 1802–1805, doi:10.1103/PhysRevLett.53.1802. 46

[103] T. Mannel, "Theory and Phenomenology of CP Violation", *Nuclear Physics B - Proceedings Supplements* **167** (2007) 170–174, doi:10.1016/j.nuclphysbps.2006.12.083. 47

[104] C. A. Baker et al., "An Improved experimental limit on the electric dipole moment of the neutron", *Phys. Rev. Lett.* **97** (2006) 131801, doi:10.1103/PhysRevLett.97.131801, arXiv:hep-ex/0602020. 47, 56

[105] R. D. Peccei and H. R. Quinn, "CP Conservation in the Presence of Pseudoparticles", *Phys. Rev. Lett.* **38** (Jun, 1977) 1440–1443, doi:10.1103/PhysRevLett.38.1440. 47

[106] J. M. Cornwall, D. N. Levin, and G. Tiktopoulos, "Derivation of gauge invariance from high-energy unitarity bounds on the S matrix", *Phys. Rev. D* **10** (Aug, 1974) 1145–1167, doi:10.1103/PhysRevD.10.1145. 47

[107] V. Khachatryan et al., "Precise determination of the mass of the Higgs boson and tests of compatibility of its couplings with the standard model predictions using proton collisions at $\sqrt{s} = 7$ and 8 TeV", *The European Physical Journal C* **75** (May, 2015) doi:10.1140/epjc/s10052-015-3351-7. 47

[108] G. Aad et al., "Measurements of the Higgs boson production and decay rates and coupling strengths using pp collision data at $\sqrt{s} = 7$ and 8 TeV in the ATLAS experiment", *The European Physical Journal C* **76** (Jan, 2016) doi:10.1140/epjc/s10052-015-3769-y. 47

[109] G. Aad et al., "Measurements of the Higgs boson production and decay rates and constraints on its couplings from a combined ATLAS and CMS analysis of the LHC pp collision data at $\sqrt{s} = 7$ and 8 TeV", *Journal of High Energy Physics* **2016** (Aug, 2016) doi:10.1007/jhep08(2016)045. 47, 51

[110] S. Weinberg, "A Model of Leptons", *Phys. Rev. Lett.* **19** (Nov, 1967) 1264–1266, doi:10.1103/PhysRevLett.19.1264. 47

[111] A. Salam, "Weak and Electromagnetic Interactions", *Conf. Proc.* **C680519** (1968) 367–377. 47

[112] V. Gribov, "The theory of quark confinement", *The European Physical Journal C - Particles and Fields* **10** (Aug, 1999) 91–105, doi:10.1007/s100529900052. 50

[113] ATLAS, CMS Collaboration, "Combined Measurement of the Higgs Boson Mass in pp Collisions at $\sqrt{s} = 7$ and 8 TeV with the ATLAS and CMS Experiments", *Phys. Rev. Lett.* **114** (2015) 191803, doi:10.1103/PhysRevLett.114.191803, arXiv:1503.07589. 50

[114] CMS Collaboration, "Measurements of properties of the Higgs boson decaying into the four-lepton final state in pp collisions at $\sqrt{s} = 13$ TeV", *JHEP* **11** (2017) 047, doi:10.1007/JHEP11(2017)047, arXiv:1706.09936. 50

[115] ATLAS Collaboration, "Measurement of the Higgs boson mass in the $H \to ZZ^* \to 4\ell$ and $H \to \gamma\gamma$ channels with $\sqrt{s} = 13$ TeV pp collisions using the ATLAS detector", *Phys. Lett.* **B784** (2018) 345–366, doi:10.1016/j.physletb.2018.07.050, arXiv:1806.00242. 50

[116] LHC Higgs Cross Section Working Group Collaboration, "Handbook of LHC Higgs Cross Sections: 4. Deciphering the Nature of the Higgs Sector", doi:10.2172/1345634,10.23731/CYRM-2017-002, arXiv:1610.07922. 50, 52, 53

[117] CMS Collaboration, "Limits on the Higgs boson lifetime and width from its decay to four charged leptons", *Phys. Rev.* **D92** (2015), no. 7, 072010, doi:10.1103/PhysRevD.92.072010, arXiv:1507.06656. 51

[118] CMS Collaboration, "Measurements of the Higgs boson width and anomalous HVV couplings from on-shell and off-shell production in the four-lepton final state", *Phys. Rev.* **D99** (2019), no. 11, 112003, doi:10.1103/PhysRevD.99.112003, arXiv:1901.00174. 51

[119] ATLAS Collaboration, "Constraints on off-shell Higgs boson production and the Higgs boson total width in $ZZ \to 4\ell$ and $ZZ \to 2\ell 2\nu$ final states with the ATLAS detector", *Phys. Lett.* **B786** (2018) 223–244, doi:10.1016/j.physletb.2018.09.048, arXiv:1808.01191. 51

[120] CMS Collaboration, "Constraints on the spin-parity and anomalous HVV couplings of the Higgs boson in proton collisions at 7 and 8 TeV", *Phys. Rev.* **D92** (2015), no. 1, 012004, doi:10.1103/PhysRevD.92.012004, arXiv:1411.3441. 51

[121] ATLAS Collaboration, "Evidence for the spin-0 nature of the Higgs boson using ATLAS data", *Phys. Lett.* **B726** (2013) 120–144, doi:10.1016/j.physletb.2013.08.026, arXiv:1307.1432. 51

[122] CMS Collaboration, "Combined measurements of Higgs boson couplings in proton-proton collisions at $\sqrt{s} = 13\,\text{TeV}$", *Eur. Phys. J.* **C79** (2019), no. 5, 421, doi:10.1140/epjc/s10052-019-6909-y, arXiv:1809.10733. 51

[123] CMS Collaboration, "Measurements of properties of the Higgs boson decaying into the four-lepton final state in pp collisions at $\sqrt{s} = 13$ TeV", *JHEP* **11** (2017) 047, doi:10.1007/JHEP11(2017)047, arXiv:1706.09936. 51

[124] CMS Collaboration, "Search for the Higgs boson decaying to two muons in proton-proton collisions at $\sqrt{s} = 13$ TeV", *Phys. Rev. Lett.* **122** (2019), no. 2, 021801, doi:10.1103/PhysRevLett.122.021801, arXiv:1807.06325. 51

[125] ATLAS Collaboration, "Combined measurements of Higgs boson production and decay using up to 80 fb^{-1} of proton-proton collision data at $\sqrt{s} = 13$ TeV collected with the ATLAS experiment", arXiv:1909.02845. 51

[126] ATLAS Collaboration, "Measurements of Higgs boson properties in the diphoton decay channel with 36 fb^{-1} of pp collision data at $\sqrt{s} = 13$ TeV with the ATLAS detector", *Phys. Rev.* **D98** (2018) 052005, doi:10.1103/PhysRevD.98.052005, arXiv:1802.04146. 51

[127] CMS Collaboration, "Observation of the Higgs boson decay to a pair of τ leptons with the CMS detector", *Phys. Lett.* **B779** (2018) 283–316, doi:10.1016/j.physletb.2018.02.004, arXiv:1708.00373. 51

[128] CMS Collaboration, "Observation of $\text{t}\bar{\text{t}}\text{H}$ production", *Phys. Rev. Lett.* **120** (2018), no. 23, 231801, doi:10.1103/PhysRevLett.120.231801, arXiv:1804.02610. 51

[129] CMS Collaboration, "Observation of Higgs boson decay to bottom quarks", *Phys. Rev. Lett.* **121** (2018), no. 12, 121801, doi:10.1103/PhysRevLett.121.121801, arXiv:1808.08242. 51

[130] ATLAS Collaboration, "Evidence for the Higgs-boson Yukawa coupling to tau leptons with the ATLAS detector", *JHEP* **04** (2015) 117, doi:10.1007/JHEP04(2015)117, arXiv:1501.04943. 51

[131] ATLAS Collaboration, "Observation of Higgs boson production in association with a top quark pair at the LHC with the ATLAS detector", *Phys. Lett.* **B784** (2018) 173–191, doi:10.1016/j.physletb.2018.07.035, arXiv:1806.00425. 51

[132] ATLAS Collaboration, "Observation of $H \to b\bar{b}$ decays and VH production with the ATLAS detector", *Phys. Lett.* **B786** (2018) 59–86, doi:10.1016/j.physletb.2018.09.013, arXiv:1808.08238. 51

[133] S. Dittmaier et al., "Handbook of LHC Higgs Cross Sections: 2. Differential Distributions", doi:10.5170/CERN-2012-002, arXiv:1201.3084. 52

[134] A. Djouadi, "The Anatomy of electro-weak symmetry breaking. I: The Higgs boson in the standard model", *Phys. Rept.* **457** (2008) 1–216, doi:10.1016/j.physrep.2007.10.004, arXiv:hep-ph/0503172. 53

[135] LHC Higgs Cross Section Working Group Collaboration, "Handbook of LHC Higgs Cross Sections: 3. Higgs Properties", doi:10.5170/CERN-2013-004, arXiv:1307.1347. 53

[136] S. Carlip, "Quantum gravity: a progress report", *Reports on Progress in Physics* **64** (jul, 2001) 885–942, doi:10.1088/0034-4885/64/8/301. 54

[137] J. F. Donoghue, "The effective field theory treatment of quantum gravity", *AIP Conference Proceedings* **1483** (2012), no. 1, 73–94, doi:10.1063/1.4756964. 54

[138] J. Polchinski, "String theory. Vol. 1: An introduction to the bosonic string". Cambridge Monographs on Mathematical Physics. Cambridge University Press, 2007. 54

[139] J. Polchinski, "String theory. Vol. 2: Superstring theory and beyond". Cambridge Monographs on Mathematical Physics. Cambridge University Press, 2007. 54

[140] C. Rovelli, "Loop Quantum Gravity", *Living Reviews in Relativity* **11** (Jul, 2008) 5, doi:10.12942/lrr-2008-5. 54

[141] N. Jarosik et al., "Seven-Year WMAP Observations: sky maps, systematic errors, and basic results", *The Astrophysical Journal Supplement Series* **192** (jan, 2011) 14, doi:10.1088/0067-0049/192/2/14. 54

[142] V. Trimble, "Existence and Nature of Dark Matter in the Universe", *Annual Review of Astronomy and Astrophysics* **25** (1987), no. 1, 425–472, doi:10.1146/annurev.aa.25.090187.002233. 54

[143] C. Copi, D. Schramm, and M. Turner, "Big-bang nucleosynthesis and the baryon density of the universe", *Science* **267** (1995), no. 5195, 192–199, doi:10.1126/science.7809624. 54

[144] L. Roszkowski, E. M. Sessolo, and S. Trojanowski, "WIMP dark matter candidates and searches–current status and future prospects", *Rept. Prog. Phys.* **81** (2018), no. 6, 066201, doi:10.1088/1361-6633/aab913, arXiv:1707.06277. 54

[145] G. Jungman, M. Kamionkowski, and K. Griest, "Supersymmetric dark matter", *Physics Reports* **267** (1996), no. 5, 195–373, doi:10.1016/0370-1573(95)00058-5. 54

[146] R. E. Allen, "Saving supersymmetry and dark matter WIMPs–a new kind of dark matter candidate with well-defined mass and couplings", *Phys. Scripta* **94** (2019), no. 1, 014010, doi:10.1088/1402-4896/aaef19, arXiv:1811.00670. 54

[147] P. J. Steinhardt and N. Turok, "Why the Cosmological Constant Is Small and Positive", *Science* **312** (2006), no. 5777, 1180–1183, doi:10.1126/science.1126231. 54

[148] D. Huterer and D. L. Shafer, "Dark energy two decades after: Observables, probes, consistency tests", *Rept. Prog. Phys.* **81** (2018), no. 1, 016901, doi:10.1088/1361-6633/aa997e, arXiv:1709.01091. 54

[149] S. Weinberg, "The cosmological constant problem", *Rev. Mod. Phys.* **61** (Jan, 1989) 1–23, doi:10.1103/RevModPhys.61.1. 55

[150] R. Davis, D. S. Harmer, and K. C. Hoffman, "Search for Neutrinos from the Sun", *Phys. Rev. Lett.* **20** (May, 1968) 1205–1209, doi:10.1103/PhysRevLett.20.1205. 55

[151] Super-Kamiokande Collaboration, "Evidence for Oscillation of Atmospheric Neutrinos", *Phys. Rev. Lett.* **81** (Aug, 1998) 1562–1567, doi:10.1103/PhysRevLett.81.1562. 55

[152] M. C. Gonzalez-Garcia and Y. Nir, "Neutrino masses and mixing: evidence and implications", *Rev. Mod. Phys.* **75** (Mar, 2003) 345–402, doi:10.1103/RevModPhys.75.345. 55

[153] B. Pontecorvo, "Mesonium and anti-mesonium", *Sov. Phys. JETP* **6** (1957) 429. 55

[154] M. Nakagawa, H. Okonogi, S. Sakata, and A. Toyoda, "Possible existence of a neutrino with mass and partial conservation of muon charge", *Prog. Theor. Phys.* **30** (1963) 727–729, doi:10.1143/PTP.30.727. 55

[155] "Lectures on Flavor Physics", *Lecture Notes in Physics* (2004) doi:10.1007/b98411. 55

[156] M. Czakon, M. Zralek, and J. Gluza, "Are neutrinos Dirac or Majorana particles?", *Acta Phys. Polon.* **B30** (1999) 3121–3138, arXiv:hep-ph/9910357. 55

[157] S. Mertens, "Direct Neutrino Mass Experiments", *J. Phys. Conf. Ser.* **718** (2016), no. 2, 022013, doi:10.1088/1742-6596/718/2/022013, arXiv:1605.01579. 55

[158] S. Weinberg, "Baryon- and Lepton-Nonconserving Processes", *Phys. Rev. Lett.* **43** (Nov, 1979) 1566–1570, doi:10.1103/PhysRevLett.43.1566. 55

[159] J. Hernandez-Garcia and S. F. King, "New Weinberg operator for neutrino mass and its seesaw origin", *JHEP* **05** (2019) 169, doi:10.1007/JHEP05(2019)169, arXiv:1903.01474. 55

[160] A. D. Sakharov, "Violation of CP invariance, Casymmetry, and baryon asymmetry of the universe", *Soviet Physics Uspekhi* **34** (may, 1991) 392–393, doi:10.1070/pu1991v034n05abeh002497. 55

[161] G. 't Hooft, "Symmetry Breaking through Bell-Jackiw Anomalies", *Phys. Rev. Lett.* **37** (Jul, 1976) 8–11, doi:10.1103/PhysRevLett.37.8. 55

[162] F. R. Klinkhamer and N. S. Manton, "A saddle-point solution in the Weinberg-Salam theory", *Phys. Rev. D* **30** (Nov, 1984) 2212–2220, doi:10.1103/PhysRevD.30.2212. 55

[163] CMS Collaboration, "Search for black holes and sphalerons in high-multiplicity final states in proton-proton collisions at $\sqrt{s} = 13$ TeV", *JHEP* **11** (2018) 042, doi:10.1007/JHEP11(2018)042, arXiv:1805.06013. 55

[164] L. Canetti, M. Drewes, and M. Shaposhnikov, "Matter and Antimatter in the Universe", *New J. Phys.* **14** (2012) 095012, doi:10.1088/1367-2630/14/9/095012, arXiv:1204.4186. 55

[165] I. Brivio and M. Trott, "The Standard Model as an Effective Field Theory", *Phys. Rept.* **793** (2019) 1–98, doi:10.1016/j.physrep.2018.11.002, arXiv:1706.08945. 55

[166] G. Panico and A. Wulzer, "The Composite Nambu-Goldstone Higgs", *Lect. Notes Phys.* **913** (2016) 1–316, doi:10.1007/978-3-319-22617-0, arXiv:1506.01961. 56, 62

[167] A. Bilal, "Introduction to supersymmetry", arXiv:hep-th/0101055. 56

[168] D. B. Kaplan and H. Georgi, "$SU(2) \times U(1)$ breaking by vacuum misalignment", *Physics Letters B* **136** (1984), no. 3, 183–186, doi:10.1016/0370-2693(84)91177-8. 56

[169] V. Agrawal, S. M. Barr, J. F. Donoghue, and D. Seckel, "Viable range of the mass scale of the standard model", *Phys. Rev.* **D57** (1998) 5480–5492, doi:10.1103/PhysRevD.57.5480, arXiv:hep-ph/9707380. 56

[170] P. W. Graham, D. E. Kaplan, and S. Rajendran, "Cosmological Relaxation of the Electroweak Scale", *Phys. Rev. Lett.* **115** (2015), no. 22, 221801, doi:10.1103/PhysRevLett.115.221801, arXiv:1504.07551. 56

[171] A. Hook, "TASI Lectures on the Strong CP Problem and Axions", *PoS* **TASI2018** (2019) 004, arXiv:1812.02669. 56

[172] S. Weinberg, "The U(1) problem", *Phys. Rev. D* **11** (Jun, 1975) 3583–3593, doi:10.1103/PhysRevD.11.3583. 56

[173] S. Coleman, "Aspects of Symmetry: Selected Erice Lectures". Cambridge University Press, 1985. 56

[174] H. Forkel, "A Primer on instantons in QCD", arXiv:hep-ph/0009136. 56

[175] J. Engel, M. J. Ramsey-Musolf, and U. van Kolck, "Electric Dipole Moments of Nucleons, Nuclei, and Atoms: The Standard Model and Beyond", *Prog. Part. Nucl. Phys.* **71** (2013) 21–74, doi:10.1016/j.ppnp.2013.03.003, arXiv:1303.2371. 56

[176] R. D. Peccei and H. R. Quinn, "Constraints imposed by CP conservation in the presence of pseudoparticles", *Phys. Rev. D* **16** (Sep, 1977) 1791–1797, doi:10.1103/PhysRevD.16.1791. 56

[177] S. Weinberg, "A New Light Boson?", *Phys. Rev. Lett.* **40** (Jan, 1978) 223–226, doi:10.1103/PhysRevLett.40.223. 56

[178] F. Wilczek, "Problem of Strong P and T Invariance in the Presence of Instantons", *Phys. Rev. Lett.* **40** (Jan, 1978) 279–282, doi:10.1103/PhysRevLett.40.279. 56

[179] G. Arcadi, A. Djouadi, and M. Raidal, "Dark Matter through the Higgs portal", arXiv:1903.03616. 56

[180] D. E. Morrissey and M. J. Ramsey-Musolf, "Electroweak baryogenesis", *New J. Phys.* **14** (2012) 125003, doi:10.1088/1367-2630/14/12/125003, arXiv:1206.2942. 56

[181] S. Coleman and J. Mandula, "All Possible Symmetries of the S Matrix", *Phys. Rev.* **159** (Jul, 1967) 1251–1256, doi:10.1103/PhysRev.159.1251. 57

[182] Yu. A. Golfand and E. P. Likhtman, "Extension of the Algebra of Poincare Group Generators and Violation of p Invariance", *JETP Lett.* **13** (1971) 323–326. 57

[183] N. Sthanumoorthy, "4 - Lie superalgebras", in *Introduction to Finite and Infinite Dimensional Lie (Super)algebras*, N. Sthanumoorthy, ed., pp. 203–255. Academic Press, 2016. doi:10.1016/B978-0-12-804675-3.00004-2. 57

[184] J. Wess and B. Zumino, "Supergauge Transformations in Four-Dimensions", *Nucl. Phys.* **B70** (1974) 39–50, doi:10.1016/0550-3213(74)90355-1. 57

[185] I. J. R. Aitchison, "Supersymmetry in Particle Physics. An Elementary Introduction". Cambridge University Press, Cambridge, 2007. 57

[186] P. Binetruy, "Supersymmetry: Theory, experiment and cosmology". 2006. 57

[187] P. West, "Introduction to Supersymmetry and Supergravity". World Scientific, revised and extended second edition, 1990. 57

[188] B. DeWitt, "Supermanifolds". Cambridge Monographs on Mathematical Physics. Cambridge University Press, 2 edition, 1992. 57

[189] MSSM Working Group Collaboration, A. Djouadi et al., "The Minimal supersymmetric standard model: Group summary report", in *GDR (Groupement De Recherche) - Supersymetrie Montpellier, France, April 15-17, 1998*. 1998. arXiv:hep-ph/9901246. 57

[190] N. Seiberg, "Naturalness versus supersymmetric nonrenormalization theorems", *Phys. Lett.* **B318** (1993) 469–475, doi:10.1016/0370-2693(93)91541-T, arXiv:hep-ph/9309335. 59

[191] D. I. Kazakov, "Radiative Corrections, Divergences, Regularization, Renormalization, Renormalization Group and All That in Examples in Quantum Field Theory", arXiv:0901.2208. 59

[192] A. Drozd, B. Grzadkowski, and J. Wudka, "Multi-Scalar-Singlet Extension of the Standard Model - the Case for Dark Matter and an Invisible Higgs Boson", *JHEP* **04** (2012) 006, doi:10.1007/JHEP04(2012)006,10.1007/JHEP11(2014)130, arXiv:1112.2582. 60

[193] T. Robens and T. Stefaniak, "Status of the Higgs Singlet Extension of the Standard Model after LHC Run 1", *Eur. Phys. J.* **C75** (2015) 104, doi:10.1140/epjc/s10052-015-3323-y, arXiv:1501.02234. 60

[194] T. Robens, T. Stefaniak, and J. Wittbrodt, "Two-real-scalar-singlet extension of the SM: LHC phenomenology and benchmark scenarios", arXiv:1908.08554. 60

[195] A. Ilnicka, T. Robens, and T. Stefaniak, "Constraining Extended Scalar Sectors at the LHC and beyond", *Mod. Phys. Lett.* **A33** (2018), no. 10n11, 1830007, doi:10.1142/S0217732318300070, arXiv:1803.03594. 61

[196] M. Battaglieri et al., "US Cosmic Visions: New Ideas in Dark Matter 2017: Community Report", in *U.S. Cosmic Visions: New Ideas in Dark Matter College Park, MD, USA, March 23-25, 2017*. 2017. arXiv:1707.04591. 61

[197] R. Essig et al., "Working Group Report: New Light Weakly Coupled Particles", 2013. arXiv:1311.0029. 61

[198] J. E. Juknevich, D. Melnikov, and M. J. Strassler, "A Pure-Glue Hidden Valley I. States and Decays", *JHEP* **07** (2009) 055, doi:10.1088/1126-6708/2009/07/055, arXiv:0903.0883. 61

[199] M. J. Strassler, "Possible effects of a hidden valley on supersymmetric phenomenology", arXiv:hep-ph/0607160. 61

[200] M. J. Strassler and K. M. Zurek, "Echoes of a hidden valley at hadron colliders", *Phys. Lett.* **B651** (2007) 374–379, doi:10.1016/j.physletb.2007.06.055, arXiv:hep-ph/0604261. 61

[201] T. Han, Z. Si, K. M. Zurek, and M. J. Strassler, "Phenomenology of hidden valleys at hadron colliders", *JHEP* **07** (2008) 008, doi:10.1088/1126-6708/2008/07/008, arXiv:0712.2041. 61

[202] B. Holdom, "Two $U(1)$'s and ϵ charge shifts", *Physics Letters B* **166** (1986), no. 2, 196–198, doi:10.1016/0370-2693(86)91377-8. 61

[203] P. Galison and A. Manohar, "Two Z's or not two Z's?", *Physics Letters B* **136** (1984), no. 4, 279–283, doi:10.1016/0370-2693(84)91161-4. 61

[204] X. Chu, T. Hambye, and M. H. G. Tytgat, "The Four Basic Ways of Creating Dark Matter Through a Portal", *JCAP* **1205** (2012) 034, doi:10.1088/1475-7516/2012/05/034, arXiv:1112.0493. 61

[205] M. Pospelov, "Secluded U(1) below the weak scale", *Phys. Rev. D* **80** (Nov, 2009) 095002, doi:10.1103/PhysRevD.80.095002. 61

[206] S. Gopalakrishna, S. Jung, and J. D. Wells, "Higgs boson decays to four fermions through an abelian hidden sector", *Phys. Rev.* **D78** (2008) 055002, doi:10.1103/PhysRevD.78.055002, arXiv:0801.3456. 61

[207] K. Agashe, R. Contino, and A. Pomarol, "The Minimal composite Higgs model", *Nucl. Phys.* **B719** (2005) 165–187, doi:10.1016/j.nuclphysb.2005.04.035, arXiv:hep-ph/0412089. 62

[208] G. Cacciapaglia and F. Sannino, "Fundamental Composite (Goldstone) Higgs Dynamics", *JHEP* **04** (2014) 111, doi:10.1007/JHEP04(2014)111, arXiv:1402.0233. 62

[209] K. Lane, "Two lectures on technicolor", arXiv:hep-ph/0202255. 62

[210] T. Appelquist and L. C. R. Wijewardhana, "Chiral hierarchies from slowly running couplings in technicolor theories", *Phys. Rev. D* **36** (Jul, 1987) 568–580, doi:10.1103/PhysRevD.36.568. 62

[211] T. Appelquist, J. Terning, and L. C. R. Wijewardhana, "Postmodern Technicolor", *Phys. Rev. Lett.* **79** (Oct, 1997) 2767–2770, doi:10.1103/PhysRevLett.79.2767. 62

[212] H. Sazdjian, "Introduction to chiral symmetry in QCD", *EPJ Web Conf.* **137** (2017) 02001, doi:10.1051/epjconf/201713702001, arXiv:1612.04078. 62

[213] S. Scherer, "Introduction to chiral perturbation theory", *Adv. Nucl. Phys.* **27** (2003) 277, arXiv:hep-ph/0210398. 62

[214] R. Barbieri, A. Pomarol, R. Rattazzi, and A. Strumia, "Electroweak symmetry breaking after LEP-1 and LEP-2", *Nucl. Phys.* **B703** (2004) 127–146, doi:10.1016/j.nuclphysb.2004.10.014, arXiv:hep-ph/0405040. 63

[215] M. Schmaltz and D. Tucker-Smith, "Little Higgs review", *Ann. Rev. Nucl. Part. Sci.* **55** (2005) 229–270, doi:10.1146/annurev.nucl.55.090704.151502, arXiv:hep-ph/0502182. 63

[216] M. Schmaltz and J. Thaler, "Collective Quartics and Dangerous Singlets in Little Higgs", *JHEP* **03** (2009) 137, doi:10.1088/1126-6708/2009/03/137, arXiv:0812.2477. 63

[217] N. Arkani-Hamed, A. G. Cohen, E. Katz, and A. E. Nelson, "The Littlest Higgs", *JHEP* **07** (2002) 034, doi:10.1088/1126-6708/2002/07/034, arXiv:hep-ph/0206021. 63

[218] C. Csaki et al., "Variations of little Higgs models and their electroweak constraints", *Phys. Rev.* **D68** (2003) 035009, doi:10.1103/PhysRevD.68.035009, arXiv:hep-ph/0303236. 63

[219] W. Kilian, D. Rainwater, and J. Reuter, "Pseudo-axions in little Higgs models", *Phys. Rev.* **D71** (2005) 015008, doi:10.1103/PhysRevD.71.015008, arXiv:hep-ph/0411213. 63, 96

[220] Z. Surujon and P. Uttayarat, "Spontaneous CP Violation and Light Particles in The Littlest Higgs", *Phys. Rev.* **D83** (2011) 076010, doi:10.1103/PhysRevD.83.076010, arXiv:1003.4779. 63

[221] G. C. Branco et al., "Theory and phenomenology of two-Higgs-doublet models", *Phys. Rept.* **516** (2012) 1–102, doi:10.1016/j.physrep.2012.02.002, arXiv:1106.0034. 63, 64, 65

[222] D. Das, "2HDM without FCNC: off the beaten tracks", *Eur. Phys. J.* **C78** (2018), no. 8, 650, doi:10.1140/epjc/s10052-018-6145-x, arXiv:1803.09430. 64

[223] N. Craig and S. Thomas, "Exclusive Signals of an Extended Higgs Sector", *JHEP* **11** (2012) 083, doi:10.1007/JHEP11(2012)083, arXiv:1207.4835. 64, 65

[224] V. Cacchio, D. Chowdhury, O. Eberhardt, and C. W. Murphy, "Next-to-leading order unitarity fits in Two-Higgs-Doublet models with soft $\mathbb{Z}_2$ breaking", *Journal of High Energy Physics* **2016** (Nov, 2016) 26, doi:10.1007/JHEP11(2016)026. 64

[225] J. Bernon et al., "Scrutinizing the alignment limit in two-Higgs-doublet models. II. $m_h = 125$ GeV", *Phys. Rev.* **D93** (2016), no. 3, 035027, doi:10.1103/PhysRevD.93.035027, arXiv:1511.03682. 64

[226] A. Broggio et al., "Limiting two-Higgs-doublet models", *JHEP* **11** (2014) 058, doi:10.1007/JHEP11(2014)058, arXiv:1409.3199. 64

[227] A. Arbey, F. Mahmoudi, O. Stal, and T. Stefaniak, "Status of the Charged Higgs Boson in Two Higgs Doublet Models", *Eur. Phys. J.* **C78** (2018), no. 3, 182, doi:10.1140/epjc/s10052-018-5651-1, arXiv:1706.07414. 64

[228] J. Haller et al., "Update of the global electroweak fit and constraints on two-Higgs-doublet models", *Eur. Phys. J.* **C78** (2018), no. 8, 675, doi:10.1140/epjc/s10052-018-6131-3, arXiv:1803.01853. 64

[229] J. Bernon et al., "Scrutinizing the alignment limit in two-Higgs-doublet models: $m_h = 125$ GeV", *Phys. Rev.* **D92** (2015), no. 7, 075004, doi:10.1103/PhysRevD.92.075004, arXiv:1507.00933. 64

[230] J. F. Gunion and H. E. Haber, "The CP conserving two Higgs doublet model: The Approach to the decoupling limit", *Phys. Rev.* **D67** (2003) 075019, doi:10.1103/PhysRevD.67.075019, arXiv:hep-ph/0207010. 64

[231] S. Baum and N. R. Shah, "Two Higgs Doublets and a Complex Singlet: Disentangling the Decay Topologies and Associated Phenomenology", doi:10.1007/JHEP12(2018)044, arXiv:1808.02667. 65

[232] G. Chalons and F. Domingo, "Analysis of the Higgs potentials for two doublets and a singlet", *Phys. Rev.* **D86** (2012) 115024, doi:10.1103/PhysRevD.86.115024, arXiv:1209.6235. 65

[233] M. Carena et al., "Alignment limit of the NMSSM Higgs sector", *Phys. Rev.* **D93** (2016), no. 3, 035013, doi:10.1103/PhysRevD.93.035013, arXiv:1510.09137. 65

[234] U. Ellwanger, C. Hugonie, and A. M. Teixeira, "The Next-to-Minimal Supersymmetric Standard Model", *Phys. Rept.* **496** (2010) 1–77, doi:10.1016/j.physrep.2010.07.001, arXiv:0910.1785. 65

[235] M. Maniatis, "The Next-to-Minimal Supersymmetric extension of the Standard Model reviewed", *Int. J. Mod. Phys.* **A25** (2010) 3505–3602, doi:10.1142/S0217751X10049827, arXiv:0906.0777. 65

[236] S. Baum, N. R. Shah, and K. Freese, "The NMSSM is within Reach of the LHC: Mass Correlations & Decay Signatures", *JHEP* **04** (2019) 011, doi:10.1007/JHEP04(2019)011, arXiv:1901.02332. 65

[237] O. S. Brüning et al., "LHC Design Report". CERN Yellow Reports: Monographs. CERN, Geneva, 2004. 68

[238] "Technical proposal: L3", Technical Report CERN-LEPC-83-5. LEPC-P-4, 1983. 68

[239] C. Lefévre, "The CERN accelerator complex. Complexe des accélérateurs du CERN", (Dec, 2008). 69

[240] E. Boltezar et al., "Performance of the new CERN 50-MeV LINAC.", *IEEE Trans. Nucl. Sci.* **26** (1979) 3674–3676, doi:10.1109/TNS.1979.4330576. 68

[241] K. HANKE, "Past and present operation of the CERN PS booster", *International Journal of Modern Physics A* **28** (2013), no. 13, 1330019, doi:10.1142/S0217751X13300196. 68

[242] D. Cundy and S. Gilardoni, "The Proton Synchrotron (PS): At the Core of the CERN Accelerators: Introduction", *Adv. Ser. Direct. High Energy Phys.* **27** (2017) 39–56. 69

[243] N. A. Tahir et al., "The CERN Super Proton Synchrotron as a tool to study high energy density physics", *New J. Phys.* **10** (2008) 073028, doi:10.1088/1367-2630/10/7/073028. 69

[244] D. Boussard and T. P. R. Linnecar, "The LHC Superconducting RF System", Technical Report LHC-Project-Report-316. CERN-LHC-Project-Report-316, CERN, Geneva, Dec, 1999. 69

[245] L. Rossi, "The LHC Superconducting Magnets",. 69

[246] ATLAS Collaboration, "The ATLAS Experiment at the CERN Large Hadron Collider", *JINST* **3** (2008) S08003, doi:10.1088/1748-0221/3/08/S08003. 70

[247] CMS Collaboration, "The CMS Experiment at the CERN LHC", *JINST* **3** (2008) S08004, doi:10.1088/1748-0221/3/08/S08004. 70, 71, 73, 74, 75

[248] ALICE Collaboration, "The ALICE experiment at the CERN LHC", *JINST* **3** (2008) S08002, doi:10.1088/1748-0221/3/08/S08002. 70

[249] LHCb Collaboration, "The LHCb Detector at the LHC", *JINST* **3** (2008) S08005, doi:10.1088/1748-0221/3/08/S08005. 70

[250] CERN, "CERN Accelerator School: Intermediate Course on Accelerator Physics". CERN, Geneva, (2006). doi:10.5170/CERN-2006-002. 70

[251] W. Herr and B. Muratori, "Concept of luminosity", doi:10.5170/CERN-2006-002.361. 70

[252] L. Evans and P. Bryant, "LHC Machine", *JINST* **3** (2008) S08001, doi:10.1088/1748-0221/3/08/S08001. 70

[253] CMS Collaboration, "Public CMS Luminosity Information". https://twiki.cern.ch/twiki/bin/view/CMSPublic/LumiPublicResults. Accessed: 2019-10-25. 71

[254] G. Apollinari et al., "High-Luminosity Large Hadron Collider (HL-LHC): Preliminary Design Report". CERN Yellow Reports: Monographs. CERN, Geneva, 2015. 71

[255] G. Apollinari, O. Brüning, T. Nakamoto, and L. Rossi, "High Luminosity Large Hadron Collider HL-LHC", *CERN Yellow Rep.* (2015), no. 5, 1–19, doi:10.5170/CERN-2015-005.1, arXiv:1705.08830. 71

[256] CMS Collaboration, J. N. Butler, "Highlights and Perspectives from the CMS Experiment", in *5th Large Hadron Collider Physics Conference (LHCP 2017) Shanghai, China, May 15-20, 2017*. 2017. arXiv:1709.03006. 71

[257] "CMS at CERN". https://cms.cern. Accessed: 2019-10-25. 71

[258] CMS Collaboration, T. Sakuma, "Cutaway diagrams of CMS detector". https://cds.cern.ch/record/2665537, May, 2019. 72

[259] Y. Hama, "A Note on Lorentz Transformation and Pseudo-Rapidity Distributions", *Journal of the Physical Society of Japan* **50** (1981), no. 1, 21–23, doi:10.1143/JPSJ.50.21. 72

[260] CMS Collaboration, "The CMS magnet project: Technical Design Report". Technical Design Report CMS. CERN, Geneva, 1997. 73

[261] CMS Collaboration, "The CMS tracker: addendum to the Technical Design Report". Technical Design Report CMS. CERN, Geneva, 2000. 73

[262] CMS Collaboration, "The CMS electromagnetic calorimeter project: Technical Design Report". Technical Design Report CMS. CERN, Geneva, 1997. 73

[263] CMS Collaboration, "The CMS hadron calorimeter project: Technical Design Report". Technical Design Report CMS. CERN, Geneva, 1997. 74

[264] CMS Collaboration, "The CMS muon project: Technical Design Report". Technical Design Report CMS. CERN, Geneva, 1997. 74

[265] CMS Collaboration, G. Bayatyan et al., "CMS TriDAS project: Technical Design Report, Volume 1: The Trigger Systems". Technical Design Report CMS. 75

[266] CMS Collaboration, S. Cittolin, A. Rácz, and P. Sphicas, "CMS The TriDAS Project: Technical Design Report, Volume 2: Data Acquisition and High-Level Trigger. CMS trigger and data-acquisition project". Technical Design Report CMS. CERN, Geneva, 2002. 75

[267] ALEPH Collaboration, "Performance of the ALEPH detector at LEP", *Nucl. Instrum. Meth.* **A360** (1995) 481–506, doi:10.1016/0168-9002(95)00138-7. 76

[268] M. Thomson, "Particle flow calorimetry and the Pandora PFA algorithm", *Nuclear Instruments and Methods in Physics Research Section A: Accelerators, Spectrometers, Detectors and Associated Equipment* **611** (Nov, 2009) 25–40, doi:10.1016/j.nima.2009.09.009. 76

[269] M. Ruan and H. Videau, "Arbor, a new approach of the Particle Flow Algorithm", in *Proceedings, International Conference on Calorimetry for the High Energy Frontier (CHEF 2013): Paris, France, April 22-25, 2013*, pp. 316–324. 2013. arXiv:1403.4784. 76

[270] CMS Collaboration, "Particle-Flow Event Reconstruction in CMS and Performance for Jets, Taus, and MET",. 76, 77

[271] CMS Collaboration, "Particle-flow reconstruction and global event description with the CMS detector", *JINST* **12** (2017), no. 10, P10003, doi:10.1088/1748-0221/12/10/P10003, arXiv:1706.04965. 76, 77

[272] CMS Collaboration, "Description and performance of track and primary-vertex reconstruction with the CMS tracker", *JINST* **9** (2014), no. 10, P10009, doi:10.1088/1748-0221/9/10/P10009, arXiv:1405.6569. 76, 78

[273] CMS Collaboration, G. L. Bayatian et al., "CMS Physics: Technical Design Report Volume 1: Detector Performance and Software". Technical Design Report CMS. CERN, Geneva, 2006. 76

[274] W. Adam, B. Mangano, T. Speer, and T. Todorov, "Track Reconstruction in the CMS tracker", Technical Report CMS-NOTE-2006-041, CERN, Geneva, Dec, 2006. 76

[275] K. Rose, "Deterministic annealing for clustering, compression, classification, regression, and related optimization problems", *Proceedings of the IEEE* **86** (Nov, 1998) 2210–2239, doi:10.1109/5.726788. 78

[276] R. Frühwirth, W. Waltenberger, and P. Vanlaer, "Adaptive Vertex Fitting", Technical Report CMS-NOTE-2007-008, CERN, Geneva, Mar, 2007. 78

[277] D. Contardo et al., "Technical Proposal for the Phase-II Upgrade of the CMS Detector", Technical Report CERN-LHCC-2015-010. LHCC-P-008. CMS-TDR-15-02, Geneva, Jun, 2015. 78

[278] CMS Collaboration, "Performance of the CMS muon detector and muon reconstruction with proton-proton collisions at $\sqrt{s} = 13$ TeV", *JINST* **13** (2018), no. 06, P06015, doi:10.1088/1748-0221/13/06/P06015, arXiv:1804.04528. 78

[279] CMS Collaboration, "Performance of Electron Reconstruction and Selection with the CMS Detector in Proton-Proton Collisions at $\sqrt{s} = 8$ TeV", *JINST* **10** (2015), no. 06, P06005, doi:10.1088/1748-0221/10/06/P06005, arXiv:1502.02701. 78, 79

[280] S. Baffioni et al., "Electron reconstruction in CMS", *The European Physical Journal C* **49** (Mar, 2007) 1099–1116, doi:10.1140/epjc/s10052-006-0175-5. 78

[281] W. Adam, R. Frühwirth, A. Strandlie, and T. Todorov, "Reconstruction of electrons with the Gaussian-sum filter in the CMS tracker at the LHC", *Journal of Physics G: Nuclear and Particle Physics* **31** (Jul, 2005) 9–20, doi:10.1088/0954-3899/31/9/n01. 79

[282] CMS Collaboration, "Observation of the Diphoton Decay of the Higgs Boson and Measurement of Its Properties", *Eur. Phys. J.* **C74** (2014), no. 10, 3076, doi:10.1140/epjc/s10052-014-3076-z, arXiv:1407.0558. 79

[283] CMS Collaboration, "Performance of Photon Reconstruction and Identification with the CMS Detector in Proton-Proton Collisions at $\sqrt{s} = 8$ TeV", *JINST* **10** (2015), no. 08, P08010, doi:10.1088/1748-0221/10/08/P08010, arXiv:1502.02702. 79

[284] CMS Collaboration, "Jet energy scale and resolution in the CMS experiment in pp collisions at 8 TeV", *JINST* **12** (2017), no. 02, P02014, doi:10.1088/1748-0221/12/02/P02014, arXiv:1607.03663. 79, 80

[285] M. Cacciari, G. P. Salam, and G. Soyez, "The anti-k_t jet clustering algorithm", *JHEP* **04** (2008) 063, doi:10.1088/1126-6708/2008/04/063, arXiv:0802.1189. 79

[286] CMS Collaboration, "Jet algorithms performance in 13 TeV data", Technical Report CMS-PAS-JME-16-003, CERN, Geneva, 2017. 80

[287] CMS Collaboration, "Performance of the CMS missing transverse momentum reconstruction in pp data at $\sqrt{s} = 8$ TeV", *JINST* **10** (2015), no. 02, P02006, doi:10.1088/1748-0221/10/02/P02006, arXiv:1411.0511. 80

[288] CMS Collaboration, "Missing transverse energy performance of the CMS detector", *Journal of Instrumentation* **6** (Sep, 2011) doi:10.1088/1748-0221/6/09/p09001. 80

[289] Particle Data Group Collaboration, "Review of Particle Physics", *Chin. Phys.* **C40** (2016), no. 10, 100001, doi:10.1088/1674-1137/40/10/100001. 80, 89, 91, 92, 93

[290] CMS Collaboration, "Performance of tau-lepton reconstruction and identification in CMS", *JINST* **7** (2012) P01001, doi:10.1088/1748-0221/7/01/P01001, arXiv:1109.6034. 80, 81

[291] CMS Collaboration, "Performance of reconstruction and identification of τ leptons decaying to hadrons and ν_τ in pp collisions at $\sqrt{s} = 13$ TeV", *JINST* **13** (2018), no. 10, P10005, doi:10.1088/1748-0221/13/10/P10005, arXiv:1809.02816. 80, 81

[292] CMS Collaboration, "Performance of reconstruction and identification of tau leptons in their decays to hadrons and tau neutrino in LHC Run-2", Technical Report CMS-PAS-TAU-16-002, CERN, Geneva, 2016. 81

[293] CMS Collaboration, "Reconstruction and identification of τ lepton decays to hadrons and τ_ν at CMS", *JINST* **11** (2016), no. 01, P01019, doi:10.1088/1748-0221/11/01/P01019, arXiv:1510.07488. 81

[294] A. Buckley et al., "General-purpose event generators for LHC physics", *Phys. Rept.* **504** (2011) 145–233, doi:10.1016/j.physrep.2011.03.005, arXiv:1101.2599. 81

[295] D. Reiter, "The Monte Carlo Method, an Introduction", pp. 63–78. Springer Berlin Heidelberg, Berlin, Heidelberg, 2008. doi:10.1007/978-3-540-74686-7_3. 81

[296] J. C. Collins, D. E. Soper, and G. F. Sterman, "Factorization of Hard Processes in QCD", *Adv. Ser. Direct. High Energy Phys.* **5** (1989) 1–91, doi:10.1142/9789814503266_0001, arXiv:hep-ph/0409313. 82

[297] NNPDF Collaboration, "Parton distributions for the LHC Run II", *JHEP* **04** (2015) 040, doi:10.1007/JHEP04(2015)040, arXiv:1410.8849. 82, 97

[298] E. Perez, "Parton distribution functions of the proton", *Nucl. Phys. Proc. Suppl.* **184** (2008) 43–46, doi:10.1016/j.nuclphysbps.2008.09.133. 82

[299] F. Caola, S. Forte, and J. Rojo, "HERA data and DGLAP evolution: Theory and phenomenology", *Nucl. Phys.* **A854** (2011) 32–44, doi:10.1016/j.nuclphysa.2010.08.009, arXiv:1007.5405. 82

[300] R. K. Ellis, W. J. Stirling, and B. R. Webber, "QCD and collider physics", *Camb. Monogr. Part. Phys. Nucl. Phys. Cosmol.* **8** (1996) 1–435. 82

[301] S. Höche, "Introduction to parton-shower event generators", pp. 235–295. 2015. arXiv:1411.4085. doi:10.1142/9789814678766_0005. 82, 83, 84

[302] T. Gleisberg et al., "Event generation with SHERPA 1.1", *JHEP* **02** (2009) 007, doi:10.1088/1126-6708/2009/02/007, arXiv:0811.4622. 83

[303] Z. Nagy and D. E. Soper, "What is a parton shower?", *Phys. Rev.* **D98** (2018), no. 1, 014034, doi:10.1103/PhysRevD.98.014034, arXiv:1705.08093. 82

[304] G. P. Korchemsky, "Sudakov Form-factor in QCD", *Phys. Lett.* **B220** (1989) 629–634, doi:10.1016/0370-2693(89)90799-5. 82

[305] T. Sjöstrand, "A model for initial state parton showers", *Physics Letters B* **157** (1985), no. 4, 321–325, doi:10.1016/0370-2693(85)90674-4. 82

[306] B. Andersson, G. Gustafson, G. Ingelman, and T. Sjöstrand, "Parton fragmentation and string dynamics", *Physics Reports* **97** (1983), no. 2, 31–145, doi:10.1016/0370-1573(83)90080-7. 83

[307] G. S. Bali, K. Schilling, and C. Schlichter, "Observing long color flux tubes in SU(2) lattice gauge theory", *Phys. Rev.* **D51** (1995) 5165–5198, doi:10.1103/PhysRevD.51.5165, arXiv:hep-lat/9409005. 83

[308] R. D. Field and S. Wolfram, "A QCD model for e^+e^- annihilation", *Nuclear Physics B* **213** (1983), no. 1, 65–84, doi:10.1016/0550-3213(83)90175-X. 84

[309] T. D. Gottschalk, "An improved description of hadronization in the QCD cluster model for e^+e^- annihilation", *Nuclear Physics B* **239** (1984), no. 2, 349–381, doi:10.1016/0550-3213(84)90253-0. 84

[310] D. Amati and G. Veneziano, "Preconfinement as a Property of Perturbative QCD", *Phys. Lett.* **83B** (1979) 87–92, doi:10.1016/0370-2693(79)90896-7. 84

[311] T. Sjöstrand et al., "An Introduction to PYTHIA 8.2", *Comput. Phys. Commun.* **191** (2015) 159–177, doi:10.1016/j.cpc.2015.01.024, arXiv:1410.3012. 84

[312] J. Alwall et al., "MadGraph 5 : Going Beyond", *JHEP* **06** (2011) 128, doi:10.1007/JHEP06(2011)128, arXiv:1106.0522. 84

[313] J. Alwall et al., "The automated computation of tree-level and next-to-leading order differential cross sections, and their matching to parton shower simulations", *JHEP* **07** (2014) 079, doi:10.1007/JHEP07(2014)079, arXiv:1405.0301. 84

[314] S. Alioli, P. Nason, C. Oleari, and E. Re, "A general framework for implementing NLO calculations in shower Monte Carlo programs: the POWHEG BOX", *JHEP* **06** (2010) 043, doi:10.1007/JHEP06(2010)043, arXiv:1002.2581. 84

[315] C. Oleari, "The POWHEG-BOX", *Nucl. Phys. Proc. Suppl.* **205-206** (2010) 36–41, doi:10.1016/j.nuclphysbps.2010.08.016, arXiv:1007.3893. 84

[316] GEANT4 Collaboration, "GEANT4: A Simulation toolkit", *Nucl. Instrum. Meth.* **A506** (2003) 250–303, doi:10.1016/S0168-9002(03)01368-8. 84

[317] "CMSSW framework". https://twiki.cern.ch/twiki/bin/view/CMSPublic/WorkBookCMSSWFramework. Accessed: 2019-11-06. 84

[318] CMS Collaboration, "Search for light pseudoscalar boson pairs produced from decays of the 125 GeV Higgs boson in final states with two muons and two nearby tracks in pp collisions at $\sqrt{s} = 13$ TeV", *Physics Letters B* **800** (2020) 135087, doi:10.1016/j.physletb.2019.135087. 86, 142

[319] A. Kolmogorov, "Foundations of the Theory of Probability". Chelsea Publishing, New York, 1956. 86

[320] S. Brandt, "Data Analysis: Statistical and Computational Methods for Scientists and Engineers". Springer, New York, NY, 1999. 86, 92

[321] S. M. Stigler, "Thomas Bayes's Bayesian Inference", *Journal of the Royal Statistical Society. Series A (General)* **145** (1982), no. 2, 250–258. 86

[322] R. von Mises, "Mathematical Theory of Probability and Statistics". Academic Press, 1964. 86

[323] J. Neyman, "Outline of a Theory of Statistical Estimation Based on the Classical Theory of Probability", *Philosophical Transactions of the Royal Society of London. Series A, Mathematical and Physical Sciences* **236** (1937), no. 767, 333–380. 86

[324] P. M. Lee, "Bayesian Statistics: An Introduction". Wiley Publishing, 4th edition, 2012. 87

[325] A. O'Hagan and J. J. Forster, "Kendall's Advanced Theory of Statistics, volume 2B: Bayesian Inference, second edition", volume 2B. Arnold, 2004. 87

[326] D. S. Sivia, "A review of Data Analysis: A Bayesian Tutorial", *European Journal of Engineering Education* **22** (1997), no. 2, 224–224, doi:10.1080/03043799708928277. 87

[327] L. Lista, "Statistical Methods for Data Analysis in Particle Physics". Springer International Publishing, Cham, 2016. 87, 91

[328] G. Cowan, "Statistical data analysis". 1998. 87, 88, 89, 90, 91, 92

[329] O. Behnke et al., "Data Analysis in High Energy Physics". John Wiley and Sons, Ltd, 2013. 87, 88, 89, 90, 93

[330] J. J. Gart, "An Extension of the Cramer-Rao Inequality", *Ann. Math. Statist.* **30** (06, 1959) 367–380, doi:10.1214/aoms/1177706257. 87, 90

[331] R. J. Rossi, "Probability". John Wiley and Sons, Ltd, 2018. 88

[332] F. James and M. Winkler, "MINUIT User's Guide",. 88

[333] R. J. Barlow, "Extended maximum likelihood", *Nucl. Instrum. Meth.* **A297** (1990) 496–506, doi:10.1016/0168-9002(90)91334-8. 88

[334] K. Pearson and O. M. F. E. Henrici, "Contributions to the mathematical theory of evolution. Skew variation in homogeneous material", *Philosophical Transactions of the Royal Society of London.* **186** (1895) 343–414, doi:10.1098/rsta.1895.0010. 89

[335] S. A. Murphy and A. W. van der Vaart, "On Profile Likelihood", *Journal of the American Statistical Association* **95** (2000), no. 450, 449–465. 89

[336] F. E. James, "Statistical Methods in Experimental Physics; 2nd ed.". World Scientific, Singapore, 2006. 90

[337] J. Neyman, "Outline of a Theory of Statistical Estimation Based on the Classical Theory of Probability", *Phil. Trans. Roy. Soc. Lond.* **A236** (1937), no. 767, 333–380, doi:10.1098/rsta.1937.0005. 90

[338] G. J. Feldman and R. D. Cousins, "Unified approach to the classical statistical analysis of small signals", *Phys. Rev. D* **57** (1998) 3873, doi:10.1103/PhysRevD.57.3873, arXiv:physics/9711021. 91

[339] J. Neyman, E. S. Pearson, and K. Pearson, "On the problem of the most efficient tests of statistical hypotheses", *Philosophical Transactions of the Royal Society of London. Series A, Containing Papers of a Mathematical or Physical Character* **231** (1933), no. 694-706, 289–337, doi:10.1098/rsta.1933.0009. 92

[340] R. Bellman, "Dynamic Programming". Princeton University Press, Princeton, NJ, USA, 2010. 92

[341] P. C. Bhat, "Multivariate Analysis Methods in Particle Physics", *Ann. Rev. Nucl. Part. Sci.* **61** (2011) 281, doi:10.1146/annurev.nucl.012809.104427. 92

[342] J. P. Marques de Sá, "Pattern Recognition: Concepts, Methods and Applications". Springer Berlin Heidelberg, Berlin, Heidelberg, 2001. 92

[343] K. Albertsson et al., "Machine Learning in High Energy Physics Community White Paper", *J. Phys. Conf. Ser.* **1085** (2018), no. 2, 022008, doi:10.1088/1742-6596/1085/2/022008, arXiv:1807.02876. 93

[344] T. Hastie, R. Tibshirani, and J. Friedman, "The Elements of Statistical Learning: Data Mining, Inference, and Prediction". Springer New York, New York, NY, 2009. 93

[345] A. Hoecker et al., "TMVA - Toolkit for Multivariate Data Analysis", (2007). arXiv:physics/0703039. 93

[346] I. Antcheva et al., "ROOT - A C++ framework for petabyte data storage, statistical analysis and visualization", *Comput. Phys. Commun.* **180** (2009) 2499, doi:10.1016/j.cpc.2009.08.005, arXiv:1508.07749. 93

[347] J. A. Koziol *Journal of Educational Statistics* **12** (1987), no. 4, 412–416. 93

[348] G. Cowan, K. Cranmer, E. Gross, and O. Vitells, "Asymptotic formulae for likelihood-based tests of new physics", *Eur. Phys. J.* **C71** (2011) 1554, doi:10.1140/epjc/s10052-011-1554-0,10.1140/epjc/s10052-013-2501-z, arXiv:1007.1727. 93, 94, 95

[349] S. S. Wilks, "The Large-Sample Distribution of the Likelihood Ratio for Testing Composite Hypotheses", *Annals Math. Statist.* **9** (1938), no. 1, 60–62, doi:10.1214/aoms/1177732360. 93

[350] O. Vitells and E. Gross, "Estimating the significance of a signal in a multi-dimensional search", *Astroparticle Physics* **35** (2011), no. 5, 230–234, doi:10.1016/j.astropartphys.2011.08.005. 94

[351] A. L. Read, "Modified frequentist analysis of search results (the CL_s method)", doi:10.5170/CERN-2000-005.81. 95

[352] ATLAS, CMS, LHC Higgs Combination Group Collaboration, "Procedure for the LHC Higgs boson search combination in Summer 2011", Technical Report CMS-NOTE-2011-005. ATL-PHYS-PUB-2011-11, CERN, Geneva, Aug, 2011. 95, 113

[353] LHC Collaboration, "LHC Higgs Combination Group". https://twiki.cern.ch/twiki/bin/view/LHCPhysics/HiggsCombination. Accessed: 2019-11-15. 95

[354] L. Moneta et al., "The RooStats Project", *PoS* **ACAT2010** (2010) 057, doi:10.22323/1.093.0057, arXiv:1009.1003. 95

[355] ATLAS, CMS Collaboration, "Measurements of the Higgs boson production and decay rates and constraints on its couplings from a combined ATLAS and CMS analysis of the LHC pp collision data at $\sqrt{s} = 7$ and 8 TeV", *JHEP* **08** (2016) 045, doi:10.1007/JHEP08(2016)045, arXiv:1606.02266. 95, 116, 134, 136

[356] CMS Collaboration, "Search for a very light NMSSM Higgs boson produced in decays of the 125 GeV scalar boson and decaying into τ leptons in pp collisions at $\sqrt{s} = 8$ TeV", *JHEP* **01** (2016) 079, doi:10.1007/JHEP01(2016)079, arXiv:1510.06534. 96

[357] CMS Collaboration, "Search for light bosons in decays of the 125 GeV Higgs boson in proton-proton collisions at $\sqrt{s} = 8$ TeV", *JHEP* **10** (2017) 076, doi:10.1007/JHEP10(2017)076, arXiv:1701.02032. 96

[358] CMS Collaboration, "A search for pair production of new light bosons decaying into muons", *Phys. Lett.* **B752** (2016) 146–168, doi:10.1016/j.physletb.2015.10.067, arXiv:1506.00424. 96

[359] CMS Collaboration, "Search for an exotic decay of the Higgs boson to a pair of light pseudoscalars in the final state of two muons and two τ leptons in proton-proton collisions at $\sqrt{s} = 13$ TeV", *JHEP* **11** (2018) 018, doi:10.1007/JHEP11(2018)018, arXiv:1805.04865. 96, 137

[360] CMS Collaboration, "Search for an exotic decay of the Higgs boson to a pair of light pseudoscalars in the final state with two b quarks and two τ leptons in proton-proton collisions at $\sqrt{s} = 13$ TeV", *Phys. Lett.* **B785** (2018) 462, doi:10.1016/j.physletb.2018.08.057, arXiv:1805.10191. 96, 137

[361] ATLAS Collaboration, "Search for the Higgs boson produced in association with a W boson and decaying to four b-quarks via two spin-zero particles in pp collisions at 13 TeV with the ATLAS detector", *Eur. Phys. J.* **C76** (2016), no. 11, 605, doi:10.1140/epjc/s10052-016-4418-9, arXiv:1606.08391. 96

[362] ATLAS Collaboration, "Search for new light gauge bosons in Higgs boson decays to four-lepton final states in pp collisions at $\sqrt{s} = 8$ TeV with the ATLAS detector at the LHC", *Phys. Rev.* **D92** (2015), no. 9, 092001, doi:10.1103/PhysRevD.92.092001, arXiv:1505.07645. 96

[363] ATLAS Collaboration, "Search for new phenomena in events with at least three photons collected in pp collisions at $\sqrt{s} = 8$ TeV with the ATLAS detector", *Eur. Phys. J.* **C76** (2016), no. 4, 210, doi:10.1140/epjc/s10052-016-4034-8, arXiv:1509.05051. 96

[364] ATLAS Collaboration, "Search for Higgs bosons decaying to aa in the $\mu\mu\tau\tau$ final state in pp collisions at $\sqrt{s} = 8$ TeV with the ATLAS experiment", *Phys. Rev.* **D92** (2015), no. 5, 052002, doi:10.1103/PhysRevD.92.052002, arXiv:1505.01609. 96

[365] ATLAS Collaboration, "Search for Higgs boson decays into pairs of light (pseudo)scalar particles in the $\gamma\gamma jj$ final state in pp collisions at $\sqrt{s} = 13$ TeV with the ATLAS detector", *Phys. Lett.* **B782** (2018) 750–767, doi:10.1016/j.physletb.2018.06.011, arXiv:1803.11145. 96

[366] ATLAS Collaboration, "Search for Higgs boson decays to beyond-the-Standard-Model light bosons in four-lepton events with the ATLAS detector at $\sqrt{s} = 13$ TeV", *JHEP* **06** (2018) 166, doi:10.1007/JHEP06(2018)166, arXiv:1802.03388. 96

[367] CMS Collaboration, "Search for an exotic decay of the Higgs boson to a pair of light pseudoscalars in the final state with two muons and two b quarks in pp collisions at 13 TeV", *Phys. Lett.* **B795** (2019) 398–423, doi:10.1016/j.physletb.2019.06.021, arXiv:1812.06359. 96

[368] CMS Collaboration, "A search for pair production of new light bosons decaying into muons in proton-proton collisions at 13 TeV", *Phys. Lett.* **B796** (2019) 131–154, doi:10.1016/j.physletb.2019.07.013, arXiv:1812.00380. 96

[369] ATLAS Collaboration, "Search for Higgs boson decays into a pair of light bosons in the $bb\mu\mu$ final state in pp collision at $\sqrt{s}$ =13 TeV with the ATLAS detector", *Phys. Lett.* **B790** (2019) 1–21, doi:10.1016/j.physletb.2018.10.073, arXiv:1807.00539. 96

[370] D. Curtin, R. Essig, S. Gori, and J. Shelton, "Illuminating Dark Photons with High-Energy Colliders", *JHEP* **02** (2015) 157, doi:10.1007/JHEP02(2015)157, arXiv:1412.0018. 96

[371] D. de Florian, G. Ferrera, M. Grazzini, and D. Tommasini, "Transverse-momentum resummation: Higgs boson production at the Tevatron and the LHC", *JHEP* **11** (2011) 064, doi:10.1007/JHEP11(2011)064, arXiv:1109.2109. 97

[372] CMS Collaboration, "Measurement of the Inclusive W and Z Production Cross Sections in pp Collisions at $\sqrt{s} = 7$ TeV", *JHEP* **10** (2011) 132, doi:10.1007/JHEP10(2011)132, arXiv:1107.4789. 111

[373] CMS Collaboration, "CMS Luminosity Measurements for the 2016 Data Taking Period", Technical Report CMS-PAS-LUM-17-001, CERN, Geneva, 2017. 113

[374] R. D. Cousins, "Generalization of Chisquare Goodness-of-Fit Test for Binned Data Using Saturated Models, with Application to Histograms". http://www.physics.ucla.edu/~cousins/stats/cousins_saturated.pdf. Accessed: 2019-11-28. 114

[375] G. Suzuki, "Kolmogorov-Smirnov Tests of Fit Based on Some General Bounds", *Journal of the American Statistical Association* **63** (1968), no. 323, 919–924. 114

[376] M. A. Stephens, "EDF Statistics for Goodness of Fit and Some Comparisons", *Journal of the American Statistical Association* **69** (1974), no. 347, 730–737. 114

[377] B. P. Roe et al., "Boosted decision trees, an alternative to artificial neural networks", *Nucl. Instrum. Meth.* **A543** (2005), no. 2-3, 577–584, doi:10.1016/j.nima.2004.12.018, arXiv:physics/0408124. 124

[378] U. Haisch, J. F. Kamenik, A. Malinauskas, and M. Spira, "Collider constraints on light pseudoscalars", *JHEP* **03** (2018) 178, doi:10.1007/JHEP03(2018)178, arXiv:1802.02156. 134

[379] H. E. D. Group, "Branching ratios (BRs) of the pseudoscalar a_1 in the 2HDM+S". https://twiki.cern.ch/twiki/bin/view/LHCPhysics/LHCHXSWGExoticDecay. Accessed: 2020-01-19. 134

[380] C.-Y. Chen and S. Dawson, "Exploring Two Higgs Doublet Models Through Higgs Production", *Phys. Rev.* **D87** (2013) 055016, doi:10.1103/PhysRevD.87.055016, arXiv:1301.0309. 136

ACKNOWLEDGMENTS

To those who have made the completion of this work possible, I extend my deepest thanks!

First, I want to thank my supervisor Dr. Alexei Raspereza for offering me such an interesting research project, which has led me to strengthen my knowledge in many areas of particle physics ranging from experimental-oriented topics to subjects of high theoretical content. I am particularly grateful for the trust he placed in me by inviting me to join his prestigious research group. I appreciate the level of freedom I have enjoyed during the PhD under his supervision, but at the same time, it was always clear to me that, when in doubt, I could turn to him, and there I would find his willingness and plenty of experience to help me. It has been a great pleasure being part of his team.

Equally important is my gratitude to my co-supervisor Prof. Dr. Elisabetta Gallo. She has been an excellent guide to me during these three years, all the time she was aware of the evolution of my PhD project and her support was always available to me. Her work as leader of the CMS group at DESY has been incredible, having achieved a very friendly atmosphere among all group members and being extremely efficient in carrying out the multiple tasks. For her dedication to all of us, thank you very much!

It is impossible not to mention a person who has been essential since my first steps in the field of particle physics. The invaluable and constant support I have received from Dr. Hannes Jung has played an important role in my professional career. That, along with his outstanding lessons on QCD and his precious advice on future steps, makes him someone to whom I owe my eternal gratitude.

During my research career at DESY, many other people have contributed to this work and development of myself as a scientist and I want to thank them as well. Special thanks to my colleagues in the HTauTau group, who have always found time to help me polishing every single presentation out of many that took place with excellent comments and suggestions. Huge "gracias" to my Cuban fellows at DESY: Armando, Daniela, Yasiel, Ignacio, Rafael, and José. They have always found a way to maintain a jovial atmosphere at work while at the same time offering their selfless and serious help when needed. In general, thanks to DESY, espe-

cially its CMS group, the secretaries, the International Office, the PIER Helmholtz Graduate School, “die Deutschlehrer”, and many others that I would like to mention.

In addition, I want to express my gratitude to all the professors that have stimulated in me the love for physics. From my teachers at the preselection for International Physics Olympiad to my university professors at InSTEC in Havana, my respect and recognition. As in all fields of science, the knowledge in physics is built on good foundations, and you all have forged in me a solid base without which it would have been impossible to get here.

My most important gratitude goes to my family. They have always been there for me, and I am pretty sure they will continue standing by me. To my beloved mom Leticia for raising me in a favorable environment for my personal and intellectual growth, and for her constant teachings of life throughout all these years. To my brother Darian, my grandparents Eneida, Tico, Oneida and Agustin, my dad Lazaro, and to all other members of the family; thanks for your infinite support and for making me feel the large physical distance emotionally negligible. Finally, I want to thank my life mate Sandra for bearing with me all these years, for her valuable contribution to this work and for the fruitful discussions on the topic. Her company has made this stay far from our loved ones considerably more pleasant.